Simulations of Molecular and Extended Porous Materials

A THESIS PRESENTED
BY
JACK D. EVANS
TO
THE SCHOOL OF PHYSICAL SCIENCES

IN PARTIAL FULFILLMENT OF THE REQUIREMENTS
FOR THE DEGREE OF
DOCTOR OF PHILOSOPHY
IN CHEMICAL SCIENCE

THE UNIVERSITY OF ADELAIDE
ADELAIDE, SOUTH AUSTRALIA

SEPTEMBER 2015

© *2015 - Jack D. Evans*

Supervisors:
A/Prof. Christopher J. Sumby
A/Prof. Christian J. Doonan
Dr David M. Huang
Dr Aaron W. Thornton

Declaration

I certify that this work contains no material which has been accepted for the award of any other degree or diploma in my name in any university or other tertiary institution and, to the best of my knowledge and belief, contains no material previously published or written by another person, except where due reference has been made in the text. In addition, I certify that no part of this work will, in the future, be used in a submission in my name for any other degree or diploma in any university or other tertiary institution without the prior approval of the University of Adelaide and where applicable, any partner institution responsible for the joint award of this degree.

I give consent to this copy of my thesis when deposited in the University Library, being made available for loan and photocopying, subject to the provisions of the Copyright Act 1968.

The author acknowledges that copyright of published works contained within this thesis resides with the copyright holder(s) of those works.

I also give permission for the digital version of my thesis to be made available on the web, via the University's digital research repository, the Library Search and also through web search engines, unless permission has been granted by the University to restrict access for a period of time.

Jack D. Evans September 16, 2015

Abstract

Porous materials play vital roles in many industries and currently there is intense interest in developing new examples due to their direct application to clean energy technologies. Many materials, currently the principal focus of research in this area, are constructed by strong covalent or coordination bonds extending in three-dimensions to produce a porous framework structure. However, there are increasing numbers of reports concerning discrete molecular materials that produce pore channels and voids by way of relatively weak intermolecular packing. An advantage of these compounds over conventional materials is that they maintain their molecular identity. As such they are soluble and can be processed into composite materials or used as molecular building blocks to build highly porous frameworks. Additionally, owing to the weak interactions present in these materials, they demonstrate complex gas adsorption resulting in on/off porosity and highly efficient separations.

This thesis describes the multi-scale modeling of these novel and often complicated porous materials using a combination of geometric analysis, classical molecular simulation, quantum density functional theory (DFT) and machine learning. Importantly, this work combines these tools with experimental observations to give an accurate and comprehensive atomistic picture of gas adsorption phenomena and the *in silico* design of new materials.

Initially, the performance of porous organic cage (POC) materials is illustrated for use as additives for mixed matrix membranes (MMMs) for environmentally relevant gas separations. The simulations reveal that a number of MMMs containing POCs exhibit enhanced selectivity and permeability compared with a neat polymer matrix, particularly for H_2/CO_2 separations.

Furthermore, as a consequence of the molecular nature of POCs, they can be observed in a crystalline or amorphous phase. The advantages of the amorphous phase is investigated for several reported and potential POC molecules using GPU-accelerated molecular dynamics simulations. The structures resulting from these simulations are extremely porous and, by careful analysis, potential design rules are obtained for producing amorphous materials with surface areas approaching 2000 $m^2.g^{-1}$.

In addition, previously unidentified porous molecules are sought through a thorough search of the Cambridge Structural Database (CSD). Voronoi network analysis in addition to classical and semi-empirical optimizations result in the identification of 481 organic porous crystal structures from an initial dataset of over 150 000 compounds. Subsequently, machine learning algorithms were applied to the structures to discover that molecular surface area is the molecular property that best predicts crystal porosity, as has been suggested previously by other researchers.

Finally, the hydrogen adsorption of unique metal-organic polyhedra (MOP) structures was investigated using DFT methods. The bimetallic clusters within these MOPs were experimentally observed to show strong interactions with hydrogen and the simulations assigned this interaction to result from either polarization or the formation of a "Kubas" complex.

The investigations presented here have provided additional and fundamental clarity to experimental observations of this exciting class of materials. Moreover, the computational methods provide predictions of material properties and efficiencies that have aided research in this burgeoning area.

Acknowledgments

The research contained within and the construction of this doctoral thesis would not be possible without the guidance and academic insight provided by my stellar supervisory team. I am fortunate to have the attention of so many talented individuals. David Huang, your support with all things computational and grammar has been invaluable. The thorough comments and simulation knowledge you offered has transformed many of my rough ideas to clear coherent investigations. Aaron Thornton, despite supervising me external to the university you have participated vitally to the research directing these investigations to present and important applications. I am especially thankful for the support you have offered through the CSIRO, which has allowed me to explore the world and science. Christian Doonan, it is not possible for me to describe the gratitude for your guidance and opportunities you have afforded me. You have challenged and transformed me into a world-class researcher. I hope that my future accomplishments will continue to illustrate my recognition of your effort. Finally, Christopher Sumby, thank you for encouragement and support during this complex and cross-disciplinary PhD. You have always inspired me and supported me along my academic journey, beginning almost 5 years ago.

My research would have been less exciting and applicable if it not for the great coworkers I have had the opportunity to work with. The Sumby-Doonan group has played an important role during my candidature. Thank you to Campbell "Cam" Coghlan and Jesse Teo for their comradery during the countless coffee breaks each day. I would like to thank my deputy Andrew Tarzia for the unwavering assistance he has offered during his time, I wish him boundless success in his future studies. Additionally, I would like to thank Professor David Sholl and his group for hosting me for a number of months at the Georgia Institute of Technology. This visit was extremely productive and developed my scientific skills significantly.

I have had the fortune of completing my PhD in the company of some great friends: Justin Spence and Noby Leong. Through the ups and downs of PhD-life we have attacked it together with either coffee or beer. Furthermore, the "SAcraftBros" and "Lofty et. al." groups have given me immense support in the activities of drinking beer or running. You have given me a great distraction from the sometimes arduous research.

My "partner in crime" and partner in life Carla Toop. Thank you for sharing this insurmountable task with me. Fortunately, we have continued to support each other during our separate doctoral studies through many sleepless nights and early mornings. You have kept me sane in so many ways I cannot start to list them off. I look forward to the future battles and challenges we will face by each others side.

Ultimately, I would like thank my family for their enduring assistance and support. Thanks to my little brother for your encouragement and friendship. Thank you utmost to my mother and father for supporting me throughout all my adventures in life. You have always inspired me to do my best and I will always continue to strive for that.

Contextual Statement

This thesis is composed of a mixture of standard chapters and manuscripts that form the two introductory chapters and the subsequent chapters of research and discussion. All of the manuscripts were completed during the doctoral candidature. Chapter 3 and Chapter 4 have been published in peer-reviewed, international journals.[1,2] Chapter 5 comprises a manuscript that will be submitted for publication in a peer-reviewed, international journal. Chapter 6 and Chapter 7 describe research that provided a vital contribution to the preparation of manuscripts subsequently published in or to be submitted to peer-reviewed, international journals.[3–5] As such, the work has been framed so as to portray the original work conducted by the candidate. Additionally, parts of Chapter 1 have been adapted from a review published in a peer-reviewed, international journal.[6]

The introductory chapters, Chapter 1 and Chapter 2, consist of overviews of the two areas that comprise the subject of the thesis. The first is a concise review of the materials investigated herein, including metal-organic frameworks (MOFs), metal-organic polyhedra (MOPs), porous organic cages (POCs) and extrinsically porous molecules. This review provides a broad context for the materials described in this thesis. Chapter 2 serves two functions. The first is to review recent work in computational descriptions of porous materials, work that is extended by the original work presented in this thesis. The second is to give the reader an introduction to methods presented in the research and discussion chapters.

Chapter 3 and Chapter 4 detail the results of molecular dynamics simulations of POCs in two states and their applications: the first of which is their use in mixed matrix membranes (MMMs) for kinetic separations of environmentally relevant gases (Chapter 3) and the second is amorphous networks of POCs for high surface area materials (Chapter 4). Chapter 5 illustrates the use of computational methods to search the Cambridge Structural Database (CSD) for new examples of organic porous crystals, such as POCs or extrinsically porous molecules. The structures identified were further analyzed by machine learning in an effort to determine the molecular features that promote formation of porous crystals. Fi-

nally, Chapter 6 and Chapter 7 describe methods that have provided useful to coworkers in their experimental investigations. Chapter 6 is particularly expansive as it demonstrates the fitting of isotherms to obtain experimentally derived adsorption enthalpies and subsequently uses quantum density functional theory (DFT) methods to explain and understand the interaction strength observed in new MOP samples. Chapter 7, on the other hand, contains the culmination of work that provided atomistic insights, which proved vital to two very different materials: firstly a new POC and secondly a new MOF.

Below is the list of manuscripts that constitute parts of this thesis. Please see Appendix A for statements of authorship that outline the contribution of the candidate and his co-authors to the work presented.

---

1. J. D. Evans, D. M. Huang, M. R. Hill, C. J. Sumby, A. W. Thornton, and C. J. Doonan. "Feasibility of Mixed Matrix Membrane Gas Separations Employing Porous Organic Cages". *The Journal of Physical Chemistry C* 118.3 (2014), pp. 1523–1529. DOI: 10.1021/jp4079184.

2. J. D. Evans, D. M. Huang, M. R. Hill, C. J. Sumby, D. S. Sholl, A. W. Thornton, and C. J. Doonan. "Molecular Design of Amorphous Porous Organic Cages for Enhanced Gas Storage". *The Journal of Physical Chemistry C* 119.14 (2015), pp. 7746–7754. DOI: 10.1021/jp512944r.

3. J. M. Teo, C. J. Coghlan, J. D. Evans, C. J. Sumby, and C. J. Doonan. "Bimetallic Metal-organic Polyhedra". to be submitted (2015).

4. A. Avellaneda, P. Valente, A. Burgun, J. D. Evans, A. W. Markwell-Heys, D. Rankine, D. J. Nielsen, M. R. Hill, C. J. Sumby, and C. J. Doonan. "Kinetically Controlled Porosity in a Robust Organic Cage Material". *Angewandte Chemie International Edition* 52.13 (2013), pp. 3746–3749. DOI: 10.1002/anie.201209922.

5. T. D. Keene, D. Rankine, J. D. Evans, P. D. Southon, C. J. Kepert, J. B. Aitken, C. J. Sumby, and C. J. Doonan. "Solvent-modified dynamic porosity in chiral 3D kagome frameworks". *Dalton Transactions* 42.22 (2013), pp. 7871–7879. DOI: 10.1039/C3DT00096F.

6. J. D. Evans, C. J. Sumby, and C. J. Doonan. "Synthesis and Applications of Porous Organic Cages". *Chemistry Letters* (2015). DOI: 10.1246/cl.150021.

Publications

During the candidature the author has contributed to the field with the following publications.

A. Avellaneda, P. Valente, A. Burgun, J. D. Evans, A. W. Markwell-Heys, D. Rankine, D. J. Nielsen, M. R. Hill, C. J. Sumby, and C. J. Doonan. "Kinetically Controlled Porosity in a Robust Organic Cage Material". *Angewandte Chemie International Edition* 52.13 (2013), pp. 3746–3749. DOI: 10.1002/anie.201209922.

T. D. Keene, D. Rankine, J. D. Evans, P. D. Southon, C. J. Kepert, J. B. Aitken, C. J. Sumby, and C. J. Doonan. "Solvent-modified dynamic porosity in chiral 3D kagome frameworks". *Dalton Transactions* 42.22 (2013), pp. 7871–7879. DOI: 10.1039/C3DT00096F.

J. D. Evans, D. M. Huang, M. R. Hill, C. J. Sumby, A. W. Thornton, and C. J. Doonan. "Feasibility of Mixed Matrix Membrane Gas Separations Employing Porous Organic Cages". *The Journal of Physical Chemistry C* 118.3 (2014), pp. 1523–1529. DOI: 10.1021/jp4079184.

J. D. Evans, C. J. Sumby, and C. J. Doonan. "Post-synthetic metalation of metal-organic frameworks". *Chemical Society Reviews* 43.16 (2014), pp. 5933–5951. DOI: 10.1039/C4CS00076E.

J. D. Evans, D. M. Huang, M. R. Hill, C. J. Sumby, D. S. Sholl, A. W. Thornton, and C. J. Doonan. "Molecular Design of Amorphous Porous Organic Cages for Enhanced Gas Storage". *The Journal of Physical Chemistry C* 119.14 (2015), pp. 7746–7754. DOI: 10.1021/jp512944r.

J. D. Evans, C. J. Sumby, and C. J. Doonan. "Synthesis and Applications of Porous Organic Cages". *Chemistry Letters* (2015). DOI: 10.1246/cl.150021.

P. Falcaro, R. Ricco, A. Yazdi, I. Imaz, S. Furukawa, D. Maspoch, R. Ameloot, J. D. Evans, and C. J. Doonan. "Application of Metal and Metal Oxide Nanoparticles@MOFs". *Coordination Chemistry Reviews* (2015). DOI: 10.1016/j.ccr.2015.08.002.

Contents

Acronyms

BET Brunauer–Emmett–Teller

IUPAC International Union of Pure and Applied Chemistry

GCMC grand canonical Monte Carlo

MD molecular dynamics

POC porous organic cage

MMM mixed matrix membrane

MOF metal-organic framework

MOP metal-organic polyhedra

ZIF zeolitic imidizolate framework

UFF universal force-field

DFT density functional theory

HOMO highest occupied molecular orbital

LUMO lowest unoccupied molecular orbital

RDF radial distribution function

PXRD powder X-ray diffraction

GGA generalized gradient approximation

LDA local-density approximation

PMC porous molecular crystal

oPMC organic porous molecular crystal

CSD Cambridge Structural Database

SVM support vector machine

RBF radial basis function

COF covalent organic framework

For Mum and Dad.

Benard of Chartres used to compare us to [puny] dwarfs perched on the shoulders of giants. He pointed out that we see more and farther than our predecessors, not because we have keener vision or greater height, but because we are lifted up and borne aloft on their gigantic stature.

John of Salisbury

1 Introduction

The field of porous materials is wide-ranging and has major applications in science and engineering. With examples found in both biological systems[1] and natural minerals,[2] porous materials have been used industrially for many years.[3] Examples of these widespread applications include petrochemical catalysis,[4] hemostatic agents[5] and soil treatment.[6]

Materials under this large umbrella can be classified by the pore sizes that traverse the material. The International Union of Pure and Applied Chemistry (IUPAC) has defined the following groups: microporous (<2 nm), mesoporous (2–50 nm) and macroporous (>50 nm).[7] As the work herein is concerned with adsorption of gases and other small molecules, the materials of focus in this thesis will be those classified as microporous. Furthermore, the above can be classified as framework materials or molecular materials. Pore structures of framework materials are constructed from covalent or metal-ligand bonds.[8] On the other hand, molecular materials have either voids intrinsic to macrocyclic molecules or pore structures supported by non-covalent interactions extrinsic to the molecule or a combination of the two.[9]

Outlined below, the porous materials that are the subject of this thesis cover a wide range of chemical makeup, dimensionality and applications.

1.1 Metal-organic Frameworks

Metal-organic frameworks (MOFs) are porous materials that have seen expansive and rapid growth since the demonstration of immense microporosity by Yaghi and coworkers of MOF-5, a three-dimensional framework constructed from Zn and 1,4-benzenedicarboxylate.[10] MOF materials are of particular interest as they are constructed using a modular chemical approach that uses different metal nodes and ligands to finely tune the structure and properties of the resulting framework, as shown in Figure 1.1. The properties of porous solids, such as porous silicas, produced from traditional hydrothermal synthetic methods are often difficult to control.[11] The reactants often do not retain their structure during the reaction, this leads to poor correlation between reactants and products. In contrast, MOF materials can be designed by beginning with well-defined molecular building blocks that maintain their structural integrity throughout the synthesis.[12]

This method has produced a multitude of framework structures using four primary strategies.[13] Firstly, the geometric addition of metal nodes and ligands of different connectivity has resulted in a number of preferred topologies.[14] Secondly, the modular approach allows for facile production of isoreticular series by altering the ligand length.[15] Thirdly, as MOFs are constructed from organic ligands, subsequent chemical modification at these sites is possible. This post-synthetic modification is a powerful strategy to access catalytically active and otherwise not synthetically feasible MOFs.[16] Finally, further variation is attained by using a number of linkers with different organic functionalities to produce multivariate MOFs.[17] This unique synthetic approach to the design of MOFs has yielded a rich variety of porous framework structures.

The powerful design principles described above allow significant control over the framework structure and pore chemistry.[18] Distinctly, the structure of a MOF can be significantly altered while retaining the underlying topology of the material, which can be used to produce a pore environment tuned for a chosen application. In particular, this is observed in the kagome MOF series described and investigated in Chapter 7. In this example, the gas adsorption characteristics of the MOF was tuned by the attachment of different solvent molecules to bare coordination sites of the Ni centers that comprised the structural building unit.[19]

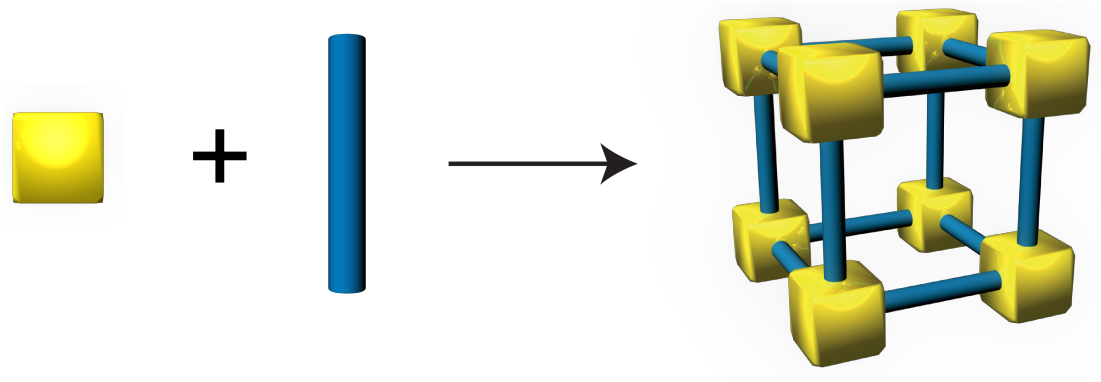

Figure 1.1: Example of the approach employed in the design and formation of metal-organic framework (MOF) materials. Here the blocks represent metal nodes and the rods the organic ligand. Please note the resulting cube is only one section of an extended structure.

1.2 Porous Molecular Solids

The majority of research in the area of porous materials has been focused on extended solids that possess open architectures with interconnected pores and three-dimensionally attached units, namely zeolites,[8] covalent organic frameworks (COFs),[20] and MOFs.[13] Recently, shape-persistent cage molecules[21,22] have garnered significant interest as a novel class of porous solids which afford ultra high porosities but maintain their molecular identity, for example they are soluble and thus can be processed into composite materials[23] or employed as molecular building blocks for highly porous frameworks.[24] Unlike extended network materials that are constructed from covalent or coordination bonds, these molecules are arranged in the solid-state via relatively weak crystal packing forces. As a result, predicting three-dimensional structures of bulk solids from a particular cage building unit is a major challenge. Nevertheless, we note that Cooper and coworkers have made great strides in predicting the crystal structure of porous molecular crystals, despite these challenges.[25,26] An advantage of such weak molecular interactions is that they can lead to adaptable structures that engender advanced properties such as adsorbate dependent on/off porosity switching,[27] organic alloys[28] and solvent template porosity control.[25] In addition, by modifying how the cages are processed, either crystalline or amorphous porous solids can be realized, thus expanding the possibilities for material fabrication.[28–30]

1.2.1 Metal-organic Polyhedra

One class of these structures are metal-organic polyhedra (MOP), self-assembled discrete coordination complexes that form cage-like structures surrounding a substantial cavity. Similar to MOFs, MOPs are produced from transition metal ions with either nitrogen or carboxylate donor organic ligands. This once again gives unprecedented ability to design the size and functionality of these molecules for specific applications.[22] Many of these large coordination molecules have been produced as synthetic receptors. Fujita and coworkers have reported a number of exceptional examples using protected Pd(II) and Pt(II) centers to produce an extensive array of geometries.[31] Though many of these beautiful structures have applications in binding large guests and have shown potential for the targeted delivery of drug molecules,[32] few have demonstrated permanent porosity for gas adsorption,[33] a vital property for a number of potential applications. The prototypical example of a MOP, MOP-1, which is constructed from 24 1,3-benzenedicarboxylate ligands and 12 copper(II) paddlewheel clusters ($Cu_2(CO_2)_4$) to give a 25 Å sized cuboctahedron, as shown in Figure 1.2.[34] Notably, 1,4-benzenedicarboxylate which has 180° (straight) angles between carboxylate donors, has previously been used to produce an infinite periodic MOF structure.[35] In contrast to this, the isomer 1,3-benzenedicarboxylate, with 120° between carboxylate donors, is optimal for constructing a discrete truncated cuboctahedron molecule. Subsequently, Zhou and coworkers have constructed similar MOP structures with a number of different ligand geometries and exohedral functionality.[36] Upon removal of solvent guests, MOP samples generally become amorphous. However, these samples can demonstrate the ability to selectively adsorb H_2 and O_2 over N_2 and Ar. Additionally, Zhou *et al.* have reported a MOP designed to trap CO_2 molecules in an engineered cavity.[37]

1.2.2 Porous Organic Cages

Alternatively, cage structures can be constructed of organic units to give porous organic cages (POCs), illustrated in Figure 1.3.[38] Dynamic covalent chemistry has been widely exploited to generate POCs as it facilitates 'one-pot' multicomponent syntheses in high yields.[39] For example, imine and boronate ester chemistry have been used to generate organic cage molecules of varied topology and cavity size, shown in Figure 1.3. Indeed, Cooper and co-workers have established high-yielding synthetic procedures for imine-linked cages of tetrahedral geometry.[40] Typically, these cages are synthesized from 1,3,5-triformylbenzene and flexible diamines via a one-pot 4(aldehyde) + 6(amine) cycloimination reac-

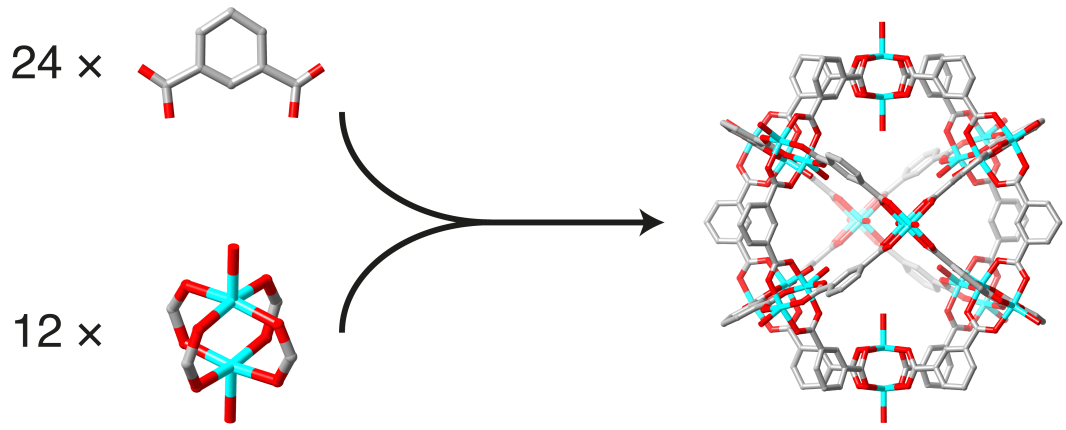

Figure 1.2: Formation and structure of the MOP-1[34] system produced by the self-assembly of 24 1,3-benzenedicarboxylate ligands and 12 copper(II) paddlewheel clusters.

tion. Furthermore, substituted diamines can be employed to precisely control the functionality of these cages. Using more synthetically challenging building blocks, the Mastalerz laboratory has synthesized a variety of porous imine-based cages of varied topology and cavity size.[41–45] Recently, this group also reported shape-persistent cages linked via boronate ester moieties.[46,47] Porous solids composed of cages with an entirely carbon based architecture have also been reported.[48,49] Given that C-C bonds are irreversible under general laboratory conditions, a stepwise synthetic approach was necessary to afford these molecules. Ultimately, a three-fold alkyne coupling reaction was employed to yield a cage molecule of elongated dipyramidal geometry. Due to the large window sizes and fluted structure, these cages are able to interdigitate and form relatively densely packed solids. However, significantly porous crystalline structures can be accessed via a kinetically trapped polymorph.

Importantly, the porosity of POCs has dramatically increased to values that are comparable to many MOFs, as shown in Figure 1.4 (approaching 4000 $m^2.g^{-1}$).[46] These advances can be attributed to early research in imine-based cages that explored some important design principles for achieving porosity in the bulk solid. For example, molecular rigidity is important for generating permanent solvent-accessible channels, as large diameter cages with flexible architectures have been found not to maintain their structure subsequent to the removal of solvent.[45,51] Furthermore, increasing the cavity size in rigid materials can lead to significant porosity, and indeed resulted in the first example of mesoporosity in a molecular species.[46] Conversely, reducing the accessible internal pore size of the cage via functionalization leads to a reduction in surface area.[52] Finally, the interplay between three-dimensional structure and porosity was clearly elucidated in

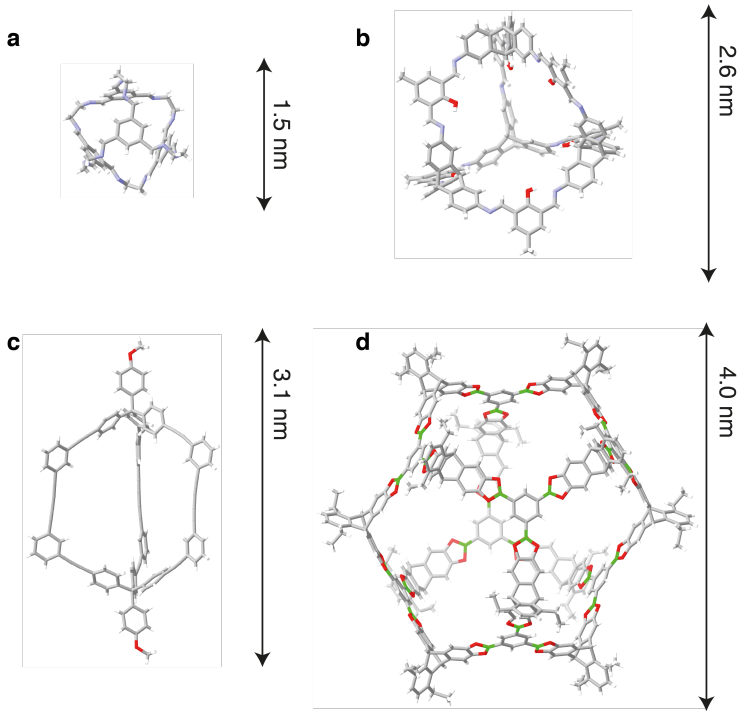

Figure 1.3: Examples of porous organic cage (POC) structures with their respective sizes indicated to the right. From a - d: an imine-based cage of tetrahedral geometry,[38] imine-based cage of adamantoid geometry,[41] a cage constructed from C-C bonds with an elongated-dipyramidal geometry[48] and a boronate-ester based cage of cuboctahedral geometry.[46] This figure was adapted from work featured in reference 50.

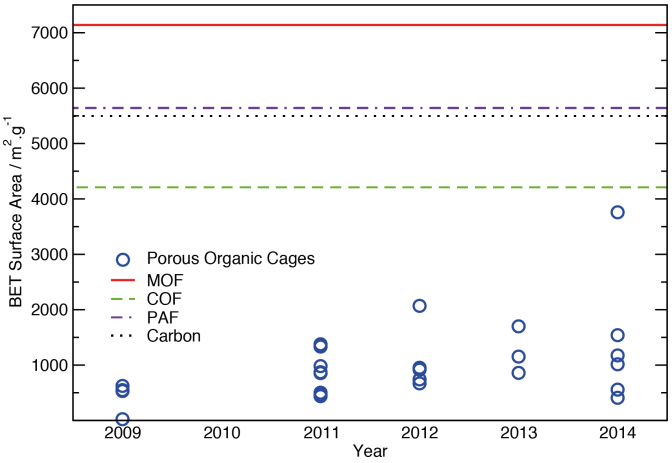

Figure 1.4: Chronological rise in surface area of porous organic cage (POC). For reference, the highest reported surface areas for metal-organic framework (MOF),[53] covalent organic frameworks (COF),[54] porous aromatic frameworks (PAF),[55] and carbon are also shown as lines.[56] This figure was taken from work featured in reference 50.

studies where exohedrally functionalized, topologically analogous cages led to dramatic differences in surface area.[43] However, controlling porosity via this strategy remains an ongoing challenge as, in general, the impact of a specific functional group on the crystal structure of the POC cannot be straightforwardly elucidated *a priori*.

A consequence of the discrete nature of POCs is that solid-state, molecular, packing forces determine the origin of porosity. These relatively weak crystal packing forces can be perturbed to afford porous amorphous solids and advanced properties such as solvent modified 'on/off' porosity switching.[27] Such characteristics are unique to molecular solids and have thus stimulated active research in the field. However, these weak packing forces also give rise to complex porosity. For example, accessible surface area can arise from the intrinsic volume deriving from each cage unit, interconnection of the extrinsic voids between the cages that are formed by virtue of inefficient packing, or a combination of both.

1.2.3 Extrinsically Porous Molecules

Interestingly, porous materials can also be produced by simple molecules that pack in the solid-state to give a pore network. In contrast to MOP and POC structures, the porosity in these systems is a result of wholly extrinsic volume.[9,57,58] In these cases, inefficient packing between molecules produces voids and pore volume. Figure 1.5 illustrates the simple molecular structure of salient examples: Dianin's compound,[59] tris(o-phenylenedioxy)cyclotriphosphazene[60] and 3,3',4,4'-

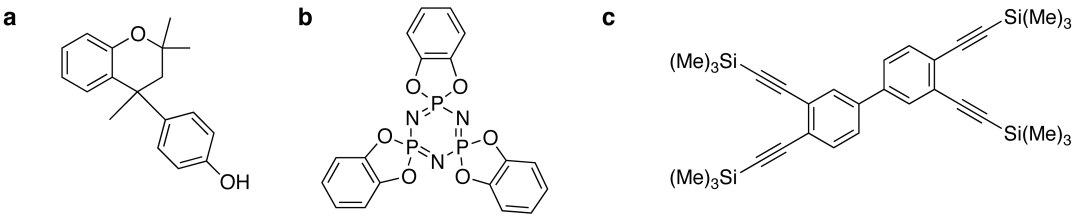

Figure 1.5: Examples of the chemical structures of extrinsically porous molecules: Dianin's compound, tris(o-phenylenedioxy)cyclotriphosphazene and 3,3',4,4'-tetra(trimethylsilylethynyl)biphenyl. (a-c, respectively)

tetra(trimethylsilylethynyl)biphenyl.[61] An important property of these materials is that they can demonstrate porosity without interconnected pores. Dianin's compound has been extensively investigated for this behavior. The crystal structure displays voids that are interconnected by hydrogen-bonded rings of narrow channel diameters (2.5 Å). It was reported that a number of gas molecules, including Ar, Kr, Xe, CO_2, CH_4 and C_2H_6, can be adsorbed by the crystal.[59] Many of these adsorbates are formally restricted from diffusing by the narrow interconnecting channels. In these cases it is likely that complex gas or vapor adsorption occurs by cooperative diffusion mechanisms. Notably, this behavior has been well-studied by Atwood *et. al.* for a number of calixarene structures, which are formally considered nonporous crystals.[58,62,63]

In MOFs, directional covalent or coordination bonds between molecular components stabilizes pore volumes subsequent to the removal of solvent and guest molecules. Contrastingly, molecular materials are comprised by only weak non-covalent interactions. As a result, these materials are quite rare compared to porous network materials as molecules generally pack as densely as possible to maximize attractive intermolecular contacts.[64]

1.3 References

1. N. Peppas, Y. Huang, M. Torres-Lugo, J. Ward, and J. Zhang. "Physicochemical foundations and structural design of hydrogels in medicine and biology". *Annual review of biomedical engineering* 2.1 (2000), pp. 9–29. DOI: 10.1146/annurev.bioeng.2.1.9.

2. J. J. Pignatello and B. Xing. "Mechanisms of slow sorption of organic chemicals to natural particles". *Environmental Science & Technology* 30.1 (1995), pp. 1–11. DOI: 10.1021/es940683g.

3. N. Chen. *Shape selective catalysis in industrial applications*. Vol. 65. CRC press, 1996.

4. W. Vermeiren and J.-P. Gilson. "Impact of Zeolites on the Petroleum and Petrochemical Industry". *Topics in Catalysis* 52.9 (2009), pp. 1131–1161. DOI: 10.1007/s11244-009-9271-8.

5. P. M. Rhee, C. Brown, M. Martin, A. Salim, D. Plurad, D. Green, L. Chambers, D. Demetriades, G. Velmahos, and H. Alam. "QuikClot Use in Trauma for Hemorrhage Control: Case Series of 103 Documented Uses". *Journal of Trauma-Injury Infection* 64.4 (2008), pp. 1093–1099. DOI: 10.1097/TA.0b013e31812f6dbc.

6. F. A. Mumpton. “La roca magica: Uses of natural zeolites in agriculture and industry”. *Proceedings of the National Academy of Sciences* 96.7 (1999), pp. 3463–3470. DOI: 10.1073/pnas.96.7.3463.

7. J. Rouquerol, D. Avnir, C. W. Fairbridge, D. H. Everett, J. M. Haynes, N. Pernicone, J. D. F. Ramsay, K. S. W. Sing, and K. K. Unger. “Recommendations for the characterization of porous solids (Technical Report)”. *Pure and Applied Chemistry* 66.8 (1994), pp. 1739–1758. DOI: 10.1351/pac199466081739.

8. M. E. Davis. “Ordered porous materials for emerging applications”. *Nature* 417.6891 (2002), pp. 813–821. DOI: 10.1038/nature00785.

9. N. B. McKeown. “Nanoporous molecular crystals”. *Journal of Materials Chemistry* 20.47 (2010), pp. 10588–10597. DOI: 10.1039/C0JM01867H.

10. H. Li, M. Eddaoudi, M. O’Keeffe, and O. M. Yaghi. “Design and synthesis of an exceptionally stable and highly porous metal-organic framework”. *Nature* 402.6759 (1999), pp. 276–279. DOI: 10.1038/46248.

11. C. S. Cundy and P. A. Cox. “The Hydrothermal Synthesis of Zeolites: History and Development from the Earliest Days to the Present Time”. *Chemical Reviews* 103.3 (2003), pp. 663–702. DOI: 10.1021/cr020060i.

12. O. M. Yaghi, H. Li, C. Davis, D. Richardson, and T. L. Groy. “Synthetic Strategies, Structure Patterns, and Emerging Properties in the Chemistry of Modular Porous Solids”. *Accounts of Chemical Research* 31.8 (1998), pp. 474–484. DOI: 10.1021/ar970151f.

13. H. Furukawa, K. E. Cordova, M. O’Keeffe, and O. M. Yaghi. “The Chemistry and Applications of Metal-Organic Frameworks”. *Science* 341.6149 (2013). DOI: 10.1126/science.1230444.

14. O. M. Yaghi, M. O’Keeffe, N. W. Ockwig, H. K. Chae, M. Eddaoudi, and J. Kim. “Reticular synthesis and the design of new materials”. *Nature* 423.6941 (2003), pp. 705–714. DOI: 10.1038/nature01650.

15. M. Eddaoudi, J. Kim, N. Rosi, D. Vodak, J. Wachter, M. O’Keeffe, and O. M. Yaghi. “Systematic Design of Pore Size and Functionality in Isoreticular MOFs and Their Application in Methane Storage”. *Science* 295.5554 (2002), pp. 469–472. DOI: 10.1126/science.1067208.

16. Z. Wang and S. M. Cohen. “Postsynthetic modification of metal-organic frameworks”. *Chemical Society Reviews* 38 (5 2009), pp. 1315–1329. DOI: 10.1039/B802258P.

17. H. Deng, C. J. Doonan, H. Furukawa, R. B. Ferreira, J. Towne, C. B. Knobler, B. Wang, and O. M. Yaghi. “Multiple Functional Groups of Varying Ratios in Metal-Organic Frameworks”. *Science* 327.5967 (2010), pp. 846–850. DOI: 10.1126/science.1181761.

18. J. D. Evans, C. J. Sumby, and C. J. Doonan. “Post-synthetic metalation of metal-organic frameworks”. *Chemical Society Reviews* 43.16 (2014), pp. 5933–5951. DOI: 10.1039/C4CS00076E.

19. T. D. Keene, D. Rankine, J. D. Evans, P. D. Southon, C. J. Kepert, J. B. Aitken, C. J. Sumby, and C. J. Doonan. “Solvent-modified dynamic porosity in chiral 3D kagome frameworks”. *Dalton Transactions* 42.22 (2013), pp. 7871–7879. DOI: 10.1039/C3DT00096F.

20. A. P. Côté, A. I. Benin, N. W. Ockwig, M. O’Keeffe, A. J. Matzger, and O. M. Yaghi. “Porous, Crystalline, Covalent Organic Frameworks”. *Science* 310.5751 (2005), pp. 1166–1170. DOI: 10.1126/science.1120411.

21. G. Zhang and M. Mastalerz. “Organic cage compounds – from shape-persistency to function”. *Chemical Society Reviews* 43.6 (2014), pp. 1934–1947. DOI: 10.1039/C3CS60358J.

22. D. J. Tranchemontagne, Z. Ni, M. O’Keeffe, and O. M. Yaghi. “Reticular Chemistry of Metal–Organic Polyhedra”. *Angewandte Chemie International Edition* 47.28 (2008), pp. 5136–5147. DOI: 10.1002/anie.200705008.

23. A. F. Bushell, P. M. Budd, M. P. Attfield, J. T. A. Jones, T. Hasell, A. I. Cooper, P. Bernardo, F. Bazzarelli, G. Clarizia, and J. C. Jansen. “Nanoporous Organic Polymer/Cage Composite Membranes”. *Angewandte Chemie International Edition* 52.4 (2013), pp. 1253–1256. DOI: 10.1002/anie.201206339.

24. J. J. Perry IV, J. A. Perman, and M. J. Zaworotko. “Design and synthesis of metal-organic frameworks using metal-organic polyhedra as supermolecular building blocks”. *Chemical Society Reviews* 38 (5 2009), pp. 1400–1417. DOI: 10.1039/B807086P.

25. T. Hasell et al. “Controlling the Crystallization of Porous Organic Cages: Molecular Analogs of Isoreticular Frameworks Using Shape-Specific Directing Solvents”. *Journal of the American Chemical Society* 136.4 (2014), pp. 1438–1448. DOI: 10.1021/ja409594s.

26. E. O. Pyzer-Knapp, H. P. G. Thompson, F. Schiffmann, K. E. Jelfs, S. Y. Chong, M. A. Little, A. I. Cooper, and G. M. Day. “Predicted crystal energy landscapes of porous organic cages”. *Chemical Science* 5.6 (2014), pp. 2235–2245. DOI: 10.1039/C4SC00095A.

27. J. T. A. Jones et al. “On–Off Porosity Switching in a Molecular Organic Solid”. *Angewandte Chemie International Edition* 50.3 (2011), pp. 749–753. DOI: 10.1002/anie.201006030.

28. T. Hasell, S. Y. Chong, M. Schmidtmann, D. J. Adams, and A. I. Cooper. “Porous Organic Alloys”. *Angewandte Chemie International Edition* 51.29 (2012), pp. 7154–7157. DOI: 10.1002/anie.201202849.

29. S. Jiang, K. E. Jelfs, D. Holden, T. Hasell, S. Y. Chong, M. Haranczyk, A. Trewin, and A. I. Cooper. “Molecular Dynamics Simulations of Gas Selectivity in Amorphous Porous Molecular Solids”. *Journal of the American Chemical Society* 135.47 (2013), pp. 17818–17830. DOI: 10.1021/ja407374k.

30. E. V. Perez, K. J. B. Jr., J. P. Ferraris, and I. H. Musselman. “Metal-organic polyhedra 18 mixed-matrix membranes for gas separation”. *Journal of Membrane Science* 463 (2014), pp. 82–93. DOI: 10.1016/j.memsci.2014.03.045.

31. M. Fujita. “Metal-directed self-assembly of two- and three-dimensional synthetic receptors”. *Chemical Society Reviews* 27 (6 1998), pp. 417–425. DOI: 10.1039/A827417Z.

32. J. E. M. Lewis, E. L. Gavey, S. A. Cameron, and J. D. Crowley. “Stimuli-responsive Pd_2L_4 metallo-supramolecular cages: towards targeted cisplatin drug delivery”. *Chemical Science* 3 (3 2012), pp. 778–784. DOI: 10.1039/C2SC00899H.

33. A. C. Sudik, A. R. Millward, N. W. Ockwig, A. P. Côté, J. Kim, and O. M. Yaghi. “Design, Synthesis, Structure, and Gas (N_2, Ar, CO_2, CH_4, and H_2) Sorption Properties of Porous Metal-Organic Tetrahedral and Heterocuboidal Polyhedra”. *Journal of the American Chemical Society* 127.19 (2005), pp. 7110–7118. DOI: 10.1021/ja042802q.

34. M. Eddaoudi, J. Kim, J. B. Wachter, H. K. Chae, M. O’Keeffe, and O. M. Yaghi. “Porous Metal—Organic Polyhedra: 25 ÅCuboctahedron Constructed from 12 $Cu_2(CO_2)_4$ Paddle-Wheel Building Blocks”. *Journal of the American Chemical Society* 123.18 (2001), pp. 4368–4369. DOI: 10.1021/ja0104352.

35. H. Li, M. Eddaoudi, T. L. Groy, and O. M. Yaghi. “Establishing Microporosity in Open Metal-Organic Frameworks: Gas Sorption Isotherms for Zn(BDC) (BDC = 1,4-Benzenedicarboxylate)”. *Journal of the American Chemical Society* 120.33 (1998), pp. 8571–8572. DOI: 10.1021/ja981669x.

36. J.-R. Li and H.-C. Zhou. “Bridging-ligand-substitution strategy for the preparation of metal–organic polyhedra”. *Nature Chemistry* 2.10 (2010), pp. 893–898. DOI: 10.1038/nchem.803.

37. J.-R. Li, J. Yu, W. Lu, L.-B. Sun, J. Sculley, P. B. Balbuena, and H.-C. Zhou. “Porous materials with pre-designed single-molecule traps for CO_2 selective adsorption”. *Nature Communications* 4 (2013), p. 1538. DOI: 10.1038/ncomms2552.

38. T. Tozawa et al. “Porous organic cages”. *Nature Materials* 8.12 (2009), pp. 973–978. DOI: 10.1038/nmat2545.

39. S. J. Rowan, S. J. Cantrill, G. R. L. Cousins, J. K. M. Sanders, and J. F. Stoddart. “Dynamic Covalent Chemistry”. *Angewandte Chemie International Edition* 41.6 (2002), pp. 898–952. DOI: 10.1002/1521-3773(20020315)41:6<898::AID-ANIE898>3.0.CO;2-E.

40. D. P. Lydon, N. L. Campbell, D. J. Adams, and A. I. Cooper. “Scalable Synthesis for Porous Organic Cages”. *Synthetic Communications* 41.14 (2011), pp. 2146–2151. DOI: 10.1080/00397911.2010.499487.

41. M. Mastalerz, M. W. Schneider, I. M. Oppel, and O. Presly. “A Salicylbisimine Cage Compound with High Surface Area and Selective CO_2/CH_4 Adsorption”. *Angewandte Chemie International Edition* 50.5 (2011), pp. 1046–1051. DOI: 10.1002/anie.201005301.

42. M. Mastalerz. “One-pot synthesis of a shape-persistent endo-functionalised nano-sized adamantoid compound”. *Chemical Communications* 39 (2008), pp. 4756–4758. DOI: 10.1039/B808990F.

43. M. W. Schneider, H.-J. S. Hauswald, R. Stoll, and M. Mastalerz. “A shape-persistent exo-functionalized [4 + 6] imine cage compound with a very high specific surface area”. *Chemical Communications* 48.79 (2012), pp. 9861–9863. DOI: 10.1039/C2CC35002E.

44. M. W. Schneider, I. M. Oppel, H. Ott, L. G. Lechner, H.-J. S. Hauswald, R. Stoll, and M. Mastalerz. “Periphery-Substituted [4+6] Salicylbisimine Cage Compounds with Exceptionally High Surface Areas: Influence of the Molecular Structure on Nitrogen Sorption Properties”. *Chemistry – A European Journal* 18.3 (2012), pp. 836–847. DOI: 10.1002/chem.201102857.

45. M. W. Schneider, I. M. Oppel, and M. Mastalerz. “Exo-Functionalized Shape-Persistent [2+3] Cage Compounds: Influence of Molecular Rigidity on Formation and Permanent Porosity”. *Chemistry – A European Journal* 18.14 (2012), pp. 4156–4160. DOI: 10.1002/chem.201200032.

46. G. Zhang, O. Presly, F. White, I. M. Oppel, and M. Mastalerz. "A Permanent Mesoporous Organic Cage with an Exceptionally High Surface Area". *Angewandte Chemie International Edition* 53.6 (2014), pp. 1516–1520. DOI: 10.1002/anie.201308924.

47. G. Zhang, O. Presly, F. White, I. M. Oppel, and M. Mastalerz. "A shape-persistent quadruply interlocked giant cage catenane with two distinct pores in the solid state". *Angewandte Chemie International Edition* 53.20 (2014), pp. 5126–5130. DOI: 10.1002/anie.201400285.

48. A. Avellaneda, P. Valente, A. Burgun, J. D. Evans, A. W. Markwell-Heys, D. Rankine, D. J. Nielsen, M. R. Hill, C. J. Sumby, and C. J. Doonan. "Kinetically Controlled Porosity in a Robust Organic Cage Material". *Angewandte Chemie International Edition* 52.13 (2013), pp. 3746–3749. DOI: 10.1002/anie.201209922.

49. C. Zhang, Q. Wang, H. Long, and W. Zhang. "A Highly C70 Selective Shape-Persistent Rectangular Prism Constructed through One-Step Alkyne Metathesis". *Journal of the American Chemical Society* 133.51 (2011), pp. 20995–21001. DOI: 10.1021/ja210418t.

50. J. D. Evans, C. J. Sumby, and C. J. Doonan. "Synthesis and Applications of Porous Organic Cages". *Chemistry Letters* (2015). DOI: 10.1246/cl.150021.

51. M. Liu, M. A. Little, K. E. Jelfs, J. T. A. Jones, M. Schmidtmann, S. Y. Chong, T. Hasell, and A. I. Cooper. "Acid- and Base-Stable Porous Organic Cages: Shape Persistence and pH Stability via Post-synthetic "Tying" of a Flexible Amine Cage". *Journal of the American Chemical Society* 136.21 (2014), pp. 7583–7586. DOI: 10.1021/ja503223j.

52. M. W. Schneider, I. M. Oppel, A. Griffin, and M. Mastalerz. "Post-Modification of the Interior of Porous Shape-Persistent Organic Cage Compounds". *Angewandte Chemie International Edition* 52.13 (2013), pp. 3611–3615. DOI: 10.1002/anie.201208156.

53. O. K. Farha, I. Eryazici, N. C. Jeong, B. G. Hauser, C. E. Wilmer, A. A. Sarjeant, R. Q. Snurr, S. T. Nguyen, A. Ö. Yazaydın, and J. T. Hupp. "Metal–Organic Framework Materials with Ultrahigh Surface Areas: Is the Sky the Limit?" *Journal of the American Chemical Society* 134.36 (2012), pp. 15016–15021. DOI: 10.1021/ja3055639.

54. H. M. El-Kaderi, J. R. Hunt, J. L. Mendoza-Cortés, A. P. Côté, R. E. Taylor, M. O'Keeffe, and O. M. Yaghi. "Designed Synthesis of 3D Covalent Organic Frameworks". *Science* 316.5822 (2007), pp. 268–272. DOI: 10.1126/science.1139915.

55. T. Ben et al. "Targeted Synthesis of a Porous Aromatic Framework with High Stability and Exceptionally High Surface Area". *Angewandte Chemie International Edition* 48.50 (2009), pp. 9457–9460. DOI: 10.1002/anie.200904637.

56. M. Hu, J. Reboul, S. Furukawa, N. L. Torad, Q. Ji, P. Srinivasu, K. Ariga, S. Kitagawa, and Y. Yamauchi. "Direct Carbonization of Al-Based Porous Coordination Polymer for Synthesis of Nanoporous Carbon". *Journal of the American Chemical Society* 134.6 (2012), pp. 2864–2867. DOI: 10.1021/ja208940u.

57. J. Tian, P. K. Thallapally, and B. P. McGrail. "Porous organic molecular materials". *CrystEngComm* 14.6 (2012), p. 1909. DOI: 10.1039/c2ce06457j.

58. S. J. Dalgarno, P. K. Thallapally, L. J. Barbour, and J. L. Atwood. "Engineering void space in organic van der Waals crystals: calixarenes lead the way". *Chemical Society Reviews* 36.2 (2007), pp. 236–245. DOI: 10.1039/B606047C.

59. R. M. Barrer and V. H. Shanson. "Dianin's compound as a zeolitic sorbent". *Journal of the Chemical Society, Chemical Communications* 9 (1976), p. 333. DOI: 10.1039/c39760000333.

60. P. Sozzani, S. Bracco, A. Comotti, L. Ferretti, and R. Simonutti. "Methane and Carbon Dioxide Storage in a Porous van der Waals Crystal". *Angewandte Chemie International Edition* 44.12 (2005), pp. 1816–1820. DOI: 10.1002/anie.200461704.

61. K. J. Msayib et al. "Nitrogen and Hydrogen Adsorption by an Organic Microporous Crystal". *Angewandte Chemie International Edition* 48.18 (2009), pp. 3273–3277. DOI: 10.1002/anie.200900234.

62. J. L. Atwood, L. J. Barbour, and A. Jerga. "Storage of Methane and Freon by Interstitial van der Waals Confinement". *Science* 296.5577 (2002), pp. 2367–2369. DOI: 10.1126/science.1072252.

63. J. L. Atwood. "Guest Transport in a Nonporous Organic Solid via Dynamic van der Waals Cooperativity". *Science* 298.5595 (2002), pp. 1000–1002. DOI: 10.1126/science.1077591.

64. L. J. Barbour. "Crystal porosity and the burden of proof". *Chemical Communications* 11 (2006), p. 1163. DOI: 10.1039/b515612m.

2

Computational Methods

A number of interesting and complex porous materials are of interest for applications in gas storage, separation and catalysis. An important tool used by researchers in this field is modeling and simulation. The computational prediction of structure, adsorption, and diffusion allows for *in silico* discovery and ranking of novel structures in addition to atomistic insight into many of the complex behaviors present in these systems.

2.1 Pore Identification and Analysis

Surface area and pore metrics are vital characteristics of porous materials, particularly for applications in gas storage and separation where the performance of materials is often correlated with these quantities. Notably, metal-organic frameworks (MOFs) are reported to have very high surface areas, over 7000 $m^2.g^{-1}$.[1] However, the surface area cannot be measured directly from experiments. Surface area is commonly obtained by the application of Brunauer–Emmett–Teller (BET) theory to a N_2 isotherm obtained at 77 K. This is a standard procedure that allows for comparisons among different materials.[2] The BET method considers the multilayer adsorption of gas molecules, but the method relies on a number of assumptions: adsorption occurs on a homogeneous surface, no interaction between multilayers and Langmuir theory is applicable to each layer. Practically, BET theory is applied by plotting $\frac{1}{\nu}[(p_0/p) - 1]$ against p_0/p, where ν is the quantity

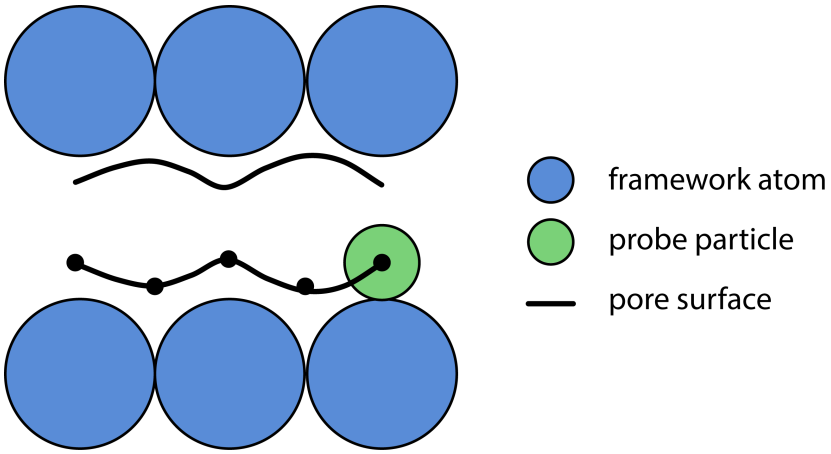

Figure 2.1: Representation of the geometric method used to measure the pore volume and surface area in porous materials.

of adsorbed gas and p and p_0 are the equilibrium and saturation pressure of the adsorbate at the temperature of adsorption. This will produce a linear plot for the pressure range $0.05 \lessapprox p_0/p \lessapprox 0.35$, with the slope and intercept directly related to the monolayer adsorbed quantity which is subsequently related to the specific surface area of the material. However, the assumptions of a homogeneous and well-defined surface may not hold true for the microporous materials present in this work. Additionally, experimental measurement of the surface area does not give insight into the atom-level properties that give rise to the surface area of the material.

There are a number of algorithms and tools that can be used to obtain pore metrics from a periodic structure, which is generally available for these crystalline materials.[3] In the most direct method, the surface area and pore volume can be calculated geometrically from the crystal structure, as illustrated in Figure 2.1.[4,5] In these methods, the surface area corresponds to the area traced out by the center of a probe particle as the probe is moved across the surface of the framework atoms. Porosity can be calculated from straightforward Monte Carlo integration where the probe particle is randomly inserted into the framework and subsequently tested for overlap. The probes that do not overlap with framework atoms are used to measure the surface area. Importantly, the probe size in these methods can be equivalent to the diameters of adsorbates of interest and the surface that is mapped can be visualized to give further information of the pore space.

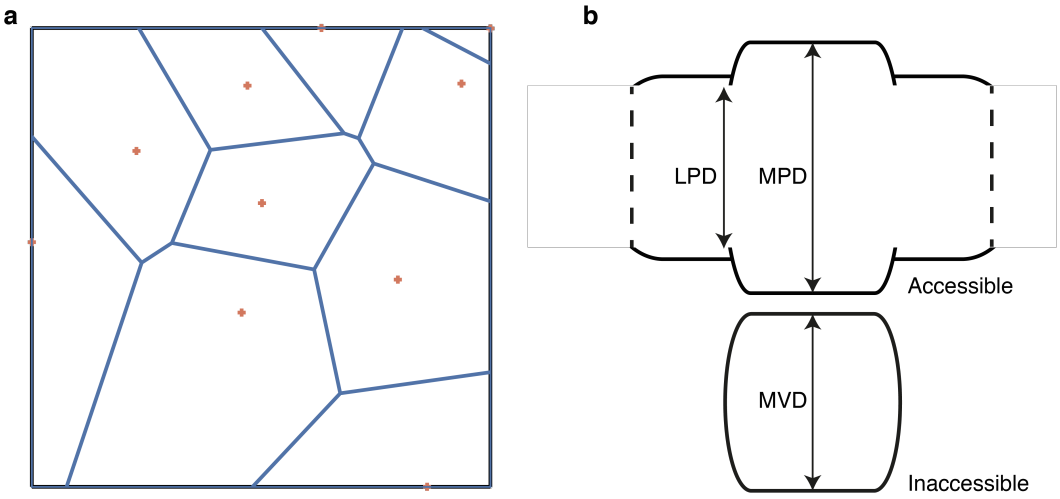

Figure 2.2: Illustration of a Voronoi decomposition of 10 randomly placed points (a) and an example of the pore metrics obtainable from the Zeo++ package[3,6] (b). The limiting pore diameter (LPD) and maximum pore diameters (MPD) can be obtained for pore channels and maximum void diameters (MVD) can be found for inaccessible voids present within the structure.

Another method that is employed by the Zeo++ package, used extensively in this work, relies on an efficient Voronoi decomposition to provide geometric characteristics of the void space as well as the pore accessibility information.[3,6] Voronoi decomposition is a mathematical formulation that in two-dimensions is used to partition a plane with a number of points into convex polygons such that each polygon contains precisely one point and polygon vertices are equidistant to three or more points,[7] as illustrated in Figure 2.2a. Accordingly, when generalized to a three-dimensional porous periodic structure, Voronoi decomposition and network analysis can provide fundamental parameters such as the diameter of the largest free sphere that can be inserted into the pore network in addition to more detailed information about pore space geometry and dimensionality, as shown in Figure 2.2b.[3]

The methods described above are essential tools for the investigation of porous materials and have been applied to justify BET surface areas for characterization of crystalline nanoporous materials.[5] Additionally, they are vital to the visualization and determination of the origin of porosity in molecular materials, in which surface area can arise from the intrinsic volume of cage units, extrinsic voids or a combination of both.[8] However, the methods above rely upon a rigid well-defined periodic structure in order to apply the analysis. Notably, this is not necessarily the case for porous organic cages (POCs) and molecular crystals that are flexible as a result of weak crystal packing forces or are found to be amorphous.[9,10]

Cooper and coworkers have made a number of advances in this area. The dynamic pore topologies present in a POC were successfully captured using a combination of molecular dynamics (MD) simulations and Voronoi decomposition.[11] The "void space histogram" presented in their work was able to illustrate transient pore channels which facilitate the diffusion of gases that are larger than the static limiting pore diameters measured from an X-ray crystal structure. Additionally, the group has also demonstrated an atomistic understanding of H_2/N_2 separations in amorphous porous solids composed of POCs. Here, MD routines were used to create a random periodic system that could be analyzed with standard pore identification techniques.[9]

2.2 Classical Molecular Dynamics

Often classical molecular simulations are used describe the geometry and dynamics of adsorbates and the framework structure. Typical molecular dynamics (MD) simulations can be performed on systems containing over 100 000 atoms for simulation times ranging from a few nanoseconds to hundreds of nanoseconds. This allows molecular level insight into macroscopic material properties, particularly diffusion.

The motion of molecules in MD is determined by numerically solving Newton's equations of motion, displayed in Equation 2.1. The force, $\boldsymbol{F}_i$ experienced by a particle i of mass m_i and position $\boldsymbol{r}$ is equal to the negative the gradient, ∇_i, of the potential energy of the system defined by the interatomic potential energy function (force field), $U(\boldsymbol{r}^N)$. Importantly, the potentials are parameterized such to reproduce the molecular geometry or thermodynamic properties reported experimentally or described by higher level *ab initio* calculations. Newton's second law relates this force to the particle's mass multiplied by the second derivative of its position, $\boldsymbol{r}_i$, with respect to time, t, *i.e.* the particle's acceleration.

$$\boldsymbol{F}_i(\boldsymbol{r}^N) = -\nabla_i U(\boldsymbol{r}^N) = m_i \frac{\mathrm{d}^2 \boldsymbol{r}_i}{\mathrm{d}t^2} \tag{2.1}$$

The general functional form of the potential energy function in molecular mechanics includes bonded terms for interactions of atoms that are linked by covalent bonds, and nonbonded or noncovalent terms that describe long-range electrostatic and van der Waals forces. The specific decomposition of the terms depends on the force field applied, but a general form for the total energy in an additive force field is illustrated in Equation 2.2, Equation 2.3 and Equation 2.4.[12]

$$U_{\text{total}} = U_{\text{bonded}} + U_{\text{nonbonded}} \tag{2.2}$$

$$U_{\text{bonded}} = U_{\text{bond}} + U_{\text{angle}} + U_{\text{dihedral}} \tag{2.3}$$

$$U_{\text{nonbonded}} = U_{\text{electrostatic}} + U_{\text{van der Waals}} \tag{2.4}$$

For atomistic systems intermolecular forces between atoms are generally described by Coulombic interactions and the Lennard-Jones potential for the electrostatic and van der Waals forces, respectively. Typical forms of these functionals for particles i, j are displayed Equation 2.5 and Equation 2.6. ε_{ij} and σ_{ij} represent Lennard-Jones energy and diameter parameters and ϵ_0 is the permittivity of free space.

$$U_{\text{electrostatic}}(r_{ij}) = \frac{1}{4\pi\epsilon_0}\frac{q_i q_j}{r_{ij}} \tag{2.5}$$

$$U_{\text{van der Waals}}(r_{ij}) = 4\varepsilon_{ij}\left[\left(\frac{\sigma_{ij}}{r_{ij}}\right)^{12} - \left(\frac{\sigma_{ij}}{r_{ij}}\right)^{6}\right] \tag{2.6}$$

In addition, potentials that describe bond lengths, bond angles and dihedral angles are generally represented by harmonic oscillator functional forms. Examples for bonded potentials are illustrated in Equation 2.7, Equation 2.8 and Equation 2.9. For a system of particles i, j, k and l where k_{ij}, κ_{ijk} and A_{ijkl} represent fitting parameters.

$$U_{\text{bond}}(l_{ij}) = \frac{k_{ij}}{2}(l_{ij} - l_{ij,0})^2 \tag{2.7}$$

$$U_{\text{angle}}(\theta_{ijk}) = \frac{\kappa_{ijk}}{2}(\theta_{ijk} - \theta_{ijk,0})^2 \tag{2.8}$$

$$U_{\text{dihedral}}(\phi_{ijkl}) = \sum_{n=0}^{4} A_{ijkl}\cos^n(\phi_{ijkl}) \tag{2.9}$$

In this thesis, the force fields used have been specifically parametrized for the description of gas molecules and optimized to describe a multitude of organic crystal structures.[13,14] It has been noted, however, that molecular materials comprise of weak intermolecular interactions and the dynamics and flexibility of these systems may not be adequately described by common force fields. As a result, Holden *et al.* have reported the reparameterization of a polymer force field using density functional theory (DFT) calculations to better describe the imine angle and dihedrals present in a POC in addition to scaling van der Waals in-

teractions.[15] This force field was used to carry out MD simulations of the POC system to rationalize the N_2 adsorption, as the static structure would show restricted diffusion. Additionally, the force field has been used in a number of other studies.[9,11,16,17]

An important application of MD is to measure the self-diffusion of gases in a porous materials. This is achieved by using a MD trajectory, comprising the positions of gas molecules moving within the pores of a structure. The average slope of mean-squared displacement of the gas molecule at long times is used with the Einstein relationship in Equation 2.10 to find the self-diffusivity, D_{self}, of the gas molecules from the coordinates, $\boldsymbol{r}$, of the molecules as a function of time, t, and the number of simulation atoms, N. The self-diffusivity is an important quantity that can be subsequently used to find the permeability and kinetic selectivity of a gas to measure the effectiveness of the material towards the application of gas separation.[18]

$$D_{\text{self}} = \frac{1}{6N} \lim_{t\to\infty} \frac{\mathrm{d}}{\mathrm{dt}} \sum_{i=1}^{N} \langle [\boldsymbol{r}_i(t) - \boldsymbol{r}_i(0)]^2 \rangle \tag{2.10}$$

For many studies, the framework dynamics have been ignored by freezing the experimental geometry of the framework when simulating gas diffusion.[19–21] However, Amirjalayer and coworkers[22] after investigating the diffusion of benzene in both rigid and flexible MOF-5, using MD, concluded that a rigid framework results in a higher diffusion coefficient than a flexible framework. When the lattice motion was included, the self-diffusivity of benzene was predicted to be 2.49×10^{-9} $\mathrm{m^2.s^{-1}}$, comparable to experimental measurements of 2.0×10^{-9} $\mathrm{m^2.s^{-1}}$.[23] Clearly, including the flexibility of framework allows for an accurate mechanism of molecular transport to be captured. This is extremely important for molecular materials, in which the pores are constructed by weak and flexible non-covalent interactions.

2.3 Grand Canonical Monte Carlo Simulations

Grand canonical Monte Carlo (GCMC) simulations can be used to quantify gas adsorption computationally. In these simulations the volume, temperature and chemical potential are held fixed while the number of molecules adsorbed in the porous structure is allowed to fluctuate. This imitates the experimental system, in which the adsorbed phase is at equilibrium with a gas reservoir.

GCMC simulations consist of trial displacement, insertion and removal of gas molecules in the framework structure. The criteria for accepting a trial displacement is described by the Metropolis algorithm. In the Metropolis algorithm the below steps are followed until a move is accepted. Please note $\beta = 1/k_B T$, where k_B is the Boltzmann constant and T temperature.

1. Calculate potential energy (U_i) of the initial state.
2. Choose a trial displacement of a random molecule from a uniform random distribution.
3. Calculate the potential energy of the new state (U_f).
4. If $U_f \leq U_i$, accept the move.
5. If $U_f > U_i$, select a random number, w, where $w \in [0, 1]$ from a uniform distribution and if $\exp[-\beta(U_f - U_i)] > w$, accept the move.
6. Repeat steps 2-5.

Importantly, for GCMC simulations criteria for accepting the trial insertion and deletions of gas molecules have the particular form, described in Equation 2.11 and Equation 2.12. These acceptance rules include the number of particles (N), chemical potential (μ) and the de Broglie thermal wavelength (Λ). Though the simulation includes only the gas in the framework, the imposition of chemical potential (μ) and temperature (T) captures the behavior of an external gas reservoir.

$$\text{acc}_{N \to N+1} = \min[1, \frac{V}{\Lambda^3 (N+1)} \exp[-\beta(U_{N+1} - U_N)] \tag{2.11}$$

$$\text{acc}_{N \to N-1} = \min[1, \frac{\Lambda^3 N}{V} \exp[-\beta(\mu + U_{N-1} - U_N)] \tag{2.12}$$

Finally, millions of these particle insertions, translations, rotations and deletions are performed. The results are subsequently averaged over the multitude of trials to obtain the number of particles for a given chemical potential (μ) and temperature (T). Frenkel and Smit have detailed descriptions and applications of this simulation method.[24] It is noted that for comparison to experiment the quantity of gas adsorbed is plotted against pressure (p), not the chemical potential (μ). Fortunately, these quantities are related by the equation displayed

in Equation 2.13, where ϕ is the fugacity coefficient of the particular gas, which can be obtained from an experimental equation of state. For an ideal gas $\phi = 1$. Furthermore, many simulations can be completed at varying pressure to produce an adsorption isotherm.[25]

$$\exp(\beta\mu) = \frac{\beta p \Lambda^3}{\phi} \tag{2.13}$$

To obtain accurate results from GCMC simulations, the adsorbate-adsorbate, adsorbate-framework, van der Waals and Coulombic interactions must be precisely modeled, captured by the function U. Fortunately, there have been a number of studies that have systematically parametrized potentials for these interactions and good agreement has been observed for many porous materials.[26–29]

The flexibility of porous materials and range of adsorbates are common challenges to using standard GCMC routines that often require a static framework and simple adsorbate sizes. However, Dubbeldam and coworkers have demonstrated that a flexible MOF, which displays a stepped isotherm, can been accurately simulated using a hybrid GCMC/MD simulation.[28] Additionally, inaccessible voids can be blocked during the simulations to better describe pockets within the structure that may not be accessible during the adsorption process.[30,31] Despite these challenges, the power of this method is clear with Chen *et al.* predicting accurately the performance of a POC for chiral and noble gas separations.[16] In their work, they were successfully able to quantitatively predict Kr, Xe and Rn isotherms in addition to showing good agreement to the separation of a racemic mixture of 1-phenylethanol.

2.4 Density Functional Theory

The methods described previously employ classical approaches that in turn treat molecules and atoms as particles that have a potential energy parameterized by a force field. As demonstrated, this approach works well for a number of applications. However, these methods cannot give accurate insight into optical, electronic and magnetic properties that require a quantum mechanical description of the system. Many of the porous materials investigated in this thesis comprise organic components that interact primarily by van der Waals interactions and are not readily polarized. As such, electronic structure calculations are unnecessary as the parameterized classical methods describe the system with good accuracy. However, for MOFs and metal-organic polyhedra (MOP), systems that contain

open metal sites, quantum interactions with adsorbates are vital to consider.[32] Among many quantum-chemical methods available, DFT is a popular choice for electronic structure calculation because of the accuracy obtained for relatively cheap computational cost.[33]

In the application of a quantum description of a molecule not only the coordinates of atoms must be defined, as is the case with classical simulations, but both the components of the atom, namely the nucleus and surrounding electrons.[34] A principal observation in this area is that atomic nuclei are orders of magnitude heavier than electrons and as such electrons will respond to changes in the environment and the nuclei are treated as fixed. This results in the Born-Oppenheimer approximation which leads to a definition of a molecular wave function in terms of electron positions and nuclei positions. Fundamentally, in quantum simulations of electronic ground-state properties, the wave function is to be solved (ψ) to satisfy the Schrödinger equation to give the energy (E) of the system. An example of the Schrödinger equation for multiple electrons interacting with multiple fixed nuclei is given in Equation 2.14, Equation 2.15 and Equation 2.16. In these equations m is the electron mass and the Hamiltonian ($\hat{H}$) has the terms relating to the kinetic energy of each electron ($\hat{T}$), the interaction energy between the atomic nuclei and each electron ($\hat{V}$) and finally the interaction energy between different electrons (i and j) for N electrons ($\hat{U}$).

$$\hat{H}\psi = E\psi \tag{2.14}$$

$$\left[\hat{T} + \hat{V} + \hat{U}\right]\psi = E\psi \tag{2.15}$$

$$\left[-\frac{\hbar^2}{2m}\sum_{i=1}^{N}\nabla_i^2 + \sum_{i=1}^{N}V(\boldsymbol{r}_i) + \sum_{i=1}^{N}\sum_{j<i}U(\boldsymbol{r}_i,\boldsymbol{r}_j)\right]\psi = E\psi \tag{2.16}$$

The complete wave function is complicated even for a simple molecule owing to the many electrons of each atom. For instance, the full electronic wave function for CO_2 is a 66-dimensional function. Furthermore, the electron–electron interaction term of the Hamiltonian ($\sum_{i=1}^{N}\sum_{j<i}U(\boldsymbol{r}_i,\boldsymbol{r}_j)$) is crucial and requires considering the correlations of each individual electron with all the other electrons. Therefore, the wave function of the system is a complicated function that makes an exact or analytical solution impractical. Notably, wave functions cannot be directly observed, however, Equation 2.17 illustrates how the density of electrons ($n(\boldsymbol{r})$) is determined from the individual electron wave functions, ψ_i.

$$n(\boldsymbol{r}) = 2\sum_{i}\psi_i^*(\boldsymbol{r})\psi_i(\boldsymbol{r}) \tag{2.17}$$

DFT methods apply two Hohenberg–Kohn theorems to reduce the complexity of the problem immensely. The first states that the ground-state energy (and other properties) is determined uniquely by the ground-state electron density. As a consequence, a solution to the Schrödinger equation requires a function of three spatial coordinates, the electron density, rather than the original wave function, which has $3N$ variables for N electrons. The second states that the correct electron density minimizes the overall energy functional and subsequently corresponds to the solution of the Schrödinger equation. This theorem affords a direction towards finding the electron density of the system. Kohn and Sham, applied these theorems to show the correct electron density can be determined by solving a set of single electron equations of the form illustrated in Equation 2.18. The solution of these equations are straightforward single-electron wave functions that depend on three spatial coordinates.

$$\left[-\frac{\hbar^2}{2m}\nabla^2 + V(\boldsymbol{r}) + V_{\mathrm{H}}(\boldsymbol{r}) + V_{\mathrm{XC}}(\boldsymbol{r})\right]\psi_i(\boldsymbol{r}) = \varepsilon_i\psi_i(\boldsymbol{r}) \tag{2.18}$$

The Kohn-Sham equations contain three potentials V, V_{H} and V_{XC}. The first, V, describes the interaction between an electron and the collection of atomic nuclei, similar to $\hat{V}$. This potential has a simple analytical form. The second, V_{H}, describes the repulsion between the single-electron and the total electron density. It is the named the Hartree potential and is defined by Equation 2.19, where the electron density is given by n. Importantly, this potential includes a self-interaction contribution as the Kohn-Sham equation describing the electron is also a member of the total electron density. Thus, V_{H} includes an unphysical Coulombic interaction concerning an electron and itself which is corrected for in V_{XC}. This final potential, V_{XC}, characterizes the electron exchange and correlation interactions to the single-electron Kohn-Sham equations. The potential is formally defined as a "functional derivative" of the exchange–correlation energy (E_{XC}) which is not known, except for a free electron gas. Nevertheless, approximations exist, which permit the calculation of certain physical quantities accurately.

$$V_{\mathrm{H}}(\boldsymbol{r}) = e^2 \int \frac{n(\boldsymbol{r}')}{|\boldsymbol{r} - \boldsymbol{r}'|}\mathrm{d}^3r' \tag{2.19}$$

To solve the Kohn–Sham equations, the definition of Hartree potential (V_{H}) requires the electron density (n), which depends on the single-electron wave functions (ψ_i), which in turn requires the solution of the Kohn–Sham equations. As such, an iterative approach is applied to obtain a solution. An example of a simplified algorithm for this purpose is outlined below:

1. Define an initial trial electron density, $n(\boldsymbol{r})$
2. Calculate corresponding potentials, V, V_H and V_{XC}, for the electron density.
3. Solve the Kohn–Sham equations to find the single-electron wave functions, ψ_i.
4. Calculate the electron density, n_{KS}, from the constructed Kohn–Sham equations using the single-electron wave functions, ψ_i, from step 3.
5. Compare the calculated electron density, $n_{\mathrm{KS}}(\boldsymbol{r})$, with the electron density used in solving the Kohn–Sham equations, $n(\boldsymbol{r})$. If the two densities are the same, then this is the ground-state electron density and it can be used to compute the total energy. If the two densities are different, then a new trial electron density, $n(\boldsymbol{r})$, is used and the process begins again from step 2.

Reliable approximations for the exchange-correlation functional (E_{XC}) are required for the solution of the the Kohn–Sham equations. The two most common forms of the approximations are local-density approximation (LDA) and generalized gradient approximation (GGA). LDA is the most widely used approximation, where the local electron density is used to define the approximate exchange-correlation functional. On the other hand, GGA combines information of the local density with the gradient in electron density to give an approximation. DFT methods often lack accurate descriptions for weak intermolecular interactions such as van der Waals (dispersion) forces.[35] The addition of empirical dispersion corrections by Grimme and coworkers have been demonstrated to reproduce crystal structures and adsorption in many porous systems.[36]

Head-Gordon and coworkers have illustrated in a number of MOF systems the accuracy of applying DFT methods to predict and understand hydrogen adsorption.[32,37,38] Using a number of DFT functionals they have described the ability for metalated organic units to polarize hydrogen molecules and illustrated dependence on the geometry and state of the metal ion coordination site.[39] This has resulted in a deep understanding of the strong electrostatic dipole or quadrupole moment required for the capture and storage of hydrogen and clues how to design these sites in MOF materials.

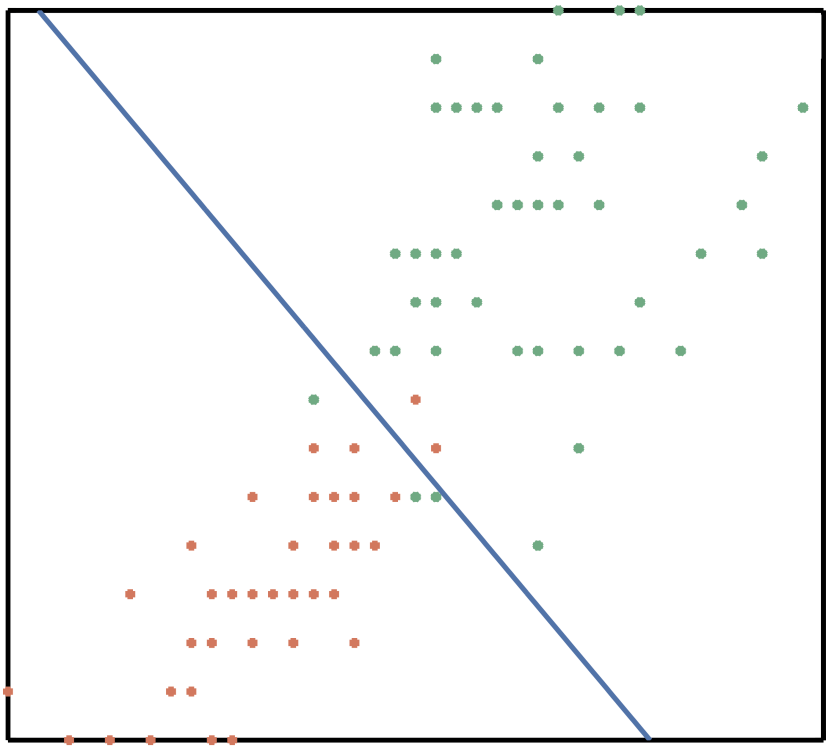

Figure 2.3: Demonstration of training an SVM classifier to separate a dataset of two categories (green and red) in two dimensions. The separating line in displayed in blue.

2.5 Support Vector Machines

Classifying data is a powerful task in machine learning. Although it has yet to be thoroughly applied in the research of porous materials machine learning algorithms have been used throughout chemistry to predict of lower flammability limit,[40] melting point,[41] solubility,[42] heat capacity[43] and propensity of crystallization[44]

Support vector machines (SVMs) are supervised learning models and algorithms. This are used to analyze data and recognize patterns in a dataset containing two or more categories. The SVM algorithm builds a model from a set training examples and subsequently can be applied to assign new examples to one of the categories. This is achieved by mapping the elements of the dataset as points in the space of variables (features) describing the data (feature space) such that the categories are divided by a margin. New examples can then be mapped into the sample space and predicted depending on their position to the plane. This is demonstrated for a simple two-dimensional example in Figure 2.3.

In practice, the SVM constructs a hyperplane in a high-dimensional space. A good separation is achieved by a hyperplane that has the largest distance to the nearest training-data point of any class and this is often used by many routines to obtain the best classification.[45]

The original algorithm results in a linear classifier from the description of the hyperplane. In this case, any hyperplane can be defined as the points $\mathbf{x}$ satisfying Equation 2.20, where $\mathbf{w}$ is the normal vector to the hyperplane and $\frac{b}{||\mathbf{w}||}$ allows for an offset of the hyperplane from the origin. The description has been improved by researchers to allow for nonlinear classifiers, which is particularly useful when the different classes of data are not linearly separable in the original feature space. In these cases, the dot product is replaced by a nonlinear kernel function in the form of a polynomial or Gaussian radial basis function (RBF). In some cases, classifying data in the transformed feature space can allow for a more optimal hyperplane.[46]

$$\mathbf{w} \cdot \mathbf{x} - b = 0 \tag{2.20}$$

The outlined methods give a plethora of tools and techniques for the *in silico* discovery and atomistic investigation into novel porous materials for applications in a variety of areas and will be applied in the subsequent sections of this thesis.

2.6 References

1. O. K. Farha, I. Eryazici, N. C. Jeong, B. G. Hauser, C. E. Wilmer, A. A. Sarjeant, R. Q. Snurr, S. T. Nguyen, A. Ö. Yazaydın, and J. T. Hupp. "Metal–Organic Framework Materials with Ultrahigh Surface Areas: Is the Sky the Limit?" *Journal of the American Chemical Society* 134.36 (2012), pp. 15016–15021. DOI: 10.1021/ja3055639.
2. J. Rouquerol, F. Rouquerol, P. Llewellyn, G. Maurin, and K. Sing. *Adsorption by Powders and Porous Solids: Principles, Methodology and Applications*. Elsevier Science, 2013.
3. T. F. Willems, C. H. Rycroft, M. Kazi, J. C. Meza, and M. Haranczyk. "Algorithms and tools for high-throughput geometry-based analysis of crystalline porous materials". *Microporous and Mesoporous Materials* 149.1 (2012), pp. 134–141. DOI: 10.1016/j.micromeso.2011.08.020.
4. T. Düren, F. Millange, G. Férey, K. S. Walton, and R. Q. Snurr. "Calculating Geometric Surface Areas as a Characterization Tool for Metal−Organic Frameworks". *The Journal of Physical Chemistry C* 111.42 (2007), pp. 15350–15356. DOI: 10.1021/jp074723h.
5. K. S. Walton and R. Q. Snurr. "Applicability of the BET Method for Determining Surface Areas of Microporous Metal−Organic Frameworks". *Journal of the American Chemical Society* 129.27 (2007), pp. 8552–8556. DOI: 10.1021/ja071174k.
6. R. L. Martin, B. Smit, and M. Haranczyk. "Addressing Challenges of Identifying Geometrically Diverse Sets of Crystalline Porous Materials". *Journal of Chemical Information and Modeling* 52.2 (2012), pp. 308–318. DOI: 10.1021/ci200386x.
7. A. Okabe, B. Boots, K. Sugihara, and S. Chiu. *Spatial Tessellations: Concepts and Applications of Voronoi Diagrams*. Wiley Series in Probability and Statistics. Wiley, 2009.
8. T. Tozawa et al. "Porous organic cages". *Nature Materials* 8.12 (2009), pp. 973–978. DOI: 10.1038/nmat2545.

9. S. Jiang, K. E. Jelfs, D. Holden, T. Hasell, S. Y. Chong, M. Haranczyk, A. Trewin, and A. I. Cooper. "Molecular Dynamics Simulations of Gas Selectivity in Amorphous Porous Molecular Solids". *Journal of the American Chemical Society* 135.47 (2013), pp. 17818–17830. DOI: 10.1021/ja407374k.

10. T. Mitra, X. Wu, R. Clowes, J. T. A. Jones, K. E. Jelfs, D. J. Adams, A. Trewin, J. Bacsa, A. Steiner, and A. I. Cooper. "A Soft Porous Organic Cage Crystal with Complex Gas Sorption Behavior". *Chemistry – A European Journal* 17.37 (2011), pp. 10235–10240. DOI: 10.1002/chem.201101631.

11. D. Holden, K. E. Jelfs, A. Trewin, D. J. Willock, M. Haranczyk, and A. I. Cooper. "Gas Diffusion in a Porous Organic Cage: Analysis of Dynamic Pore Connectivity Using Molecular Dynamics Simulations". *The Journal of Physical Chemistry C* 118.24 (2014), pp. 12734–12743. DOI: 10.1021/jp500293s.

12. M. Allen and D. Tildesley. *Computer Simulation of Liquids*. Oxford Science Publ. Clarendon Press, 1989.

13. A. K. Rappe, C. J. Casewit, K. S. Colwell, W. A. Goddard, and W. M. Skiff. "UFF, a full periodic table force field for molecular mechanics and molecular dynamics simulations". *Journal of the American Chemical Society* 114.25 (1992), pp. 10024–10035. DOI: 10.1021/ja00051a040.

14. H. Sun. "Ab initio calculations and force field development for computer simulation of polysilanes". *Macromolecules* 28.3 (1995), pp. 701–712. DOI: 10.1021/ma00107a006.

15. D. Holden, K. E. Jelfs, A. I. Cooper, A. Trewin, and D. J. Willock. "Bespoke Force Field for Simulating the Molecular Dynamics of Porous Organic Cages". *The Journal of Physical Chemistry C* 116.31 (2012), pp. 16639–16651. DOI: 10.1021/jp305129w.

16. L. Chen et al. "Separation of rare gases and chiral molecules by selective binding in porous organic cages". *Nature Materials* 13.10 (2014), pp. 954–960. DOI: 10.1038/nmat4035.

17. J. D. Evans, D. M. Huang, M. R. Hill, C. J. Sumby, D. S. Sholl, A. W. Thornton, and C. J. Doonan. "Molecular Design of Amorphous Porous Organic Cages for Enhanced Gas Storage". *The Journal of Physical Chemistry C* 119.14 (2015), pp. 7746–7754. DOI: 10.1021/jp512944r.

18. R. Krishna and J. M. van Baten. "In silico screening of zeolite membranes for CO_2 capture". *Journal of Membrane Science* 360.1 (2010), pp. 323–333. DOI: 10.1016/j.memsci.2010.05.032.

19. G. Garberoglio, A. I. Skoulidas, and J. K. Johnson. "Adsorption of Gases in Metal Organic Materials: Comparison of Simulations and Experiments". *The Journal of Physical Chemistry B* 109.27 (2005), pp. 13094–13103. DOI: 10.1021/jp0509481.

20. L. Sarkisov, T. Düren, and R. Q. Snurr. "Molecular modelling of adsorption in novel nanoporous metal–organic materials". *Molecular Physics* 102.2 (2004), pp. 211–221. DOI: 10.1080/00268970310001654854.

21. A. I. Skoulidas and D. S. Sholl. "Self-Diffusion and Transport Diffusion of Light Gases in Metal-Organic Framework Materials Assessed Using Molecular Dynamics Simulations". *The Journal of Physical Chemistry B* 109.33 (2005), pp. 15760–15768. DOI: 10.1021/jp051771y.

22. S. Amirjalayer, M. Tafipolsky, and R. Schmid. "Molecular Dynamics Simulation of Benzene Diffusion in MOF-5: Importance of Lattice Dynamics". *Angewandte Chemie International Edition* 46.3 (2007), pp. 463–466. DOI: 10.1002/anie.200601746.

23. F. Stallmach, S. Gröger, V. Künzel, J. Kärger, O. M. Yaghi, M. Hesse, and U. Müller. "NMR Studies on the Diffusion of Hydrocarbons on the Metal-Organic Framework Material MOF-5". *Angewandte Chemie International Edition* 45.13 (2006), pp. 2123–2126. DOI: 10.1002/anie.200502553.

24. D. Frenkel and B. Smit. *Understanding Molecular Simulation: From Algorithms to Applications*. Computational science series. Elsevier Science, 2001.

25. S. Keskin, J. Liu, R. B. Rankin, J. K. Johnson, and D. S. Sholl. "Progress, Opportunities, and Challenges for Applying Atomically Detailed Modeling to Molecular Adsorption and Transport in Metal-Organic Framework Materials". *Industrial & Engineering Chemistry Research* 48.5 (2009), pp. 2355–2371. DOI: 10.1021/ie800666s.

26. W. Li, S. Grimme, H. Krieg, J. Möllmann, and J. Zhang. "Accurate Computation of Gas Uptake in Microporous Organic Molecular Crystals". *The Journal of Physical Chemistry C* 116.16 (2012), pp. 8865–8871. DOI: 10.1021/jp2112632.

27. T. Düren, L. Sarkisov, O. M. Yaghi, and R. Q. Snurr. "Design of New Materials for Methane Storage". *Langmuir* 20.7 (2004), pp. 2683–2689. DOI: 10.1021/la0355500.

28. K. S. Walton, A. R. Millward, D. Dubbeldam, H. Frost, J. J. Low, O. M. Yaghi, and R. Q. Snurr. "Understanding Inflections and Steps in Carbon Dioxide Adsorption Isotherms in Metal-Organic Frameworks". *Journal of the American Chemical Society* 130.2 (2008), pp. 406–407. DOI: 10.1021/ja076595g.

29. E. D. Akten, R. Siriwardane, and D. S. Sholl. "Monte Carlo Simulation of Single- and Binary-Component Adsorption of CO_2, N_2, and H_2 in Zeolite Na-4A". *Energy & Fuels* 17.4 (2003), pp. 977–983. DOI: 10.1021/ef0300038.

30. R. Krishna and J. M. van Baten. "Comment on Comparative Molecular Simulation Study of CO_2/N_2 and CH_4/N_2 Separation in Zeolites and Metal-Organic Frameworks". *Langmuir* 26.4 (2010), pp. 2975–2978. DOI: 10.1021/la9041875.

31. J. Kim, R. L. Martin, O. Rübel, M. Haranczyk, and B. Smit. "High-Throughput Characterization of Porous Materials Using Graphics Processing Units". *Journal of Chemical Theory and Computation* 8.5 (2012), pp. 1684–1693. DOI: 10.1021/ct200787v.

32. K. Sumida et al. "Impact of Metal and Anion Substitutions on the Hydrogen Storage Properties of M-BTT Metal–Organic Frameworks". *Journal of the American Chemical Society* 135.3 (2012), pp. 1083–1091. DOI: 10.1021/ja310173e.

33. T. Schwabe and S. Grimme. "Theoretical Thermodynamics for Large Molecules: Walking the Thin Line between Accuracy and Computational Cost". *Accounts of Chemical Research* 41.4 (2008), pp. 569–579. DOI: 10.1021/ar700208h.

34. D. Sholl and J. Steckel. *Density Functional Theory: A Practical Introduction*. Wiley, 2011.

35. M. P. Waller, H. Kruse, C. Muck-Lichtenfeld, and S. Grimme. "Investigating inclusion complexes using quantum chemical methods". *Chemical Society Reviews* 41 (8 2012), pp. 3119–3128. DOI: 10.1039/C2CS15244D.

36. S. Grimme, J. Antony, S. Ehrlich, and H. Krieg. "A consistent and accurate ab initio parametrization of density functional dispersion correction (DFT-D) for the 94 elements H-Pu". *The Journal of Chemical Physics* 132.15, 154104 (2010), pages. DOI: 10.1063/1.3382344.

37. R. C. Lochan, R. Z. Khaliullin, and M. Head-Gordon. "Interaction of Molecular Hydrogen with Open Transition Metal Centers for Enhanced Binding in Metal-Organic Frameworks: A Computational Study". *Inorganic Chemistry* 47.10 (2008), pp. 4032–4044. DOI: 10.1021/ic701625g.

38. R. C. Lochan and M. Head-Gordon. "Computational studies of molecular hydrogen binding affinities: The role of dispersion forces, electrostatics, and orbital interactions". *Physical Chemistry Chemical Physics* 8 (12 2006), pp. 1357–1370. DOI: 10.1039/B515409J.

39. E. Tsivion, J. R. Long, and M. Head-Gordon. "Hydrogen Physisorption on Metal–Organic Framework Linkers and Metalated Linkers: A Computational Study of the Factors That Control Binding Strength". *Journal of the American Chemical Society* 136.51 (2014), pp. 17827–17835. DOI: 10.1021/ja5101323.

40. Y. Pan, J. Jiang, R. Wang, H. Cao, and Y. Cui. "A novel QSPR model for prediction of lower flammability limits of organic compounds based on support vector machine". *Journal of Hazardous Materials* 168.2-3 (2009), pp. 962–969. DOI: 10.1016/j.jhazmat.2009.02.122.

41. A. Varnek, N. Kireeva, I. V. Tetko, I. I. Baskin, and V. P. Solov'ev. "Exhaustive QSPR Studies of a Large Diverse Set of Ionic Liquids: How Accurately Can We Predict Melting Points?" *Journal of Chemical Information and Modeling* 47.3 (2007), pp. 1111–1122. DOI: 10.1021/ci600493x.

42. B. Louis, J. Singh, B. Shaik, V. K. Agrawal, and P. V. Khadikar. "QSPR Study on the Estimation of Solubility of Drug-like Organic Compounds: A Case of Barbiturates". *Chemical Biology & Drug Design* 74.2 (2009), pp. 190–195. DOI: 10.1111/j.1747-0285.2009.00844.x.

43. C. X. Xue, R. S. Zhang, H. X. Liu, M. C. Liu, Z. D. Hu, and B. T. Fan. "Support Vector Machines-Based Quantitative Structure−Property Relationship for the Prediction of Heat Capacity". *Journal of Chemical Information and Computer Sciences* 44.4 (2004), pp. 1267–1274. DOI: 10.1021/ci049934n.

44. J. G. P. Wicker and R. I. Cooper. "Will it crystallise? Predicting crystallinity of molecular materials". *CrystEngComm* 17.9 (2015), pp. 1927–1934. DOI: 10.1039/c4ce01912a.

45. C.-w. Hsu, C.-c. Chang, and C.-j. Lin. *A practical guide to support vector classification*. Department of Computer Science and Information Engineering, National Taiwan University, 2010.

46. N. Cristianini and J. Shawe-Taylor. *An Introduction to Support Vector Machines and Other Kernel-based Learning Methods*. Cambridge University Press, 2000.

This work has appeared in the following publication.

> J. D. Evans, D. M. Huang, M. R. Hill, C. J. Sumby, A. W. Thornton, and C. J. Doonan. "Feasibility of Mixed Matrix Membrane Gas Separations Employing Porous Organic Cages". *The Journal of Physical Chemistry C* 118.3 (2014), pp. 1523–1529. DOI: 10.1021/jp4079184.

Author statements can be found in Appendix A.

3

Mixed Matrix Membranes Employing Porous Organic Cages

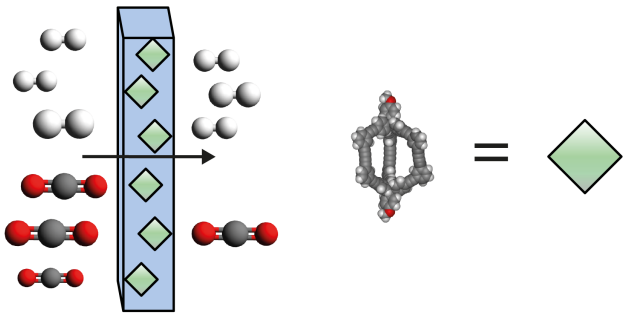

3.1 Abstract

Porous additives offer an attractive pathway to enhance the performance of polymeric gas separation membranes. Previously reported porous additives, such as zeolites and metal-organic frameworks, suffer from poor interfacial binding with the polymer matrix, which leads to nonselective gas transport pathways. porous organic cages (POCs) are an exciting new family of soluble additives that could ameliorate these transport issues by integrating intimately with the polymer matrix. By using Voronoi network analysis, grand canonical Monte Carlo simula-

tions, and molecular dynamics, we provide a theoretical assessment of the benefit of using POCs as additives for mixed matrix membranes (MMMs). We reveal that some MMMs containing POCs exhibit enhanced selectivity and permeability compared with the neat polymer matrix, particularly for H_2/CO_2 separations.

3.2 Introduction

Novel strategies that increase the efficiency of industrial gas separations are of great interest due to their direct application to green energy technologies.[1,2] The specific challenges in this area are to reduce the overall energy cost of separating (i) H_2/N_2 and H_2/CO_2 for the production of hydrogen and the precombustion capture of carbon dioxide from gasified coal following the water-gas shift reaction,[3,4] (ii) CO_2/N_2 for postcombustion 'carbon capture' from gas flue streams,[5] and (iii) CO_2/CH_4 for biofuel purification and natural gas sweetening.[6]

Membrane systems are often used to perform gas separations on an industrial scale as they operate via a continuous process. This is more energy efficient than batchwise methods such as physical or chemical adsorption that require periodic energy intensive regeneration.[3,7,8] Membranes are commonly prepared from organic polymers as they are stable, readily scalable, and cost-efficient. However, pure polymer membranes are hampered by an empirical permeability versus selectivity trade-off limit termed the 'upper bound'.[9,10] Accordingly, one of the current challenges in membrane separation technology is to design new materials that surpass the upper bound limit and achieve enhanced selectivity, ideally in combination with increased permeability. A promising strategy is to synthesize multicomponent MMMs in which a gas-selective porous solid of fixed pore diameter is embedded into a polymer host. Porous additives with narrow pore size distributions, of the order of the kinetic diameter of the target gas, can facilitate efficient size-sieving separations. Additionally, these additives can introduce chemical functionality into the polymer to improve solubility of a target gas and thus enhance membrane selectivity. Porous adsorbents that have been explored as membrane additives include zeolites, metal-organic frameworks (MOFs), and zeolitic imidizolate frameworks (ZIFs).[11–14] Such materials have yielded MMMs that show increased permeability and selectivity compared with neat polymers.[11] However, inhomogeneity of the surface chemistry between the polymer and adsorbent can give rise to nonselective interphase voids that allow unrestricted gas diffusion.[15] This ultimately leads to less than optimal performance for these multicomponent membranes.[16] Thus, in order for MMMs to reach their full potential, synthetic methods that afford 'gas-tight' integration between the two phases are required.

Recently, microporous solids composed of solution-processable POC molecules have attracted significant attention due to the potential to combine the atomic-scale control over pore size seen in MOFs and ZIFs, with the solution processability of molecular species.[17,18] These novel materials have been reported with surface areas in excess of 1500 $m^2.g^{-1}$ and have also been shown to carry out size- and shape specific molecular separations.[19,20] It is noteworthy that for such POC materials the accessible surface area can arise from interconnection of the intrinsically porous cage cavities (intrinsic porosity), from void spaces surrounding the cages that result from inefficient packing (extrinsic porosity) or from a combination of both. As a result, polymorphs of POCs are reported to have very different physical properties.[21,22] Thus, in the present study we have used the reported crystalline structures of POCs as the basis for our feasibility analysis. This approach is validated by the work of Bushell *et al.* who reported MMMs incorporating a POC that showed both in situ crystal growth and crystal inclusion.[23]

Our study builds upon recent computational work that considered the use of MOFs and ZIFs as additives for MMMs. These studies have enabled the identification of important trends and targeted the development of novel materials.[24,25] POCs are attractive as they are soluble in many common organic solvents, which facilitates intimate mixing with the polymer host at the molecular scale. In silico screening will assist the development of POC-based MMMs as it can provide design principles for new materials.

Figure 3.1 shows the molecular structure and accessible pore surfaces of five organic cage molecules of varying cavity dimensions, pore window sizes, and molecular architectures. As the packing of cage molecules defines the bulk porosity of the materials we used the reported crystal structures of cages 1–5.[17,19,21] The selectivity and permeability of MMMs containing POCs 1–5 were determined from grand canonical Monte Carlo (GCMC) and molecular dynamics (MD) simulations. Furthermore, we considered the effects of structural dynamics of the pore windows using Voronoi network analysis and MD simulations. To verify our modeling data, we calculated MMM permeabilities of 3 and PIM-1, a polymeric host of intrinsic microporosity, and compared these to experimental results.

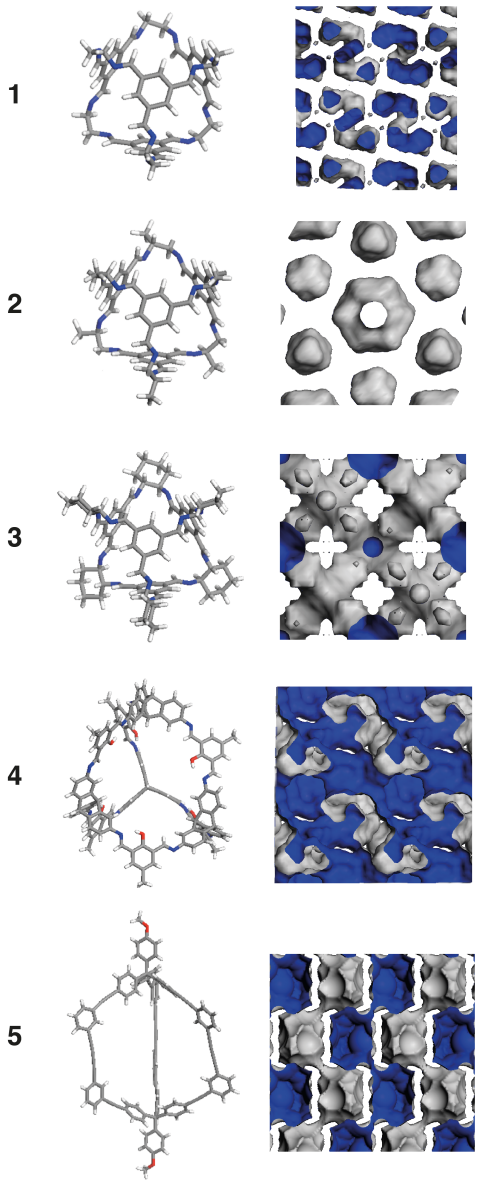

Figure 3.1: Summary of molecular structures and accessible pore surface (1.2 Å probe radius, equivalent to the kinetic diameter of helium) of POCs 1–5.

3.3 Methodology

To simulate the intrinsic permeabilities of 1–5 we extracted their structural data from the Cambridge Structural Database.[26] Supercells (2×2×2) of structures 1, 2, 4 and 5 were used. As 2 contains disorder, with respect to the position of methyl functionality, as such this was randomly assigned, analogous to a recent another study.[27] Owing to the larger size, a single unit cell of system of 3 was used and desolvated crystal structures were used where available. Structures of 1–5 were analyzed by Voronoi network analysis using the Zeo++ code.[28,29] to calculate the accessible surface area, size, and dimensionality of the pores. A probe radius of 1.82 Å, equivalent to the kinetic diameter of N_2, was used to calculate surface areas.[9] Equilibrium gas uptakes for H_2, N_2, CH_4, and CO_2 at 10 bar and 298 K were calculated by GCMC simulations employing the RASPA code. Analogous methods have been successfully employed to model porous carbons, zeolites, and metal-organic frameworks.[24,30,31] The universal force-field (UFF)[32] was used to describe the non-bonded interactions of the cage atoms. H_2 was described by the Darkrim and Levesque model,[33] N_2, and CH_4 molecules were represented using the TraPPe model,[34] and CO_2 was described using the Elementary Physics 2 model.[35] Mixed-atom interactions were expressed using Lorentz-Berthelot mixing rules.[36] The cage volume of 2 was blocked by a 4 Å diameter sphere at the center of mass of the cage to prevent the inaccessible cage interior from being included in the calculation of the pore volume. Inspection of the gas density plots from the simulation ensured that the cage volume was blocked and the extrinsic volume was unchanged. Each simulation used 1 million equilibration steps followed by 1 million production steps. The particular force field chosen has precedence in literature, having been used in previous studies of MOFs.[37] Diffusion was simulated using equilibrium MD in the Forcite module within Materials Studio 5.0. UFF was used to describe the dynamics of bonds, angles and torsions of the systems during the MD simulation. Gas molecules at the density predicted by GCMC simulations at 10 bar were randomly placed into the crystal structure with the Amorphous Cell module. NVT dynamics were simulated for 6 ns with a time step of 1 fs with temperature controlled at 300 K using the Nosé-Hoover thermostat.[38] Only the last 5 ns of each simulation trajectory was used to calculate the mean-squared displacement of the gas molecules. The structure was allowed to be flexible to ensure that the dynamic nature of the systems was captured. A total of 5 unique trajectories were simulated so that an average slope of mean-squared

displacement could be calculated. The Einstein relationship in Equation 3.1 was used to find the self-diffusivity, D_{self}, of the gas molecules from the coordinates, $\boldsymbol{r}(t)$, of the molecules as a function of time, t and number of simulation atoms N.

$$D_{\text{self}} = \frac{1}{6N} \lim_{t\to\infty} \frac{\mathrm{d}}{\mathrm{dt}} \sum_{i=1}^{N} \langle [\boldsymbol{r}_i(t) - \boldsymbol{r}_i(0)]^2 \rangle \tag{3.1}$$

Intrinsic permeabilities of POC crystals were approximated using Equation 3.2, where c is the equilibrium gas concentration, and f is the operating fugacity.[39] Single-gas properties were computed and selectivity was calculated using this data.

$$P = D_{\text{self}} \frac{c}{f} \tag{3.2}$$

Pore dynamics were calculated using the Zeo++ code for the last nanosecond of a 2 ns NVT dynamics trajectory at 298 K and 10 bar in the absence of gas molecules. MMM permeabilities were calculated for a cage volumetric fraction of 40% using the Bruggeman's effective-medium model described in Equation 3.3, where P_{MMM} is the permeability of the MMM, P_{P} the permeability of the polymer, P_{POC} the permeability of the POC, and φ the volume fraction of POC in the membrane.[40]

$$\left(\frac{P_{\text{MMM}}}{P_{\text{P}}}\right)^{-\frac{1}{3}} \left(\frac{\frac{P_{\text{MMM}}}{P_{\text{P}}} - \frac{P_{\text{POC}}}{P_{\text{P}}}}{1 - \frac{P_{\text{POC}}}{P_{\text{P}}}}\right) = (1 - \phi) \tag{3.3}$$

3.4 Results and Discussion

3.4.1 Structural Properties

Figure 3.1 depicts POCs 1–5 showing their different geometries, pore networks, and chemical functionality. Cages 1–3 have tetrahedral geometry of equivalent cavity size and can be differentiated by their vertex functionality. Cage 4 is an adamantoid and possesses the largest pore cavity of all the cages being investigated. We note that an analogue of this structure has the highest reported surface area for a POC of 2071 $\text{m}^2.\text{g}^{-1}$.[19] Finally, cage 5 is best described as an elongated triangular dipyramid and is constructed from carbon-carbon bonds. This molecular connectivity is in contrast to cages 1–4, which are composed of imine moieties.

Static pore sizes, structure metrics, and N_2-accessible surfaces areas were calculated for structures 1–5 (Table 3.2). The internal pore cavities range from 5.4 to 9.8 Å. The pore limiting (or window) sizes for each of the crystalline POC networks were calculated to lie between 1.8 and 5.1 Å; these values are germane to size-sieving separation of industrially relevant gases N_2, CO_2, CH_4, and H_2. Cages 3 and 5 possess 'zeolite-type' pore structures with limiting diameters of 3.7 and 4.4 Å, respectively. Such pore architectures show excellent potential for gas separations, as they contain pore windows in the range of the kinetic diameter of target gases and also have larger cavities providing good solubility.[41]

Structures 1–5 were investigated using combined GCMCs and Voronoi network analysis simulations to determine representative surface areas. Good agreement between the experimental and calculated data for 1 and 2 was observed. However, discrepancies between experimental and predicted surface areas were found for the structures of cages 3, 4, and 5. This incongruity can be attributed to the 'soft' nature of these structures, which arises from the cage molecules packing in the crystalline phase via relatively weak dispersion forces.[42] In the present study, we find that the simulated surface area of 3 is underestimated. This is as anticipated as the simulation uses a 'perfect' crystal and increased crystallinity of experimental samples has been shown to result in decreased surface area.[43] In addition, the dynamic pore aperture has been suggested to account for a greater N_2 porosity than expected for a static structure.[44] In contrast to structure 3, the surface area of 4 is overestimated by a factor of two (2410 $m^2.g^{-1}$ compared with 1291 $m^2.g^{-1}$). This significant difference can be accounted for by a structural contraction upon solvent removal.[19] Lastly, the difference between the experimental and simulated surface area for cage 5 arises from confinement of N_2 within the pores at the experimental temperature of 77 K.[21]

3.4.2 Equilibrium Gas Uptake

GCMC routines are commonly used to simulate gas uptakes in porous materials. The potential parameters for the cage atoms were obtained from the UFF. To validate our approach we simulated CO_2 and CH_4 isotherms for structures 2 and 3 and compared the results with experimental data by Tozawa *et al.* (Figure 3.2).[17] We note that CO_2 and CH_4 gas adsorption isotherms have not been reported for 1, 4, and 5 and thus could not be included in this comparison. Inaccessible voids of cage 2 were blocked to ensure that the simulated isotherms were not overestimated.[45,46] Inaccessible regions observed in the static crystal structures have been found to contribute to the porosity and it is suggested that dynamic molecular motion allows diffusion into these formally inaccessible cage voids.[17,27]

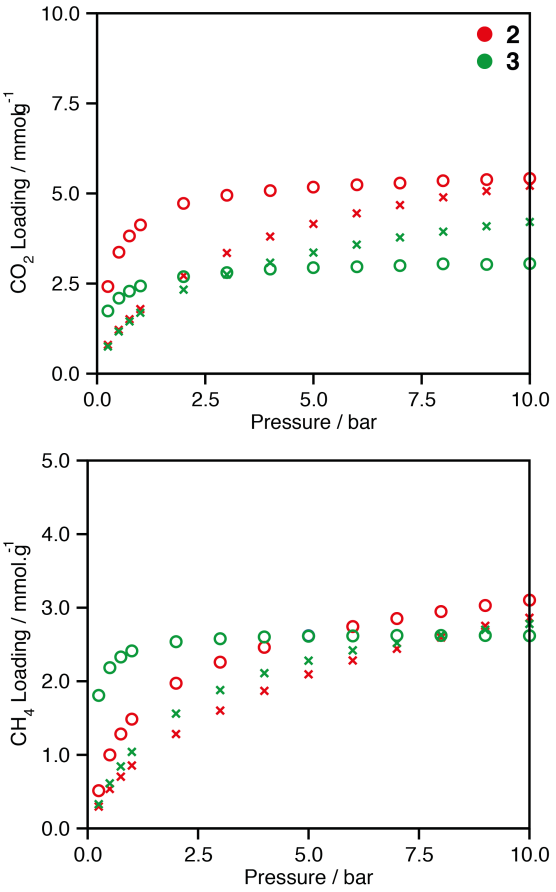

Figure 3.2: Comparison of experimental (crosses) and theoretical (cricles) CO_2 and CH_4 of POCs 2 and 3.

This process is not well understood so the amount of blocked volume was assessed to ensure the best fit to experimental data (Figure 3.6). The best agreement to CO_2 and CH_4 experimental data was found for simulations containing 50% and 100% blocked cage volume, respectively.

Figure 3.2 shows that the larger pores of 2 result in larger uptake at high pressures for CO_2 and CH_4 adsorption. At low pressure, CH_4 has greater adsorption in 3 due to the smaller cavity sizes as they give rise to stronger binding sites from 'wall-wall' potential overlaps. This effect is not observed for CO_2 adsorption because of its smaller size and aspherical shape. The observed difference between the calculated and experimental isotherms at low pressure can be attributed to artifacts in the force field, pressure-dependent accessible pockets within the structures, or defects in the experimental crystal. We note that in general, the gas adsorption of porous molecular crystals are inherently difficult to simulate due to their 'soft' 3D structures in contrast to extended framework materials such as

Table 3.1: Self-diffusion coefficient of gas molecules in POCs 1–5.

	D_{self} / 10^{-10} $m^2.s^{-1}$			
cage	H_2	N_2	CO_2	CH_4
1	0.00167	0.332	0.0161	0.00250
2	468	11.5	5.92	3.46
3	532	9.02	3.45	2.16
4	762	81.7	6.43	19.4
5	363	36.8	6.05	23.6

MOFs, which have more well-defined, rigid 3D structures. As such, we find the agreement to be within an acceptable range.[42] We also simulated the gas loading of H_2, N_2, CH_4, and CO_2 at 10 bar for structures 1–5 (Table 3.3). The gas uptakes at this pressure are comparable to other porous materials such as ZIFs.[25]

3.4.3 Diffusion and Structural Flexibility

MD simulations at 298 K were employed to estimate the adsorbate diffusion throughout the pore structures of 1–5. We selected these conditions to allow comparison with previously reported data that predicted the kinetic gas separation properties of ZIFs and MOFs.[24,25] As the series of POCs under investigation include different chemical structures a consistent generic force field (UFF) was chosen to describe the systems, in lieu of an imine-specific cage force field.[44] To test the accuracy for the imine moieties, systems 1–4 were optimized and compared to the crystal structures. The optimized imine angles (Table 3.4) are observed to be different to that of the crystal. However, a superimposed comparison of the structural geometries of systems 1–5 (Figure 3.7) show little difference for the supramolecular structures, demonstrating the accuracy of the UFF for the range of systems compared in this study. From these MD simulations we computed the self-diffusion coefficients of cages 1–5 for H_2, N_2, CO_2, and CH_4 (Table 3.1).

The diffusivities calculated are consistent with the window sizes of the structures. The diminutive pore aperture of 1 results in poor diffusion of all gas molecules. Without the specific pore size required for the kinetic separation of CO_2/N_2, the diffusivities follow the trend for the bulk diffusion of N_2 over CO_2. Structures 2 and 3 show lower diffusivity for CH_4 than CO_2, which is attributed to their limiting pore diameters of 3.9 Å and 3.7 Å, respectively. In contrast,

the larger pore diameters of cages 4 and 5 allow the rapid diffusion of CH_4 (3.8 Å). We note in the absence of molecular sieving, the diffusion of CO_2 and CH_4 compete by surface diffusion with the strong adsorption of CO_2 producing slower diffusivity compared to CH_4.

Our results indicate that a static pore model does not accurately represent the selectivities for CH_4 separations. As the pore structures of 1–5 are formed from weak intermolecular forces, it is likely that the pore window distribution is greater than that of extended frameworks in which the pore network is constructed by strong covalent bonds. Notably, pore size fluctuations have been reported to decrease the CH_4 selectivity in ZIF-8.[47] To gain further insight into the dynamic nature of the cage structures, NVT molecular dynamic simulations were carried out at analogous temperatures to the diffusion simulations described earlier. In these simulations the limiting pore size was calculated at each femtosecond over a 1 ns trajectory, after 1 ns equilibration. The resulting pore size distributions for cages 1–5 were calculated (see Figure 3.3 and Table 3.5). Based on its static structure, 2 was not expected to be a promising candidate for size sieving of CH_4, due to the crystallographic limiting pore size of 3.9 Å. However, the flexible diffusion simulations showed slower diffusivity of CH_4 than CO_2 (Table 3.1). We observe from the window size distributions that thermal fluctuations of 2 produce a mean window size of 3.56 Å (Table 3.5), similar to that of cage 3, thus limiting the diffusion of CH_4.

The largest standard deviation of window sizes, 0.3 Å, was calculated for 4 (Figure 3.3). This may be attributed to the pore network composed of largely extrinsic volume, which is found to fluctuate by a considerable amount over the time scale of the simulation. In contrast, the structures of 1 and 3 are found to produce narrow distributions of window sizes (standard deviations of 0.05 and 0.07 Å, respectively). The pore structures of these cages are wholly comprised of intrinsic cage volume with cage-to-cage packing linking the pore cavities. These results suggest cage molecules with functionalities that direct strong packing between molecular windows of appropriate dimensions may be more efficient for separations requiring precise size selection.

We note that the distribution of 3 found in the present work is different to that found in a previous study.[44] The difference can be attributed to a difference in definition: we have taken the window size to be the narrowest point in the whole cell at a given point in time, whereas the previous study assigned the window

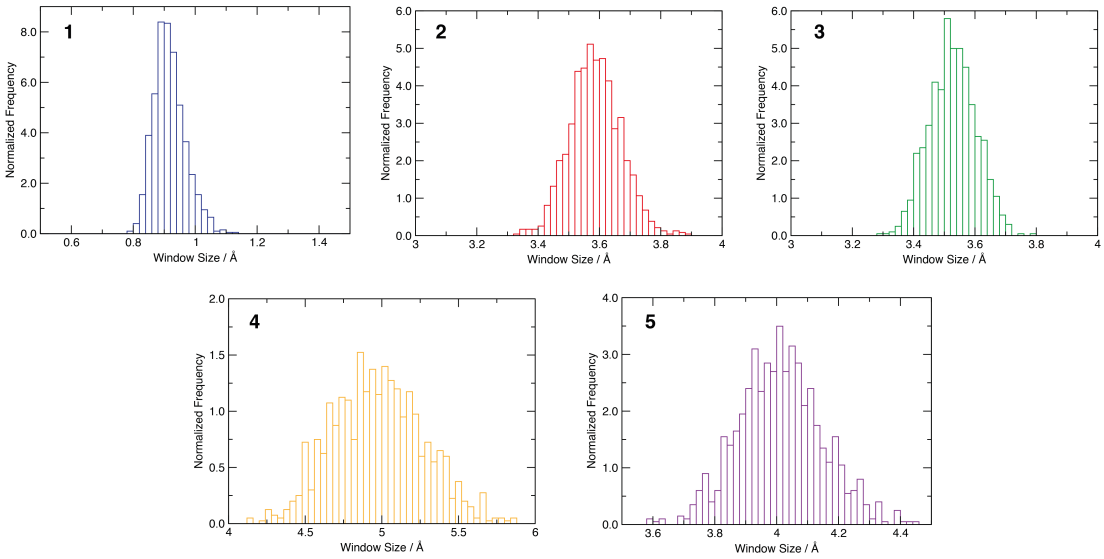

Figure 3.3: Window size distributions of POCs 1–5 over 1 ns at 298 K.

size to the diameter of the entrance to the cage cavity. Our definition, which in general gives smaller window sizes, accounts for the effects of fluctuations in the inter-cage regions and (mis)alignment of cage windows on the accessibility of cage volumes.

3.4.4 MMM Properties

Diffusion data was combined with the simulated gas uptakes to compute the permeabilities for the crystalline cage structures 1–5. MMM permeabilities were extrapolated from intrinsic permeance values using Bruggeman's model, which has been shown to accurately simulate the properties of MMMs composed of polymers and ZIFs for high fractions of additives: up to 40% by volume.[48] Recent work by Bushell *et al.* reported the permeabilites of a MMM composed of PIM-1 and cage 3.[23] We compared these experimental results with our simulation data to verify the use of our approach. The simulations were carried out at 1 bar to allow comparison with the experimental work. Figure 3.4 compares the experimental permeability of CO_2, N_2, and CH_4 with our calculated values.

Both the simulated and experimental data show an increase in permeability for N_2, CO_2, and CH_4 with increasing loading of 3. Although the modeled data follow the experimental trends and show good agreement with respect to N_2 permeability, the permeability of CO_2 and CH_4 is underestimated. The observed difference may suggest that additional mechanisms influence the MMM configuration, in-

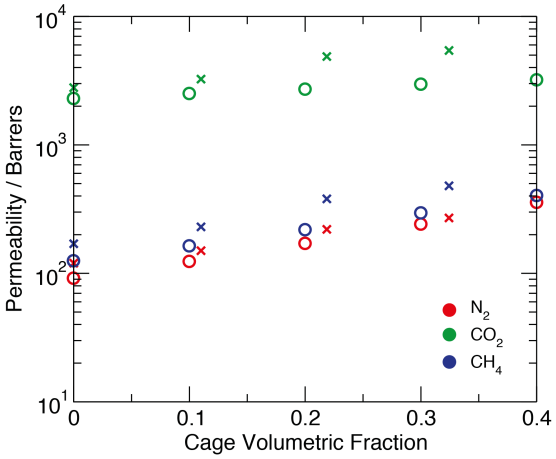

Figure 3.4: Comparison of the experimental (crosses) and predicted (circles) permeabilities of PIM-1:3 at increasing loading of 3.

cluding interfacial diffusion paths produced by disruption of chain packing at the polymer-POC interface. This effect has been observed to a significant extent for other additives in MMMs[49] and, although minimized by the organic make up of POCs, it cannot be excluded.

Using Bruggeman's model, the permeabilities and selectivities for 40% volume compositions of MMMs comprised of the polymer hosts Matrimid, Ultem, PIM-1, and PIM-7 were computed.[14,50,51] The permeability and selectivity trade-off plots for the separation of H_2/N_2, H_2/CO_2, CO_2/N_2 and CO_2/CH_4 were predicted for neat POC membranes and MMMs. These are displayed in Figure 3.5. We find that MMMs containing cage structures 2–5 significantly improve the permeability for H_2/N_2 and H_2/CO_2 separations. This enhancement is concomitant with a minor increase in the selectivity for H_2.

Figure 3.5 shows that the permeability for CO_2/N_2 and CO_2/CH_4 separations increases upon introduction of cages 1–5, bringing the Ultem and Matrimid MMMs toward the polymer upper bound; however, a decrease in selectivity is observed for the PIM membranes. The plots for MMMs composed of cages 2–5 and Ultem and Matrimid show considerable overlap of data points. This is due to the difference in permeability of cages being negligible when combined with the low permeability polymer and results in MMMs with very similar permeabilities. We also note that as a result of the discontinuous pore volume of 1, the MMMs simulated have decreased permeabilities and selectivities compared to cages 2–5.

These results show that the inclusion of crystalline aggregates of POCs in neat polymer matrices result in MMMs that lie on or surpass the polymer upper bound for H_2/N_2 and H_2/CO_2 separations. The separations of CO_2 show an increase in permeability, with the addition of cage molecules advancing Matrimid-based

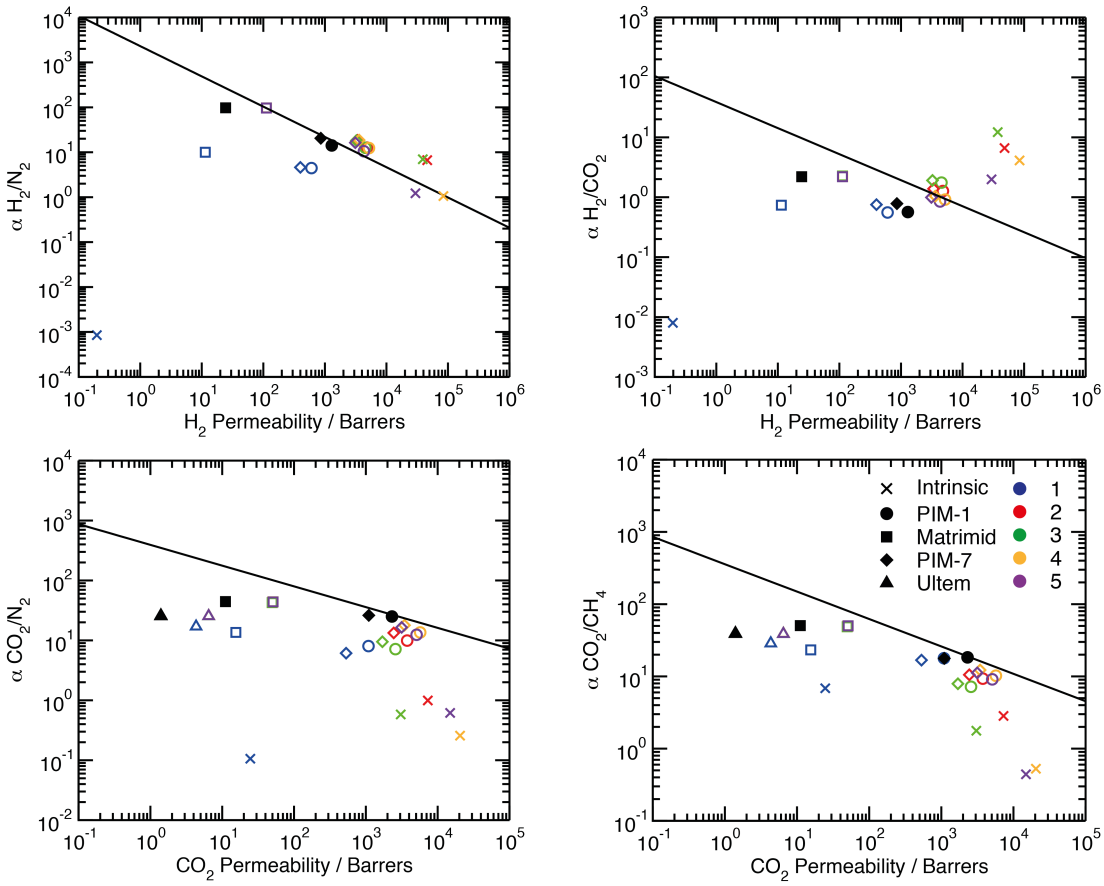

Figure 3.5: Permeability vs selectivity trade-off plots for neat polymers (solid black symbols), intrinsic POCs 1–5 (crosses), POC/polymer MMM predictions (open symbols), and Robeson's 2008 upper bound (line).[10] Open symbols represent 40% volume fraction of POC (see color code) within polymer (see symbol shape).

MMMs toward the polymer upper bound. In comparison to previous studies, the performance of POC MMMs are comparable to that predicted for ZIF containing MMMs, despite their marginally lower affinity for the investigated gases.[25] It is expected, however, that the exclusively organic construction of POCs will improve the poor integration between the two phases.

3.5 Conclusion

In summary, we have investigated a series of POC-based MMMs for the separation of industrially relevant gas mixtures H_2/N_2, H_2/CO_2, CO_2/N_2 and CO_2/CH_4. This was achieved by employing Voronoi network analysis, GCMC and MD simulations, with calculations compared to experimental data for validation. Conservative estimates of gas transport properties within these materials revealed that MMMs composed of POCs can exceed the polymer upper bound for H_2/N_2 separations and more substantially for H_2/CO_2 gas pairs. We note the importance of considering flexibility in these materials, as weak packing forces define the pore structures. Accordingly, window size distributions over a 1 ns trajectory were calculated. These properties determined by our investigation, combined with the facile processability and good compatibility with the polymer, indicate that POC-based MMMs have exciting potential for clean energy applications.

3.6 References

1. R. S. Haszeldine. "Carbon Capture and Storage: How Green Can Black Be?" *Science* 325.5948 (2009), pp. 1647–1652. DOI: 10.1126/science.1172246.
2. M. Z. Jacobson. "Review of solutions to global warming, air pollution, and energy security". *Energy & Environmental Science* 2.2 (2009), pp. 148–173. DOI: 10.1039/B809990C.
3. A. Y. Ku, P. Kulkarni, R. Shisler, and W. Wei. "Membrane performance requirements for carbon dioxide capture using hydrogen-selective membranes in integrated gasification combined cycle (IGCC) power plants". *Journal of Membrane Science* 367.1 (2011), pp. 233–239. DOI: 10.1016/j.memsci.2010.10.066.
4. C. A. Scholes, K. H. Smith, S. E. Kentish, and G. W. Stevens. "CO_2 capture from pre-combustion processes—Strategies for membrane gas separation". *International Journal of Greenhouse Gas Control* 4.5 (2010), pp. 739–755. DOI: 10.1016/j.ijggc.2010.04.001.
5. M. T. Ho, G. W. Allinson, and D. E. Wiley. "Reducing the Cost of CO_2 Capture from Flue Gases Using Membrane Technology". *Industrial & Engineering Chemistry Research* 47.5 (2008), pp. 1562–1568. DOI: 10.1021/ie070541y.
6. H. B. Park, S. H. Han, C. H. Jung, Y. M. Lee, and A. J. Hill. "Thermally rearranged (TR) polymer membranes for CO_2 separation". *Journal of Membrane Science* 359.1 (2010), pp. 11–24. DOI: 10.1016/j.memsci.2009.09.037.
7. R. W. Baker. *Membrane Technology and Applications*. John Wiley & Sons, 2004. 556 pp.
8. B. Freeman, Y. Yampolskii, and I. Pinnau, eds. *Materials Science of Membranes for Gas and Vapor Separation*. 1 edition. Chichester, England ; Hoboken, NJ: Wiley, 2006. 466 pp.
9. L. M. Robeson. "Correlation of separation factor versus permeability for polymeric membranes". *Journal of Membrane Science* 62.2 (1991), pp. 165–185. DOI: 10.1016/0376-7388(91)80060-J.

10. L. M. Robeson. “The upper bound revisited”. *Journal of Membrane Science* 320.1 (2008), pp. 390–400. DOI: 10.1016/j.memsci.2008.04.030.

11. Y. Li, F. Liang, H. Bux, W. Yang, and J. Caro. “Zeolitic imidazolate framework ZIF-7 based molecular sieve membrane for hydrogen separation”. *Journal of Membrane Science* 354.1 (2010), pp. 48–54. DOI: 10.1016/j.memsci.2010.02.074.

12. M. G. Süer, N. Baç, and L. Yilmaz. “Gas permeation characteristics of polymer-zeolite mixed matrix membranes”. *Journal of Membrane Science* 91.1 (1994), pp. 77–86. DOI: 10.1016/0376-7388(94)00018-2.

13. E. V. Perez, K. J. Balkus Jr., J. P. Ferraris, and I. H. Musselman. “Mixed-matrix membranes containing MOF-5 for gas separations”. *Journal of Membrane Science* 328.1 (2009), pp. 165–173. DOI: 10.1016/j.memsci.2008.12.006.

14. M. J. C. Ordoñez, K. J. Balkus Jr., J. P. Ferraris, and I. H. Musselman. “Molecular sieving realized with ZIF-8/Matrimid® mixed-matrix membranes”. *Journal of Membrane Science* 361.1 (2010), pp. 28–37. DOI: 10.1016/j.memsci.2010.06.017.

15. R. Mahajan and W. J. Koros. “Mixed matrix membrane materials with glassy polymers. Part 1”. *Polymer Engineering & Science* 42.7 (2002), pp. 1420–1431. DOI: 10.1002/pen.11041.

16. T. C. Merkel, B. D. Freeman, R. J. Spontak, Z. He, I. Pinnau, P. Meakin, and A. J. Hill. “Ultrapermeable, Reverse-Selective Nanocomposite Membranes”. *Science* 296.5567 (2002), pp. 519–522. DOI: 10.1126/science.1069580.

17. T. Tozawa et al. “Porous organic cages”. *Nature Materials* 8.12 (2009), pp. 973–978. DOI: 10.1038/nmat2545.

18. S. Jiang, J. T. A. Jones, T. Hasell, C. E. Blythe, D. J. Adams, A. Trewin, and A. I. Cooper. “Porous organic molecular solids by dynamic covalent scrambling”. *Nature Communications* 2 (2011), p. 207. DOI: 10.1038/ncomms1207.

19. M. W. Schneider, I. M. Oppel, H. Ott, L. G. Lechner, H.-J. S. Hauswald, R. Stoll, and M. Mastalerz. “Periphery-Substituted [4+6] Salicylbisimine Cage Compounds with Exceptionally High Surface Areas: Influence of the Molecular Structure on Nitrogen Sorption Properties”. *Chemistry – A European Journal* 18.3 (2012), pp. 836–847. DOI: 10.1002/chem.201102857.

20. T. Mitra, K. E. Jelfs, M. Schmidtmann, A. Ahmed, S. Y. Chong, D. J. Adams, and A. I. Cooper. “Molecular shape sorting using molecular organic cages”. *Nature Chemistry* 5.4 (2013), pp. 276–281. DOI: 10.1038/nchem.1550.

21. A. Avellaneda, P. Valente, A. Burgun, J. D. Evans, A. W. Markwell-Heys, D. Rankine, D. J. Nielsen, M. R. Hill, C. J. Sumby, and C. J. Doonan. “Kinetically Controlled Porosity in a Robust Organic Cage Material”. *Angewandte Chemie International Edition* 52.13 (2013), pp. 3746–3749. DOI: 10.1002/anie.201209922.

22. J. T. A. Jones et al. “On–Off Porosity Switching in a Molecular Organic Solid”. *Angewandte Chemie International Edition* 50.3 (2011), pp. 749–753. DOI: 10.1002/anie.201006030.

23. A. F. Bushell, P. M. Budd, M. P. Attfield, J. T. A. Jones, T. Hasell, A. I. Cooper, P. Bernardo, F. Bazzarelli, G. Clarizia, and J. C. Jansen. “Nanoporous Organic Polymer/Cage Composite Membranes”. *Angewandte Chemie International Edition* 52.4 (2013), pp. 1253–1256. DOI: 10.1002/anie.201206339.

24. R. Krishna and J. M. v. Baten. “In silico screening of metal–organic frameworks in separation applications”. *Physical Chemistry Chemical Physics* 13.22 (2011), pp. 10593–10616. DOI: 10.1039/C1CP20282K.

25. A. W. Thornton, D. Dubbeldam, M. S. Liu, B. P. Ladewig, A. J. Hill, and M. R. Hill. “Feasibility of zeolitic imidazolate framework membranes for clean energy applications”. *Energy & Environmental Science* 5.6 (2012), pp. 7637–7646. DOI: 10.1039/C2EE21743K.

26. F. H. Allen. “The Cambridge Structural Database: a quarter of a million crystal structures and rising”. *Acta Crystallographica Section B* 58.3 (2002), pp. 380–388. DOI: 10.1107/S0108768102003890.

27. T. Hasell, J. A. Armstrong, K. E. Jelfs, F. H. Tay, K. M. Thomas, S. G. Kazarian, and A. I. Cooper. “High-pressure carbon dioxide uptake for porous organic cages: comparison of spectroscopic and manometric measurement techniques”. *Chemical Communications* 49.82 (2013), pp. 9410–9412. DOI: 10.1039/C3CC45924A.

28. R. L. Martin, B. Smit, and M. Haranczyk. “Addressing Challenges of Identifying Geometrically Diverse Sets of Crystalline Porous Materials”. *Journal of Chemical Information and Modeling* 52.2 (2012), pp. 308–318. DOI: 10.1021/ci200386x.

29. M. Pinheiro, R. L. Martin, C. H. Rycroft, A. Jones, E. Iglesia, and M. Haranczyk. "Characterization and comparison of pore landscapes in crystalline porous materials". *Journal of Molecular Graphics and Modelling* 44 (2013), pp. 208–219. DOI: 10.1016/j.jmgm.2013.05.007.

30. Q. Cai, A. Buts, M. J. Biggs, and N. A. Seaton. "Evaluation of methods for determining the pore size distribution and pore-network connectivity of porous carbons". *Langmuir* 23.16 (2007), pp. 8430–8440. DOI: 10.1021/la7007057.

31. E. D. Akten, R. Siriwardane, and D. S. Sholl. "Monte Carlo Simulation of Single- and Binary-Component Adsorption of CO_2, N_2, and H_2 in Zeolite Na-4A". *Energy & Fuels* 17.4 (2003), pp. 977–983. DOI: 10.1021/ef0300038.

32. A. K. Rappe, C. J. Casewit, K. S. Colwell, W. A. Goddard, and W. M. Skiff. "UFF, a full periodic table force field for molecular mechanics and molecular dynamics simulations". *Journal of the American Chemical Society* 114.25 (1992), pp. 10024–10035. DOI: 10.1021/ja00051a040.

33. F. Darkrim and D. Levesque. "Monte Carlo simulations of hydrogen adsorption in single-walled carbon nanotubes". *The Journal of Chemical Physics* 109.12 (1998), pp. 4981–4984. DOI: 10.1063/1.477109.

34. B. Chen and J. I. Siepmann. "Transferable Potentials for Phase Equilibria. 3. Explicit-Hydrogen Description of Normal Alkanes". *The Journal of Physical Chemistry B* 103.25 (1999), pp. 5370–5379. DOI: 10.1021/jp990822m.

35. J. G. Harris and K. H. Yung. "Carbon Dioxide's Liquid-Vapor Coexistence Curve And Critical Properties as Predicted by a Simple Molecular Model". *The Journal of Physical Chemistry* 99.31 (1995), pp. 12021–12024. DOI: 10.1021/j100031a034.

36. D. Boda and D. Henderson. "The effects of deviations from Lorentz–Berthelot rules on the properties of a simple mixture". *Molecular Physics* 106.20 (2008), pp. 2367–2370. DOI: 10.1080/00268970802471137.

37. S. Keskin, J. Liu, R. B. Rankin, J. K. Johnson, and D. S. Sholl. "Progress, Opportunities, and Challenges for Applying Atomically Detailed Modeling to Molecular Adsorption and Transport in Metal-Organic Framework Materials". *Industrial & Engineering Chemistry Research* 48.5 (2009), pp. 2355–2371. DOI: 10.1021/ie800666s.

38. S. Nosé. "A unified formulation of the constant temperature molecular dynamics methods". *The Journal of Chemical Physics* 81.1 (1984), pp. 511–519. DOI: 10.1063/1.447334.

39. R. Krishna and J. M. van Baten. "In silico screening of zeolite membranes for CO_2 capture". *Journal of Membrane Science* 360.1 (2010), pp. 323–333. DOI: 10.1016/j.memsci.2010.05.032.

40. G. Bánhegyi. "Comparison of electrical mixture rules for composites". *Colloid and Polymer Science* 264.12 (1986), pp. 1030–1050. DOI: 10.1007/BF01410321.

41. J.-R. Li, R. J. Kuppler, and H.-C. Zhou. "Selective gas adsorption and separation in metal–organic frameworks". *Chemical Society Reviews* 38.5 (2009), pp. 1477–1504. DOI: 10.1039/B802426J.

42. W. Li, S. Grimme, H. Krieg, J. Möllmann, and J. Zhang. "Accurate Computation of Gas Uptake in Microporous Organic Molecular Crystals". *The Journal of Physical Chemistry C* 116.16 (2012), pp. 8865–8871. DOI: 10.1021/jp2112632.

43. T. Hasell, S. Y. Chong, K. E. Jelfs, D. J. Adams, and A. I. Cooper. "Porous Organic Cage Nanocrystals by Solution Mixing". *Journal of the American Chemical Society* 134.1 (2012), pp. 588–598. DOI: 10.1021/ja209156v.

44. D. Holden, K. E. Jelfs, A. I. Cooper, A. Trewin, and D. J. Willock. "Bespoke Force Field for Simulating the Molecular Dynamics of Porous Organic Cages". *The Journal of Physical Chemistry C* 116.31 (2012), pp. 16639–16651. DOI: 10.1021/jp305129w.

45. R. Krishna and J. M. van Baten. "Comment on Comparative Molecular Simulation Study of CO_2/N_2 and CH_4/N_2 Separation in Zeolites and Metal-Organic Frameworks". *Langmuir* 26.4 (2010), pp. 2975–2978. DOI: 10.1021/la9041875.

46. J. Kim, R. L. Martin, O. Rübel, M. Haranczyk, and B. Smit. "High-Throughput Characterization of Porous Materials Using Graphics Processing Units". *Journal of Chemical Theory and Computation* 8.5 (2012), pp. 1684–1693. DOI: 10.1021/ct200787v.

47. E. Haldoupis, T. Watanabe, S. Nair, and D. S. Sholl. "Quantifying Large Effects of Framework Flexibility on Diffusion in MOFs: CH_4 and CO_2 in ZIF-8". *ChemPhysChem* 13.15 (2012), pp. 3449–3452. DOI: 10.1002/cphc.201200529.

48. S. Keskin and D. S. Sholl. "Selecting metal organic frameworks as enabling materials in mixed matrix membranes for high efficiency natural gas purification". *Energy & Environmental Science* 3.3 (2010), pp. 343–351. DOI: 10.1039/B923980B.

49. B. Shimekit, H. Mukhtar, and T. Murugesan. "Prediction of the relative permeability of gases in mixed matrix membranes". *Journal of Membrane Science* 373.1 (2011), pp. 152–159. DOI: 10.1016/j.memsci.2011.02.038.

50. D. Q. Vu, W. J. Koros, and S. J. Miller. "Mixed matrix membranes using carbon molecular sieves: I. Preparation and experimental results". *Journal of Membrane Science* 211.2 (2003), pp. 311–334. DOI: 10.1016/S0376-7388(02)00429-5.

51. P. M. Budd, K. J. Msayib, C. E. Tattershall, B. S. Ghanem, K. J. Reynolds, N. B. McKeown, and D. Fritsch. "Gas separation membranes from polymers of intrinsic microporosity". *Journal of Membrane Science* 251.1 (2005), pp. 263–269. DOI: 10.1016/j.memsci.2005.01.009.

3.A Supporting Information

Table 3.2: Simulated and experimental surface areas (SA), window and cavity dimensions of POCs 1–5.

cage	sim. SA / $m^2.g^{-1}$	exp. SA / $m^2.g^{-1}$	window size / Å	cavity size / Å
1	0	40	1.82	5.39
2	631	533	3.9	7.73
3	249	409	3.66	5.4
4	2410	1291	5.13	9.76
5	1520	0	4.35	9.14

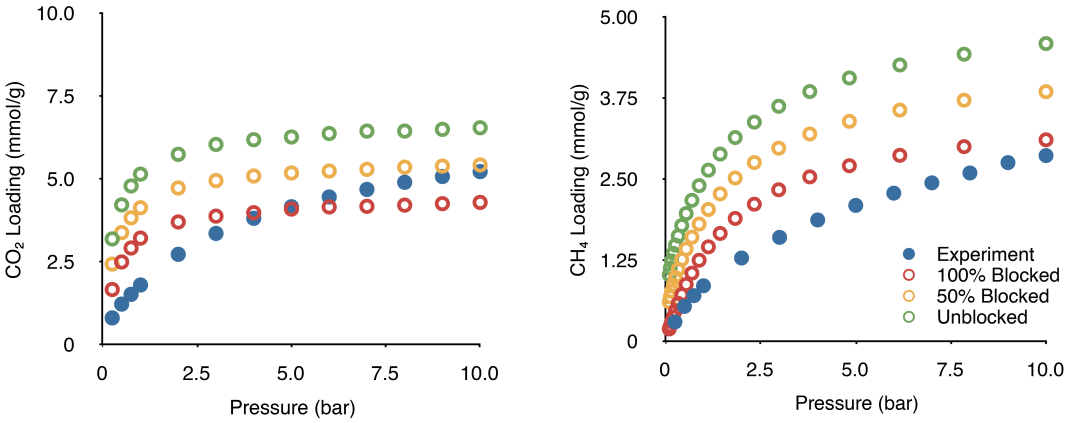

Figure 3.6: CO_2 and CH_4 isotherms of POC 2 with unblocked, 50% and 100% blocked cage volume.

Table 3.3: Simulated gas concentrations of POCs 1–5 at 298 K and 10 bar.

Simulated Concentration / mol.m^{-3}				
cage	H_2	N_2	CO_2	CH_4
1	396	2340	4810	5110
2	345	2130	2350	4100
3	235	1950	2540	2970
4	370	3270	6720	10700
5	273	2200	4780	8240

Table 3.4: Optimized and crystal structure imine angles (°) for POCs 1–5.

cage	**crystal structure**	**optimized structure**
1	114	122
2	116	122
3	119	122
4	121	122

Table 3.5: Arithmetic mean and standard deviations of the window size distributions of POCs 1–5 over 1 ns at 298 K.

cage	**mean / Å**	**std. dev. / Å**
1	0.895	0.0489
2	3.560	0.0842
3	3.500	0.0731
4	4.940	0.2990
5	3.990	0.1360

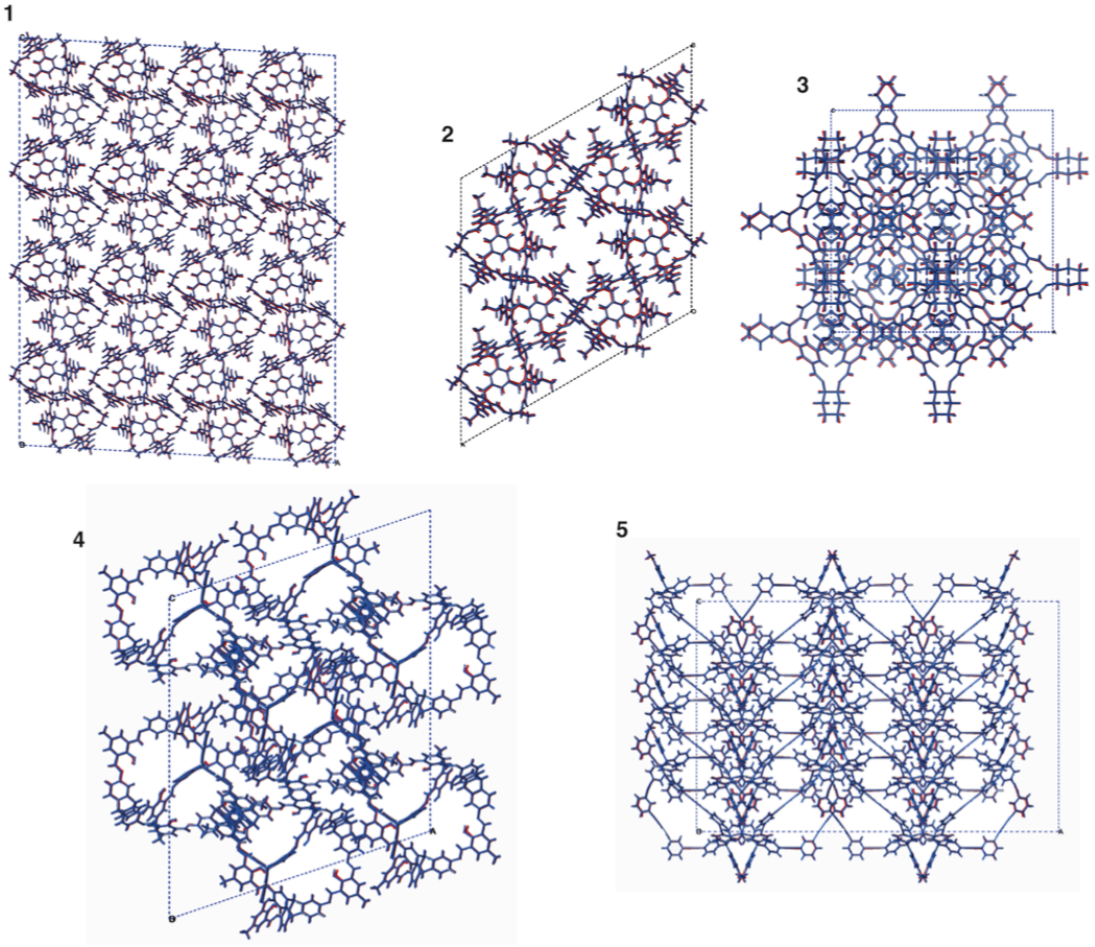

Figure 3.7: Superimposed comparison of UFF optimized simulation cells (blue) and crystal structures (red) of POCs 1–5.

This work has appeared in the following publication.

> J. D. Evans, D. M. Huang, M. R. Hill, C. J. Sumby, D. S. Sholl, A. W. Thornton, and C. J. Doonan. "Molecular Design of Amorphous Porous Organic Cages for Enhanced Gas Storage". *The Journal of Physical Chemistry C* 119.14 (2015), pp. 7746–7754. DOI: 10.1021/jp512944r.

Author statements can be found in Appendix A.

4

Molecular Design of Amorphous Porous Organic Cages

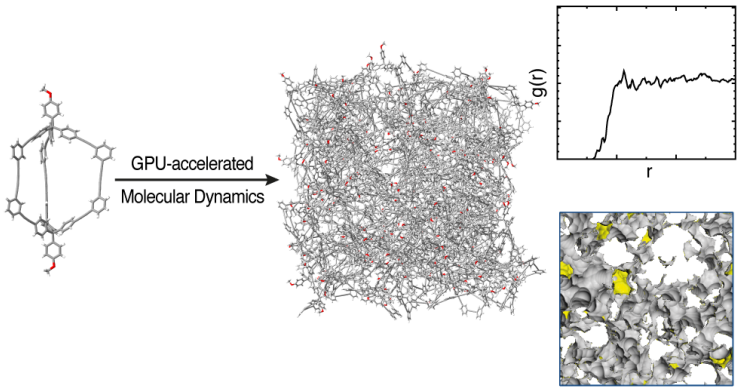

4.1 Abstract

Porous molecular solids are garnering increasing attention with examples of high surface areas and applications in molecular separations. Recently, amorphous networks of molecular cages have shown increased porosity with respect to their crystalline counterparts. However, the structures of amorphous materials cannot be precisely elucidated by X-ray diffraction techniques, thus molecular simulations are vital to understanding their pore structures and origin of porosity. Here we use GPU-accelerated molecular dynamics simulations as an efficient method-

ology to construct representative amorphous network structures. We employ Voronoi network analysis to amorphous networks of seven previously reported cage molecules, providing insight into structure-property relationships. Accordingly, we apply this understanding to delineate synthetic design features that give rise to highly porous analogues of robust cages constructed from carbon-carbon bonds.

4.2 Introduction

Porous solids are widely researched for their application to heterogeneous catalysis,[1] gas storage,[2] and molecular separations.[3] The majority of such materials are extended networks with interconnected pore channels that facilitate diffusion of adsorbates throughout the material. Recently, solids composed of shape-persistent organic cage molecules have been investigated for their bulk porosity.[4] In contrast to extended materials, such as metal-organic frameworks (MOFs)[5] or zeolites,[6] these discrete cages are soluble and thus may be readily fabricated into composite materials such as mixed-matrix membranes.[7,8]

Porosity in molecular solids can arise from the interconnection of the cage pores (intrinsic porosity), voids surrounding the cages that result from inefficient packing (extrinsic porosity), or a combination of both.[9] Accordingly, intermolecular packing has a dramatic effect on the surface accessibility of the bulk solids. This is clearly demonstrated in recent work by Doonan *et al.*, in which two different polymorphs of the same molecule gave rise to vastly different N_2 adsorption.[10] Structure-dependent porosity has also been reported by Cooper *et al.* for imine-based cages.[11] Identifying the origin of porosity is most easily achieved via X-ray diffraction experiments; however, in cases where the bulk solid is amorphous, precisely characterizing the pore structure can be challenging. Consequently, the development of non-structural methods for understanding gas diffusion in such materials is necessary.

Molecular simulations have been used to provide insight into the porosity of disordered systems, such as polymers and rigid molecules.[12,13] Recently, Jiang *et al.* demonstrated an atomistic understanding of H_2/N_2 separations in amorphous porous solids composed of organic cages of tetrahedral geometry.[14] In the present study, we have improved upon this approach by employing a GPU-accelerated molecular dynamics process to simulate substantially larger amorphous cage net-

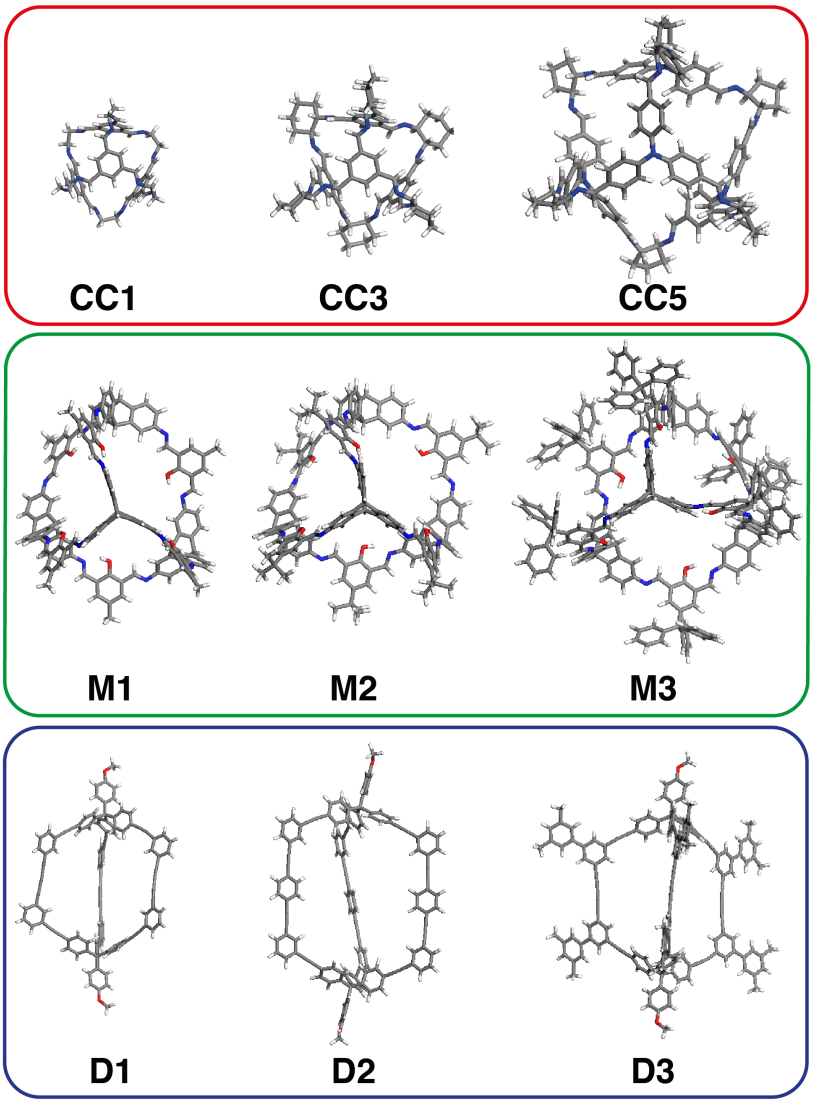

Figure 4.1: Molecular structures of cages investigated. The structures CC1, CC3, CC5, M1–M3, and D1 have been synthesized, but D2 and D3 are hypothetical structures.

works comprising 100 cages, which was found necessary to adequately sample the configuration space of the porous networks. We simulated amorphous networks of nine cage structures, depicted in Figure 4.1, to provide insight into how the porosity of these systems can be optimized.

The cage molecules used in this investigation were selected as they encompass a range of geometries, internal volumes, and external functionalities, as shown in Table 4.4. Specifically, CC1 and CC3 have equivalent volumes but possess different exohedral functionality; CC5 is topologically equivalent to CC1 and CC3 but has approximately 3.8 times the internal pore volume; cage D1 is of trigonal dipyramidal geometry and is constructed from "rod-like" alkyne moieties that give rise to very large window sizes and internal voids; finally, cages M1–M3 are of octahedral geometry with identical internal volumes, but are differentiated by their external functionality: methyl (M1), t-butyl (M2), and triphenylmethyl (M3).[15] Analysis of these systems, which have been synthesized and characterized experimentally, afforded design principles for optimizing the bulk porosity of amorphous solids composed of organic cage molecules, as described below. These principles were applied to generate the hypothetical cages D2 and D3 in Figure 4.1. In particular, we determined that for amorphous systems, decorating the surface of cage D1 with sterically demanding groups gives rise to large voids in the packing structure and thus higher surface area.

4.3 Simulation Methodology

Molecular dynamics simulations were employed using the LAMMPS GPU-accelerated code.[16,17] A judicious choice of the force field is critical for ensuring that the packing and structural properties are accurately described. Accordingly, we used a cage-specific force field for the structures that was developed exclusively for imine cage systems.[18] Parameters not listed in the cage-specific force field were taken from a polymer-specific force field[19] that was used as the basis for the cage-specific force field. Long-range electrostatic interactions were calculated using the PPPM method.[20] A Nosé–Hoover thermostat and barostat were used to fix the temperature and pressure of the simulations.[21] Notably, the cages CC1 and CC3 exist in two different conformers as investigated by Jelfs and co-workers.[22] We have simplified the systems, herein, by simulating only tetrahedral conformers, specifically CC1-R and CC3-R enantiomers.

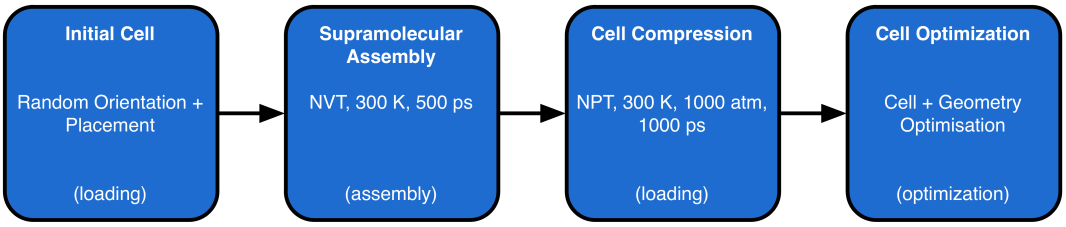

Figure 4.2: Outline of simulation procedure used for production of amorphous cells.

The simulation procedure used in this study is outlined in Figure 4.2. In the loading stage, the simulation cells were packed with 100 molecular cage structures at a density of 0.1 g.cm^{-3}, as performed by the amorphous cell module in Materials Studio 6.0. A low-density structure was used to ensure that interlocking of cage molecules or ring spearing was minimized. The assembly step comprised an NVT molecular dynamics simulation at 300 K for 500 ps with a step size of 1 fs. As depicted in Figure 4.3, this assembly step equilibrates the low-density structure, allowing for self-assembly and aggregation of molecules. Following the assembly step was the compression step, which was composed of an NPT molecular dynamics simulation with 1000 atm of external pressure applied at 300 K for 1000 ps with a step size of 1 fs. During this step, the simulation cell shrinks to give a reasonable target density for the amorphous structure when compared with an experimentally measured density of a known amorphous cage structure.[23] Finally, the amorphous system and simulation cell were optimized by minimizing the system energy to give a final amorphous structure for subsequent analysis, as shown in Figure 4.4. The generation procedure was repeated for 10 independent, randomly generated initial configurations so as to sample the amorphous structural landscape and to allow the sensitivity of the amorphous porous structure to initial conditions be quantified. All analyses discussed below are averaged over these 10 independent representations of the amorphous structure.

This procedure was adapted from the work of Jiang *et al.*, with the addition of cell compression performed under an external pressure of 1000 atm. The generation methodology of Jiang and co-workers[14] required over 16×10^6 steps, whereas in this work we were able to decrease this to 2×10^6 molecular dynamic steps. To ensure the compression pressure did not collapse the cage molecules, we tested it on crystalline cells of CC1, CC3, CC5, D1, and M1 and found the external pressure did not appreciably compress the molecules or cells, as shown in Table 4.5.

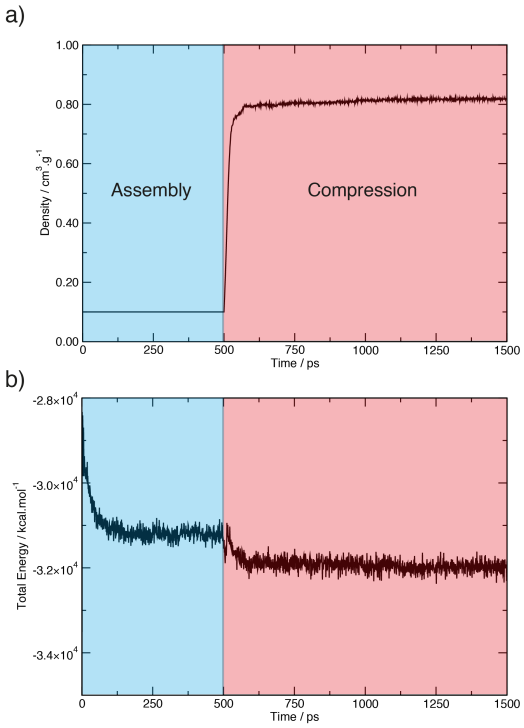

Figure 4.3: Representative sample of the density and total energy during assembly and compression steps of the generation procedure.

Geometric surface areas and pore volumes for the amorphous systems were calculated using the Zeo++ code. This code uses a Voronoi network to obtain a representation of the pore space for a periodic system.[24,25] For a specified probe size Zeo++ can determine the accessible and inaccessible pore volume. Importantly, soft materials such as porous organic cages have been reported to have dynamic connectivity between accessible and inaccessible regions. This has been investigated in crystalline materials,[26] but has not been elucidated for amorphous systems owing to the disordered alignment of pores. As a consequence, we have defined the total surface area and pore volume as the sum of the accessible and inaccessible regions as defined by Zeo++, such that regions accessible by dynamic pore-opening events are not overlooked. Finally, extrinsic volumes were calculated for He probe sizes and by blocking the internal cage volume with a sphere of size equivalent to the internal van der Waals diameter of the cage, as shown in Table 4.6.

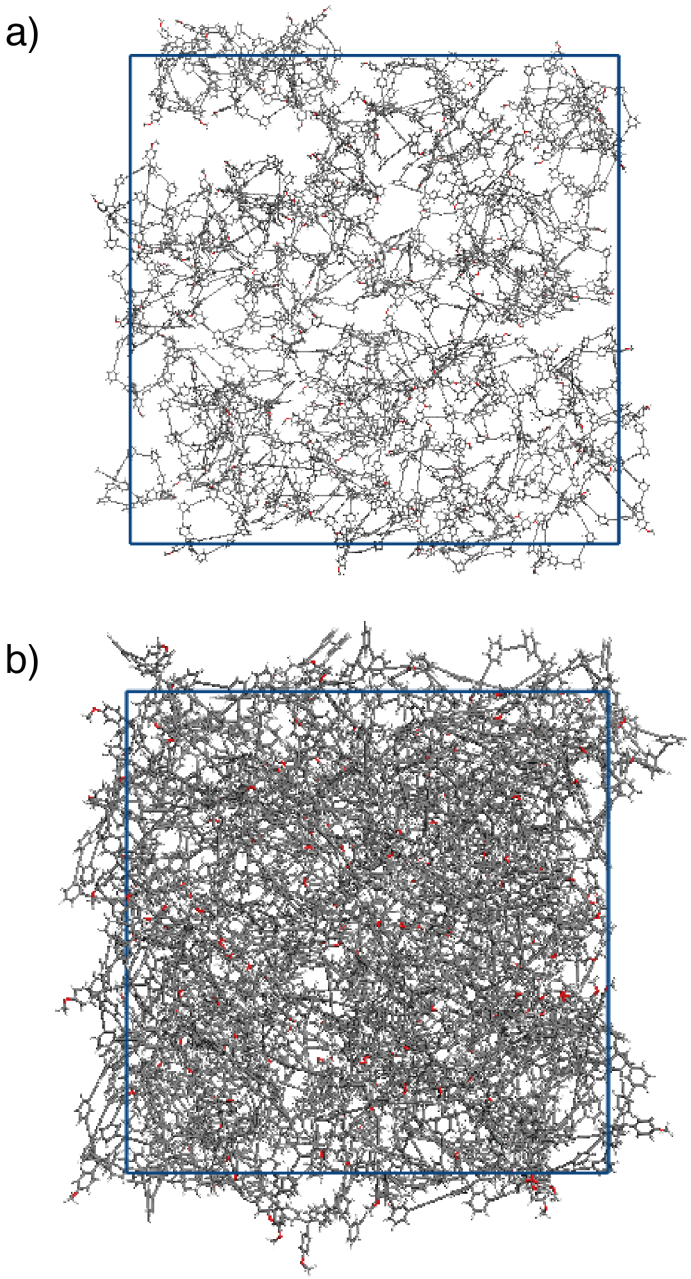

Figure 4.4: Example of structure D1 at the loading step (density of 0.10 g.cm^{-3}) and after the minimization step (density of 0.78 g.cm^{-3}).

4.4 Results and Discussion

4.4.1 Effect of System Size on Porosity and Density of CC3

One of the primary challenges encountered when simulating amorphous materials is to efficiently capture the disorder of a real system with finite periodic simulation cells. To accurately describe such systems, large periodic cells combined with many independent iterations are required. The methodology employed in this study allows us to efficiently simulate cells with more than 100 molecules. We note that a previous report used cells that contained a maximum of 60 molecules.[14] As a test, we chose to study the resulting density and porosity of CC3 as a function of the number of cage molecules per periodic cell. CC3 was chosen for this preliminary investigation as it had been previously studied in detail by Cooper *et al.* Figure 4.5 shows that the average density and total surface area of the amorphous networks are essentially the same for all system sizes studied, but a significant change in variance is observed as the number of molecules per simulation cell is increased, as expected from the Central Limit Theorem.[27] This is consistent with simulation data reported for amorphous polymeric structures and is attributed to the inability of small simulation sizes to effectively sample the 3-D molecular arrangement and pore structures.[28] Upon increasing the sample size to 100 or more molecules per simulation cell, the simulations converge to a density and surface area in reasonable agreement with the experimentally reported surface area.[14] For systems of 50 molecules or less, the simulated surface area overlaps the experimental value, but the standard deviation is over 18%. This analysis highlights the importance of employing large molecular sample sizes to capture, with minimal variance, the density and porosity of amorphous materials.

To further highlight the importance of sample size in molecular amorphous materials, we measured radial distribution functions (RDFs) of the molecular centers-of-mass for the systems with 25, 50, and 100 molecules per simulation cell, as shown in Figure 4.6. The RDF measures the density distribution of cage molecules around a cage molecule centered at the origin. It is clear from this plot that structural correlations between molecules extend beyond half the simulation box length for samples of less than 50 molecules. This means that a molecule could be spatially correlated with more than one periodic image of another particle, potentially introducing unphysical structural correlations that would make the

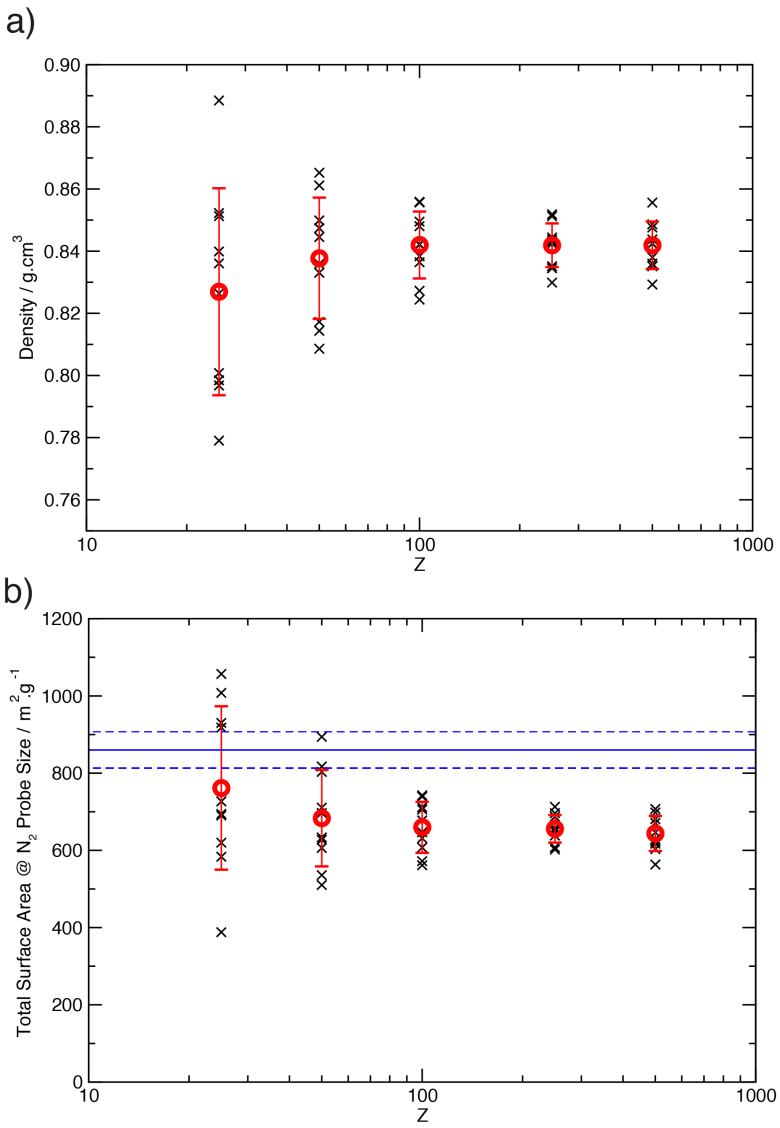

Figure 4.5: (a) Density and (b) total surface area of amorphous CC3 structures as a function of number of molecules per simulation cell (Z). Data from unique simulations are depicted as crosses (black) and the average over these simulations is shown as circles (red). A blue solid line denotes the experimental surface area, with the error depicted as a blue dotted line.

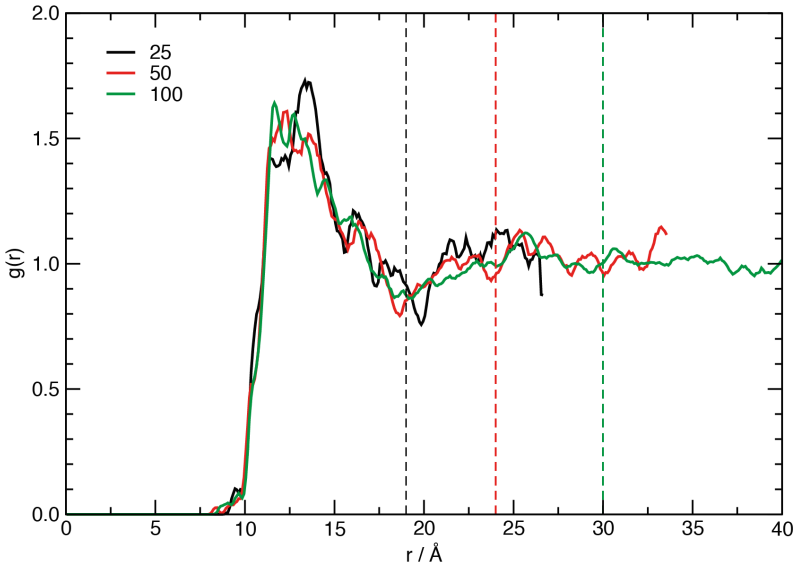

Figure 4.6: RDFs for the cage center-of-mass for samples of CC3 with 25, 50, and 100 molecules per simulation cell. Half-cell lengths are depicted by vertical dotted lines.

simulated structure unrepresentative of that of an extended amorphous system. In contrast, the RDF of the sample containing 100 molecules converges to one at half the box length and thus finite-size effects should not be significant in this system.

4.4.2 Amorphous Networks of CC1, CC3, CC5, D1, and M1-3

We applied the methodology outlined in Figure 4.2 to seven reported cage systems: CC1, CC3, CC5, D1, and M1–M3 (Figure 4.1), resulting in structural models of amorphous networks with average densities listed in Table 4.1. We note that the density of the amorphous networks lies between 0.566 and 0.873 g.cm^{-3} and varies significantly for the selected cage molecules. The densest amorphous structure is observed for CC1 as a consequence of the smaller cage volume and bare external functionality. By comparison, a much less dense structure is found for M3 as a result of the large cage volume and bulky external triphenylmethyl moieties.

To aid in the comparison of supramolecular arrangements, we calculated the radial distribution function for the centers-of-mass of each of the cages in the simulation cell. The average RDF from the 10 independent simulations for each of the seven cage systems is displayed in Figure 4.7. The RDFs calculated for networks of CC1, CC3, and CC5 (Figure 4.7a) demonstrate the effect of external

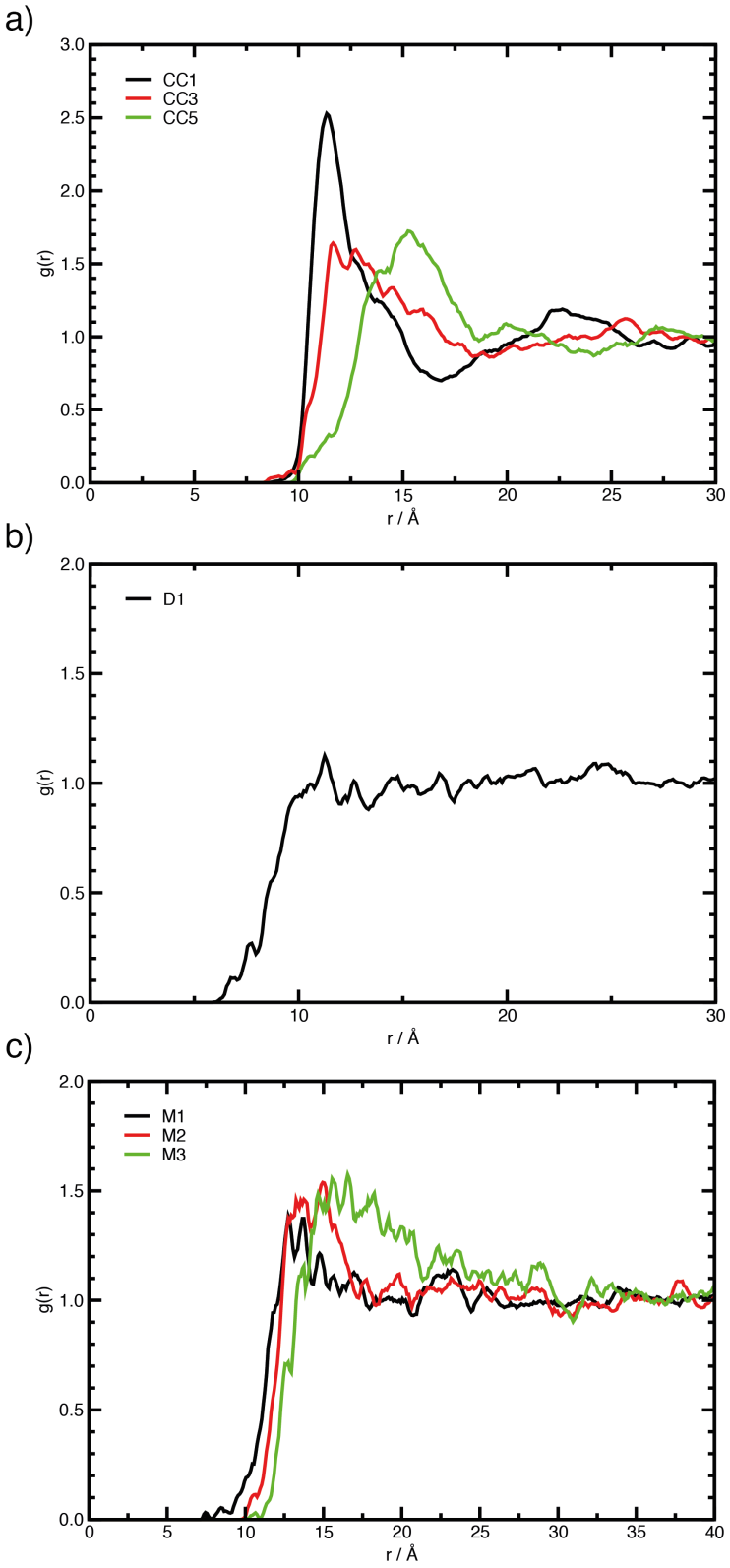

Figure 4.7: RDFs for the cage center-of-mass for structures (a) CC1, CC3, and CC5; (b) D1; and (c) M1–M3.

Table 4.1: Amorphous cell densities.

cage	density/ g.cm^{-3}
CC1	0.873 ± 0.013
CC3	0.842 ± 0.011
CC5	0.658 ± 0.018
D1	0.791 ± 0.010
M1	0.838 ± 0.018

functionality and cage size on the supramolecular arrangement of the molecular units. Attachment of sterically demanding cyclohexyl moieties in CC3 yields a broad distribution, an effect of the cyclohexyl groups directing the cage units to pack into a less dense network than the functionally bare units of CC1. The distribution is broadened further and displaced to greater distance as a consequence of the larger cage size of CC5 generating an increased average cage–cage distance of 15 Å, thus producing low-density amorphous structures. The first peak in the RDF of D1 (Figure 4.7b), unlike that in the RDFs of CC1, CC3, and CC5, does not correspond to the size of the molecule, with significant density observed at distances less than 10 Å. This behavior can be attributed to the elongated pyramidal geometry of the cage unit, which allows the units to pack in a dense interdigitated fashion, as shown in Figure 4.8. Finally, the calculated RDFs for the amorphous structures of M1–M3 provide further evidence that bulky functional groups yield inefficient packing and larger cage–cage distances. For example, increasing the external functional groups from methyl (M1) to t-butyl (M2) and triphenylmethyl (M3) results in a broadening of the primary RDF peak and a displacement to a larger average distance.

4.4.3 Pore Structure Analysis of CC1, CC3, CC5, D1 and M1-3: Role of Extrinsic Porosity

The bulk porosity of the amorphous networks was probed by Voronoi network analysis. Pore volumes and surface areas were simulated using probe sizes equivalent to the kinetic diameters of He (2.60 Å) and N_2 (3.64 Å), respectively, to give the resulting average values in Table 4.2. The average pore volume is plotted against the intrinsic cage volume and radius of gyration in Figure 4.9. The radius of gyration was used as a measure of the size of the cage molecule. Our simulations show no correlation between the cage volume and total pore volume. For example, a large difference in pore volume is observed for the series M1–M3

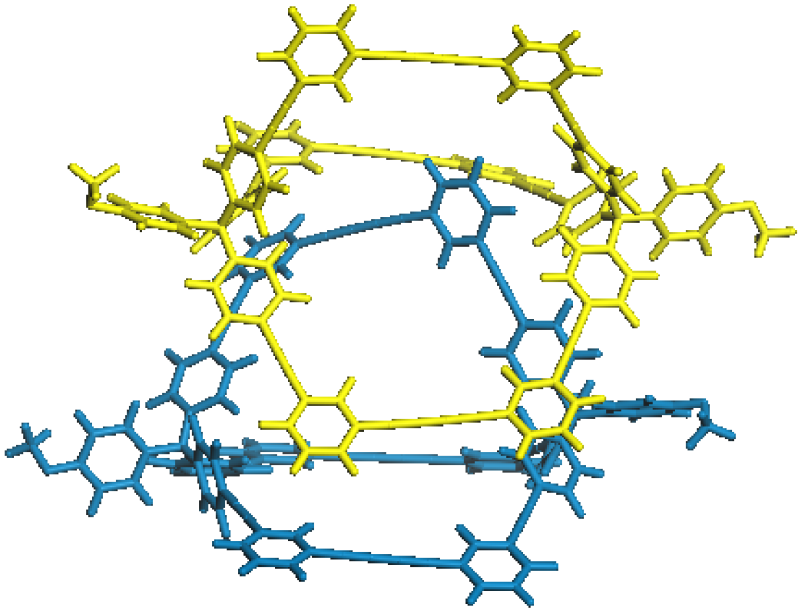

Figure 4.8: Representation of the interdigitated motif observed in amorphous structures of D1.

as a result of external functionality influencing the pore structure, but the cage volume itself does not vary across this series of molecules. In addition, in spite of the large cage volume of D1, the resulting pore volume is modest by virtue of the close packing of molecular units. In contrast to the lack of correlation for cage volume, there is a general trend for porosity with the radius of gyration, which varies with both the internal cage volume and external functionality (Figure 4.9b). For instance, the largest radii of gyration are a result of bulky external functionality (M3) or large cage structure (CC5), which in turn produce amorphous pore networks of large volumes and surface areas. From these results we can qualitatively conclude that molecules with large size produce amorphous structures with high surface areas and pore volumes and that this can be achieved by either constructing large cages or by decorating the surface of the cage with sterically bulky groups.

To further understand the porosity in these systems, pore size distributions were calculated and averaged over the 10 independent simulations; the distributions are depicted in Figure 4.10. Pore size distributions were simulated using the Zeo++ code; details of this method have been reported previously.[29] Cage CC1, as the result of close packing of cage units, has a pore size distribution with a sharp peak at 5 Å. Sholl and co-workers have shown that materials with sharp and rigid pore size distributions are amendable to kinetic gas separations.[30] Im-

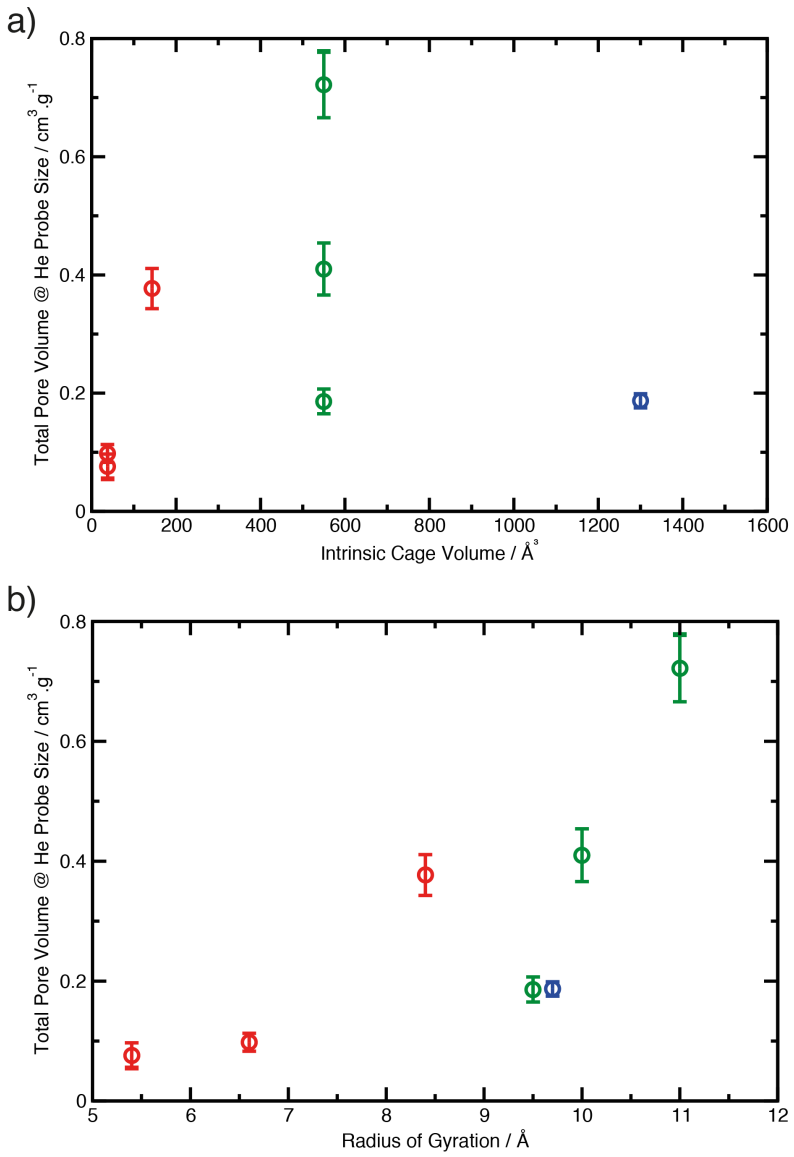

Figure 4.9: Average total pore volume for He probe radius against the (a) intrinsic cage volume and (b) radius of gyration. CC1, CC3, and CC5 (red), D1 (blue), and M1–M3 (green).

Table 4.2: Average total surface areas for N_2 probe size and total pore volume for He probe size for the amorphous cage structures.

cage	total surface area / $\mathbf{m^2.g^{-1}}$	total pore volume / $\mathbf{cm^3.g^{-1}}$
CC1	528 ± 77	0.076 ± 0.021
CC3	660 ± 66	0.097 ± 0.013
CC5	1815 ± 73	0.377 ± 0.034
D1	1211 ± 70	0.187 ± 0.012
M1	1168 ± 95	0.186 ± 0.021
M2	1759 ± 100	0.410 ± 0.044
M3	1892 ± 73	0.722 ± 0.056

portantly, this has been observed experimentally with amorphous samples of CC1 prepared by freeze-drying, which possess excellent H_2/N_2 selectivity.[14] The pore structure of CC3 differs from that of CC1, with exohedral cyclohexane groups supporting larger pore diameters with sizes of 5–10 Å. Notably, CC1 and CC3 possess identical cages and this results in their pore networks having equivalent limiting pore sizes. Finally, the pore structure of CC5 has a broad distribution, owing to the combination of the large cage volume and bulky external functionality. The pore size distributions of M1–M3 clearly demonstrate the increase in porosity supported by increasingly bulky moieties. First, the distribution for M1 reflects the internal cage cavities, as the peak observed is equivalent to the internal diameter of the molecular cage. In comparison, M2 and M3 have larger molecular size increased by the attachment of bulky functionality. This produces broader pore size distributions as the disruption of close packing by the external functionality creates large extrinsic voids. Experimentally, Mastalerz and co-workers found that amorphous materials of M1–M3 had similar Brunauer–Emmett–Teller (BET) surface area.[15] However, these materials were analyzed as synthesized, not produced amorphously on purpose and thus may not be truly amorphous networks.

Amorphous molecular cage structures differ from their polymer analogues, as the source of disordered porous networks made from molecular cages differ fundamentally from their polymer analogues in that porosity can originate from two distinct sources: the internal cavity of the molecule (intrinsic porosity) and the space external to the molecules formed by the supramolecular arrangement (extrinsic porosity). It is important to consider the source of the porosity when discussing the pore structure in these materials; as such the intrinsic and extrinsic

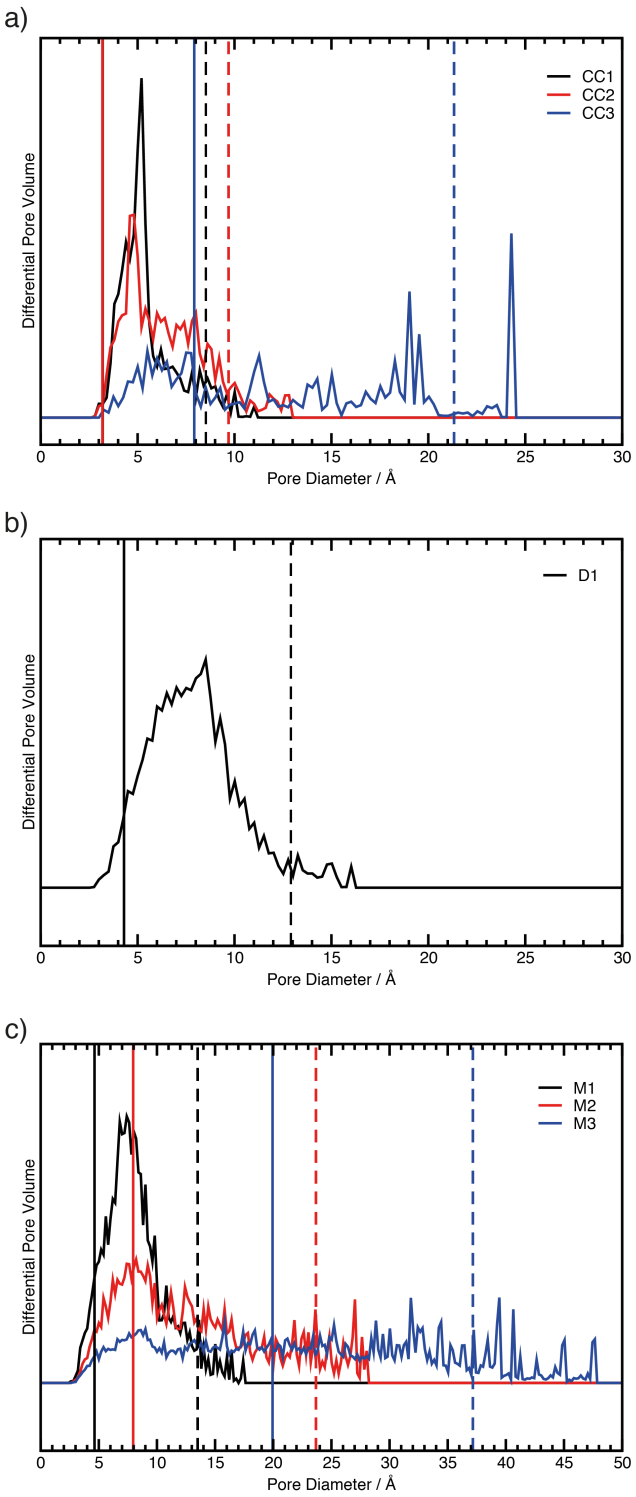

Figure 4.10: Pore size distributions for the amorphous networks resulting from structures (a) CC1, CC3, and CC5, (b) D1, and (c) M1–M3, along with average limiting pore diameter (vertical solid line) and average largest pore diameter (vertical dotted line).

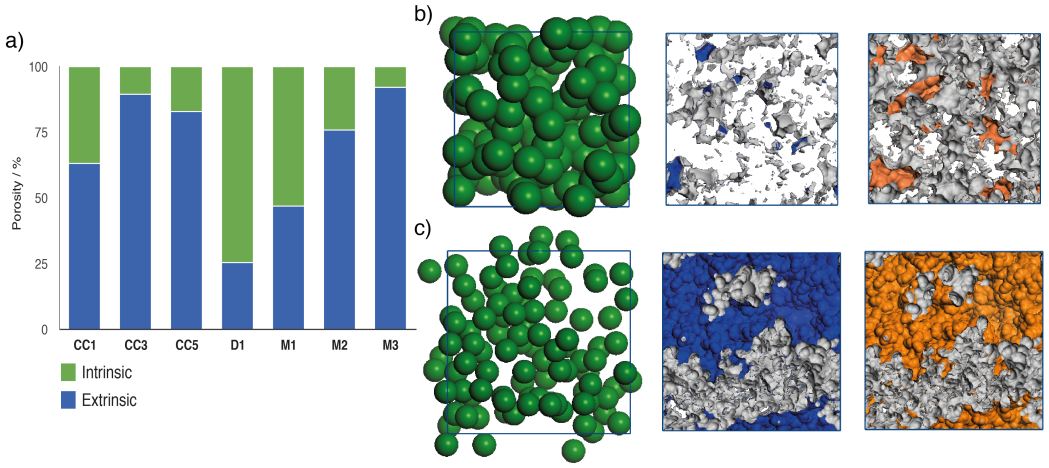

Figure 4.11: (a) Averaged contribution to the pore structure from intrinsic and extrinsic porosity and an example for (b) D1 and (c) M3, with green spheres denoting the intrinsic pore structure, blue regions showing the extrinsic pore structure, and orange regions illustrating the total.

pore volumes were measured in our generated systems, with the results displayed in Figure 4.11. Importantly, the amount of extrinsic porosity observed for CC1 and CC3 amorphous systems is equivalent to estimates previously reported; the larger cyclohexyl groups in CC3 produce a greater extrinsic volume by disrupting close packing. Increasing the cage size in CC5 results in an amorphous network with a slightly smaller ratio of extrinsic:intrinsic volume compared with CC3, as the intrinsic volume of the cage is larger but the external packing is similar to that of CC3. In contrast, D1 has significantly less extrinsic porosity than CC1, CC3, and CC5, as shown in Figure 4.11b, as a result of the molecular units packing in close proximity, which interconnects cage volumes. Finally, the trend in pore volume and pore size distributions for M1–M3 is clearly explained by the extrinsic pore percentage. Cages with bulky external moieties, such as M3, support large extrinsic voids, as depicted in Figure 4.11c. This packing results in broad and undefined pore sizes, as observed in the pore size distributions. In summary, the source of porosity in these materials is vital to understand the trends in porosity observed in this study: we find an increase in porosity in these amorphous systems is primarily a result of increasing the extrinsic porosity.

The potential advantages of amorphous networks are clearly evident when their surface areas and densities are compared with those of their crystalline counterparts. For example, Table 4.7 shows how amorphous packing is able to unlock porosity that may not be possible to realize in crystalline polymorphs.

Table 4.3: Average total surface areas for N_2 probe size and total pore volume for He probe size for the amorphous cage structures.

cage	density / $\mathbf{g.cm^{-3}}$	total surface area / $\mathbf{m^2.g^{-1}}$	total pore volume / $\mathbf{cm^3.g^{-1}}$
D1	0.791 ± 0.010	1211 ± 70	0.187 ± 0.012
D2	0.859 ± 0.011	804 ± 66	0.118 ± 0.011
D3	0.593 ± 0.024	1933 ± 70	0.554 ± 0.069

4.4.4 In Silico Design of D1 Analogues

The analysis above has outlined several general principles for designing the porosity of amorphous cage molecules. We sought to use these observations to optimize D1 analogues for increased surface area in the amorphous state. The present study has found two general strategies, applied to the molecular units, to increase the porosity of amorphous cage systems: increasing the encapsulated cage volume (CC3 and CC5) and introducing sterically bulky groups to the external surface of the cage (M1–M3). Accordingly, we have applied these principles to D1 in the effort to produce an extremely porous structure. The hypothetical structure D2 was realized by increasing the volume of D1 by incorporation of phenyl rings to the dialkyne struts. Furthermore, a cage with bulky external functionality, D3, was constructed by adding mesityl groups to the vertices of D1. The two D1 analogues, both shown in Figure 4.1, were selected to be synthetically feasible.

The density, surface area, and pore volume of amorphous cage networks for the D1–D3 series is displayed in Table 4.3. It is clear that the larger volume cage D2 structure produces an amorphous network with higher density and lower surface area and pore volume than the original D1. In contrast, functionalization by bulky mesityl groups in D3 results in a less dense amorphous structure with increased surface area and pore volume.

Examination of RDFs in Figure 4.12a reveals the underlying reason for these observations. The increased cage size of D2 not only produces large internal volume but also generates larger molecular windows and greater flexibility. A consequence of this is a greater degree of interdigitation, as evidenced by the peak in the RDF at shorter distances and higher density compared with D1. In contrast, the RDF for amorphous structures of D3 is displaced to larger distance and broadened. Absence of close packing cages at <8 Å and the broad distribution suggests that the mesityl functionality disrupts the close-packing motif observed for D1 and D2. Additionally, calculation of the ratio of extrinisic:intrinsic poros-

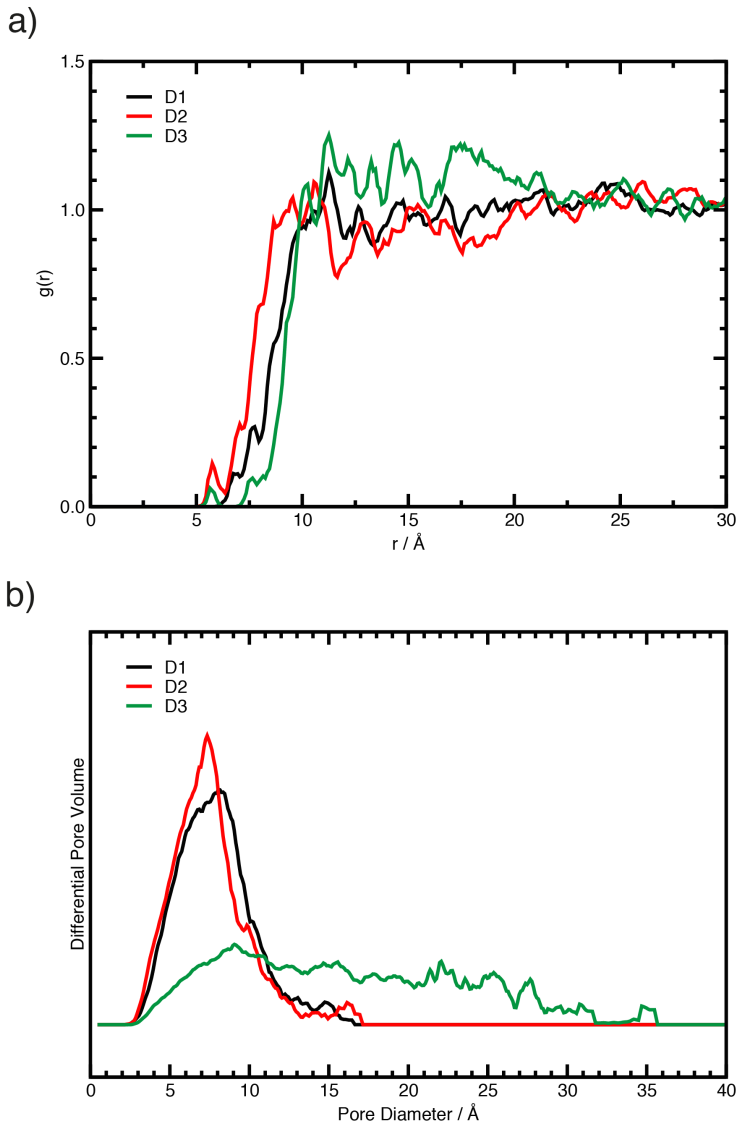

Figure 4.12: Average (a) RDFs and (b) pore size distributions for D1–D3

ity of the amorphous networks supports this conclusion, as shown in Table 4.8. Porosity for D1 and D2 structures is primarily a consequence of the intrinsic volume of the molecular cages, whereas D3 has 76% of its pore volume associated with regions extrinsic to molecular units. Furthermore, the pore size distribution (Figure 4.12b) for D3 demonstrates larger pore sizes are present in the amorphous system and the lack of defined pore sizes observed for D1 and D2.

We have successfully tested the amorphous networks of hypothetical analogues of D1 for porosity and morphology. In contrast to what was found for the CC1 analogues, CC3 and CC5, we find that increasing the internal volume in D2 results in lower porosity due to the shape of molecular units allowing closer packing. However, by increasing the steric bulk external to the cage, as observed for M1–M3, we find the structure D3 has increased pore volume and surface area, making this cage molecule an ideal candidate for synthesis.

4.5 Conclusion

Herein we describe an efficient computational methodology for generating representative amorphous cells composed of porous organic cages. Importantly, we have improved significantly on previously reported methods through the use of external pressure during the compression stage and the use of GPU-accelerated molecular dynamics. Moreover, we have examined the porosity and morphology of the structures using Voronoi network analysis and center-of-mass radial distribution functions. We find good agreement between the simulated surface area of our CC3 model and previously reported adsorption experiments. It is clear that the models described in this study give fundamental insight into these amorphous materials, which is unobtainable by experimental methods alone.

Our investigation has elucidated several important features of the nature of porous organic cage amorphous networks. First, on the subject of generation of representative amorphous models, we have demonstrated a modest effect of system size on the resulting density and porosity of the generated amorphous structure. Specifically, the CC3 system demonstrates a large variance in the density and porosity of systems comprising less than 100 molecules per simulation cell. This result directed our methodology to use simulation cells of 100 molecules to ensure an accurate and precise representation of random packing of cage units. Second, we have gleaned general principles that govern the morphology and porosity in the amorphous state by applying our methodology to seven reported cage structures encompassing several distinct molecular geometries. Two key relationships were observed: a large encapsulated internal volume of the cage molecule can produce high-porosity amorphous structures (CC5), and bulky external functionality can yield highly porous structures by supporting greater pore volume extrinsic to the molecular units (M3). However, cage geometry is crucial to defining the resulting morphology. In particular, we find that the cage D1 is able to interdigitate and consequently produces amorphous networks with unexceptional pore volume despite the large internal volume and cage size. Lastly, we have ap-

plied this understanding to optimizing the surface area of hypothetical analogues of D1. A novel analogue, D3, with bulky mesityl groups attached external to the cage was found to produce an amorphous structure with increased porosity as a consequence of extrinsic pore volume.

This investigation has unequivocally demonstrated that molecular simulations can give atomistic insight into amorphous porous organic cages. This has allowed us to carry out de novo design of amorphous solids for applications in gas storage, which has previously only been applied for crystalline porous solids.

4.6 References

1. J. Lee, O. K. Farha, J. Roberts, K. A. Scheidt, S. T. Nguyen, and J. T. Hupp. "Metal–organic framework materials as catalysts". *Chemical Society Reviews* 38.5 (2009), pp. 1450–1459. DOI: 10.1039/B807080F.
2. R. E. Morris and P. S. Wheatley. "Gas Storage in Nanoporous Materials". *Angewandte Chemie International Edition* 47.27 (2008), pp. 4966–4981. DOI: 10.1002/anie.200703934.
3. J.-R. Li, J. Sculley, and H.-C. Zhou. "Metal–Organic Frameworks for Separations". *Chemical Reviews* 112.2 (2011), pp. 869–932. DOI: 10.1021/cr200190s.
4. A. I. Cooper. "Nanoporous Organics Enter the Cage Age". *Angewandte Chemie International Edition* 50.5 (2011), pp. 996–998. DOI: 10.1002/anie.201006664.
5. H. Furukawa, K. E. Cordova, M. O'Keeffe, and O. M. Yaghi. "The Chemistry and Applications of Metal-Organic Frameworks". *Science* 341.6149 (2013), p. 1230444. DOI: 10.1126/science.1230444.
6. M. E. Davis. "Ordered porous materials for emerging applications". *Nature* 417.6891 (2002), pp. 813–821. DOI: 10.1038/nature00785.
7. J. D. Evans, D. M. Huang, M. R. Hill, C. J. Sumby, A. W. Thornton, and C. J. Doonan. "Feasibility of Mixed Matrix Membrane Gas Separations Employing Porous Organic Cages". *The Journal of Physical Chemistry C* 118.3 (2014), pp. 1523–1529. DOI: 10.1021/jp4079184.
8. A. F. Bushell, P. M. Budd, M. P. Attfield, J. T. A. Jones, T. Hasell, A. I. Cooper, P. Bernardo, F. Bazzarelli, G. Clarizia, and J. C. Jansen. "Nanoporous Organic Polymer/Cage Composite Membranes". *Angewandte Chemie International Edition* 52.4 (2013), pp. 1253–1256. DOI: 10.1002/anie.201206339.
9. T. Tozawa et al. "Porous organic cages". *Nature Materials* 8.12 (2009), pp. 973–978. DOI: 10.1038/nmat2545.
10. A. Avellaneda, P. Valente, A. Burgun, J. D. Evans, A. W. Markwell-Heys, D. Rankine, D. J. Nielsen, M. R. Hill, C. J. Sumby, and C. J. Doonan. "Kinetically Controlled Porosity in a Robust Organic Cage Material". *Angewandte Chemie International Edition* 52.13 (2013), pp. 3746–3749. DOI: 10.1002/anie.201209922.
11. J. T. A. Jones et al. "On–Off Porosity Switching in a Molecular Organic Solid". *Angewandte Chemie International Edition* 50.3 (2011), pp. 749–753. DOI: 10.1002/anie.201006030.
12. L. J. Abbott and C. M. Colina. "Formation of Microporosity in Hyper-Cross-Linked Polymers". *Macromolecules* 47.15 (2014), pp. 5409–5415. DOI: 10.1021/ma500579x.
13. L. J. Abbott, A. G. McDermott, A. Del Regno, R. G. D. Taylor, C. G. Bezzu, K. J. Msayib, N. B. McKeown, F. R. Siperstein, J. Runt, and C. M. Colina. "Characterizing the Structure of Organic Molecules of Intrinsic Microporosity by Molecular Simulations and X-ray Scattering". *The Journal of Physical Chemistry B* 117.1 (2013), pp. 355–364. DOI: 10.1021/jp308798u.
14. S. Jiang, K. E. Jelfs, D. Holden, T. Hasell, S. Y. Chong, M. Haranczyk, A. Trewin, and A. I. Cooper. "Molecular Dynamics Simulations of Gas Selectivity in Amorphous Porous Molecular Solids". *Journal of the American Chemical Society* 135.47 (2013), pp. 17818–17830. DOI: 10.1021/ja407374k.
15. M. W. Schneider, I. M. Oppel, H. Ott, L. G. Lechner, H.-J. S. Hauswald, R. Stoll, and M. Mastalerz. "Periphery-Substituted [4+6] Salicylbisimine Cage Compounds with Exceptionally High Surface Areas: Influence of the Molecular Structure on Nitrogen Sorption Properties". *Chemistry – A European Journal* 18.3 (2012), pp. 836–847. DOI: 10.1002/chem.201102857.

16. W. M. Brown, P. Wang, S. J. Plimpton, and A. N. Tharrington. "Implementing molecular dynamics on hybrid high performance computers – short range forces". *Computer Physics Communications* 182.4 (2011), pp. 898–911. DOI: 10.1016/j.cpc.2010.12.021.

17. S. Plimpton. "Fast Parallel Algorithms for Short-Range Molecular Dynamics". *Journal of Computational Physics* 117.1 (1995), pp. 1–19. DOI: 10.1006/jcph.1995.1039.

18. D. Holden, K. E. Jelfs, A. I. Cooper, A. Trewin, and D. J. Willock. "Bespoke Force Field for Simulating the Molecular Dynamics of Porous Organic Cages". *The Journal of Physical Chemistry C* 116.31 (2012), pp. 16639–16651. DOI: 10.1021/jp305129w.

19. H. Sun. "Ab initio calculations and force field development for computer simulation of polysilanes". *Macromolecules* 28.3 (1995), pp. 701–712. DOI: 10.1021/ma00107a006.

20. E. L. Pollock and J. Glosli. "Comments on P3M, FMM, and the Ewald method for large periodic Coulombic systems". *Computer Physics Communications* 95.2 (1996), pp. 93–110. DOI: 10.1016/0010-4655(96)00043-4.

21. D. J. Evans and B. L. Holian. "The Nose–Hoover thermostat". *The Journal of Chemical Physics* 83.8 (1985), pp. 4069–4074. DOI: 10.1063/1.449071.

22. K. E. Jelfs, F. Schiffmann, J. T. A. Jones, B. Slater, F. Cora, and A. I. Cooper. "Conformer interconversion in a switchable porous organic cage". *Physical Chemistry Chemical Physics* 13.45 (2011), pp. 20081–20085. DOI: 10.1039/C1CP22527H.

23. S. Jiang, J. T. A. Jones, T. Hasell, C. E. Blythe, D. J. Adams, A. Trewin, and A. I. Cooper. "Porous organic molecular solids by dynamic covalent scrambling". *Nature Communications* 2 (2011), p. 207. DOI: 10.1038/ncomms1207.

24. R. L. Martin, B. Smit, and M. Haranczyk. "Addressing Challenges of Identifying Geometrically Diverse Sets of Crystalline Porous Materials". *Journal of Chemical Information and Modeling* 52.2 (2012), pp. 308–318. DOI: 10.1021/ci200386x.

25. T. F. Willems, C. H. Rycroft, M. Kazi, J. C. Meza, and M. Haranczyk. "Algorithms and tools for high-throughput geometry-based analysis of crystalline porous materials". *Microporous and Mesoporous Materials* 149.1 (2012), pp. 134–141. DOI: 10.1016/j.micromeso.2011.08.020.

26. D. Holden, K. E. Jelfs, A. Trewin, D. J. Willock, M. Haranczyk, and A. I. Cooper. "Gas Diffusion in a Porous Organic Cage: Analysis of Dynamic Pore Connectivity Using Molecular Dynamics Simulations". *The Journal of Physical Chemistry C* 118.24 (2014), pp. 12734–12743. DOI: 10.1021/jp500293s.

27. L. E. Reichl. *A Modern Course in Statistical Physics*. 3rd Revised and Updated Edition edition. Weihheim: Wiley-VCH, 2009. 427 pp.

28. K. E. Hart, L. J. Abbott, and C. M. Colina. "Analysis of force fields and BET theory for polymers of intrinsic microporosity". *Molecular Simulation* 39.5 (2013), pp. 397–404. DOI: 10.1080/08927022.2012.733945.

29. M. Pinheiro, R. L. Martin, C. H. Rycroft, A. Jones, E. Iglesia, and M. Haranczyk. "Characterization and comparison of pore landscapes in crystalline porous materials". *Journal of Molecular Graphics and Modelling* 44 (2013), pp. 208–219. DOI: 10.1016/j.jmgm.2013.05.007.

30. E. Haldoupis, T. Watanabe, S. Nair, and D. S. Sholl. "Quantifying Large Effects of Framework Flexibility on Diffusion in MOFs: CH_4 and CO_2 in ZIF-8". *ChemPhysChem* 13.15 (2012), pp. 3449–3452. DOI: 10.1002/cphc.201200529.

4.A Supporting Information

Table 4.4: Structure metrics of cages investigated.

cage	geometry	internal volume / Å^3	window size / Å	external functionality
C1	tetrahedral	37.9	6	-
C2	tetrahedral	37.9	6	cyclohexyl
C3	tetrahedral	143	10	cyclohexyl
D1	trigonal dipyramidal	1300	12	-
D2	trigonal dipyramidal	1500	14	-
D3	trigonal dipyramidal	1300	12	Mesityl
M1	octahedral	550	10	methyl
M2	octahedral	550	10	t-butyl
M3	octahedral	550	10	triphenylmethyl

Table 4.5: Reported density of crystalline cage structures and their resulting density after the generation procedure is applied.

cage	crystalline density / g.cm^{-3}	post-simulation density / g.cm^{-3}
C1	1.0330	1.0330
C2	0.9733	0.9950
C3	0.7989	0.8147
D1	0.7943	0.7410
M1	0.7122	0.7844

Table 4.6: Blocking sphere diameters used to calculate intrinsic:extrinsic pore volume ratio.

cage	blocking sphere diameter / Å
C1	7
C2	7
C3	11
D1	14
D2	18
D3	14
M1	13
M2	13
M3	13

Table 4.7: Comparison of simulated total surface areas (SA) for reported crystalline cage packings with simulated amorphous surface areas from the present study.

cage	crystalline total SA / $\mathbf{m^2.g^{-1}}$	amorphous total SA / $\mathbf{m^2.g^{-1}}$
C1	173	528 ± 77
C2	249	660 ± 66
C3	1500	1815 ± 73
D1	1520	1211 ± 70
M1	2400	1168 ± 95

Table 4.8: Average extrinsic and intrinsic pore volumes for cages.

cage	average intrinsic volume / %	average extrinsic volume / %
D1	74.6	25.4
D2	88.6	11.4
D3	23.3	76.7

This work may appear in the following publication.

> J. D. Evans, D. M. Huang, C. J. Sumby, A. W. Thornton, and C. J. Doonan. "Computational Identification of Organic Porous Molecular Crystals". to be submitted (2015).

Author statements can be found in Appendix A.

5

Computational Identification of Organic Porous Molecular Crystals

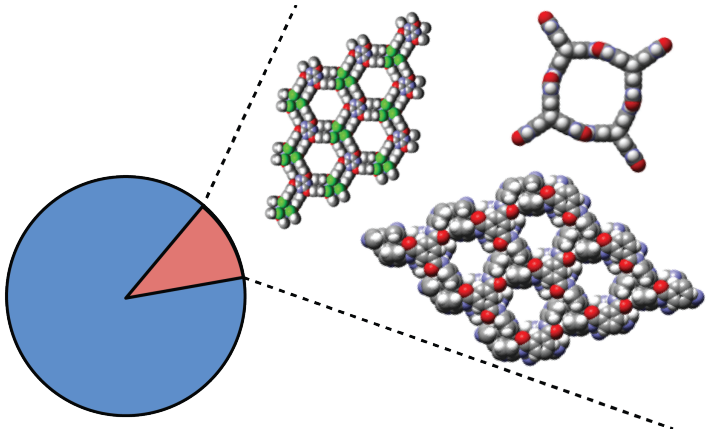

5.1 Abstract

Many nanoporous materials are composed of extended three-dimensional covalent or coordination bond networks to produce porous structures such metal–organic frameworks and zeolites. On the other hand, there are a number of reports of molecular crystals that display surface areas and separation efficiencies rivaling these conventional materials. In this investigation, we have used Voronoi network analysis and molecular simulations to screen over 150 000 organic molecular crystal structures resulting in the identification of a database of 481 potential organic

porous molecular crystals (oPMCs), a testament to the rarity of these materials. Subsequently, we have measured the surface area and pore dimensions of these structures, placing these materials in context with conventional porous frameworks. The database has been used to demonstrate a number of unique trends and properties that previously could not be quantified as a result of the limited reported examples. Finally, we have applied machine learning algorithms to find the molecular property that is the best predictor of crystal porosity is molecular surface area. The identified database is a promising tool for discovering candidate structures for applications in gas separations while also providing design rules for the production of new porous crystals.

5.2 Introduction

Microporous materials constructed from discrete molecules have recently been highlighted as attractive alternatives to polymeric framework materials such as zeolites and metal-organic frameworks (MOFs). Porous molecular solids have been shown to outperform many classic porous materials and due to their molecular nature they can exhibit features not achievable in framework materials, for instance, solubility and switchable porosity.[1,2]

Porous molecular crystals are porous networks formed from discrete molecular units by way of non-covalent interactions, by macrocyclic voids or a combination of both. This interplay of intrinsic and extrinsic porosity has been heavily featured and described by Cooper and coworkers.[3] Despite the relatively soft interactions these materials retain porosity upon removal of solvent and result in materials with surface areas approaching 4000 $m^2.g^{-1}$.[4] Crystalline porous molecules are favored over their amorphous analogues[5] as their long-range structural order allows for *a priori* design towards applications such as molecular separations.[6] In particular, we note that these materials display outstanding performance in chiral molecule and kinetic gas separations.[7]

The primary challenge in the investigation of porous molecular crystals (PMCs) is there are countless examples of materials that contain cavities and channels occupied by solvent. For many of these examples, the void structure collapses upon guest removal to form a denser or amorphous phase. As a result, molecular crystals that possess permanent micropore structures are considered rare.[8] Importantly, new and novel examples of PMCs are often fortuitously discovered, akin to finding a needle in a haystack. McKeown and coworkers have described a search of the Cambridge Structural Database (CSD) for a previously unexplored PMC for gas adsorption.[9] In their investigation they targeted materials of very low density (<9.0 $g.cm^{-3}$), narrowing the search of the entire CSD to 519 ini-

tial structures that were able individually scrutinized. Ultimately, this search was fruitful leading researchers to 3,3',4,4'-tetra(trimethylsilylethynyl)biphenyl, which crystallizes to give the structure BALNIM (please note CSD codes will be used throughout this chapter to refer to structures). The material was successfully evacuated to give a Brunauer–Emmett–Teller (BET) surface area of 278 $m^2.g^{-1}$ and displayed impressive hydrogen adsorption. Subsequently, there have been significant strides by researchers to efficiently simulate surface areas and porosity of crystalline solids, primarily zeolites and MOFs, based upon periodic structure.[10,11]

Herein we report an exhaustive and thorough search of over 150 000 CSD[12] crystal structures in an effort to find new and unrealized examples of organic porous molecular crystals (oPMCs). This search has used Voronoi network analysis to measure the pore volume of all potential structures (156 333 systems) and subsequently applied molecular simulations to the identified porous (16 000 systems) to obtain experimentally reasonable structures (481 systems). Additionally, we have used support vector machines (SVMs) to investigate the chemical functionality and design that can result in crystals with void systems.

5.3 Methods

The procedure for the generation of the oPMC database is shown in Figure 5.1 and will be described below.

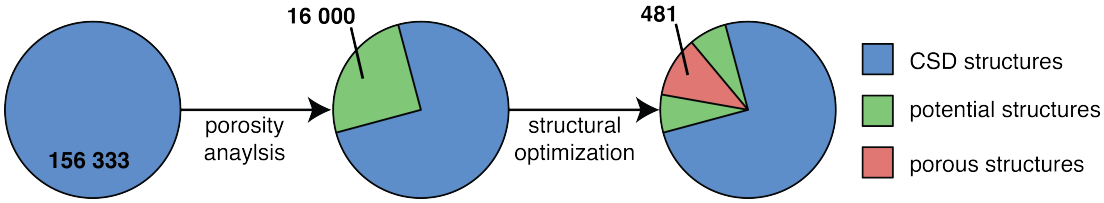

Figure 5.1: Scheme for the production of the database.

5.3.1 Structure Collection

Initially, potential oPMCs were collected from the Cambridge Structural Database (CSD),[12] version 5.35, including structures submitted through to March 2014. Conquest, version 1.16 was used to search through the entire CSD database using the following criteria: only organic elements, density ≤ 2 g.cm^{-3}, one residue and excluding disordered structures, powder structures, organic polymers, amino acids, peptides and complexes. This search produced over 160 000 potential structures, but further refinement to ensure only organic structures with hydrogens included resulted in 156 333 structures.

the helium pore volume (probe size 1.30 Å) for each of the potential structures was determined using Zeo++, which uses a Voronoi network to obtain a representation of the pore space for a periodic system.[11,13] Importantly, soft materials such as porous organic cages have been reported to have dynamic connectivity between accessible and inaccessible regions.[14] As a consequence, we have defined the total pore volume as the sum of the accessible and inaccessible regions as defined by Zeo++ so that regions accessible by dynamic pore opening events are not overlooked.

Structures were determined to be potentially porous if they contained a pore volume $> 10^{-5}$ $cm^3.g^{-1}$, for a probe size equivalent to the size of helium. This resulted in a total of 16 000 structures that had pockets or channels porous to helium.

5.3.2 Structure Refinement

Interestingly, there were a number of structures that showed extreme pore volumes and extremely low densities. The source of these anomalous results may be a result of incorrect space-group assignment, crystallographic information file errors or extreme use of the SQUEEZE routine.[15] Here, the SQUEEZE routine removes electron density associated from disordered solvent molecules present in a void and may result in unsupported pore structures. In any case, a number of unphysical and unstable structures were included in the possibly porous set as identified from the CSD structure and Zeo++ alone. In order to consider only robust structures, optimization using the universal force-field (UFF)[16] was applied to the 16 000 potential structures as demonstrated in Figure 5.2.

The optimization was carried out using the Accelrys Materials Studio software with UFF parameters chosen automatically through the Forcite module in addition to 'ultra-fine' convergence criteria and relaxation of the unit cell with 1 atm of applied pressure. Figure 5.3 shows parity plots of the density and total pore volume of the original and optimized structures. It is observed that many of the lowest density structures increase in density considerably post optimization. Many of the systems, like that exemplified in Figure 5.2, have large regions unsupported by inter- or intra-molecular interactions and, as such, optimize to a more physical higher density structure. The structural refinement narrows the number of crystals found to be porous to more physically and chemically sensible structures, which halved the number of compounds to 8169 potential structures. Notably, we found these porous structures to be extremely skewed to low porosity: 94% of potential structures show less than 10^{-3} $cm^3.g^{-1}$ total pore volume. This is in stark contrast to the computation-ready experimental (CoRE) MOF

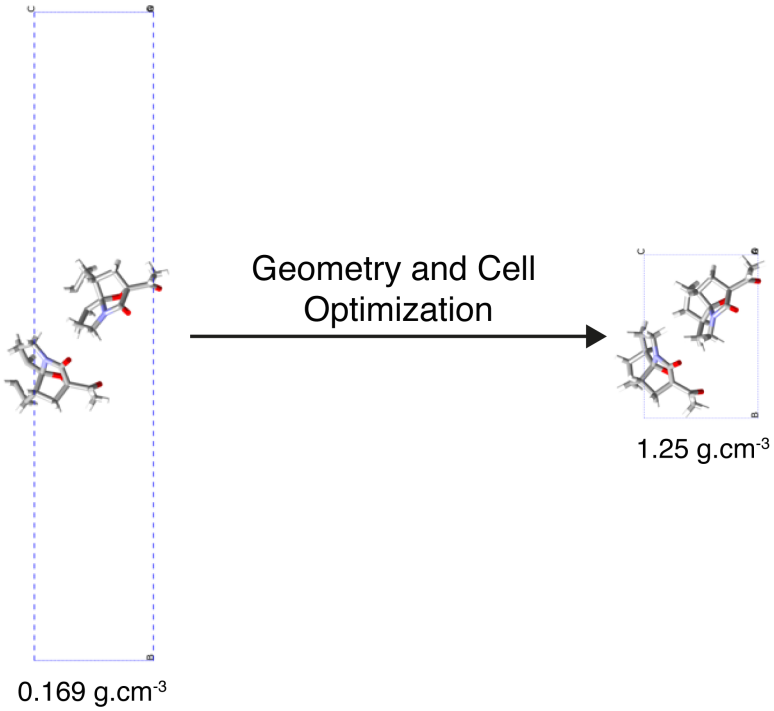

Figure 5.2: Structural optimization as applied to original crystal structure of LICROE from CSD and post-optimization with cell densities labeled.

database[17] that contains 12% of structures with the similarly small total pore volumes. To focus on relevant porous structures and combat the extreme skew, we have chosen to label structures with total pore greater than 10^{-3} $cm^3.g^{-1}$ as porous, resulting in 481 porous crystals identified. In addition to optimization using classical molecular mechanics, identified porous crystals were further optimized using semi-empirical methods. The PM6-dh2x method[18] was applied using MOPAC,[19] and the resulting structures showed good agreement to UFF densities, see Figure 5.4.

5.3.3 Structure Analysis

For each of the identified porous structures the following pore metrics were measured using the Zeo++ code described previously: He pore volume, N_2 surface area (probe size 1.64 Å), limiting pore diameter, maximum pore diameter and pore channel dimensions.

As these compounds are molecular species, further analysis was applied by considering the molecular properties of the structures. RDKit[20] was used to calculate 195 molecular descriptors for all 156 333 molecules investigated in this study. A list of the descriptors and fragments calculated can be found in Section 5.A. In an effort to identify potential molecular characteristics that give rise to porous crys-

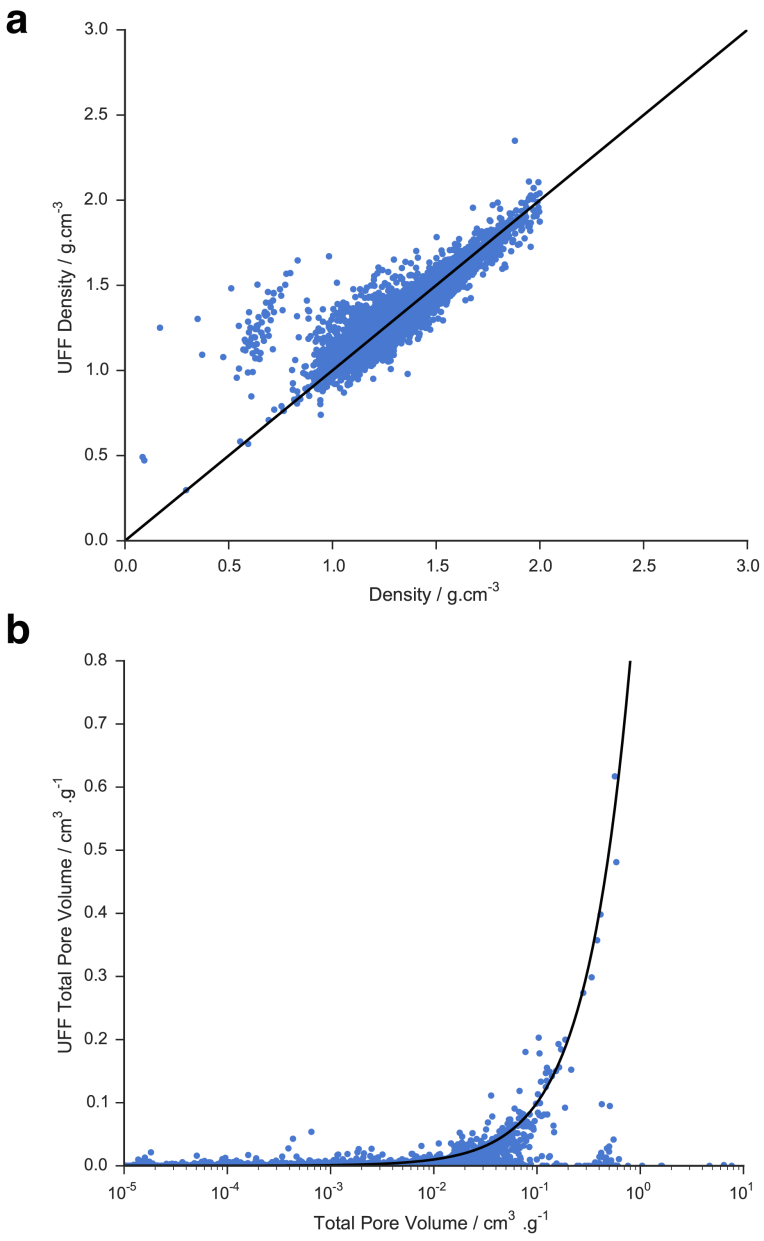

Figure 5.3: Parity plots for density (a) and total pore volume (b) for CSD structures and UFF optimized structures. Please note that total pore volume before optimization is displayed on a logarithmic axes due to the large range of values.

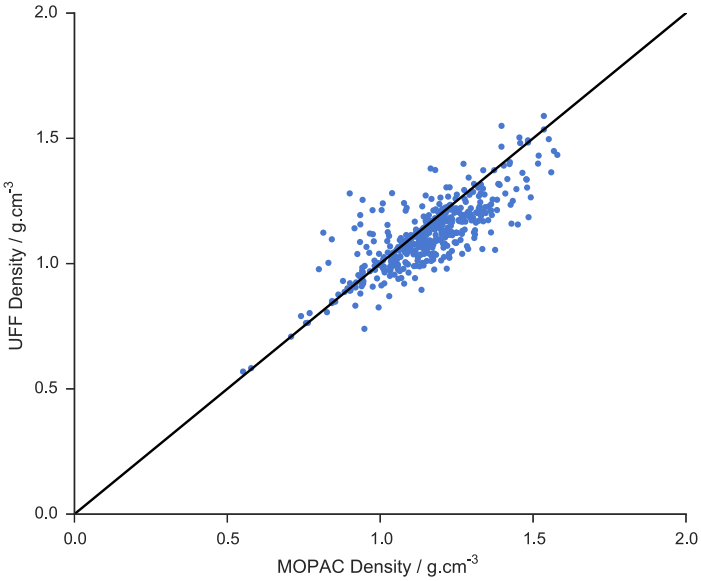

Figure 5.4: Parity plot for density for UFF optimized structures and PM6-DH2x optimized structures.

tals, we have applied machine learning, inspired by Wicker and Cooper's recent work.[21] Machine learning algorithms provide an efficient means to identify patterns in multi-dimensional data sets. Supervised pattern-recognition algorithms were used in the form of support vector machines (SVMs), in which the structures were classified as either 'porous' or 'non-porous'. In essence, the SVMs find a separating hyperplane separating the 'porous' and 'non-porous' classes that is optimized for a maximal margin. In this study we investigated the success rate of a number of SVMs with different kernel functions: linear, quadratic, polynomial and gaussian radial basis function (RBF) in addition to considering all molecular descriptors simultaneously and one molecular descriptor at time to find the most important predictors of crystalline porous molecules. SVM training and testing was achieved using the `SVMtrain` function in MATLAB.

For this analysis, the 'non-porous' class was randomly under-sampled to counteract the imbalance due to the large number of 'non-porous' structures.[22] This was achieved by randomly selecting 481 structures from the 'non-porous' dataset for training and testing and repeating the process 100 times to obtain convergence. The training data comprised a randomly selected group containing 50% of each of the sampled 'non-porous' dataset and 'porous' dataset. The remaining 50% became the test data to which the predictive algorithm attempted to classify structure as 'porous' or 'non-porous' based on the values of their molecular descriptors. The accuracy of the algorithm was measured by comparing predicted and known classifications of the structures.

Table 5.1: Summary of experimentally reported porous structures (crys.) identified in the oPMC database with their experimentally reported crystal density ($g.cm^{-3}$) and BET surface areas (SA, $m^2.g^{-1}$) compared to MOPAC optimized density and simulated surface area (sim.).

structure	crys. density	sim. density	exp. SA	sim. SA
BALNIM	0.830	0.863	278	351
DEBXIT	0.755	0.741	2796	2400
DOFSUM03	1.321	1.323	240	350
FEQXAC	0.555	0.578	1700	3860
HEXWIQ	1.327	1.808	-	309
PUDXES	0.973	0.919	409	258
QQQESP01	1.165	1.247	-	103
XUDVOH	1.069	1.268	-	34

5.4 Results and discussion

5.4.1 Pore Characteristics of oPMC

The identified oPMC database contains 481 crystal structures with total pore volume greater than 10^{-3} $cm^3.g^{-1}$. The term 'porous' is subjective, with many researchers requiring that porosity be verified by gas adsorption experiments[23] and because of this truly porous molecular crystals are relatively rare, as described by Barbour.[8] As an illustration of the power of our screening algorithm, a number of structures identified in this database have been previously reported experimentally to demonstrate porosity, as indicated in Table 5.1.

Importantly, for these crystalline structures we find only minute changes upon optimization, as indicated by the small changes in density. Furthermore, we find simulated surface areas from the optimized structures compare very well to those reported by researchers. In particular, the compound DEBXIT reported by Mastalerz and coworkers is one of the most porous examples of an oPMC in the literature.[24] The structure FEQXAC, however, has an overestimated surface area as a result of the crystal structure desolvating and changing dramatically under desolvation in experiments, described previously.[6,25] Ultimately, the inclusion of these examples in the database is a good indication that the screening and optimization procedures employed in this investigation are physical and relevant to the identification of previously unrealized examples of oPMCs. Additionally, this study has identified 14 crystal structures that are predicted to have N_2 surface areas >1000 $m^2.g^{-1}$ and have yet to be studied experimentally for gas adsorption.

Upon pore metric analysis of the structures present in the oPMC database, we observe general trends present in porous materials constructed from organic molecular units. Figure 5.5 shows the distribution of density, surface area, void fraction and pore sizes for the oPMC database. This information shows that many of these structures are of low density with a mean density of 1.2 g.cm^{-3}. Notably, a previous search for oPMCs limited their search for structures of density less than 0.9 g.cm^{-3}.[9] The distribution of densities observed here shows that extremely low-density structures are not necessarily required for the construction of a porous molecular crystal. However, we note that the magnitude of the porosity is correlated with density. The surface areas and helium void fraction population distributions demonstrate that oPMCs generally display minute pore volumes and surface areas, with rare extremely porous examples such as DEBXIT (He void fraction of 0.29). Analysis of the pore environments presented in Figure 5.5d explains the resulting low pore volumes and surface areas. Particularly, we find a large proportion of structures (>20%) with a limiting pore diameter <2 Å, which would find them being classified as non-porous by standard nitrogen adsorption experiments conducted at 77 K. Despite this, we retain these structures in our collection as there have been a number of reports of structures, for example calixarenes, that can show porosity by guest transport without connected pore volumes.[26] The maximum pore diameter shows that many of these structures have significant cavities that could be use for guest transport and storage. The pore dimensionality of each of the systems was also measured. Figure 5.6 shows that for He a majority of structures demonstrate a pore structure comprising one-dimensional tubular-like channels. Interestingly, for probe sizes equivalent to N_2 we find the distribution of pore dimensions shifts such that a majority of structures have unconnected void volumes. These measurements demonstrate clearly the rarity of interconnected two or three-dimensional porosity in discrete organic molecules.

To place this database in context with conventional porous framework materials we have the computed density, volumetric surface area, helium void fraction and pore diameters for the international zeolite association (IZA) zeolite and CoRE MOF collections.[17,27] Figure 5.7 shows a comparison of the normalized population distribution of the materials. The distribution of densities of these classes shows a very interesting relationship. oPMCs exhibit structures with lower densities than zeolites - this is expected due to the organic and inorganic components that make up these respective materials. The CoRE MOF structures are observed to have a broad range of densities overlapping the range of both oPMCs and zeolites, consistent with the combination of inorganic and organic components

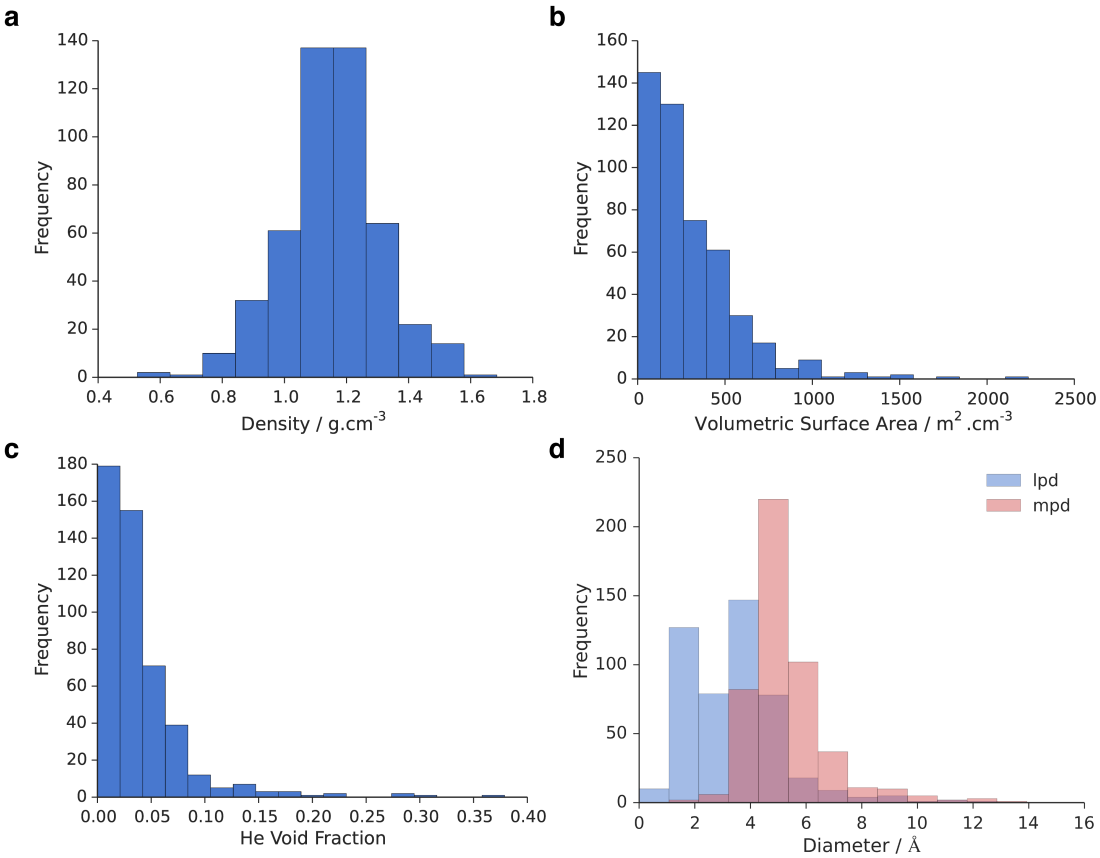

Figure 5.5: Histograms of density (a), volumetric surface area (b), helium void fraction (c), limiting pore diameters (lpd) and maximum pore diameters (mpd) (d) showing the distribution for oPMCs identified in this study.

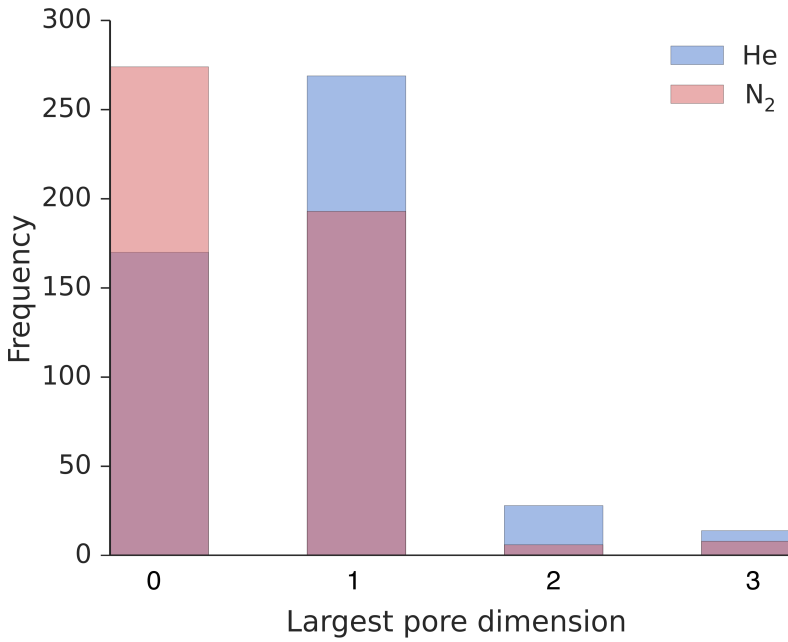

Figure 5.6: Histogram of the dimensonality of largest pore identified for the oPMCs database. Dimensionality was analyzed for probe sizes equivalent to the kinetic diameters of He (2.60 Å) and N_2 (3.64 Å).

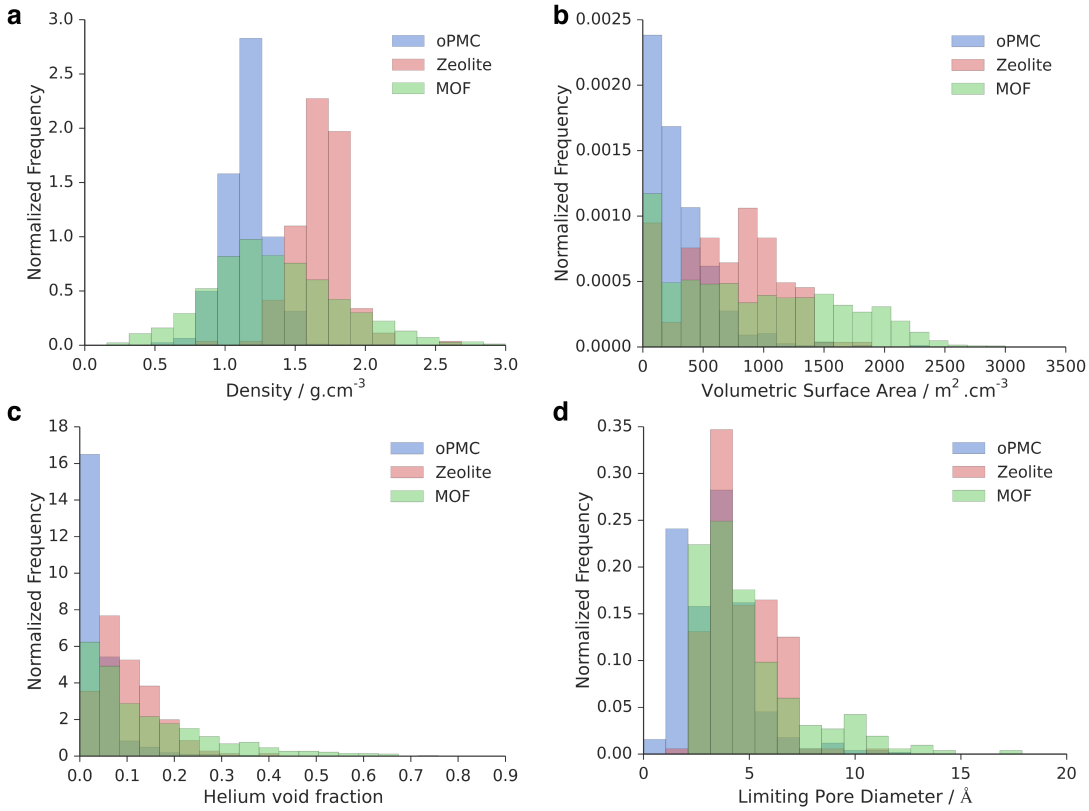

Figure 5.7: Histograms of density (a), volumetric surface area (b), helium void fraction (c) and pore diameters showing the distribution for oPMCs identified in this study.

that are used to construct MOFs. Comparisons of the surface areas and void fractions further demonstrates the lack of significant pore volume in oPMCs. Despite this we observe in Figure 5.7(d) an advantage of oPMCs, which include more materials with smaller limiting pore diameters. This may prove useful in areas of niche kinetic gas separations or chiral molecular separations, which is currently an area of intense investigation.[7,28,29]

We have successfully demonstrated that the screening methodology used in this study can identify experimentally reported oPMCs and possibly unknown porous molecular crystals. The techniques used here have allowed for the database to be probed for measurable quantities, namely surface area, pore volume and dimensionality.

5.4.2 Molecular Characteristics of oPMCs

In an effort to discover the molecular properties that result in crystalline molecular porosity, we applied machine learning algorithms to molecular descriptors measured for each of the molecular units. As oPMCs are generated from the packing of discrete molecular units we can apply detailed analysis to the molecular

units. Researchers using these machine learning algorithms have reported success in the prediction of solubility,[30] heat capacity[31] and propensity of crystallization[21] based on descriptors of the molecular structure. In this study, we have tested the predictive accuracy of four support vector machine (SVM) kernels (linear, quadratic and polynomial and gaussian RBF) trained using all 195 descriptors generated by RDKit, compared in Table 5.2. The algorithms are observed to correctly classify between 53.3% and 64.6% of molecules. The averaged data for 100 unique iterations show small variance in the accuracy of classification. The linear and polynomial classifiers show the greatest accuracy with the lowest accuracy achieved with the RBF kernel. Individual class results in Table 5.2 show that the lack of accuracy observed for the RBF kernel is a result of an imbalance in the misclassification between the two classes, which is not observed for the other functions. In practice, it has been observed that the linear kernel performs very well when the number of features is large, as is the case with this investigation.[32]

Table 5.2: Average total, non-porous (NP) and porous (P) accuracy rate for SVM classifiers applied to all 195 RDKit descriptors.

kernel function	**total / %**	**NP / %**	**P / %**
linear	64.7	64.7	64.6
quadratic	60.7	60.0	61.5
polynomial	65.7	64.5	67.1
rbf	53.3	52.0	78.4

To identify the most important descriptors of the molecules for making these predictions, an independent feature selection analysis was performed as the importance of each descriptor cannot be computed explicitly from a nonlinear SVM. We compared the accuracy of classifiers built using only a single molecular descriptor, for each descriptor measured with RDKit, in order to find the most important descriptor, as shown in Table 5.3. We found that the labuteASA descriptor gave the highest predictive accuracy from a single-variable linear SVM classifier. The descriptor, labuteASA, gives an approximation for the van der Waals surface area of a molecule and has been used to describe partition-coefficients (octanol/water) and molar refractivity based upon only two-dimensional molecular connectivity.[33] Furthermore, the descriptor is highly correlated with the information contained in many descriptors that are related to molecular size.[34] This results in the similar predictive accuracy from the top single variable classifiers, Table 5.3.

Table 5.3: Average single-variable classifier accuracy and the standard error in accuracy resulting from a linear SVM classifier.

descriptor	total / %	standard error / %
LabuteASA	69.7	1
Chi1	69.6	1
Chi1n	69.5	1
ExactMolWt	69.4	1
HeavyAtomCount	69.3	1
MolWt	69.3	1
HeavyAtomMolWt	69.2	1
Chi0	69.2	1
NumValenceElectrons	69.2	1
Chi0v	69.2	1
Chi2n	69.0	1
MolMR	69.0	1
Chi3n	68.9	1
Chi0n	68.8	1
Kappa1	68.5	1
Chi4n	68.2	1
Chi1v	68.1	1
BertzCT	67.9	1
VSA_EState9	67.0	1
Chi2v	66.9	1

Further analysis to find two-descriptor classifiers which used labuteASA paired with every other descriptor did not result in a significant increase in the accuracy rate suggesting that labuteASA and correlated descriptors provide the accuracy of classification observed for the total descriptor analysis in Table 5.2. We find in Table 5.4 that the labuteASA descriptor is a successful one-variable classifier with a predictive accuracy of approximately 70%, which indicates that the majority of the accuracy obtained with 195 descriptors can be achieved using the labuteASA descriptor. It is not surprising that we observe an increase in accuracy upon using a single descriptor. Various important definitions such as separation between points often become less convincing at higher dimensions, as more dimensions have been noted to make the proximity between points more uniform. As a result, for a high number of features or variables, like that in Table 5.2, often leads to a lower classification accuracy and clustering of poor quality.[35]

Table 5.4: Average total, non-porous (NP) and porous(P) accuracy percentage for SVM classifiers applied to the labuteASA descriptor.

kernel function	total / %	NP / %	P / %
linear	69.7	65.8	74.6

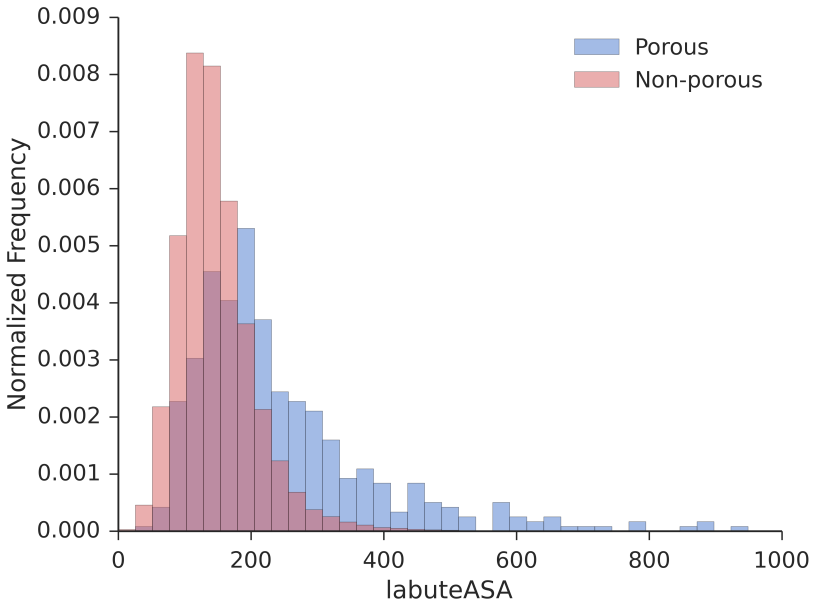

Figure 5.8: Normalized Histograms of the Labute surface area descriptor for the porous and non-porous classes.

Figure 5.8 shows that non-porous molecules are concentrated in a region where the labuteASA is <200, while the porous molecules set has a wider distribution and mostly have a labuteASA greater than 200. This follows the suggestion from the SVM algorithm that determined the value separating the two categories corresponds to a labuteASA value of 196. We note, however, that there is significant overlap between the classes around this point, which results in the accuracy rate of only 70%.

The influence of the van der Waals surface area of a molecule on the formation of porous structures can be readily rationalized by considering that many reported oPMCs rely upon awkward and high surface area shapes. For example, these are often cups, macrocycles, cages, or molecular structures with concave surfaces that prevent space-efficient packing. Furthermore, larger molecular surfaces give greater opportunities for π-π stacking and sites for intermolecular hydrogen bonding that encourage the formation of large voids, as demonstrated for recent example.[36]

While the accuracy obtained from our analysis may not be outstanding when compared with other related studies that have applied machine learning techniques to molecular classification.[30,31] It is, however, remarkable to demonstrate any meaningful classification, owing to the large number of unknown factors influencing crystallization and in turn the porosity of the structure. Significantly, the set of 481 porous structures used in the classification is small compared with the datasets used in many machine learning investigations, which have used 10^4 (or orders of magnitude more) examples to provide accuracies above 90%. This issue is inherent to the research addressed herein, which is concerned with relatively rare porous molecular solids. Additionally, examples of the diversity of porous structures illustrated in Figure 5.9a give insight into the rich variety of chemical structures and functionalities that can produce porous crystals. Thus, no simple set of molecular characteristics appears to define whether a molecule will form a porous crystal. Moreover, many of these molecules can have a number of polymorphs that can have extremely different porosities. One example, 2,4,6-tris-(4-bromophenoxy)-1,3,5-triazine, demonstrated in Figure 5.9b, crystallizes to give the structures HEXWIQ and HEXWIQ01. Here, the molecule is exactly the same. However, it can form either one-dimensional porous channels or a dense completely non-porous structure, depending on the conditions of crystallization.

5.5 Conclusion

We have successfully constructed a database of 481 organic porous molecular crystal (oPMC) systems derived from experimental crystal structures. Efficient methodologies were applied to screen the original structures for porosity and subsequently refine unreliable examples using a combination of classical molecular simulations and semi-empirical methods. This screening algorithm has successfully identified previously reported porous crystals and a large number of unexplored structures. Additionally, we have measured surface areas and pore metrics of each structure and compared these to two databases of conventional porous materials.

The identified database has been used to demonstrate a number of unique trends and properties for these materials that previously were difficult to recognize as a result of the limited selection of reported systems. Additionally, we have applied machine learning algorithms in an effort to understand the important chemical functionalities and molecular structures that yields porous crystal structures. Despite the challenges, we observed that structures with large molecular surface area were responsible for a large proportion of porous structures. This

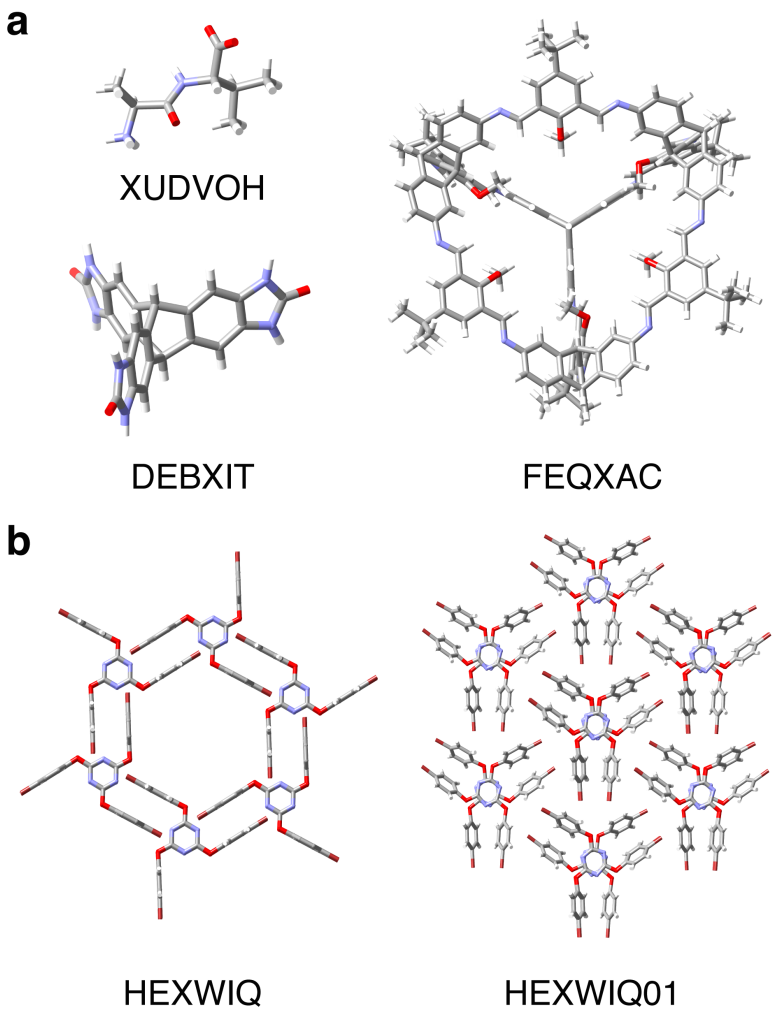

Figure 5.9: Examples of the wide variety in chemical and geometric diversity of structures that produce the porous crystals captured in the oPMC database (a) and the two drastically different polymorphs of 2,4,6-tris-(4-bromophenoxy)-1,3,5-triazine (b).

has resulted in vital, quantitative, insight into features that promote lattice voids and channels. The database described is a promising tool for identifying candidate structures for applications in gas separations. In addition, it can provide design rules for the production of new extremely porous crystals.

5.6 References

1. E. V. Perez, K. J. B. Jr., J. P. Ferraris, and I. H. Musselman. "Metal-organic polyhedra 18 mixed-matrix membranes for gas separation". *Journal of Membrane Science* 463 (2014), pp. 82–93. DOI: 10.1016/j.memsci.2014.03.045.

2. J. T. A. Jones et al. "On–Off Porosity Switching in a Molecular Organic Solid". *Angewandte Chemie International Edition* 50.3 (2011), pp. 749–753. DOI: 10.1002/anie.201006030.

3. A. I. Cooper. "Nanoporous Organics Enter the Cage Age". *Angewandte Chemie International Edition* 50.5 (2011), pp. 996–998. DOI: 10.1002/anie.201006664.

4. G. Zhang, O. Presly, F. White, I. M. Oppel, and M. Mastalerz. "A Permanent Mesoporous Organic Cage with an Exceptionally High Surface Area". *Angewandte Chemie International Edition* 53.6 (2014), pp. 1516–1520. DOI: 10.1002/anie.201308924.

5. J. D. Evans, D. M. Huang, M. R. Hill, C. J. Sumby, D. S. Sholl, A. W. Thornton, and C. J. Doonan. "Molecular Design of Amorphous Porous Organic Cages for Enhanced Gas Storage". *The Journal of Physical Chemistry C* 119.14 (2015), pp. 7746–7754. DOI: 10.1021/jp512944r.

6. J. D. Evans, D. M. Huang, M. R. Hill, C. J. Sumby, A. W. Thornton, and C. J. Doonan. "Feasibility of Mixed Matrix Membrane Gas Separations Employing Porous Organic Cages". *The Journal of Physical Chemistry C* 118.3 (2014), pp. 1523–1529. DOI: 10.1021/jp4079184.

7. L. Chen et al. "Separation of rare gases and chiral molecules by selective binding in porous organic cages". *Nature Materials* 13.10 (2014), pp. 954–960. DOI: 10.1038/nmat4035.

8. L. J. Barbour. "Crystal porosity and the burden of proof". *Chemical Communications* 11 (2006), p. 1163. DOI: 10.1039/b515612m.

9. K. J. Msayib et al. "Nitrogen and Hydrogen Adsorption by an Organic Microporous Crystal". *Angewandte Chemie International Edition* 48.18 (2009), pp. 3273–3277. DOI: 10.1002/anie.200900234.

10. J. Kim, R. L. Martin, O. Rübel, M. Haranczyk, and B. Smit. "High-Throughput Characterization of Porous Materials Using Graphics Processing Units". *Journal of Chemical Theory and Computation* 8.5 (2012), pp. 1684–1693. DOI: 10.1021/ct200787v.

11. T. F. Willems, C. H. Rycroft, M. Kazi, J. C. Meza, and M. Haranczyk. "Algorithms and tools for high-throughput geometry-based analysis of crystalline porous materials". *Microporous and Mesoporous Materials* 149.1 (2012), pp. 134–141. DOI: 10.1016/j.micromeso.2011.08.020.

12. F. H. Allen. "The Cambridge Structural Database: a quarter of a million crystal structures and rising". *Acta Crystallographica Section B* 58.3 (2002), pp. 380–388. DOI: 10.1107/S0108768102003890.

13. R. L. Martin, B. Smit, and M. Haranczyk. "Addressing Challenges of Identifying Geometrically Diverse Sets of Crystalline Porous Materials". *Journal of Chemical Information and Modeling* 52.2 (2012), pp. 308–318. DOI: 10.1021/ci200386x.

14. D. Holden, K. E. Jelfs, A. Trewin, D. J. Willock, M. Haranczyk, and A. I. Cooper. "Gas Diffusion in a Porous Organic Cage: Analysis of Dynamic Pore Connectivity Using Molecular Dynamics Simulations". *The Journal of Physical Chemistry C* 118.24 (2014), pp. 12734–12743. DOI: 10.1021/jp500293s.

15. P. van der Sluis and A. L. Spek. "BYPASS: an effective method for the refinement of crystal structures containing disordered solvent regions". *Acta Crystallographica Section A* 46.3 (1990), pp. 194–201. DOI: 10.1107/s0108767389011189.

16. A. K. Rappe, C. J. Casewit, K. S. Colwell, W. A. Goddard, and W. M. Skiff. "UFF, a full periodic table force field for molecular mechanics and molecular dynamics simulations". *Journal of the American Chemical Society* 114.25 (1992), pp. 10024–10035. DOI: 10.1021/ja00051a040.

17. Y. G. Chung, J. Camp, M. Haranczyk, B. J. Sikora, W. Bury, V. Krungleviciute, T. Yildirim, O. K. Farha, D. S. Sholl, and R. Q. Snurr. "Computation-Ready, Experimental Metal–Organic Frameworks: A Tool To Enable High-Throughput Screening of Nanoporous Crystals". *Chemistry of Materials* 26.21 (2014), pp. 6185–6192. DOI: 10.1021/cm502594j.

18. P. Dobeš, J. Řezáč, J. Fanfrlík, M. Otyepka, and P. Hobza. "Semiempirical Quantum Mechanical Method PM6-DH2X Describes the Geometry and Energetics of CK2-Inhibitor Complexes Involving Halogen Bonds Well, While the Empirical Potential Fails". *The Journal of Physical Chemistry B* 115.26 (2011), pp. 8581–8589. DOI: 10.1021/jp202149z.

19. J. J. P. Stewart. "Optimization of parameters for semiempirical methods VI: more modifications to the NDDO approximations and re-optimization of parameters". *Journal of Molecular Modeling* 19.1 (2012), pp. 1–32. DOI: 10.1007/s00894-012-1667-x.

20. G. Landrum. *RDKit: Open-source cheminformatics*.

21. J. G. P. Wicker and R. I. Cooper. "Will it crystallise? Predicting crystallinity of molecular materials". *CrystEngComm* 17.9 (2015), pp. 1927–1934. DOI: 10.1039/c4ce01912a.

22. N. Japkowicz. "The Class Imbalance Problem: Significance and Strategies". *Proceedings of the 2000 International Conference on Artificial Intelligence (ICAI)*. 2000, pp. 111–117.

23. S. Kitagawa and K. Uemura. "Dynamic porous properties of coordination polymers inspired by hydrogen bonds". *Chemical Society Reviews* 34.2 (2005), p. 109. DOI: 10.1039/b313997m.

24. M. Mastalerz and I. M. Oppel. "Rational Construction of an Extrinsic Porous Molecular Crystal with an Extraordinary High Specific Surface Area". *Angewandte Chemie International Edition* 51.21 (2012), pp. 5252–5255. DOI: 10.1002/anie.201201174.

25. M. Mastalerz, M. W. Schneider, I. M. Oppel, and O. Presly. "A Salicylbisimine Cage Compound with High Surface Area and Selective CO_2/CH_4 Adsorption". *Angewandte Chemie International Edition* 50.5 (2011), pp. 1046–1051. DOI: 10.1002/anie.201005301.

26. J. L. Atwood. "Guest Transport in a Nonporous Organic Solid via Dynamic van der Waals Cooperativity". *Science* 298.5595 (2002), pp. 1000–1002. DOI: 10.1126/science.1077591.

27. C. Baerlocher and L. McCusker. *Database of Zeolite Structures*.

28. A. Kewley, A. Stephenson, L. Chen, M. E. Briggs, T. Hasell, and A. I. Cooper. "Porous Organic Cages for Gas Chromatography Separations". *Chemistry of Materials* 27.9 (2015), pp. 3207–3210. DOI: 10.1021/acs.chemmater.5b01112.

29. J.-H. Zhang, S.-M. Xie, L. Chen, B.-J. Wang, P.-G. He, and L.-M. Yuan. "Homochiral Porous Organic Cage with High Selectivity for the Separation of Racemates in Gas Chromatography". *Analytical Chemistry* 87.15 (2015), pp. 7817–7824. DOI: 10.1021/acs.analchem.5b01512.

30. B. Louis, J. Singh, B. Shaik, V. K. Agrawal, and P. V. Khadikar. "QSPR Study on the Estimation of Solubility of Drug-like Organic Compounds: A Case of Barbiturates". *Chemical Biology & Drug Design* 74.2 (2009), pp. 190–195. DOI: 10.1111/j.1747-0285.2009.00844.x.

31. C. X. Xue, R. S. Zhang, H. X. Liu, M. C. Liu, Z. D. Hu, and B. T. Fan. "Support Vector Machines-Based Quantitative Structure—Property Relationship for the Prediction of Heat Capacity". *Journal of Chemical Information and Computer Sciences* 44.4 (2004), pp. 1267–1274. DOI: 10.1021/ci049934n.

32. C.-w. Hsu, C.-c. Chang, and C.-j. Lin. *A practical guide to support vector classification*. Department of Computer Science and Information Engineering, National Taiwan University, 2010.

33. J. Bajorath and P. Labute. "Methods in Molecular Biology™". *Chemoinformatics*. Vol. 275. Humana Press, 2004, pp. 261–278. DOI: 10.1385/1-59259-802-1:261.

34. P. Labute. "A widely applicable set of descriptors". *Journal of Molecular Graphics and Modelling* 18.4–5 (2000), pp. 464–477. DOI: 10.1016/S1093-3263(00)00068-1.

35. A. G. Janecek, W. N. Gansterer, M. A. Demel, and G. F. Ecker. "On the Relationship Between Feature Selection and Classification Accuracy". *JMLR: Workshop and Conference Proceedings 4*. 2008, pp. 90–105.

36. T.-H. Chen, I. Popov, W. Kaveevivitchai, Y.-C. Chuang, Y.-S. Chen, O. Daugulis, A. J. Jacobson, and O. Š. Miljanić. "Thermally robust and porous noncovalent organic framework with high affinity for fluorocarbons and CFCs". *Nature Communications* 5 (2014). DOI: 10.1038/ncomms6131.

5.A Supporting Information

Table 5.5: Descriptors calculated by the RDKit program.

RDKit Descriptors
MolWt, exactMolWt, HeavyAtomMolWt, NumRadicalElectrons, NumValenceElectrons, HeavyAtomCount, NumHeteroatoms, NumRotatableBonds, RingCount
BalabanJ
BertzCT
Chi0v, Chi1v, Chi2v, Chi3v, Chi4v, ChiNv, Chi0n, Chi1n, Chi2n, Chi3n, Chi4n, ChiNn, HallKierAlpha , Kappa1, Kappa2, Kappa3
EState-VSA1 – EState-VSA11 VSA-EState1 – VSA-EState10
LabuteASA PEOE-VSA1 – PEOE-VSA14 SMR-VSA1 – SMR-VSA10 SlogP-VSA1 – SlogP-VSA12
MolLogP, MolMR
TPSA

Table 5.6: Molecular fragments calculated by the RDKit program.

fragment title	description
NumHAcceptors	Number of hydrogen bond acceptors
NumHDonors	Number of hydrogen bond donors
NHOHCount	Number of NHs and OHs
NOCount	Number of nitrogen and oxygen atoms
fr_ Al_ COO	Number of aliphatic carboxylic acids
fr_ Al_ OH_ noTert	Number of aliphatic hydroxyl groups excluding tert-OH
fr_ Al_ OH	Number of aliphatic hydroxyl groups
fr_ aldehyde	Number of aldehyde groups
fr_ alkyl_ carbamate	Number of alkyl carbamates
fr_ alkyl_ halide	Number of alkyl halide groups
fr_ allylic_ oxid	Number of allylic oxidation sites excluding steroid dienone
fr_ amide	Number of amide groups
fr_ amidine	Number of amidine groups
fr_ aniline	Number of aniline groups
fr_ Ar_ COO	Number of aromatic carboxylic acids
fr_ Ar_ N	Number of aromatic nitrogens
fr_ Ar_ NH	Number of aromatic amines
fr_ Ar_ OH	Number of aromatic hydroxyl groups
fr_ ArN	Number of N functional groups attached to aromatics
fr_ aryl_ methyl	Number of aryl methyl sites
fr_ azide	Number of azide groups
fr_ azo	Number of azo groups
fr_ barbitur	Number of barbiturate groups
fr_ benzene	Number of benzene rings
fr_ benzodiazepine	Number of benzodiazepines with no additional fused rings
fr_ bicyclic	Number of bicyclic rings
fr_ C_ O_ noCOO	Number of carbonyl O, excluding COOH
fr_ C_ O	Number of carbonyl groups
fr_ C_ S	Number of thiocarbonyl groups
fr_ COO	Number of carboxylic acids
fr_ COO2	Number of carboxylates
fr_ diazo	Number of diazo groups

fragment title	description
fr_ dihydropyridine	Number of dihydropyridines
fr_ epoxide	Number of epoxide rings
fr_ ester	Number of esters
fr_ ether	Number of ether oxygens (including phenoxy)
fr_ furan	Number of furan rings
fr_ guanido	Number of guanidine groups
fr_ halogen	Number of halogens
fr_ hdrzine	Number of hydrazine groups
fr_ hdrzone	Number of hydrazone groups
fr_ HOCCN	Number of C(OH)CCN-Ctert-alkyl or C(OH)CCNcyclic
fr_ imidazole	Number of imidazole rings
fr_ imide	Number of imide groups
fr_ Imine	Number of imine groups
fr_ isocyan	Number of isocyanates
fr_ isothiocyan	Number of isothiocyanates
fr_ ketone_ Topliss	Number of ketones excluding diaryl, a and b-unsat
fr_ ketone	Number of ketones
fr_ lactam	Number of beta lactams
fr_ lactone	Number of cyclic esters (lactones)
fr_ methoxy	Number of methoxy groups -OCH3
fr_ morpholine	Number of morpholine rings
fr_ N_ O	Number of hydroxylamine groups
fr_ Ndealkylation1	Number of XCCNR groups
fr_ Ndealkylation2	Number of tert-alicyclic amines (no heteroatoms, not quinine-like bridged N)
fr_ NH0	Number of tertiary amines
fr_ NH1	Number of secondary amines
fr_ NH2	Number of primary amines
fr_ Nhpyrrole	Number of H-pyrrole nitrogens
fr_ nitrile	Number of nitriles
fr_ nitro_ arom_ nonortho	Number of non-ortho nitro benzene ring substituents
fr_ nitro_ arom	Number of nitro benzene ring substituents
fr_ nitro	Number of nitro groups
fr_ nitroso	Number of nitroso groups, excluding NO2
fr_ oxazole	Number of oxazole rings

fragment title	description
fr_ oxime	Number of oxime groups
fr_ para_ hydroxylation	Number of para-hydroxylation sites
fr_ phenol_ noOrthoHbond	Number of phenolic OH excluding ortho intramolecular hydrogen bond substituents
fr_ phenol	Number of phenols
fr_ phos_ acid	Number of phosphoric acid groups
fr_ phos_ ester	Number of phosphoric ester groups
fr_ piperdine	Number of piperdine rings
fr_ piperzine	Number of piperzine rings
fr_ priamide	Number of primary amides
fr_ prisulfonamd	Number of primary sulfonamides
fr_ pyridine	Number of pyridine rings
fr_ quatN	Number of quarternary nitrogens
fr_ SH	Number of thiol groups
fr_ sulfide	Number of thioether
fr_ sulfonamd	Number of sulfonamides
fr_ sulfone	Number of sulfone groups
fr_ term_ acetylene	Number of terminal acetylenes
fr_ tetrazole	Number of tetrazole rings
fr_ thiazole	Number of thiazole rings
fr_ thiocyan	Number of thiocyanates
fr_ thiophene	Number of thiophene rings
fr_ unbrch_ alkane	Number of unbranched alkanes of at least 4 members (excludes halogenated alkanes)
fr_ urea	Number of urea groups
FractionCSP3	Fraction of C atoms that are SP3 hybridized

Parts of this research may appear in the following publication.

> J. M. Teo, C. J. Coghlan, J. D. Evans, C. J. Sumby, and C. J. Doonan.
> "Bimetallic Metal-organic Polyhedra". to be submitted (2015).

Author statements can be found in Appendix A.

6

Understanding Hydrogen Adsorption in MOP Systems

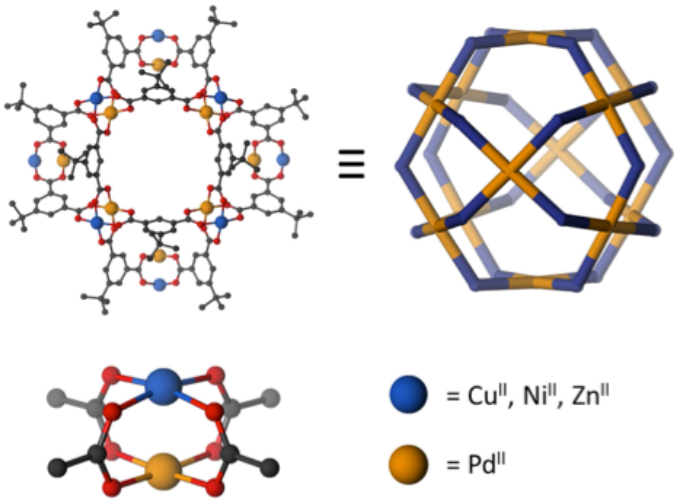

6.1 Introduction

A series of metal-organic polyhedra (MOP) were produced by Teo and coworkers. These MOPs are of particular interest as the metallic nodes consist of a M(II)-Pd(II) paddlewheel, where M can be Zn, Cu, Ni, or Co. Analysis of these structures revealed that amorphous samples adsorb appreciable amounts of hydrogen gas.[1]

MOPs are discrete molecular entities assembled from metal clusters and organic molecules.[2] This construction allows for careful adjustment of size, chemical functionality and metal sites to provide a tailored host molecule for a number of potential applications, one of which is the storage of gases. Alternative energy sources are paramount with present concerns of climate change, energy security and pollution. One such alternative is hydrogen gas as it can be produced from domestic resources and is able to power fuel cells in zero-emission passenger vehicles.[3] Despite the advantages of hydrogen there are concerns over safe storage methods due to its low volumetric density and explosiveness. There are a number of methods that mitigate these issues. One such solution is the storage by adsorption of hydrogen on porous frameworks.[4] Most porous materials store hydrogen by way of weak van der Waals interactions. In contrast, transition metals can adsorb hydrogen much more strongly as a result of charge-transfer interactions and chemisorption driving the dissociation of H_2 to form metal hydrides.[5]

MOPs were synthesized by mixing 5-tert-butyl-1,3-benzenedicarboxylic acid (H_2-L) and a bimetallic paddlewheel acetate Pd(II)–M(II) (M = Co^{2+}, Ni^{2+}, Cu^{2+} or Zn^{2+}) in N,N-dimethylacetamide (DMA) at ambient temperature for 24 hrs under dry, anaerobic, conditions. This afforded single crystals suitable for X-ray diffraction studies. Close analysis of the diffraction data indicated that each MOP is best described by a cuboctahedral geometry with bimetallic paddlewheel units at each of the 12 vertices. The Pd(II) and M(II) ions, predominantly, adopt endo- and exo-hedral positions of the 12 vertices, respectively. The structure is summarized in Figure 6.1.

We assessed the porosity of these unique materials by performing H_2 and N_2 gas adsorption experiments. Careful activation of the MOPs was carried out to ensure the removal of co-ordinated solvent molecules. To completely remove the DMA solvent molecules MOP crystals were soaked in a solution of dry acetone for 7 days, followed by supercritical CO_2 drying and finally heating at 50°C under vacuum for 3 hr. By employing this activation protocol only trace amounts of DMA were detected by ^{1}H NMR. Brunauer–Emmett–Teller (BET) analysis of the isotherms yielded surface areas ranging from 200 to 1100 $m^2.g^{-1}$ (Figure 6.2a and

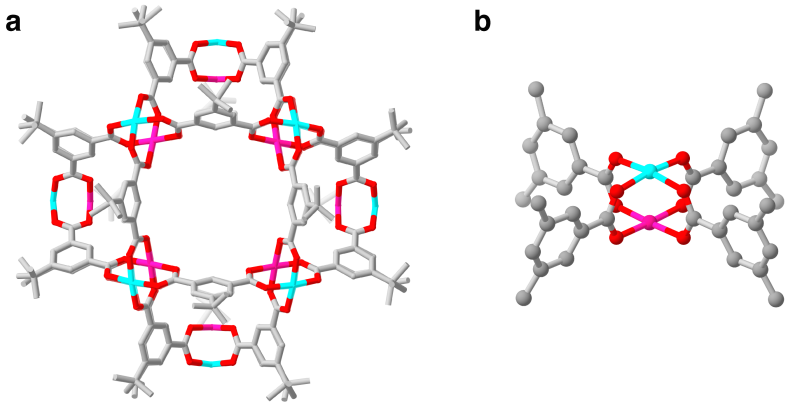

Figure 6.1: Cuboctahedral crystal structure of MOPs described in this chapter (a) and the unique bimetallic paddlewheel local environment (b). Note hydrogens have been removed for clarity.

Table 6.1: BET surface areas for MOPs: ZnPd(L) CuPd(L), NiPd(L), CoPd(L) and CuCu(L) calculated from N_2 isotherms collected at 77K.

	BET surface area / $m^2.g^{-1}$
ZnPd(L)	702
CuPd(L)	215
NiPd(L)	923
CoPd(L)	1090
CuCu(L)	293

Table 6.1). The highest surface areas were attributed to ZnPd(L) and NiPd(L) with lower surface areas observed for CuCu(L) and CuPd(L). Upon activation, the materials become amorphous and it is not possible to describe the pore structure atomistically. However, some information can be obtained from density functional theory (DFT) derived pore size distributions calculated from N_2 and Ar isotherms. These results show smaller pore sizes for CuPd(L) and ZnPd(L), consistent with the lower pore volumes observed for these materials, as shown in Figure 6.2b.

In an effort to quantify the strength of hydrogen adsorption in these MOP materials, we show the fitting of a virial model to the isotherms which is subsequently used to obtain the isosteric heat of adsorption. Finally, we show that DFT methods give insight into the nature of the metal cluster and suggest the mechanism behind the strong interaction with hydrogen.

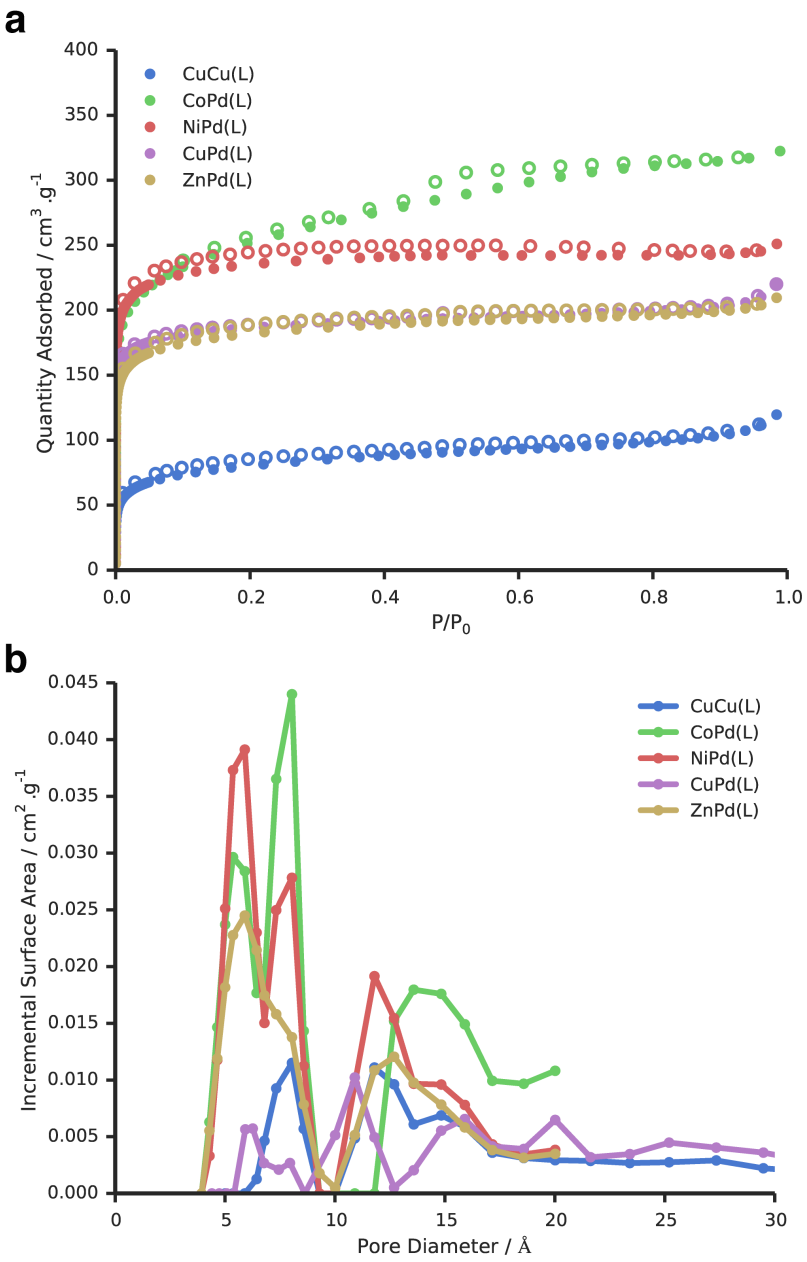

Figure 6.2: N_2 adsorption isotherms at 77 K (a) and DFT derived pore size distributions (b) of binary metal MOPs: CuCu(L), CoPd(L), NiPd(L), CuPd(L) and ZnPd(L). Adsorption and desorption is represented by filled and unfilled markers, respectively.

6.2 Methodology

6.2.1 Isosteric heat of adsorption

The isosteric heat of adsorption for the MOPs were generated by first fitting the 77 and 87 K H_2 adsorption isotherms using either the dual-site Langmuir model or a virial expansion (Equation 6.1 and Equation 6.2), where q is the quantity adsorbed, p is pressure, T is temperature. and q_{sat}, a_i and b_i are fitting parameters.

$$q = \frac{q_{\mathrm{sat,A}} b_{\mathrm{A}} p}{1 + b_{\mathrm{A}} p} + \frac{q_{\mathrm{sat,B}} b_{\mathrm{B}} p}{1 + b_{\mathrm{B}} p} \tag{6.1}$$

$$\ln(p) = \frac{1}{T} \sum_i a_i q^i + \sum_i b_i q^i \tag{6.2}$$

Empirical equations, for example the dual-site Langmuir model, Equation 6.1, are often used to model the adsorption of gases and in most cases where there is a strong adsorption site and a weak adsorption site, this is adequate.[6] However, in a number of cases, to estimate reliable isosteric heats of adsorption, a virial-type expansion, Equation 6.2, comprising the temperature-independent parameters a_i and b_i is used.[7] In this study we have investigated the application of both these models to the hydrogen isotherms of amorphous MOP samples.

Curve-fitting of H_2 adsorption isotherms was achieved by optimizing the fitting parameters, $q_{\mathrm{sat,A,B}}$, $b_{\mathrm{A,B}}$ and a, b for Equation 6.1 and Equation 6.2 respectively, such that the square of the difference between the model and the experimental data was minimized. This was achieved through the use of the `lsqcurvefit` function in MATLAB. As a test case CuCu(L) was fit with increasing terms in the virial expansion and the expansion up to third order in q was found necessary to achieve a good fit to the experimental hydrogen isotherm.

Finally, the isotherm models were subsequently used to solve the Clausius–Clapeyron relation for the isosteric heat of adsorption (Q_{st}) by numerically differentiating the relation, Equation 6.3.[8]

$$Q_{\mathrm{st}} = RT^2 \left(\frac{\partial \ln p}{\partial T} \right)_q \tag{6.3}$$

6.2.2 Computational Methods

Owing to the size of the MOP structures (408 atoms including 24 metal atoms) it is computational unfeasible to investigate the entire structure using DFT methods. As the bimetallic paddlewheel cluster is the most complex component of the MOPs, it was chosen for analysis. Figure 6.3 shows the formate, benzoate and water-solvated clusters investigated by DFT methods.

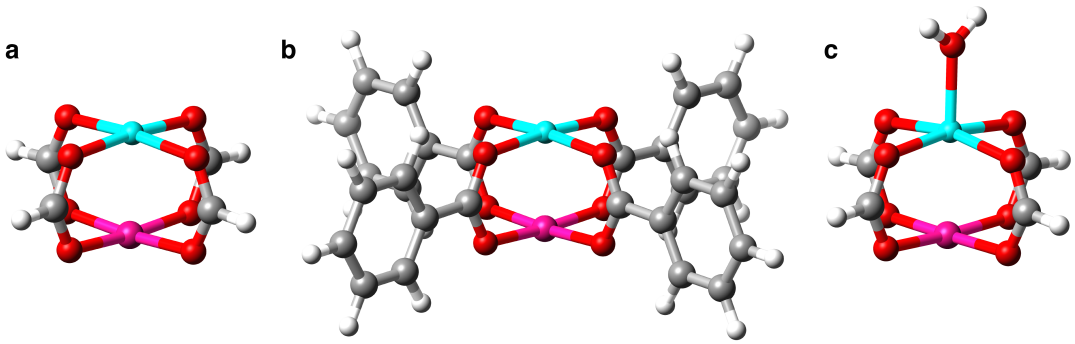

Figure 6.3: Clusters investigated by DFT methods; formate (a), benzoate (b) and water solvated formate (c).

Formate clusters were optimized with the B97-D functional[9] with empirical dispersion correction (D3)[10] and def2-tzdvp[11,12] basis set as employed by Gaussian09.[13] Very tight convergence criteria and ultrafine integration grids were used in all calculations. Additionally, benzoate and water solvated (at the Zn, Cu, Ni and Co site) clusters were optimized to give a comparison for size effects and solvation. Formate clusters optimized with the B97-D3 functional were further compared with structures optimized with PBE0[14] and B3LYP*, which contains 15% exact exchange.[15] Subsequently, interactions with dihydrogen were investigated by optimizing formate clusters with a H_2 molecule placed above the transition metal to give a C2v symmetric dimer. As the B97-D3/def2-tzdvp combination described the monomer paddlewheel clusters correctly and has used in a number of other studies, it was used here to characterize the interaction with H_2.[16,17] Hydrogen-bound structures were optimized and verified to be minima on the potential energy surface with zero negative eigenvalue of the Hessian. Interaction energies of bimetallic clusters were compared with the acclaimed CuCu paddlewheel cluster, which was modeled in the triplet state.[18,19] All hydrogen interaction energies were corrected for basis set superposition errors[20] and enthalpy contributions.

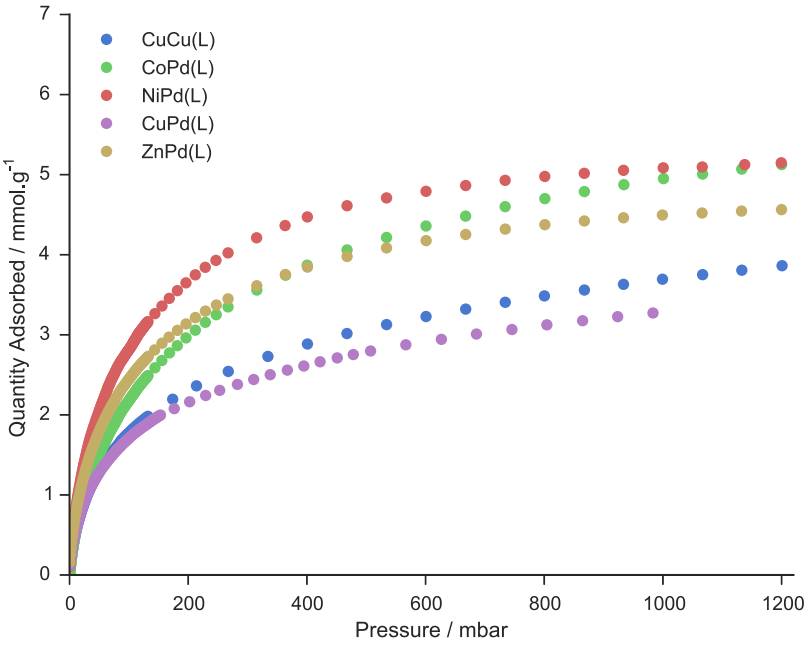

Figure 6.4: H_2 adsorption isotherms at 77 K of MOPs, CuCu(L), CoPd(L), NiPd(L), CuPd(L) and ZnPd(L).

6.3 Results and Discussion

6.3.1 Isosteric heat of adsorption

The low-pressure H_2 adsorption isotherms for CuCu(L), CoPd(L), NiPd(L), CuPd(L) and ZnPd(L) MOPs as shown in Figure 6.4. The isotherms for each MOP show reversible adsorption with steep uptake at low pressures. The H_2 uptake capacity of the MOPs range between between 0.65 and 1.0 wt % at 77 K and 1 bar for CuPd(L) and NiPd(L), respectively. This trend is consistent with the lower pore volume observed by N_2 adsorption for the CuCu(L) and CuPd(L) compared with the NiPd(L) and ZnPd(L) analogues.

In order to quantify the strength of the hydrogen interaction and to calculate the isosteric heat of adsorption (Q_{st}), the isotherms were fit using Equation 6.1 and Equation 6.2 as described previously in Section 6.2.1. Examples of fits for the respective models for ZnPd(L) are shown in Figure 6.5. Notably, the dual-site Langmuir model at low coverage shows a poor fit, despite it being a physical representation of the adsorption process. This poor fit at low pressures is likely due to the disordered nature of these materials, which lose periodicity upon activation.

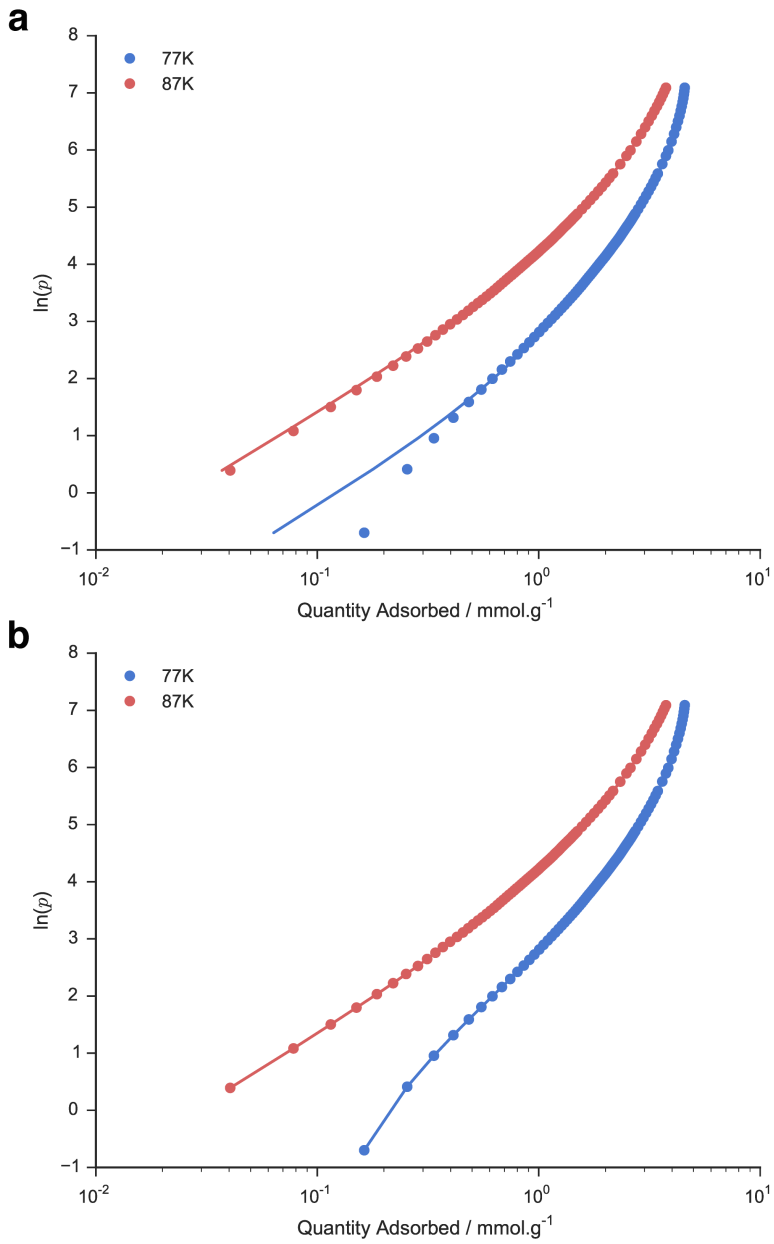

Figure 6.5: Fit comparison for ZnPd(L) H_2 adsorption isotherm at 77 K and 87 K for the dual-site Langmuir model (a) and temperature-independent virial model (b). Experimental points are indicated by circles and the the model fit is represented by a line.

Table 6.2: Optimized parameters for the temperature-independent virial model for the 77 K and 87 K H_2 adsorption isotherms for MOPs, CuCu(L), CoPd(L), NiPd(L), CuPd(L) and ZnPd(L). Note the units of these parameters are mmol.g^{-1}.

		CuCu(L)	**CoPd(L)**	**NiPd(L)**	**CuPd(L)**	**ZnPd(L)**
77K	a_0	0.0312	-0.0425	0.0228	0.0312	0.0182
	a_1	0.0142	0.2964	0.0148	0.0129	0.0234
	a_2	-0.0018	0.5418	-0.0040	-0.0005	-0.0069
	a_3	0.0002	-0.0884	0.0007	0.0001	0.0009
	b_0	2.4208	2.4528	1.7607	2.4200	1.4132
	b_1	1.1008	0.9100	1.1192	1.0039	1.8123
	b_2	-0.1450	-0.1855	-0.2796	-0.0456	-0.5382
	b_3	0.0218	0.0236	0.0381	0.0146	0.0741
87K	a_0	-0.2477	-0.0815	0.0416	0.0508	-0.0919
	a_1	1.5466	0.3922	0.0084	0.0124	-0.5234
	a_2	1.8610	0.5652	-0.0005	-0.0024	0.0952
	a_3	0.8816	-0.2044	-0.0004	0.0010	-0.2769
	b_0	3.8421	3.7193	3.4484	4.1843	3.5863
	b_1	1.2484	0.9081	0.6977	0.9373	0.7563
	b_2	-0.4531	-0.2543	-0.1135	-0.1913	-0.1381
	b_3	0.1458	0.0442	0.0133	0.0750	0.0278

The virial model with parameters given in Table 6.2 was used to calculated the isosteric heat of adsorption (Q_{st}) using the Clausius–Clapeyron relation, Equation 6.3. The Q_{st} curves are displayed in Figure 6.6.

The isosteric curves, Figure 6.6, for ZnPd(L) and NiPd(L) indicate strong adsorption with initial Q_{st} values of -12.1 and -9.50 kJ.mol^{-1}. As the hydrogen loading is increased and the high affinity sites are saturated, the adsorption enthalpy decreases to approximately -7.5 kJ.mol^{-1}. Such high adsorption enthalpies are competitive with exposed metal ion metal-organic frameworks (MOFs) such as HKUST-1 and CPO-27-Ni, which have interaction enthalpies of -10.1 and -13.5 kJ.mol^{-1}, respectively.[21] These bimetallic MOPs show significantly stronger affinity for hydrogen than the CuCu(L) structure, which has an enthalpy of approximately -8.0 kJ.mol^{-1} over the hydrogen loading range. In contrast to the other bimetallic MOPs, the adsorption enthalpy of CuPd(L) and CoPd(L) gradually decrease upon loading, suggesting there is minimal energetic heterogeneity to the adsorption of H_2. The different enthalpy

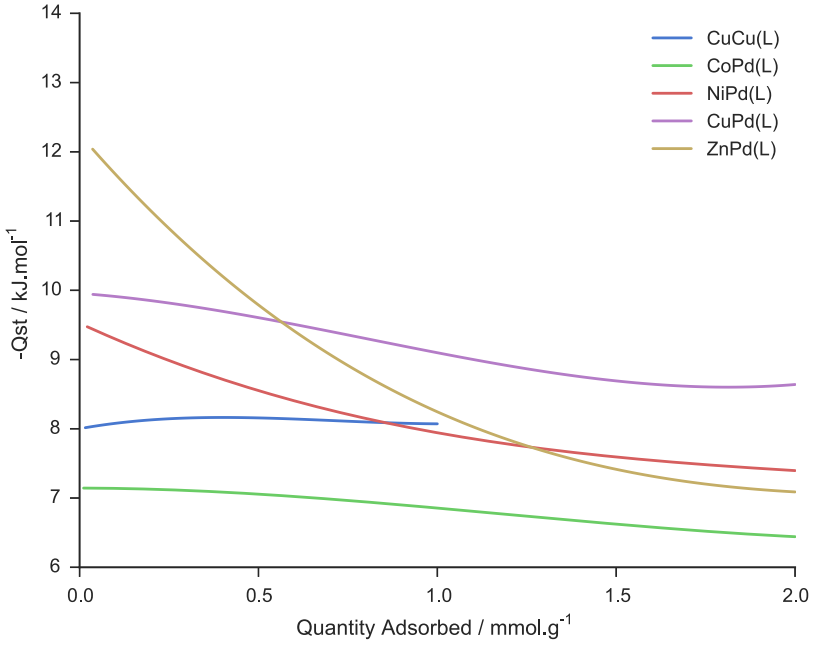

Figure 6.6: Isosteric heats of adsorption of MOPs CuCu(L), CoPd(L), NiPd(L), CuPd(L) and ZnPd(L), calculated using a temperature-independent virial model.

profiles compared with the other bimetallic MOPs is most likely the result of the different pore structure present for CuPd(L); as evidenced by N_2 adsorption experiments. In this case the strong adsorption would result from the small cavity sizes that bind hydrogen strongly by favorable "wall-wall" overlaps, rather than at an open metal site.[22] A similar phenomenon is observed for CoPd(L), but in this case the larger pore volumes produce a lower enthalpy.

The calculated isosteric heat shows that ZnPd(L) has the strongest interaction with H_2. However, as these materials are amorphous, the accessibility of the adsorption site is unclear in addition to whether the Pd(II) or M(II), the transition metal, is the primary site of adsorption. To provide further understanding of the interaction of H_2 with the binary metal cluster, a DFT study of the systems was performed.

6.3.2 DFT Analysis of Binary Metal Cluster

Initially, we screened two functionals and two cluster sizes for describing the binary metal paddlewheel cluster. Formate- and benzoate-based clusters (Figure 6.3) were optimized with B97-D3 and PBE0 with the def2-tzdvp basis set. These specific functionals were chosen to enable a comparison of generalized gradient approximation (GGA) and hybrid GGA functionals. The resulting bond lengths and angles from the optimizations are summarized in Table 6.3. The area of greatest contrast is observed to be in the O-M-O angle, which is more shallow

Table 6.3: Optimized geometries for formate, benzoate, and water-solvated clusters of ZnPd, CuPd, NiPd and CoPd for various DFT functionals compared with geometries from crystal structures.

		B97-D3	PBE0	benzoate	solvate	exp.
	M-Pd / Å	2.481	2.483	2.459	2.547	2.558
ZnPd	O-M-O / °	173.9	171.7	174.0	166.7	165.6
	O-Pd-O / °	175.4	175.6	175.7	178.9	176.8
	M-Pd / Å	2.514	2.385	2.490	2.554	2.552
CuPd	O-M-O / °	173.5	171.9	173.7	168.9	168.8
	O-Pd-O / °	173.8	180.6	174.2	176.1	174.4
	M-Pd / Å	2.515	2.498	2.491	2.553	2.462
NiPd(s)	O-M-O / °	176.2	175.2	176.3	174.0	171.1
	O-Pd-O / °	171.0	171.1	171.6	172.2	177.2
	M-Pd / Å	2.419	2.415	2.397	2.459	
NiPd(t)	O-M-O / °	175.1	174.6	175.0	171.1	
	O-Pd-O / °	177.3	176.3	177.9	179	
	M-Pd / Å	2.439	2.531	2.412	2.475	2.509
CoPd(d)	O-M-O / °	177.5	173.3	177.9	174.3	168.8
	O-Pd-O / °	173.7	175.9	174.1	174.9	176.0
	M-Pd / Å	2.643	2.633	2.436	2.519	
CoPd(q)	O-M-O / °	163.3	162.4	174.1	165.4	
	O-Pd-O / °	176.2	176.1	176.8	179.3	

in the DFT optimized structures. This difference can be attributed to the state of the cluster in the crystal structure. The crystal structures were obtained for solvated samples with a DMA molecule bound to each transition metal. Upon optimization of clusters bound to a water molecule, we find very good agreement between the optimized structures and the crystal structures (Table 6.3).

Importantly, there are two possible spin states for the NiPd and CoPd structures owing to the d^8 and d^7 electron configurations of Ni and Co, respectively. These systems are labeled by the resulting multiplicity: s (singlet), d (doublet), t (triplet) and q (quartet). In a previous study by Markov *et al.*, which employed the B3LYP functional, similar acetate NiPd and CoPd clusters were to determined to favor the high-spin states.[23] Square planar and square pyramidal complexes should be low spin, by crystal field theory arguments.[24] However, the high-spin geometries are more consistent with the crystal structures. Compari-

Table 6.4: Difference in spin state energies of NiPd and CoPd formate clusters for B97-D3, PBE0 and B3LYP* functionals.

	NiPd $\Delta E_{s\rightarrow t}$ / kJ.mol^{-1}	CoPd $\Delta E_{d\rightarrow q}$ / kJ.mol^{-1}
B97-D3	-34.3	8.74
PBE0	-64.7	-53.6
B3LYP*	-40.8	-24.2

son of the geometries of the different spin states, given in Table 6.3, shows that the low-spin states for the NiPd and CoPd clusters produce O-M-O angles much closer at 180° as expected for the square planar nature of the transition metal. However, the formate bridge applies a strain to the O-Pd-O angle and as a result the low-spin structures have O-M-O angles greater than the O-Pd-O angles. This feature is not observed in any of the other structures or the experimental crystal structures.

To further aid in identification of the spin states of these structures the energies were compared for a pure functional (B97D), a hybrid functional (PBE0) and a functional with 15% exact exchange (B3LYP*) (Table 6.4). The energies suggest that the high-spin configuration is favored. As discussed previously, this is likely due to Pd favoring a square planar geometry. Notably, B97-D3 functional disagrees with the other two functionals on the stability of the spin states of CoPd. Literature suggests that a functional with 15% exact exchange gives the best performance in these problems (B3LYP*).[15] Although the evidence proposes NiPd and CoPd exist in the high-spin state, it is important to note that the local environment of the cluster, for example solvent effects, can drastically effect the stabilities of spin states in an experimental system. In the absence of higher-level calculations and further experimental evidence, both spin-states of these clusters will be considered.

A significant feature of this series is the distance between the transition metal and palladium center. This feature has been previously studied by Markov *et al.* in similar bimetallic species.[23] They applied DFT calculations to determine the existence of metal-metal bonding. The resulting study determined the short metal-metal distances to be caused by the acetate bridges with no electronic interaction between Pd-M observed. Our DFT results support these findings, with highest occupied molecular orbitals (HOMOs) displaying strong anti-bonding character, as shown in Figure 6.7.

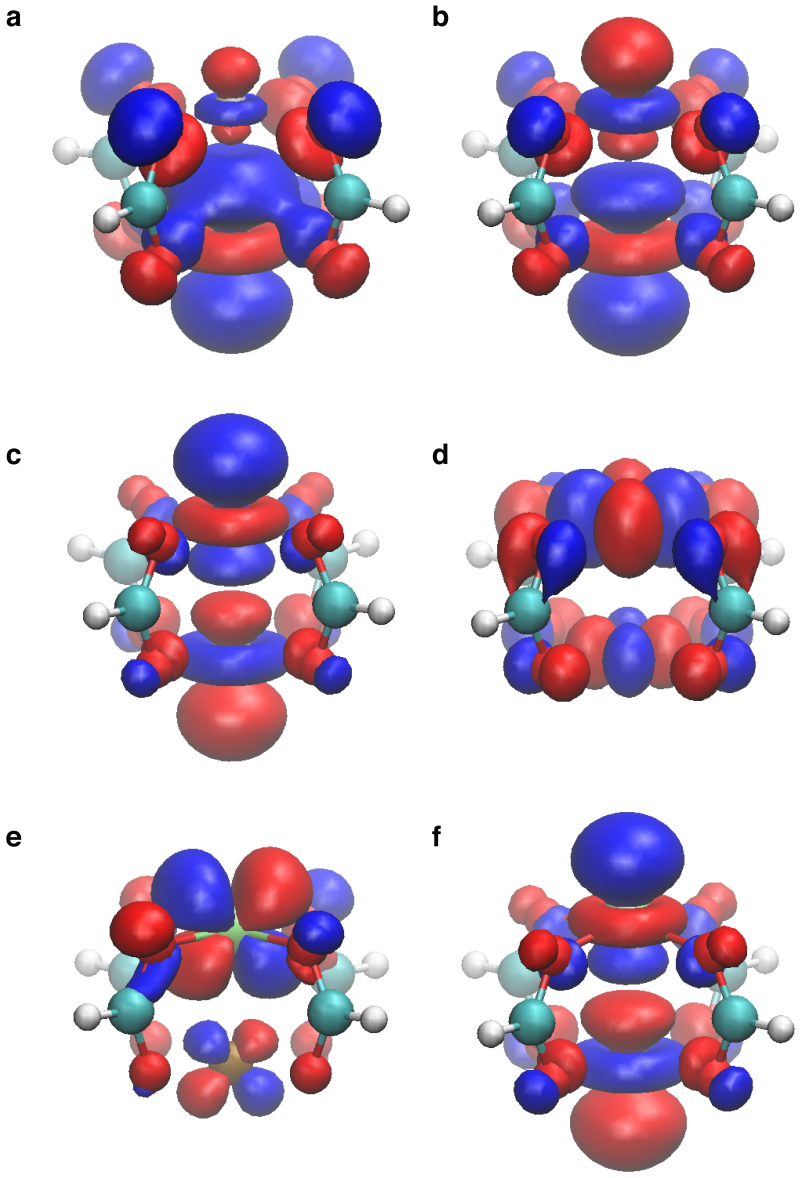

Figure 6.7: HOMOs for ZnPD, CuPd, NiPd(s), NiPd(t), CoPd(d) and CoPd(q) (a-f, respectively). Orbital surfaces generated at B97-D3/def2-tzdvp level.

6.3.3 DFT Analysis of Hydrogen Adsorption

The formate clusters were again optimized with one H_2 molecule positioned above each metal center, such that the dimer had C2v symmetry. Interestingly, the Pd metal center showed no appreciable interaction with H_2 molecules, with no local minima discovered. There is a wealth of literature that describes the strong interaction between hydrogen and palladium; however in these studies palladium was in the Pd(0) state. In the systems described here, palladium exists as Pd(II), which results in the electronic configuration [Kr]$4d^8$. Yonezawa and coworkers have previously described, in great detail, the interaction of Pd(0) with hydrogen.[25] In their study, upon interaction, electrons are transferred from the hydrogen molecule to the Pd atom. Pd orbitals rehybridize and the electrons in the d_z orbital flow into the 5s and 5p. It is expected that this favorable pathway cannot occur as a result of the unfilled d-orbitals of Pd(II).

On the other hand, the exo-hedral transition metals (Zn, Cu, Ni and Co) showed strong interactions with hydrogen, resulting in geometries and energies described in Table 6.5. Importantly, we compare the interactions with those of the well-documented CuCu formate paddlewheel. The trend observed for the bimetallic clusters is Co > Ni > Zn > Cu, if we consider the high-spin states of Co and Ni. The CuCu formate paddlewheel produced an interaction energy of -9.96 kJ.mol^{-1} which compares quite well to the isosteric heat of interaction determined in Section 6.3.1 and enthalpies determined in other studies of HKUST-1, a MOF composed of CuCu paddlewheel units.[21]

ZnPd shows a relatively strong interaction resulting from the charge density associated with the bare Zn site. This is evidenced by Hirshfeld partial charge analysis, which shows the partial charge density is greatest for Zn and decreases across the series, as shown in Table 6.6. The charge density on the M and O sites is such that it polarizes the electron density of H_2, facilitating a favorable electrostatic interaction. A pertinent example of this has been described by Tsivion and coworkers in the description of a catechol-AlF complex that has a theoretical adsorption enthalpy of -14.1 kJ.mol^{-1} of similar magnitude to that of the ZnPd cluster.[17]

In contrast to ZnPd and CuPd, which bind H_2 by polarization, we find the strong adsorption in the NiPd and CoPd analogues to be a result of the formation of a "Kubas" complex. This is observed as Co and Ni analogues bear partially occupied or unoccupied σ^* molecular orbitals. This interaction has been described for a number of transition metal structures.[26] Kubas first discovered this phenomena for a hydrogen bound tungsten complex,[27] which demonstrated a long H-H

Table 6.5: Optimized geometries and interaction energy of formate-H_2 dimers of ZnPd, CuPd, NiPd, CoPd and CuCu clusters compared with experimental enthalpy of interaction.

		B97-D3	exp.
ZnPd	H_2-M / Å	2.206	
	H-H / Å	0.754	
	ΔE / kJ.mol^{-1}	-15.8	-12.0
CuPd	H_2-M / Å	2.434	
	H-H / Å	0.750	
	ΔE / kJ.mol^{-1}	-8.24	-9.94
NiPd(s)	H_2-M / Å	3.096	
	H-H / Å	0.746	
	ΔE / kJ.mol^{-1}	-3.22	-9.47
NiPd(t)	H_2-M / Å	1.998	
	H-H / Å	0.760	
	ΔE / kJ.mol^{-1}	-21.3	
CoPd(d)	H_2-M / Å	2.065	
	H-H / Å	0.757	
	ΔE / kJ.mol^{-1}	-14.1	-7.14
CoPd(q)	H_2-M / Å	1.986	
	H-H / Å	0.765	
	ΔE / kJ.mol^{-1}	-24.5	
CuCu	H_2-M / Å	2.418	
	H-H / Å	0.750	
	ΔE / kJ.mol^{-1}	-9.96	-8.02

Table 6.6: Hirshfeld partial charges on the transition metal and adjacent oxygen atoms for the clusters ZnPd, CuPd, NiPd, CoPd and CuCu calculated at the B97-D3/def2-tzdvp level of theory.

	M / e	O / e
ZnPd	0.454	-0.253
CuPd	0.421	-0.239
NiPd(s)	0.205	-0.202
NiPd(t)	0.323	-0.233
CoPd(d)	0.120	-0.199
CoPd(q)	0.323	-0.227
CuCu	0.424	-0.239

bond of 0.84 Å; free H_2 has a bond length of 0.74 Å. The interaction is defined by donation of electron density from the H_2 σ orbital to empty d orbitals of the transition metal in addition to π back donation from filled transition metal d orbitals to the vacant σ^* H_2 orbital, resulting in lengthening of the H-H bond. Upon consideration of the HOMO and lowest unoccupied molecular orbital (LUMO) of NiPd(t), given in Figure 6.8, the overlap of these states is clear. Donation of electrons from the H_2 HOMO (Figure 6.8a) to NiPd(t) LUMO (Figure 6.8d) and backdonation NiPd(t) HOMO (Figure 6.8c) to H_2 LUMO (Figure 6.8b), occupied bonding orbitals are observed in the NiPd(t)-H_2 dimer, as shown in Figure 6.9. The orbital interactions are also observed in the H-H bond lengths, displayed in Table 6.5, in which NiPd(t), CoPd(d) and CoPd(q) dimers have bond lengths greater than 0.757 Å. This orbital interaction produces extremely strong interaction energies in excess of -21.3 kJ.mol^{-1}, which is of the magnitude of hydrogen interactions identified in previous studies, such as Mg^{2+} containing clusters.[28]

The formation of a "Kubas" complex is especially evidenced by the large difference in interaction energy for the singlet and triple state of NiPd. The singlet state of NiPd has a fully occupied σ^* orbital and as a result is unable to accept electrons from the H_2 molecule, which results in a weak affinity of -3.22 kJ.mol^{-1}.

The DFT analysis has produced binding affinities of bimetallic clusters to H_2 that we can compare to the isosteric heats determined in Section 6.3.1. DFT predicts binding energies in reasonable agreement for the ZnPd-, CuPd- and CuCu-based systems; however there is some incongruity observed for NiPd and CoPd. The discrepancy for CoPd may be a result of the pore structure rather than spe-

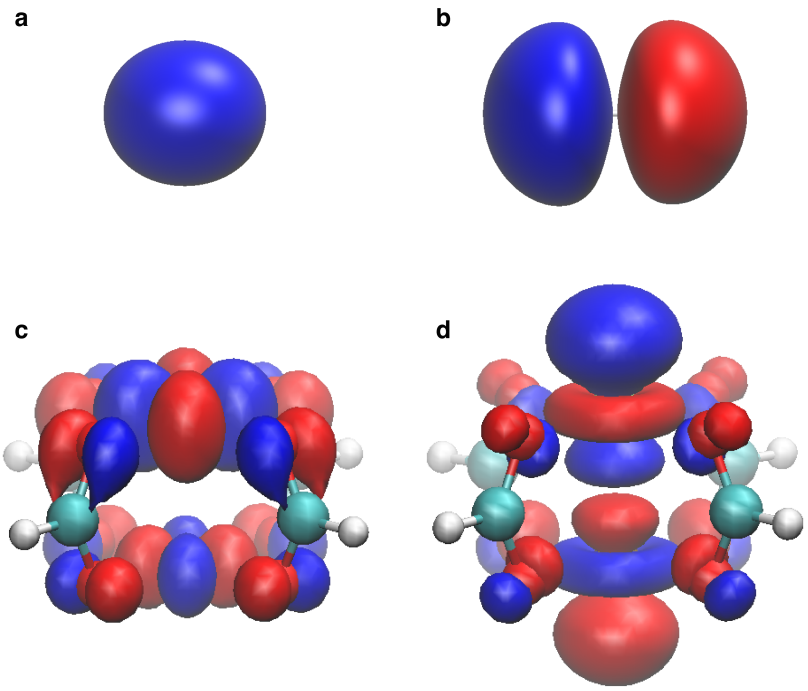

Figure 6.8: Orbitals that form a "Kubas" complex where there is donation from H_2 HOMO (a) to NiPd(t) LUMO (d) and backdonation from NiPd(t) HOMO (c) to the H_2 LUMO (b). Surfaces generated using B97-D3/def2-tzdvp level of theory.

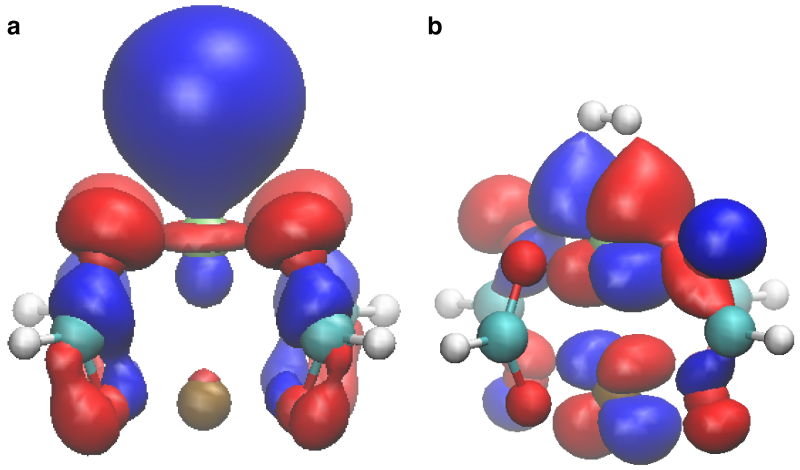

Figure 6.9: Occupied molecular orbitals of NiPd(t)-H_2 showing the "Kubas" bonding present in this interaction. Surfaces generated using B97-D3/def2-tzdvp level.

cific interactions with open metal sites. This is supported by the vastly different experimental N_2 isotherm (Figure 6.2) and isosteric curve (Figure 6.6), which suggests the porosity for this structure is different from that of the other analogues. In addition, as the activation procedure renders the structure amorphous it is plausible that the resulting material is different to the clusters investigated here, one such possible species is cobalt oxide ($Co(II)O_4$). Moreover, the CoPd and NiPd structures have two distinct spin states that interact with H_2 either strongly or weakly. The DFT evidence may suggest high-spin structures are favorable; however the experimental evidence is lacking and as such these systems may exist as a mixture of spin states that would greatly effect the interaction with H_2. Finally, the experimental systems have been identified as amorphous upon activation, which results in the local environment during adsorption experiments being unknown. As a result, the pore structure and accessibility of sites is unclear and makes comparison ambiguous.

6.4 Conclusion

In summary, a series of permanently porous bimetallic MOPs were synthesized by coworkers.[1] The structure, composed of 5-tert-butyl-1,3-benzenedicarboxylic acid with bimetallic Pd(II)–M(II) (M = Co^{2+}, Ni^{2+}, Cu^{2+} or Zn^{2+}) paddlewheel clusters, produces a cuboctahedral supramolecular entity. A virial adsorption model was fit to the H_2 isotherms to obtain the experimental isosteric heat of adsorption, which revealed a strong interaction of between -7.14 and -12.0 $kJ.mol^{-1}$. This affinity to H_2 is among the strongest recorded for a metal-organic material.[29] To further investigate this interaction we applied DFT methods to the bimetallic clusters and were able to assign the strong interactions to a combination of either polarization (ZnPd) or the formation of a "Kubas" complex (NiPd and CoPd). Although there is some ambiguity in the comparison of DFT interaction energies with those obtained experimentally, this study clearly illustrates the potential of this bimetallic cluster for the adsorption of H_2. Accordingly, we may find that three-dimensionally connected and high pore volume MOF materials unlock even stronger H_2 adsorption enthalpies than the molecular analogues described here.

6.5 References

1. J. M. Teo, C. J. Coghlan, J. D. Evans, C. J. Sumby, and C. J. Doonan. "Bimetallic Metal-organic Polyhedra". to be submitted (2015).

2. D. J. Tranchemontagne, Z. Ni, M. O'Keeffe, and O. M. Yaghi. "Reticular Chemistry of Metal–Organic Polyhedra". *Angewandte Chemie International Edition* 47.28 (2008), pp. 5136–5147. DOI: 10.1002/anie.200705008.

3. L. Schlapbach and A. Zuttel. “Hydrogen-storage materials for mobile applications”. *Nature* 414.6861 (2001), pp. 353–358. DOI: 10.1038/35104634.

4. N. L. Rosi, J. Eckert, M. Eddaoudi, D. T. Vodak, J. Kim, M. O’Keeffe, and O. M. Yaghi. “Hydrogen Storage in Microporous Metal-Organic Frameworks”. *Science* 300.5622 (2003), pp. 1127–1129. DOI: 10.1126/science.1083440.

5. M. Yamauchi, H. Kobayashi, and H. Kitagawa. “Hydrogen Storage Mediated by Pd and Pt Nanoparticles”. *ChemPhysChem* 10.15 (2009), pp. 2566–2576. DOI: 10.1002/cphc.200900289.

6. J. A. Mason, K. Sumida, Z. R. Herm, R. Krishna, and J. R. Long. “Evaluating metal-organic frameworks for post-combustion carbon dioxide capture via temperature swing adsorption”. *Energy & Environmental Science* 4 (8 2011), pp. 3030–3040. DOI: 10.1039/C1EE01720A.

7. H. Furukawa, M. A. Miller, and O. M. Yaghi. “Independent verification of the saturation hydrogen uptake in MOF-177 and establishment of a benchmark for hydrogen adsorption in metal-organic frameworks”. *Journal of Materials Chemistry* 17 (30 2007), pp. 3197–3204. DOI: 10.1039/B703608F.

8. D. Shen, M. Bülow, F. Siperstein, M. Engelhard, and A. Myers. “Comparison of Experimental Techniques for Measuring Isosteric Heat of Adsorption”. 6.4 (2000), pp. 275–286. DOI: 10.1023/A:1026551213604.

9. S. Grimme. “Semiempirical GGA-type density functional constructed with a long-range dispersion correction”. *Journal of Computational Chemistry* 27.15 (2006), pp. 1787–1799. DOI: 10.1002/jcc.20495.

10. S. Grimme, J. Antony, S. Ehrlich, and H. Krieg. “A consistent and accurate ab initio parametrization of density functional dispersion correction (DFT-D) for the 94 elements H-Pu”. *The Journal of Chemical Physics* 132.15, 154104 (2010), pages. DOI: 10.1063/1.3382344.

11. F. Weigend and R. Ahlrichs. “Balanced basis sets of split valence, triple zeta valence and quadruple zeta valence quality for H to Rn: Design and assessment of accuracy”. *Physical Chemistry Chemical Physics* 7 (18 2005), pp. 3297–3305. DOI: 10.1039/B508541A.

12. D. Rappoport and F. Furche. “Property-optimized Gaussian basis sets for molecular response calculations”. *The Journal of Chemical Physics* 133.13, 134105 (2010), pages. DOI: 10.1063/1.3484283.

13. M. J. Frisch et al. *Gaussian 09, Revision B.01*. Wallingford CT, 2009.

14. C. Adamo and V. Barone. “Toward reliable density functional methods without adjustable parameters: The PBE0 model”. *The Journal of Chemical Physics* 110.13 (1999), pp. 6158–6170.

15. J. N. Harvey. “DFT Computation of Relative Spin-State Energetics of Transition Metal Compounds”. *Principles and Applications of Density Functional Theory in Inorganic Chemistry I*. Structure and Bonding 112. Springer Berlin Heidelberg, 2004, pp. 151–184.

16. L. Grajciar, P. Nachtigall, O. Bludský, and M. Rubeš. “Accurate Ab Initio Description of Adsorption on Coordinatively Unsaturated Cu^{2+} and Fe^{3+} Sites in MOFs”. *Journal of Chemical Theory and Computation* 11.1 (2015), pp. 230–238. DOI: 10.1021/ct500711z.

17. E. Tsivion, J. R. Long, and M. Head-Gordon. “Hydrogen Physisorption on Metal–Organic Framework Linkers and Metalated Linkers: A Computational Study of the Factors That Control Binding Strength”. *Journal of the American Chemical Society* 136.51 (2014), pp. 17827–17835. DOI: 10.1021/ja5101323.

18. J. Toda, M. Fischer, M. Jorge, and J. R. B. Gomes. “Water adsorption on a copper formate paddlewheel model of CuBTC: A comparative MP2 and DFT study”. *Chemical Physics Letters* 587 (2013), pp. 7–13. DOI: 10.1016/j.cplett.2013.09.049.

19. L. Grajciar, O. Bludský, and P. Nachtigall. “Water Adsorption on Coordinatively Unsaturated Sites in CuBTC MOF”. *The Journal of Physical Chemistry Letters* 1.23 (2010), pp. 3354–3359. DOI: 10.1021/jz101378z.

20. S. F. Boys and F. Bernardi. “The calculation of small molecular interactions by the differences of separate total energies. Some procedures with reduced errors”. *Molecular Physics* 19.4 (1970), pp. 553–566. DOI: 10.1080/00268977000101561.

21. J. G. Vitillo, L. Regli, S. Chavan, G. Ricchiardi, G. Spoto, P. D. C. Dietzel, S. Bordiga, and A. Zecchina. “Role of Exposed Metal Sites in Hydrogen Storage in MOFs”. *Journal of the American Chemical Society* 130.26 (2008), pp. 8386–8396. DOI: 10.1021/ja8007159.

22. K. Tada, S. Furuya, and K. Watanabe. “*Ab initio* study of hydrogen adsorption to single-walled carbon nanotubes”. *Physical Review B* 63 (15 2001), p. 155405. DOI: 10.1103/PhysRevB.63.155405.

23. A. A. Markov, A. P. Klyagina, S. P. Dolin, N. S. Akhmadullina, N. Y. Kozitsyna, N. V. Cherkashina, S. E. Nefedov, M. N. Vargaftik, and I. I. Moiseev. "On the nature of the chemical bond in heterobimetallic palladium(II) complexes with divalent 3d metals". *Russian Journal of Inorganic Chemistry* 54.6 (2009), pp. 885–892. DOI: 10.1134/S0036023609060114.

24. P. Atkins. *Shriver and Atkins' Inorganic Chemistry*. OUP Oxford, 2010.

25. H. Nakatsuji, M. Hada, and T. Yonezawa. "Theoretical study on the chemisorption of a hydrogen molecule on palladium". *Journal of the American Chemical Society* 109.7 (1987), pp. 1902–1912. DOI: 10.1021/ja00241a003.

26. G. Kubas. *Metal Dihydrogen and σ-Bond Complexes*. Modern Inorganic Chemistry. Springer US, 2006.

27. G. J. Kubas, R. R. Ryan, B. I. Swanson, P. J. Vergamini, and H. J. Wasserman. "Characterization of the first examples of isolable molecular hydrogen complexes, $M(CO)_3(PR_3)_2(H_2)$ (M = molybdenum or tungsten; R = Cy or isopropyl). Evidence for a side-on bonded dihydrogen ligand". *Journal of the American Chemical Society* 106.2 (1984), pp. 451–452. DOI: 10.1021/ja00314a049.

28. R. C. Lochan and M. Head-Gordon. "Computational studies of molecular hydrogen binding affinities: The role of dispersion forces, electrostatics, and orbital interactions". *Physical Chemistry Chemical Physics* 8 (12 2006), pp. 1357–1370. DOI: 10.1039/B515409J.

29. K. Sumida et al. "Impact of Metal and Anion Substitutions on the Hydrogen Storage Properties of M-BTT Metal–Organic Frameworks". *Journal of the American Chemical Society* 135.3 (2012), pp. 1083–1091. DOI: 10.1021/ja310173e.

Parts of this research has appeared in the following publications.

A. Avellaneda, P. Valente, A. Burgun, J. D. Evans, A. W. Markwell-Heys, D. Rankine, D. J. Nielsen, M. R. Hill, C. J. Sumby, and C. J. Doonan. "Kinetically Controlled Porosity in a Robust Organic Cage Material". *Angewandte Chemie International Edition* 52.13 (2013), pp. 3746–3749. DOI: 10.1002/anie.201209922.

T. D. Keene, D. Rankine, J. D. Evans, P. D. Southon, C. J. Kepert, J. B. Aitken, C. J. Sumby, and C. J. Doonan. "Solvent-modified dynamic porosity in chiral 3D kagome frameworks". *Dalton Transactions* 42.22 (2013), pp. 7871–7879. DOI: 10.1039/C3DT00096F.

Author statements can be found in Appendix A.

7

Application of Computational Methods to Experimental Observations

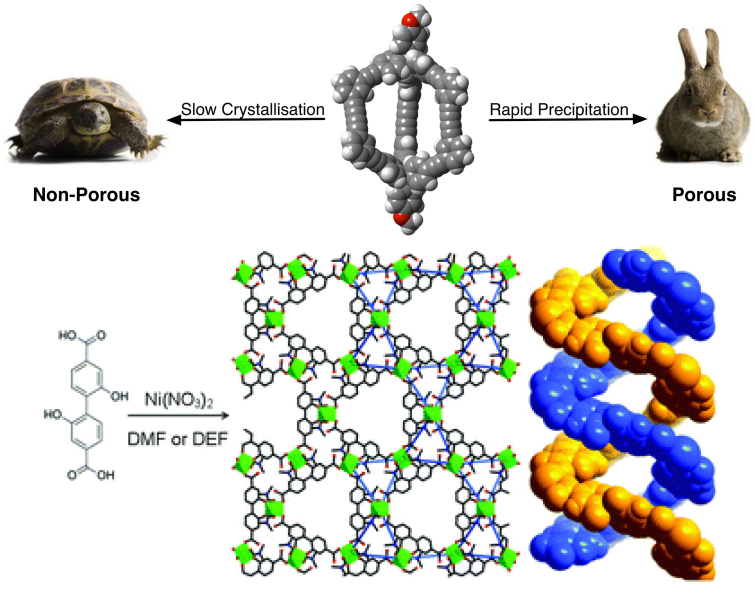

7.1 Introduction

Within the previous chapters, computational methods proved to be useful in the description of porous materials. In particular, methods were exhibited that describe the diffusion of gases in crystalline molecular cages (Chapter 3) and quantify porosity and pore architectures (Chapter 4). An important application of these techniques is to provide explanation of complex behaviors observed by researchers in experimental systems.

Notably, simulations have played an important role in explaining experimental observations. A salient example is described by Düren and coworkers on the characterization of gas diffusion in ZIF-8.[1] The sodalite topology of ZIF-8 contains a pore structure with windows of ≈ 3.40 Å that connect large cavities (≈ 11.6 Å).[2] Owing to the narrow pore windows, this material has been investigated for the kinetic separation of hydrogen gas (2.98 Å) from other larger gases, nitrogen (3.64 Å) and methane (3.40 Å), that are formally unable to diffuse through the material.[3] However, there are a number of reports of ZIF-8 adsorbing nitrogen and methane in addition to even larger molecules.[4–6] Düren and coworkers applied grand canonical Monte Carlo (GCMC) simulations to the conventional ZIF-8 structure and a structure obtained at very high pressure to produce theoretical N_2 isotherms for the two phases of ZIF-8. By comparing theoretical N_2 isotherms to the experimental isotherm it was evident that ZIF-8 undergoes a structural transition, comprised of rotation of the imidazolate ligands, at 2×10^{-4} p/p_0 of N_2 to produce a pore structure similar to the structure at high pressure. This rotation of imidazolate ligands results in the pore aperture opening such that it can diffuse large guests. Consequently, molecular simulation in cooperation with experiments produced atomistic evidence to accurately describe the complex gas adsorption in ZIF-8, an important consideration for the industrial application of this material.[7]

Herein, two systems, a porous organic cage (POC) and a metal-organic framework (MOF), that showed complex and unintuitive gas adsorption results are described. By applying molecular simulations to these systems, the phenomena responsible are explained atomistically.

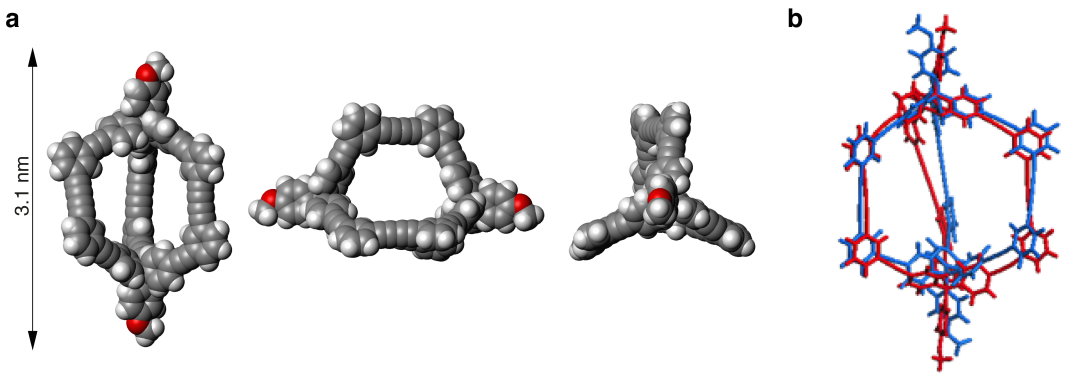

Figure 7.1: DFT energy minimized molecular structure of D1 (a) and comparison of the optimized cage structure (blue) and crystal structure (red) (b).

Table 7.1: Comparison of mean bond distances and angles in the optimized and crystal.

	DFT	Crystal
Tetraphenyl Angle / °	109.6	109.7
Strut Alkyne Length / Å	1.221	1.190
Tripodal Alkyne Length / Å	1.216	1.198
Strut Length / Å	6.637	6.614
Cage Diameter / Å	16.93	18.06

7.2 Understanding gas adsorption in a new POC

Microporous molecular solids consisting of organic cage molecules have a number of advantages over conventional framework materials, such as zeolites and MOFs, including solution-processability[8] and switchable porosity.[9] Many POCs described previously are produced by reversible reactions, exploiting both imine[10] and boronate ester[11] chemistry, with cages of carbon-carbon architecture being comparatively rare.[12]

The molecule D1 was produced using Eglington homocoupling of two alkyne-terminated building units.[13] This wholly carbon cage molecule was modelled using density functional theory (DFT) methods, optimized at the B3LPY/6-31G(d,p) level of theory with default convergence criteria employed by the Gaussian09 software.[14] The energy minimized structure has a distorted triangular prism structure, shown in Figure 7.1a, with internal horizontal (measured as twice the average distance between cage centroid and diyene moiety) and vertical (measured between the two sp^3 carbon atoms) diameters of 14.0 Å and 13.5 Å, respectively.

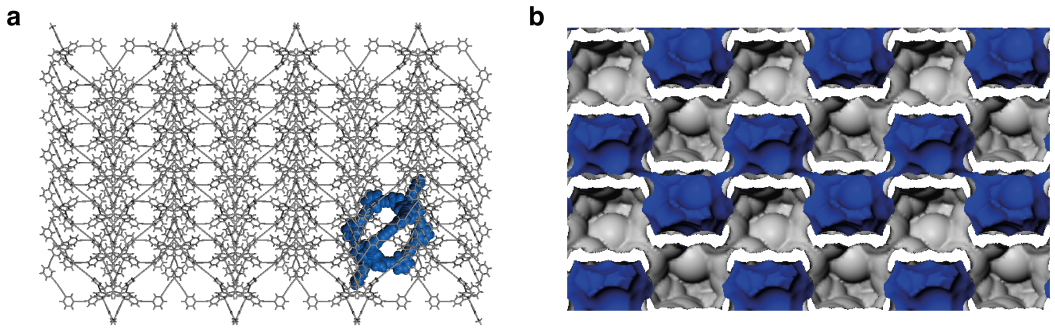

Figure 7.2: Depiction of the packing present in the crystal structure of D1α viewed down the *b*-axis (a) and simulated N_2 accessible surface area of D1α.

The X-ray crystal structure of D1 was identified from crystals produced by slow evaporation of a dichloromethane/methanol solution. A comparison of the DFT structure and crystal structure, in Figure 7.1b and Table 7.1, illustrates the accuracy of DFT for predicting the geometry of cage structures. This single-crystalline polymorph, D1α, crystallizes in the orthorhombic space group *Pbcn*. The cages pack in a herringbone-type arrangement, where each individual molecule of D1 packs closely with four other molecules of D1 in the same orientation and two sets of four additional cages, with a near-orthogonal direction of their molecular axis, as illustrated in Figure 7.2a. This has the effect of placing at least two molecules of D1 into each window of a neighboring cage. Owing to the lack of functional groups directing the packing, the primary intercage forces in the crystal are van der Waals interactions and edge-to-face π-stacking interactions involving both phenyl and alkyne moieties. Powder X-ray diffraction (PXRD) was used to confirm that the single crystal structure was representative of the bulk sample and to determine that the α polymorph was retained subsequent to removal of solvent.

The accessible pore space to N_2 for this α polymorph was computed using the "Atoms Volumes & Surfaces" tool in Accelrys Materials Studio, displayed in Figure 7.2b. The pore network shows that the structure of D1α contains one-dimensional channels consisting of adjacent cages connected by windows of $\approx$4 Å. Given that the comparable kinetic diameter of N_2 (3.64 Å) it was expected that that these windows may restrict the diffusion of N_2 through the material. To support this hypothesis, molecular dynamics was employed to simulate the diffusion of H_2 and N_2 within the pore structure of D1α.

Molecular dynamics simulations were carried out using the Forcite module within Materials Studio 5.0. NVT dynamics were simulated at a temperature of 77 K with a step size of 1 fs; temperature controlled using the Nosé-Hoover thermostat.[15] The simulated system included the periodic unit cell of the crystal

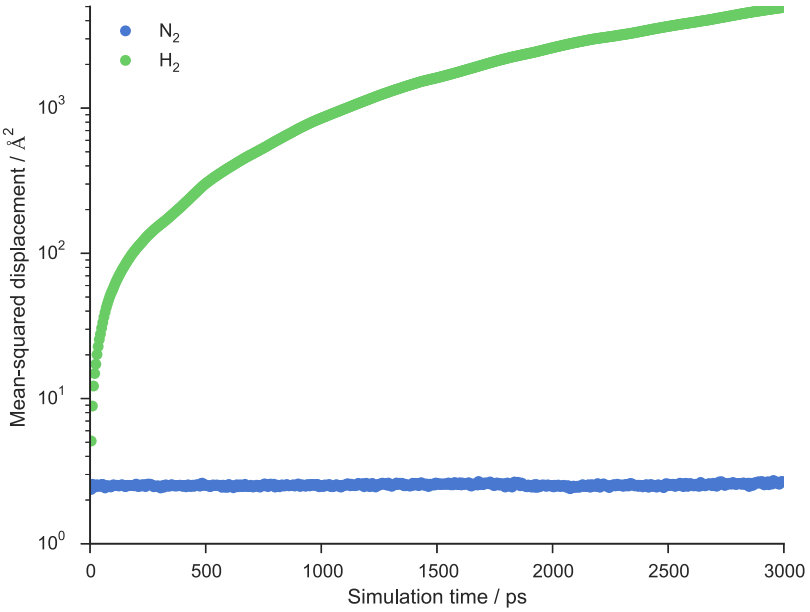

Figure 7.3: Simulated mean-squared of N_2 and H_2 through the crystal structure of D1α.

structure and a N_2 or H_2 molecule placed within the previously identified porous channels. All bonds, angles, dihedral angles and intermolecular forces were described using the universal force-field (UFF).[16] Mean square displacements were measured for a 3 ns simulation, initially equilibrated for 1 ns, and averaged over three unique simulations.

The mean-square displacement of single N_2 and H_2 molecules (Figure 7.3) clearly show the motion of N_2 is constrained within polymorph D1α. The smaller H_2 is able to diffuse rapidly through the structure by traversing the 4 Å windows. During the simulation no significant structural changes of the porous material were observed.

In accordance with these diffusion simulations, 77 K N_2 isotherms indicated that activated samples of D1α were non-porous to N_2 but porous to H_2, affording a total uptake of approximately 40 $cm^3.g^1$ at 77 K.[13] However, D1α could be considered a "soft" porous crystal, and it is plausible that with greater gas loading pressures and temperature, slight structural deformations may allow N_2, in addition to other larger gases, to move through the pores as observed in Chapter 3. Subsequently, further experimental analysis of D1 produced a second kinetically favored polymorph that showed diffusion of N_2 at 77 K. This β polymorph exhibited a Brunauer–Emmett–Teller (BET) surface area of 1153 $m^2.g^{-1}$, notably high for a POC material.[12]

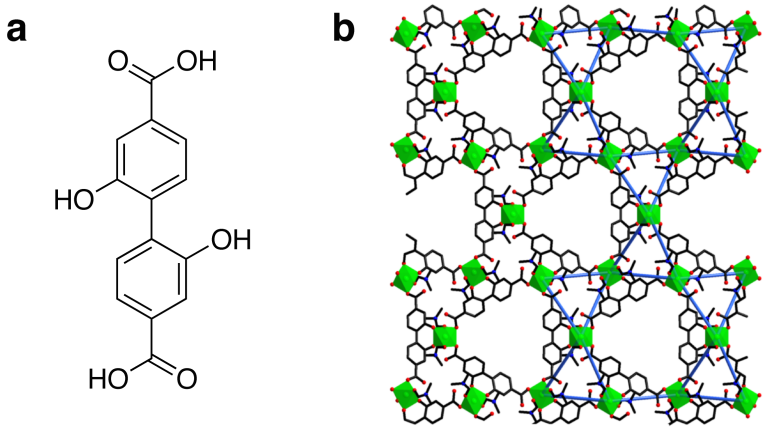

Figure 7.4: Biphenyl-dicarboxylic acid ligand (a) and structural representation of the MOF framework (b) showing the large pores that align with the crystallographic *c*-axis.

In summary, this study demonstrates the use of molecular simulations to characterize the geometry of a new POC and visualize the pore network from an X-ray crystal structure. Additionally, molecular dynamics were applied to investigate the accessibility of identified pore space to gases used by experimental probes. This produced a clear understanding of the N_2 adsorption experiments performed on the α polymorph, that could not be simply captured by a static geometric model.

7.3 Dynamic porosity in chiral 3D kagome MOF

Metal-organic frameworks (MOFs) are porous materials that are generally connected in three dimensions by a combination of metal nodes and organic ligands. There have been a number of reports of MOF materials that display flexible and dynamic behaviour upon changes in pressure, temperature and introduction of guest molecules.[17,18] This nature can result in number of attractive phenomena, including gate opening and breathing, that may be exploited for gas separation applications.[19] Importantly, these properties are generally associated with flexibility in either the metal node or organic linker.[20] However, using molecular simulations it is shown that dynamic porosity in a new MOF is a result of solvent attached to the metal node.

Coworkers produced a series of MOFs constructed from octahedral Ni(II) centres bridged by multidentate biphenyl-dicarboxylic acid ligands, shown in Figure 7.4a with either N,N'-dimethylformamide (DMF) or N,N'-diethylformamide (DEF) solvent attached to the bare coordination sites. These structures will be referred to as 1-DMF and 1-DEF, respectively.[21] Single crystal X-ray diffraction

revealed the MOF structure as chiral with a quartz-like 3D kagome structure, as illustrated in Figure 7.4b. Notably, the structure presents double-helical pores along the crystallographic *c*-axis that are connected to neighboring channels to form the 1D pore network. 1-DMF and 1-DEF were found to be isostructural with very similar unit cell parameters.

Visualization of the pore space accessible to N_2 reveals the pore structure is comprised of large one-dimensional channels with pleats associated with the layer spacing of the framework. The experimental porosity of 1-DMF and 1-DEF was ascertained by performing N_2 adsorption isotherms at 77 K (Figure 7.5). The isotherms of both materials are best described as type I and BET analysis results in surface areas of 733 and 767 $m^2.g^{-1}$ for 1-DMF and 1-DEF, respectively. Interestingly, the isotherm of 1-DMF displays a prominent shoulder in the low pressure region $p/p_0 = 0.001$ to 0.05, as shown in Figure 7.5b, which is reproducible over multiple samples.

The isotherm shoulder was of particular interest as the only difference between the structures is the attached solvent. It was hypothesized that this artifact could be a result of dynamics associated with the solvent molecule. Molecular simulations of the 1-DMF and 1-DEF structures were employed to discern the effect of solvent on porosity.[22] Initial structures were taken from crystal structures with excess solvent molecules removed. DMF and DEF molecules were rotated around the pore, by rotating the Ni–O formamide coordination axis in 10° increments. For each step of rotation the framework was held rigid and the methyl and ethyl groups allowed to relax in *P1* symmetry. Relaxation and final structure energies were calculated using UFF[16] within the Forcite module of Accelrys Materials Studio 5.0. Nitrogen surface area for each structure were calculated, using a probe radius of 1.84 Å, with the "Atoms Volume & Surfaces" package of Materials Studio.

Simulations of 1-DMF suggest that the shoulder in the 77 K N_2 adsorption isotherm is a result of rotation of DMF molecules with respect to the Ni center. By stepping the rotation of the DMF molecules in 10° increments with respect to the O–Ni–O–C torsion angle, significant fluctuation in the simulated surface area is observed (Figure 7.6b). The calculated global energy minimum, in Figure 7.6a, occurs at 10° (with 0° being the position seen in the crystal structure of 1-DMF) and results in a calculated surface area of 1068 $m^2.g^{-1}$. Another local minimum is identified at 180° with a lower surface area and a moderately small energy barrier between the two conformations. Given the low energy barrier to rotation of the DMF, it is likely that the two DMF energy minima positions are almost equally populated and that the shoulder begins at saturation of the lower surface

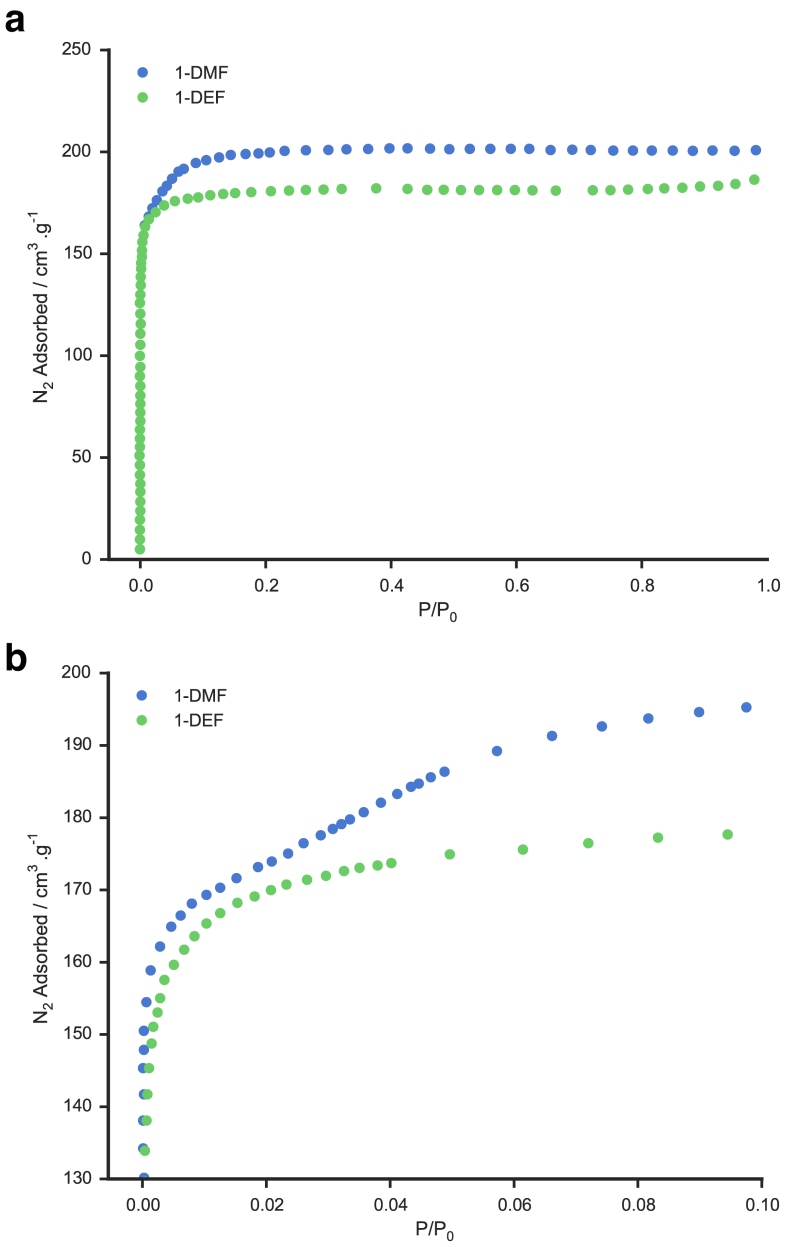

Figure 7.5: 1-DMF and 1-DEF N_2 adsorption isotherms performed at 77 K (a) and enlargement of the low pressure region (b).

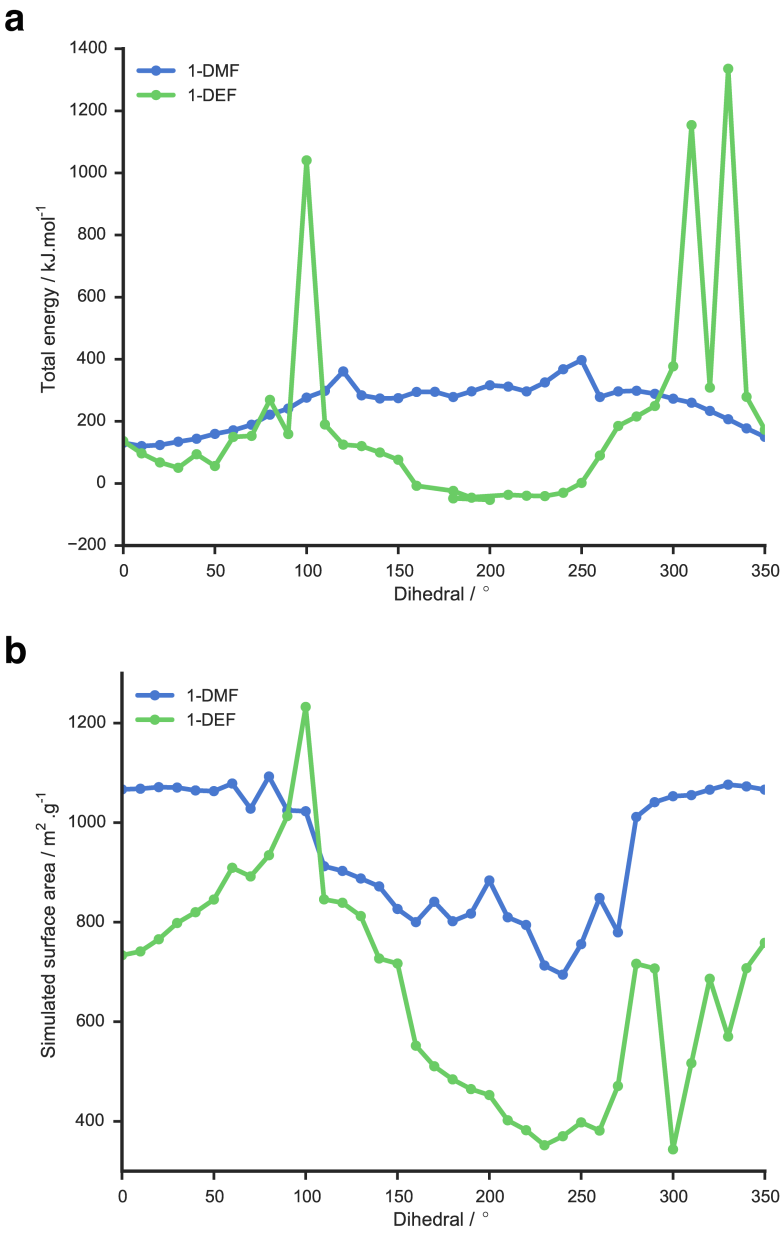

Figure 7.6: Calculated total energy for 1-DMF and 1-DEF (a) and the corresponding simulated accessible surface area (b) as the coordinated solvents are rotated via changes in the O–Ni–O–C dihedral angle.

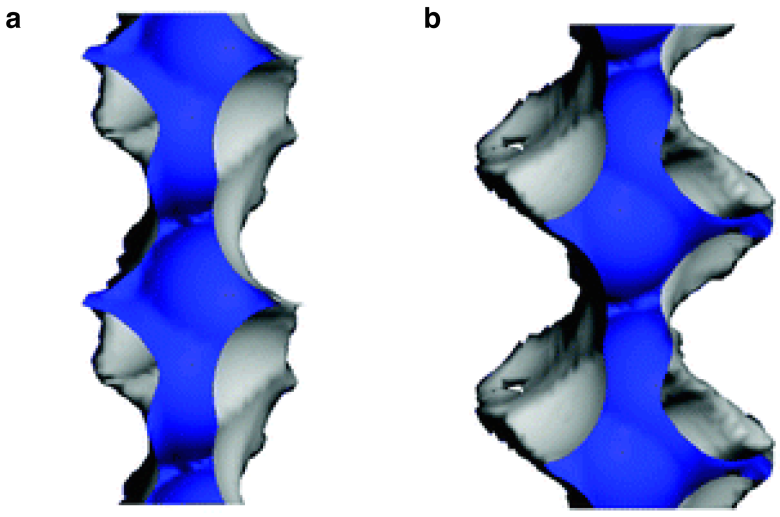

Figure 7.7: Accessible N_2 pore surface of 1-DMF arising from the minimum (a) and maximum (b) surface area conformations as the O–Ni–O–C torsion angle is varied.

area form. The rotation of DMF molecules may be mediated by adsorption of N_2 gas as the isotherm progresses through the low pressure region, similar to what has been described for the ligands of ZIF-8.[1] As the DMF molecules rotate, further pore volume is opened, which is then filled, locking the DMF into the energy minimum at 10°. A depiction of the pore volume for 1-DMF is shown in Figure 7.7. The calculated energy of rotation of 1-DEF shows two almost equal minima with large energy barriers produced by framework sterics, which almost certainly disallows rotation of the coordinated DEF. Consequently, 1-DEF shows a typical type I isotherm (Figure 7.5b) without a shoulder as a result of this rotational locking.

The unusual N_2 adsorption observed for 1-DMF can be attributed to the rotational motion of attached solvent. This has highlighted a novel pathway to producing dynamically porous materials by modifying attached solvent while retaining the relatively rigid metal nodes and ligands. Classical simulations were vital to the understanding of this phenomena, which could not be captured wholly by experimental methods.

7.4 Conclusion

In summary, the investigations have employed molecular simulations to provide further understanding of experimental observations of new POC and MOF materials. Using classical molecular dynamics the diffusion of H_2 and N_2 in the pores of D1 were able to show the lack of N_2 adsorption is a result of the window

and pore structure. Secondly, the dynamic adsorption of a kagome MOF structure was atomistically investigated. From molecular simulations, it was possible to assign the unusual gas adsorption characteristics of 1-DMF to the rotational dynamics of attached DMF molecules, which is sterically disallowed for the 1-DEF analogue. It is clear that these techniques have provided additional and fundamental clarity to the atomistic dynamics present in these new materials.

7.5 References

1. D. Fairen-Jimenez, S. A. Moggach, M. T. Wharmby, P. A. Wright, S. Parsons, and T. Düren. "Opening the Gate: Framework Flexibility in ZIF-8 Explored by Experiments and Simulations". *Journal of the American Chemical Society* 133.23 (2011), pp. 8900–8902. DOI: 10.1021/ja202154j.
2. K. S. Park, Z. Ni, A. P. Côté, J. Y. Choi, R. Huang, F. J. Uribe-Romo, H. K. Chae, M. O'Keeffe, and O. M. Yaghi. "Exceptional chemical and thermal stability of zeolitic imidazolate frameworks". *Proceedings of the National Academy of Sciences* 103.27 (2006), pp. 10186–10191. DOI: 10.1073/pnas.0602439103.
3. A. W. Thornton, D. Dubbeldam, M. S. Liu, B. P. Ladewig, A. J. Hill, and M. R. Hill. "Feasibility of zeolitic imidazolate framework membranes for clean energy applications". *Energy & Environmental Science* 5.6 (2012), pp. 7637–7646. DOI: 10.1039/C2EE21743K.
4. W. Zhou, H. Wu, M. R. Hartman, and T. Yildirim. "Hydrogen and Methane Adsorption in Metal−Organic Frameworks: A High-Pressure Volumetric Study". *The Journal of Physical Chemistry C* 111.44 (2007), pp. 16131–16137. DOI: 10.1021/jp074889i.
5. K. Zhang, R. P. Lively, C. Zhang, W. J. Koros, and R. R. Chance. "Investigating the Intrinsic Ethanol/Water Separation Capability of ZIF-8: An Adsorption and Diffusion Study". *The Journal of Physical Chemistry C* 117.14 (2013), pp. 7214–7225. DOI: 10.1021/jp401548b.
6. X.-C. Huang, Y.-Y. Lin, J.-P. Zhang, and X.-M. Chen. "Ligand-Directed Strategy for Zeolite-Type Metal–Organic Frameworks: Zinc(II) Imidazolates with Unusual Zeolitic Topologies". *Angewandte Chemie International Edition* 45.10 (2006), pp. 1557–1559. DOI: 10.1002/anie.200503778.
7. G. Lu and J. T. Hupp. "Metal−Organic Frameworks as Sensors: A ZIF-8 Based Fabry−Pérot Device as a Selective Sensor for Chemical Vapors and Gases". *Journal of the American Chemical Society* 132.23 (2010), pp. 7832–7833. DOI: 10.1021/ja101415b.
8. A. F. Bushell, P. M. Budd, M. P. Attfield, J. T. A. Jones, T. Hasell, A. I. Cooper, P. Bernardo, F. Bazzarelli, G. Clarizia, and J. C. Jansen. "Nanoporous Organic Polymer/Cage Composite Membranes". *Angewandte Chemie International Edition* 52.4 (2013), pp. 1253–1256. DOI: 10.1002/anie.201206339.
9. J. T. A. Jones et al. "On–Off Porosity Switching in a Molecular Organic Solid". *Angewandte Chemie International Edition* 50.3 (2011), pp. 749–753. DOI: 10.1002/anie.201006030.
10. D. P. Lydon, N. L. Campbell, D. J. Adams, and A. I. Cooper. "Scalable Synthesis for Porous Organic Cages". *Synthetic Communications* 41.14 (2011), pp. 2146–2151. DOI: 10.1080/00397911.2010.499487.
11. G. Zhang, O. Presly, F. White, I. M. Oppel, and M. Mastalerz. "A Permanent Mesoporous Organic Cage with an Exceptionally High Surface Area". *Angewandte Chemie International Edition* 53.6 (2014), pp. 1516–1520. DOI: 10.1002/anie.201308924.
12. J. D. Evans, C. J. Sumby, and C. J. Doonan. "Synthesis and Applications of Porous Organic Cages". *Chemistry Letters* (2015). DOI: 10.1246/cl.150021.
13. A. Avellaneda, P. Valente, A. Burgun, J. D. Evans, A. W. Markwell-Heys, D. Rankine, D. J. Nielsen, M. R. Hill, C. J. Sumby, and C. J. Doonan. "Kinetically Controlled Porosity in a Robust Organic Cage Material". *Angewandte Chemie International Edition* 52.13 (2013), pp. 3746–3749. DOI: 10.1002/anie.201209922.
14. M. J. Frisch et al. *Gaussian 09, Revision B.01*. Wallingford CT, 2009.
15. S. Nosé. "A unified formulation of the constant temperature molecular dynamics methods". *The Journal of Chemical Physics* 81.1 (1984), pp. 511–519. DOI: 10.1063/1.447334.

16. A. K. Rappe, C. J. Casewit, K. S. Colwell, W. A. Goddard, and W. M. Skiff. "UFF, a full periodic table force field for molecular mechanics and molecular dynamics simulations". *Journal of the American Chemical Society* 114.25 (1992), pp. 10024–10035. DOI: 10.1021/ja00051a040.

17. D. Tanaka, K. Nakagawa, M. Higuchi, S. Horike, Y. Kubota, T. C. Kobayashi, M. Takata, and S. Kitagawa. "Kinetic Gate-Opening Process in a Flexible Porous Coordination Polymer". *Angewandte Chemie International Edition* 47.21 (2008), pp. 3914–3918. DOI: 10.1002/anie.200705822.

18. R. Kitaura, K. Seki, G. Akiyama, and S. Kitagawa. "Porous Coordination-Polymer Crystals with Gated Channels Specific for Supercritical Gases". *Angewandte Chemie International Edition* 42.4 (2003), pp. 428–431. DOI: 10.1002/anie.200390130.

19. J.-R. Li, R. J. Kuppler, and H.-C. Zhou. "Selective gas adsorption and separation in metal-organic frameworks". *Chemical Society Reviews* 38 (5 2009), pp. 1477–1504. DOI: 10.1039/B802426J.

20. F.-X. Coudert, A. Boutin, A. H. Fuchs, and A. V. Neimark. "Adsorption Deformation and Structural Transitions in Metal–Organic Frameworks: From the Unit Cell to the Crystal". *The Journal of Physical Chemistry Letters* 4.19 (2013), pp. 3198–3205. DOI: 10.1021/jz4013849.

21. T. D. Keene, D. Rankine, J. D. Evans, P. D. Southon, C. J. Kepert, J. B. Aitken, C. J. Sumby, and C. J. Doonan. "Solvent-modified dynamic porosity in chiral 3D kagome frameworks". *Dalton Transactions* 42.22 (2013), pp. 7871–7879. DOI: 10.1039/C3DT00096F.

22. F. Salles, A. Ghoufi, G. Maurin, R. G. Bell, C. Mellot-Draznieks, and G. Férey. "Molecular Dynamics Simulations of Breathing MOFs: Structural Transformations of MIL-53(Cr) upon Thermal Activation and CO_2 Adsorption". *Angewandte Chemie International Edition* 47.44 (2008), pp. 8487–8491. DOI: 10.1002/anie.200803067.

I am turned into a sort of machine for observing facts and grinding out conclusions...

Charles Darwin

8 Conclusion

8.1 Summary

This thesis describes the multi-scale modeling of emerging porous materials, primarily porous molecular solids. This was achieved using a amalgamation of classical molecular simulation, quantum density functional theory (DFT), geometric analysis and machine learning. Importantly, experimental observations were aided using these tools to give an accurate and comprehensive atomistic picture of gas adsorption phenomena and contribute to the *in silico* design of new examples.

Chapter 3 and Chapter 4 detail the results of molecular dynamics simulations of porous organic cages in two states and their applications. Firstly, the performance of porous organic cage (POC) materials were investigated for use as additives for mixed matrix membranes (MMMs) for environmentally relevant gas separations. The simulations reveal that a number of MMMs containing POCs exhibit enhanced selectivity and permeability compared with a neat polymer matrix, particularly for H_2/CO_2 separations. Secondly, in Chapter 4, the advantages of the amorphous phase for several reported examples of POCs and a number of potential POC molecules were investigated using GPU-accelerated molecular dynamics simulations. The methodologies employed in Chapter 4 improved sig-

nificantly on previously reported methods, allowing for amorphous models of cage molecules that had previously been ignored. Subsequently, the analysis presented elucidated potential design rules for producing amorphous materials with surface areas approaching 2000 $m^2.g^1$.

Furthermore, in Chapter 5, the Cambridge Structural Database (CSD) was thoroughly searched for previously unreported porous molecules. An initial dataset of over 150 000 crystal structures was analyzed using Voronoi network analysis in addition to classical and semi-empirical optimizations, generating a database of 481 organic porous molecular crystal structures, a number of which have been previously reported. Subsequently, to investigate the molecular features that promote porous molecular crystals, machine learning was employed. These methods determined that large molecular surface area was responsible for a large proportion of porous structures. The creation of the database also allowed for comprehensive examination of materials with specific pore diameter and capacity.

Finally, Chapter 6 and Chapter 7, describe the use of computational methods to provide fundamental insight into experimental observations. Chapter 6 describes the hydrogen adsorption of unique metal-organic polyhedra (MOP) structures. These unique structures were experimentally observed to show strong interactions with hydrogen and by using DFT simulations the interaction was assigned to either polarization or the formation of a "Kubas" complex. Chapter 7, chronicles the atomistic understanding provided by classical molecular simulations on interesting adsorption behavior observed in new POC and metal-organic framework (MOF) structures.

Despite the challenges involved in the application of computational methods to these emerging materials, the thesis presented here demonstrates their capabilities towards the prediction of vital macroscopic properties, such as, permeability and the molecular basis for these properties. Undoubtedly, molecular simulation is a vital tool in modern chemistry with far-reaching applications in areas outside the scope of this thesis.

8.2 Future Directions

The work reported herein can be extended in a number of ways. Firstly, the assessment of POC-based MMMs was based on using Bruggeman's effective-medium model, which approximates the permeability of a mixture of materials as a linear combination of the individual permeabilities.[1] Although, this has been shown to give good agreement, it is important to note that this cannot capture the integration between the two phases. To thoroughly capture the complex interactions between polymers and cage molecules, full atomistic simulation could

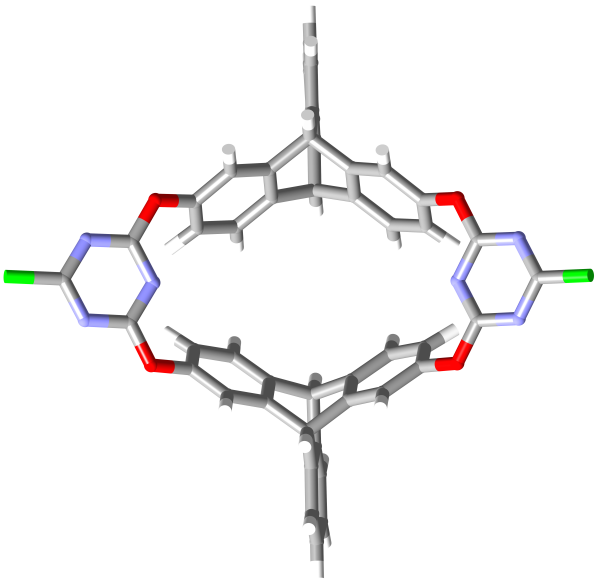

Figure 8.1: Molecular depiction of DIHGOR which results in an extremely porous crystal structure yet to be demonstrated experimentally.

be employed to generate a complete model of the MMM. This has been recently achieved by Jiang and coworkers in an investigation of MMM comprising polybenzimidazole and zeolitic imidazolate framework.[2] It is important to note, that the size of these simulations often hindered by computational cost. However, the advantages of GPU-accelerated molecular simulations described in Chapter 4 could be used to ameliorate this issue.[3,4] Furthermore, the simulation methodology used to generate amorphous models of POCs in Chapter 4 could be applied to several more examples. One interesting application is towards the consideration of amorphous alloys of cage molecules.[5]

Further analysis of the candidate structures identified in Chapter 5 is required. The study established a database of a number of reported structures that have yet to be studied for use in gas adsorption. One structure, DIHGOR, was found to have a surface area of over 1500 $m^2.g^{-1}$. The macrocyclic structure of this molecule,[6] shown in Figure 8.1, corresponds well with the outcomes of the machine learning algorithms. Experimental demonstration of permanent porosity in this material would provide an excellent application of the organic porous molecular crystal (oPMC) database and an unequivocal demonstration of the power of the computational screening method developed.

8.3 References

1. G. Bánhegyi. "Comparison of electrical mixture rules for composites". *Colloid and Polymer Science* 264.12 (1986), pp. 1030–1050. DOI: 10.1007/BF01410321.

2. L. Zhang, Z. Hu, and J. Jiang. "Metal–Organic Framework/Polymer Mixed-Matrix Membranes for H_2/CO_2 Separation: A Fully Atomistic Simulation Study". *The Journal of Physical Chemistry C* 116.36 (2012), pp. 19268–19277. DOI: 10.1021/jp3067124.

3. W. M. Brown, P. Wang, S. J. Plimpton, and A. N. Tharrington. "Implementing molecular dynamics on hybrid high performance computers – short range forces". *Computer Physics Communications* 182.4 (2011), pp. 898–911. DOI: 10.1016/j.cpc.2010.12.021.

4. S. Plimpton. "Fast Parallel Algorithms for Short-Range Molecular Dynamics". *Journal of Computational Physics* 117.1 (1995), pp. 1–19. DOI: 10.1006/jcph.1995.1039.

5. T. Hasell, S. Y. Chong, M. Schmidtmann, D. J. Adams, and A. I. Cooper. "Porous Organic Alloys". *Angewandte Chemie International Edition* 51.29 (2012), pp. 7154–7157. DOI: 10.1002/anie.201202849.

6. C. Zhang and C.-F. Chen. "Triptycene-Based Expanded Oxacalixarenes: Synthesis, Structure, and Tubular Assemblies in the Solid State". *The Journal of Organic Chemistry* 72.10 (2007), pp. 3880–3888. DOI: 10.1021/jo0702490.

A

Statements of Authorship

Feasibility of Mixed Matrix Membrane Gas Separations Employing Porous Organic Cages

Published

Featured in Chapter 3.

J. D. Evans, D. M. Huang, M. R. Hill, C. J. Sumby, A. W. Thornton, and C. J. Doonan. "Feasibility of Mixed Matrix Membrane Gas Separations Employing Porous Organic Cages". *The Journal of Physical Chemistry C* 118.3 (2014), pp. 1523–1529. DOI: 10.1021/jp4079184.

Principal Author

Jack D. Evans (Principal Author, Candidate)

Designed and carried out simulations, analyzed resulting data, interpreted results. In addition to conceiving and preparing the manuscript.

85% Contribution.

This paper reports on original research I conducted during the period of my Higher Degree by Research candidature and is not subject to any obligations or contractual agreements with a third party that would constrain its inclusion in this thesis. I am the primary author of this paper. I hereby certify the statement of contribution is accurate.

9/9/2015

Jack D. Evans — Date

Co-Author Contributions

By signing the statement of authorship, each author certifies that:

1. the candidate's stated contribution to the publication is accurate (as detailed above);
2. permission is granted for the candidate to include the publication in the thesis; and
3. the sum of all co-author contributions is equal to 100% less the candidate's stated contribution.

David M. Huang

Assisted with the design of molecular dynamics simulations and revision of the manuscript.

I hereby certify the statement of contribution is accurate.

9/9/15

David M. Huang Date

Matthew R. Hill

Provided assistance with the interpretation of results and revision of the manuscript.

I hereby certify the statement of contribution is accurate.

11/9/15

Matthew R. Hill Date

Christopher J. Sumby

Supervised the development of the work, assisting in the interpretation of results and the revision of the manuscript.

I hereby certify the statement of contribution is accurate.

9/9/15

Christopher J. Sumby Date

Aaron W. Thornton

Supervised the application of mixed-matrix membrane theoretical models in addition to conception and revision of the manuscript.

I hereby certifiy the statement of contribution is accurate.

10/9/15

Date

Christian J. Doonan

Supervised the development of the work, assisting in the interpretation of results. Additionally, aided in the conception and revision of the manuscript, acting as corresponding author.

I hereby certifiy the statement of contribution is accurate.

9/9/2015

Christian J. Doonan Date

Molecular Design of Amorphous Porous Organic Cages for Enhanced Gas Storage

Published

Featured in Chapter 4.

J. D. Evans, D. M. Huang, M. R. Hill, C. J. Sumby, D. S. Sholl, A. W. Thornton, and C. J. Doonan. "Molecular Design of Amorphous Porous Organic Cages for Enhanced Gas Storage". *The Journal of Physical Chemistry C* 119.14 (2015), pp. 7746–7754. DOI: 10.1021/jp512944r.

Principal Author

Jack D. Evans (Principal Author, Candidate)

Designed and carried out simulations, analyzed resulting data, interpreted results. In addition to conceiving and preparing the manuscript.

85% Contribution.

This paper reports on original research I conducted during the period of my Higher Degree by Research candidature and is not subject to any obligations or contractual agreements with a third party that would constrain its inclusion in this thesis. I am the primary author of this paper. I hereby certify the statement of contribution is accurate.

9/9/2015

Jack D. Evans — Date

Co-Author Contributions

By signing the statement of authorship, each author certifies that:

1. the candidate's stated contribution to the publication is accurate (as detailed above);
2. permission is granted for the candidate to include the publication in the thesis; and
3. the sum of all co-author contributions is equal to 100% less the candidate's stated contribution.

David M. Huang

Assisted with the design of molecular dynamics simulations and revision of the manuscript.

I hereby certify the statement of contribution is accurate.

9/9/15

David M. Huang Date

Matthew R. Hill

Provided assistance with the interpretation of results and revision of the manuscript.

I hereby certifiy the statement of contribution is accurate.

11/9/15

Matthew R. Hill Date

Christopher J. Sumby

Supervised the development of the work, assisting in the interpretation of results and the revision of the manuscript.

I hereby certifiy the statement of contribution is accurate.

9/9/15

Christopher J. Sumby Date

David S. Sholl

Supervised the development of amorphous model generation in addition to revision of the manuscript.

I hereby certify the statement of contribution is accurate.

9/9/15

David S. Sholl Date

Aaron W. Thornton

Supervised the application of amorphous models. Assisted in the conception and revision of the manuscript, acting as corresponding author.

I hereby certifiy the statement of contribution is accurate.

10/9/15

Aaron W. Thornton Date

Christian J. Doonan

Supervised the development of the work, assisting in the interpretation of results. Additionally, aided in the conception and revision of the manuscript, acting as corresponding author.

I hereby certifiy the statement of contribution is accurate.

9/9/2015

Christian J. Doonan Date

Computational Identification of Organic Porous Molecular Crystals

Unpublished and unsubmitted work written in manuscript style

Featured in Chapter 5.

J. D. Evans, D. M. Huang, C. J. Sumby, A. W. Thornton, and C. J. Doonan. "Computational Identification of Organic Porous Molecular Crystals". to be submitted (2015).

Please note that this chapter is yet to be published, however, it is written in the style of a manuscript ready for submission in a peer-reviewed, international journal.

Principal Author

Jack D. Evans (Principal Author, Candidate)

Designed and carried out simulations, analyzed resulting data, interpreted results. In addition to conceiving and preparing the manuscript.

85% Contribution.

This paper reports on original research I conducted during the period of my Higher Degree by Research candidature and is not subject to any obligations or contractual agreements with a third party that would constrain its inclusion in this thesis. I am the primary author of this paper. I hereby certify the statement of contribution is accurate.

9/9/2015

Jack D. Evans Date

Co-Author Contributions

By signing the statement of authorship, each author certifies that:

1. the candidate's stated contribution to the publication is accurate (as detailed above);
2. permission is granted for the candidate to include the publication in the thesis; and
3. the sum of all co-author contributions is equal to 100% less the candidate's stated contribution.

David M. Huang

Assisted with the design of molecular dynamics simulations and revision of the manuscript.

I hereby certifiy the statement of contribution is accurate.

9/9/15

David M. Huang Date

Christopher J. Sumby

Supervised the development of the work, assisting in the interpretation of results and the revision of the manuscript.

I hereby certifiy the statement of contribution is accurate.

9/9/15

Christopher J. Sumby Date

Aaron W. Thornton

Supervised the development of screening methodology. Assisted in the conception and revision of the manuscript, acting as corresponding author.

I hereby certifiy the statement of contribution is accurate.

10/9/15

Aaron W. Thornton Date

Christian J. Doonan

Supervised the development of the work, assisting in the interpretation of results. Additionally, aided in the conception and revision of the manuscript, acting as corresponding author.

I hereby certify the statement of contribution is accurate.

9/9/2015

Christian J. Doonan Date

Bimetallic Metal-organic Polyhedra

Unpublished and unsubmitted research written in conventional thesis chapter style

Featured in Chapter 6.

> J. M. Teo, C. J. Coghlan, J. D. Evans, C. J. Sumby, and C. J. Doonan. "Bimetallic Metal-organic Polyhedra". to be submitted (2015).

Please note that this chapter has been written in the style of a conventional thesis chapter. The work in this chapter has been conceptualized, realized and documented by the author of this thesis. Coworkers have aided by providing experimental samples and experimental results. Parts of this work will be used in a manuscript currently in preparation for submission in a peer-reviewed, international journal.

Principal Author

Jack D. Evans (Principal Author, Candidate)

Designed and carried out the fitting of isotherms and production of isosteric heat data. Subsequently, investigated structures with quantum chemistry routines and interpreted results. In addition to conceiving and preparing the chapter as contained herein.

85% Contribution.

This chapter reports on original research I conducted during the period of my Higher Degree by Research candidature and is not subject to any obligations or contractual agreements with a third party that would constrain its inclusion in this thesis. I am the primary author of this chapter. I hereby certify the statement of contribution is accurate.

9/9/2015

Jack D. Evans — Date

Co-Author Contributions

By signing the statement of authorship, each author certifies that:

1. the candidate's stated contribution to the chapter is accurate (as detailed above);
2. permission is granted for the candidate to include the work in the thesis; and
3. the sum of all co-author contributions is equal to 100% less the candidate's stated contribution.

Jesse M. Teo

Synthesized MOP structures and conducted gas adsorption experiments.

I hereby certifiy the statement of contribution is accurate.

9-9-2015

Jesse M. Teo Date

Campbell J. Coghlan

Supervised and assisted in the synthesis of MOP structures and undertaking of gas adsorption experiments.

I hereby certifiy the statement of contribution is accurate.

9/9/15

Campbell J. Coghlan Date

Christopher J. Sumby

Supervised the development of the work, assisting in the interpretation of results and the revision of the chapter.

I hereby certifiy the statement of contribution is accurate.

9/9/15

Christopher J. Sumby Date

Christian J. Doonan

Supervised the development of the work, assisting in the interpretation of results. Additionally, aided in the revision of the chapter.

I hereby certifiy the statement of contribution is accurate.

9/9/2015

Christian J. Doonan Date

Application of Computational Methods to Experimental Observations

Published and submitted research written in conventional thesis chapter style

Featured in Chapter 7.

A. Avellaneda, P. Valente, A. Burgun, J. D. Evans, A. W. Markwell-Heys, D. Rankine, D. J. Nielsen, M. R. Hill, C. J. Sumby, and C. J. Doonan. "Kinetically Controlled Porosity in a Robust Organic Cage Material". *Angewandte Chemie International Edition* 52.13 (2013), pp. 3746–3749. DOI: 10.1002/anie.201209922.

T. D. Keene, D. Rankine, J. D. Evans, P. D. Southon, C. J. Kepert, J. B. Aitken, C. J. Sumby, and C. J. Doonan. "Solvent-modified dynamic porosity in chiral 3D kagome frameworks". *Dalton Transactions* 42.22 (2013), pp. 7871–7879. DOI: 10.1039/C3DT00096F.

Please note that this chapter has been written in the style of a conventional thesis chapter. The chapter contains an amalgamation of research that has contributed partially to manuscripts that have been published in peer-reviewed, international journals. The author has originally written and constructed this chapter as to highlight the contribution provided to these two manuscripts. Additionally, the original manuscripts are attached.

Principal Author

Jack D. Evans (Principal Author, Candidate)

Designed and carried out the application of classical molecular simulations to provide insight to the diffusion of gases and rotational flexibility. Subsequently, investigated structures with geometric routines and interpreted results. In addition to conceiving and preparing the chapter as contained herein.

This chapter reports on original research I conducted during the period of my Higher Degree by Research candidature and is not subject to any obligations or contractual agreements with a third party that would constrain its inclusion in this thesis. I am the primary author of this chapter. I hereby certify the statement of contribution is accurate.

8/9/2015

Jack D. Evans — Date

Corresponding Author Certification

By signing the statement of authorship, each author certifies that:

1. the candidate's stated contribution to the chapter is accurate (as detailed above);

2. permission is granted for the candidate to include the work in the thesis; and

Christian J. Doonan

Supervised the development of the research and additionally the conception and revision of the manuscript, acting as corresponding author.

I hereby certifiy the statement of contribution is accurate.

9/9/2015

Christian J. Doonan Date

Christopher J. Sumby

Supervised the development of the research and additionally the conception and revision of the manuscript, acting as corresponding author.

I hereby certifiy the statement of contribution is accurate.

9/9/15

Christopher J. Sumby Date

B

Publications

Attached are reprints of publications that constitute part of this thesis, as listed below.

A. Avellaneda, P. Valente, A. Burgun, J. D. Evans, A. W. Markwell-Heys, D. Rankine, D. J. Nielsen, M. R. Hill, C. J. Sumby, and C. J. Doonan. "Kinetically Controlled Porosity in a Robust Organic Cage Material". *Angewandte Chemie International Edition* 52.13 (2013), pp. 3746–3749. DOI: 10.1002/anie.201209922.

T. D. Keene, D. Rankine, J. D. Evans, P. D. Southon, C. J. Kepert, J. B. Aitken, C. J. Sumby, and C. J. Doonan. "Solvent-modified dynamic porosity in chiral 3D kagome frameworks". *Dalton Transactions* 42.22 (2013), pp. 7871–7879. DOI: 10.1039/C3DT00096F.

J. D. Evans, D. M. Huang, M. R. Hill, C. J. Sumby, A. W. Thornton, and C. J. Doonan. "Feasibility of Mixed Matrix Membrane Gas Separations Employing Porous Organic Cages". *The Journal of Physical Chemistry C* 118.3 (2014), pp. 1523–1529. DOI: 10.1021/jp4079184.

J. D. Evans, D. M. Huang, M. R. Hill, C. J. Sumby, D. S. Sholl, A. W. Thornton, and C. J. Doonan. "Molecular Design of Amorphous Porous Organic Cages for Enhanced Gas Storage". *The Journal of Physical Chemistry C* 119.14 (2015), pp. 7746–7754. DOI: 10.1021/jp512944r.

Porous Molecular Solids

DOI: 10.1002/anie.201209922

Kinetically Controlled Porosity in a Robust Organic Cage Material**

Antonio Avellaneda, Peter Valente, Alexandre Burgun, Jack D. Evans, Adrian W. Markwell-Heys, Damien Rankine, David J. Nielsen, Matthew R. Hill, Christopher J. Sumby, and Christian J. Doonan**

Microporous materials are of significant interest owing to their central role in gas storage, separation processes, and catalysis.[1–4] Recently, microporous molecular solids composed of discrete, shape-persistent organic cages have received growing attention[1] because they possess unique properties that set them apart from conventional, extended network materials, such as zeolites,[2] metal–organic frameworks,[3] and covalent organic frameworks.[4] For example, molecular solids are readily solution-processable,[5] provide facile access to multicomponent materials by mix-and-match synthesis,[6] and, by virtue of their noncovalent intermolecular packing, can exhibit advanced properties, such as adsorbate-triggered on/off porosity switching.[7]

Unlike extended networks, where solvent-accessible voids are linked through rigid covalent framework solids composed of discrete organic cages predominantly aggregate by relatively weak dispersion forces. Predicting the crystal structures of such weakly aggregating materials is a long-standing challenge in solid-state chemistry,[8] and is, in this field, inherently coupled to estimating the ultimate porosity of a molecular solid from its building units, as different polymorphs can afford solids with dramatically different surface areas.[9] Accordingly, relatively few examples of porous organic solids have been reported.[1d] Nevertheless, recent work from the laboratories of Cooper and Mastalerz have demonstrated that the porosity of such materials can be modified through crystal engineering strategies and synthetic processing.[5a,10] Herein we describe the synthesis and characterization of a novel, permanently porous, shape-persistent cage molecule (**C1**) that is constructed entirely from thermodynamically robust carbon–carbon bonds and has the molecular formula $C_{112}H_{62}O_2$ (Scheme 1). Furthermore, we demonstrate kinetically controlled access to two crystalline polymorphs **C1α** and **C1β** that possess dramatically different N_2 porosities: polymorph **C1α**, which is nonporous to N_2, and polymorph **C1β**, which affords a BET surface area of 1153 $m^2 g^{-1}$.

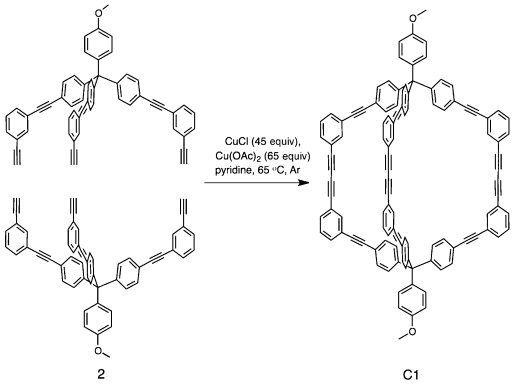

Scheme 1. Procedure for the synthesis of trigonal-prismatic cage **C1**.

Molecule **C1** was synthesized by Eglinton homocoupling of two rigid, alkyne-terminated building units (Scheme 1; **2**). Such reactions, which are often conducted with a stoichiometric excess of copper reagents, have been widely employed in macrocycle synthesis.[11] The cage precursor, compound **2**, can be elaborated from a tripodal building block, 4-[tris(4-iodophenyl)methyl]phenol,[12] by sequential phenol methylation, Sonogashira coupling, and silyl deprotection reactions in 53% yield over three steps.[13] The ultimate homocoupling step proceeds under high-dilution conditions with a large excess of catalyst to maximize the yield of the kinetic product **C1**. The yield of **C1** (20%) is remarkable given the irreversible nature of the bonding involved and the fact that one incorrect bond formation step during cage synthesis will direct the reaction towards the formation of oligomers. No other major products are isolated in this reaction that requires three Eglinton homocoupling reactions. The energy-minimized structure of **C1** is best described as a distorted triangular prism with internal vertical and horizontal diameters of 13.5 Å and 12 Å, respectively.[14]

[*] Dr. A. Avellaneda, Dr. P. Valente, Dr. A. Burgun, J. D. Evans, A. W. Markwell-Heys, D. Rankine, Dr. C. J. Sumby, Dr. C. J. Doonan
School of Chemistry and Physics, The University of Adelaide
Adelaide, South Australia, 5005 (Australia)
E-mail: christian.doonan@adelaide.edu.au
Dr. D. J. Nielsen
Human Protection and Performance Division
Defence Science and Technology Organisation
506 Lorimer St, Fishermans Bend, Victoria, 3207 (Australia)
Dr. M. R. Hill
CSIRO, Materials Science and Engineering
Private Bag 33, Clayton South MDC, Victoria 3169 (Australia)

[**] C.J.D. and C.J.S. would like to acknowledge the Australian Research Council for funding (DP 120103909 (C.J.D.) and FT 100100400 (C.J.D.), and FT0991910 (C.J.S.)). D.J.N. and C.J.D. acknowledge support from the DSTO Fellowship programme. J.D.E. thanks CSIRO Materials Science and Engineering for a top-up Ph.D. scholarship.

Supporting information for this article is available on the WWW under http://dx.doi.org/10.1002/anie.201209922.

© 2013 Wiley-VCH Verlag GmbH & Co. KGaA, Weinheim

The most common strategy used to synthesize organic cages is to employ covalent dynamic imine chemistry to facilitate isolation of the thermodynamic molecular product from a one-step reaction. Inspired by analogous chemistry,[15] we aimed to expand the reaction space of such porous molecular solids by synthesizing a thermodynamically robust shape-persistent cage molecule by homocoupling of a single component. Furthermore, we note that the one-step synthesis of related multicomponent cages may be possible, under such bond-forming conditions, by judicious choice of templating strategies.[16]

The formation of **C1** was confirmed by ^{1}H NMR and ^{13}C NMR spectroscopy, which showed aromatic resonances in the range 7.76–6.85 ppm and a resonance for the methoxy group at 3.83 ppm in the ^{1}H NMR spectrum; these are all consistent with the cage structure.[13] The alkyne proton of **2** is notably absent from the ^{1}H NMR spectrum of **C1**, and electrospray ionization mass spectrometry (ESI-MS) showed a peak for the parent ion at *m*/*z* 1439, which corresponds to [**C1**]H^{+}. Two weak IR bands for the C≡C stretches at 2219 and 2207 cm^{-1} were readily apparent. Bulk samples of **C1** were readily desolvated and stable up to about 400 °C, as determined by concomitant thermal gravimetric analysis–differential scanning calorimetry (TGA-DSC) experiments. It is noteworthy that the DSC trace showed no evidence of chemical transformations below 400 °C. This is quite remarkable given the close proximity of three diyne moieties but points to the overall rigidity and thermal robustness of the structure. **C1** is soluble in common organic solvents, such as chloroform, dichloromethane, and benzene, but insoluble in alcohols, H_2O, and other highly polar solvents.

Large colorless block-shaped crystals of **C1** formed in approximately 24 h from slow evaporation of a dichloromethane/methanol solution of **C1**. The crystal structure of **C1**[17] (Figure 1) closely resembles the energy-minimized structure identified by computational approaches. The vertical and horizontal outer dimensions of **C1** are circa 3.1 nm by 1.6 nm, and these enclose an internal cavity of the dimensions noted. The volume occupied by a cage molecule is about 1300 Å^3. The preorganized tripodal building block adopts the geometry anticipated from initial modeling and structure prediction with angles of 104.1(3)–111.5(3)° around the tetraphenyl carbon atom. The dialkynyl struts are close to linear and all alkyne moieties have the expected bond lengths (in the range 1.171(5)–1.224(5) Å). This single-crystalline polymorph, **C1α**, crystallizes in the orthorhombic space group *Pbcn* with four molecules in the unit cell. Consideration of the packing reveals that the cages pack in a herringbone-type arrangement, if the cages are treated as rods along their long molecular axis. Each individual molecule of **C1** packs closely with four other molecules of **C1** in the same orientation and two sets of four additional cages, with a near-orthogonal direction of their molecular axis, at the poles of the first cage (Figure 1b). This has the effect of placing at least two molecules of **C1** into each window of an individual cage. Owing to the lack of functional groups directing the packing, the primary intercage forces in the crystal packing are van der Waals interactions and edge-to-face π-stacking interactions

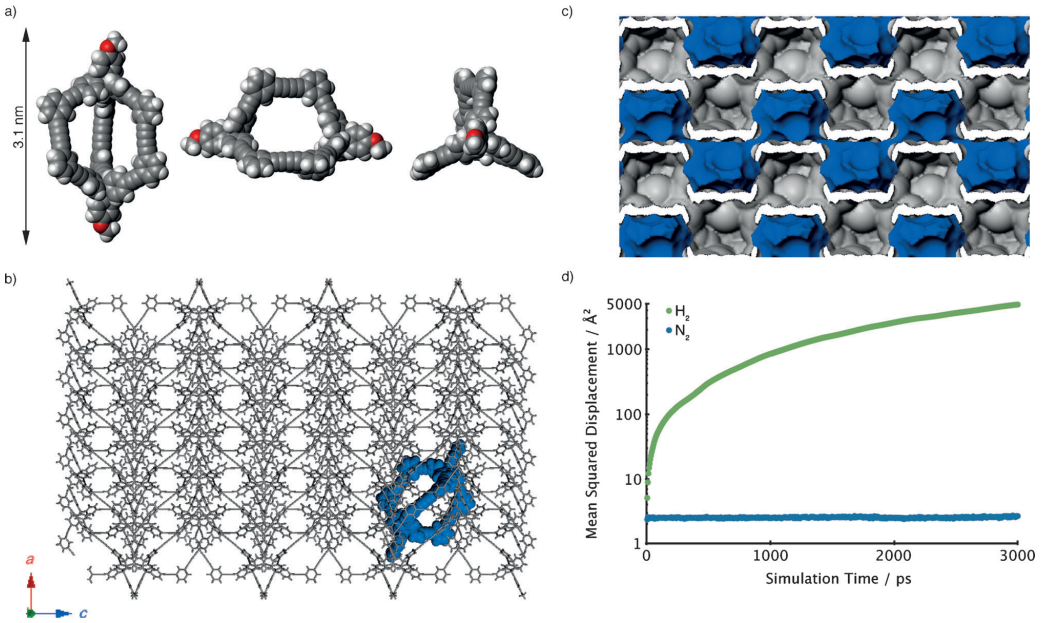

Figure 1. a) Representations of the structure of **C1** and b) wire-framed depiction of the packing of **C1α** down the *b* axis. c) N_2 accessible surface area of **C1α** and d) the simulated mean-squared displacement of N_2 and H_2 through **C1α**.

© 2013 Wiley-VCH Verlag GmbH & Co. KGaA, Weinheim

involving both phenyl and alkyne moieties.[18] The crystals of **C1** contain residual solvent electron density peaks that could not be definitively identified and the SQUEEZE routine of Platon[19] was applied to the collected data.[20] Powder X-ray diffraction (PXRD) was used to confirm that the single crystal structure was representative of the bulk sample and determine that the α polymorph was retained subsequent to evacuation of residual solvent.[13]

The simulated accessible pore space of N_2 displayed in Figure 1c shows that the structure of **C1α** contains one-dimensional channels comprised of adjacent cages connected by windows of about 4 Å. Given that the kinetic diameter of N_2 is 3.64 Å[21] it was expected that that these windows would restrict the diffusion of N_2 through the material. To support this hypothesis we employed molecular dynamics to simulate the diffusion of H_2 and N_2 within the pore structure of **C1α**.[22] This was determined by measuring the mean-square displacement of single N_2 and H_2 molecules for 3 ns after 1 ns of equilibration at 77 K. Figure 1d clearly shows that the motion of N_2 is constrained within polymorph **C1α** while the smaller H_2 is able to diffuse through the structure by the circa 4 Å windows. In accordance with these structure simulations, 77 K N_2 isotherms indicated that activated samples of **C1α** were non-porous to N_2 but porous to H_2, affording a total uptake of approximately 40 $cm^3 g^{-1}$ at 77 K. However, **C1α** can be considered a "soft" porous crystal, and it is plausible that with greater gas loading pressures and temperature, slight structural deformations may allow N_2 to diffuse through the framework.

Rapid precipitation of **C1** was found to reliably form a second, kinetically trapped polymorph **C1β**. Addition of an antisolvent to solutions of **C1** or freeze drying from benzene both form microcrystalline powders with identical PXRD patterns (Figure 2). Upon solvent removal and drying, polymorph **C1β** retains crystallinity and yields a PXRD pattern that corresponds to the solvated forms, indicating structural uniformity subsequent to guest removal. The propensity of **C1** to form a crystalline material following freeze drying is very unusual for porous molecular solids, however, we note that PXRD methods are silent to the presence of an amorphous component. Scanning electron microcoscopy (SEM) indicated that polymorph **C1β** forms thin plate-like crystallites, in contrast to polymorph **C1α** that form block-shaped crystals.[13] This plate-like morphology of the **C1β** polymorph accounts for the broadness of the peaks and weak high-angle diffraction in the PXRD. Our contention that access to crystalline polymorphs **C1α** and **C1β** is a kinetically driven process is supported by PXRD experiments carried out on samples of **C1** generated from supersaturated solutions on a rotary evaporator (Figure 2). Solvent evaporation from a solution of **C1** in dichloromethane gives rise to crystalline solids with PXRD patterns that are consistent with a mixture of both polymorphs. On the qualitative time scales investigated in this work, solvent evaporation (minutes) lies in the intermediate range between single crystal growth by slow evaporation (hours to days) and rapid precipitation (seconds). We acknowledge that exploration of other crystallization techniques, solvent combinations, and temperatures may provide access to additional polymorphs. Nevertheless, we clearly demonstrate predictable and reproducible access to polymorphs **C1α** and **C1β** by simple kinetic control. These observations suggest that crystallization of **C1** follows Ostwald's rule, as **C1β** is kinetically trapped in a metastable crystalline phase that upon dissolution and slow crystallization affords the thermodynamically favored form **C1α**.[23] Although the formation of **C1α** and **C1β** is kinetically driven, variable-temperature PXRD experiments showed no evidence that a thermodynamic phase transition occurs in the solid state.

We assessed the permanent porosity of polymorph **C1β** by first evacuating solvent molecules from its pores (12 hours, 2 μTorr, 298 K) and then measuring a N_2 isotherm at 77 K (Figure 3). The isotherm shape is best described as type 1, which is consistent with pore diameters of less than 2 nm. The slight hysteretic behavior suggests the presence of structural inhomogeneity or poor uniformity in crystal size distribution and this has been observed in other porous molecular solids and flexible metal–organic framework materials.[10a] BET analysis of the isotherm in Figure 3 indicates that **C1β** has a surface area of 1153 $m^2 g^{-1}$. It is noteworthy that surface areas in excess of 1000 $m^2 g^{-1}$ are rare for molecular cages.[1] Additionally, polymorph **C1β** can be dissolved and precipi-

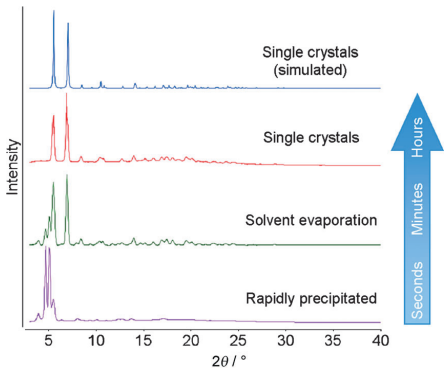

Figure 2. PXRD patterns of desolvated samples of **C1α** (red) and **C1β** (mauve). The green PXRD pattern shows a mixture of polymorphs **C1α**, and **C1β**. The blue arrow on the right of the Figure is a guide for the timescale in which each solid sample was crystallized.

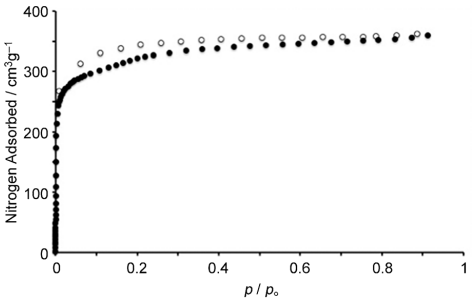

Figure 3. N_2 77 K isotherm of **C1β**. ● adsorption, ○ desorption.

© 2013 Wiley-VCH Verlag GmbH & Co. KGaA, Weinheim

tated several times without diminishing the accessible surface area. These properties highlight the facile processability of **C1**. Pore size distributions calculated by nonlocal density functional theory from the adsorption data shows two main peaks centered at approximately 6 Å and 11 Å. The larger pore size corresponds well to the predicted internal pore diameter of **C1** and the presence of a second pore suggests solvent accessible extrinsic voids. However, in the absence of structural data, the contribution of intrinsic and extrinsic porosity to the total surface area cannot be confirmed.

In summary, we have described the synthesis and characterization of a robust organic cage that is constructed entirely from carbon–carbon bonds. Solids of **C1** can be predictably crystallized by kinetic control into two separate polymorphs **C1α** and **C1β**. Rapid precipitation of **C1** leads to the permanently porous polymorph **C1β**, which has a notably high surface area of $1153\ m^2 g^{-1}$ for a molecular solid; however, slow crystallization methods yield **C1α**, which was found to be nonporous to N_2 gas. Such control of polymorphism is of great interest, as the properties of polymorphic materials can, as in this present case, show remarkable variation. Furthermore, fine control of polymorphism can provide insight into the mechanism of multistage polymorphic transitions from the beginning of crystallization to the formation of stable solids. We are currently investigating if the kinetic trapping methods observed in this work can be generally applied to derivatives of **C1**. Additionally, we are also synthesizing **C1** analogues functionalized with moieties designed to enhance its selective gas adsorption properties.

Received: December 12, 2012
Published online: February 20, 2013

Keywords: cage compounds · crystallization landscapes · kinetic control · polymorphism · porosity

[1] a) J. R. Holst, A. Trewin, A. I. Cooper, *Nat. Chem.* **2010**, *2*, 915; b) A. I. Cooper, *Angew. Chem.* **2011**, *123*, 1028; *Angew. Chem. Int. Ed.* **2011**, *50*, 996; c) M. Mastalerz, *Angew. Chem.* **2010**, *122*, 5164; *Angew. Chem. Int. Ed.* **2010**, *49*, 5042; d) M. Mastalerz, *Chem. Eur. J.* **2012**, *18*, 10082.

[2] M. E. Davis, *Nature* **2002**, *417*, 813.

[3] a) M. Eddaoudi, J. Kim, N. Rosi, D. Vodak, J. Wachter, M. O'Keeffe, O. M. Yaghi, *Science* **2002**, *295*, 469; b) J. L. C. Rowsell, O. M. Yaghi, *Microporous Mesoporous Mater.* **2004**, *73*, 3; c) S. Kitagawa, R. Kitaura, S. Noro, *Angew. Chem.* **2004**, *116*, 2388; *Angew. Chem. Int. Ed.* **2004**, *43*, 2334; d) O. K. Farha, J. T. Hupp, *Acc. Chem. Res.* **2010**, *43*, 1166.

[4] a) A. P. Côté, A. I. Benin, N. W. Ockwig, A. J. Matzger, M. O'Keeffe, O. M. Yaghi, *Science* **2005**, *310*, 1166; b) H. M. El-Kaderi, J. R. Hunt, J. L. Mendoza-Cortés, A. P. Côté, R. E. Taylor, M. O'Keeffe, O. M. Yaghi, *Science* **2007**, *316*, 268; c) F. J. Uribe-Romo, J. R. Hunt, H. Furukawa, C. Klock, M. O'Keeffe, O. M. Yaghi, *J. Am. Chem. Soc.* **2009**, *131*, 4570; d) J. R. Hunt, C. J. Doonan, J. D. LeVangie, A. P. Côté, O. M. Yaghi, *J. Am. Chem. Soc.* **2008**, *130*, 11872; e) F. J. Uribe-Romo, C. J. Doonan, H. Furukawa, K. Oisaki, O. M. Yaghi, *J. Am. Chem. Soc.* **2011**, *133*, 11478.

[5] a) T. Hasell, S. Y. Chong, K. E. Jelfs, D. J. Adams, A. I. Cooper, *J. Am. Chem. Soc.* **2012**, *134*, 588; b) T. Hasell, A. I. Cooper, *Adv. Mater.* **2012**, *24*, 5732.

[6] a) S. Jiang, J. T. A. Jones, T. Hasell, C. E. Blythe, D. J. Adams, A. Trewin, A. I. Cooper, *Nat. Commun.* **2011**, *2*, 207; b) T. Hasell, S. Y. Chong, M. Schmidtmann, D. J. Adams, A. I. Cooper, *Angew. Chem.* **2012**, *124*, 7266; *Angew. Chem. Int. Ed.* **2012**, *51*, 7154.

[7] J. T. A. Jones, D. Holden, T. Mitra, T. Hasell, D. J. Adams, K. E. Jelfs, A. Trewin, D. J. Willock, G. M. Day, J. Bacsa, A. Steiner, A. I. Cooper, *Angew. Chem.* **2011**, *123*, 775; *Angew. Chem. Int. Ed.* **2011**, *50*, 749.

[8] G. R. Desiraju, *Nat. Mater.* **2002**, *1*, 77.

[9] T. Tozawa, J. T. A. Jones, S. I. Swamy, S. Jiang, D. J. Adams, S. Shakespeare, R. Clowes, D. Bradshaw, T. Hasell, S. Y. Chong, C. Tang, S. Thompson, J. Parker, A. Trewin, J. Basca, A. M. Z. Slawin, A. Steiner, A. I. Cooper, *Nat. Mater.* **2009**, *8*, 973.

[10] a) M. J. Bojdys, M. E. Briggs, J. T. A. Jones, D. J. Adams, S. Y. Chong, M. Schmidtmann, A. I. Cooper, *J. Am. Chem. Soc.* **2011**, *133*, 16566; b) M. W. Schneider, I. M. Oppel, H. Ott, L. G. Lechner, H.-J. S. Hauswald, R. Stoll, M. Mastalerz, *Chem. Eur. J.* **2012**, *18*, 836.

[11] a) J. J. Li, *Name Reactions: A Collection of Detailed Mechanisms and Synthetic Applications*, Springer, Berlin, **2009**; b) H. A. Stefani, A. S. Guarezemini, R. Cella, *Tetrahedron* **2010**, *66*, 7871.

[12] M. E. Gallina, B. Baytekin, C. Schalley, P. Ceroni, *Chem. Eur. J.* **2012**, *18*, 1528.

[13] See the Supporting Information for full experimental details.

[14] The structure of **C1** was optimized to B3LYP/6-31G(d,p) theory with default convergence criteria. The vertical diameter was measured between the two sp^3 carbon atoms of the cage framework and the horizontal diameter was defined as twice the average distance between the cage centroid and the diyne moiety. Full reference to these methods is in the Supporting Information.

[15] a) C. Zhang, C.-F. Chen, *J. Org. Chem.* **2007**, *72*, 9339; b) C. Zhang, Q. Wang, H. Long, W. Zhang, *J. Am. Chem. Soc.* **2011**, *133*, 20995.

[16] a) R. L. E. Furlan, S. Otto, J. K. M. Sanders, *Proc. Natl. Acad. Sci. USA* **2002**, *99*, 4801; b) C. D. Meyer, C. S. Joiner, J. F. Stoddart, *Chem. Soc. Rev.* **2007**, *36*, 1705.

[17] Selected data for **C1**: $C_{112}H_{62}O_2$, M_r 1439.72, $T = 150(2)$ K, orthorhombic, *Pbcn*, $\alpha = 31.9812(14)$, $\beta = 18.5193(8)$, $\gamma = 20.3265(7)$ Å, $V = 12038.8(8)$ Å^3, $Z = 4$, $\rho_{calc.} = 0.794\ Mg\,m^{-3}$, $\mu = 0.046\ mm^{-1}$, $F(000)$ 3000, colorless block, $0.33 \times 0.31 \times 0.06\ mm^3$, 56266 reflections collected, 14052 independent reflections [$R_{int} = 0.1347$], completeness 99.9%, data/restraints/parameters 14052/0/515, GOF 0.871, $R_1 = 0.0888$, $wR_2 = 0.2291$, (all data: $R_1 = 0.2581$, $wR_2 = 0.2839$). CCDC 913184 contains the supplementary crystallographic data for this paper. These data can be obtained free of charge from The Cambridge Crystallographic Data Centre via www.ccdc.cam.ac.uk/data_request/cif.

[18] S. Dawn, M. B. Dewal, D. Sobransingh, M. C. Paderes, A. C. Wibowo, M. D. Smith, J. A. Krause, P. J. Pellechia, L. S. Shimizu, *J. Am. Chem. Soc.* **2011**, *133*, 7025.

[19] A. L. Spek, *Acta Crystallogr. Sect. D* **2009**, *65*, 148.

[20] The SQUEEZE routine of PLATON was applied to the collected data, which resulted in significant reductions in R_1 and wR_2 and an improvement in the GOF. R_1, wR_2 and GOF before SQUEEZE routine: 18.6%, 52.4% and 1.22; after SQUEEZE routine: 8.88%, 28.4% and 0.87.

[21] L. M. Robeson, *J. Membr. Sci.* **1991**, *62*, 165–185.

[22] T. X. Nguyen, S. K. Bhatia, *J. Phys. Chem. C* **2007**, *111*, 2212.

[23] T. Threlfall, *Org. Process Res. Dev.* **2003**, *7*, 1017.

 © 2013 Wiley-VCH Verlag GmbH & Co. KGaA, Weinheim

Dalton Transactions

An international journal of inorganic chemistry

www.rsc.org/dalton

Volume 42 | Number 22 | 14 June 2013 | Pages 7825–8148

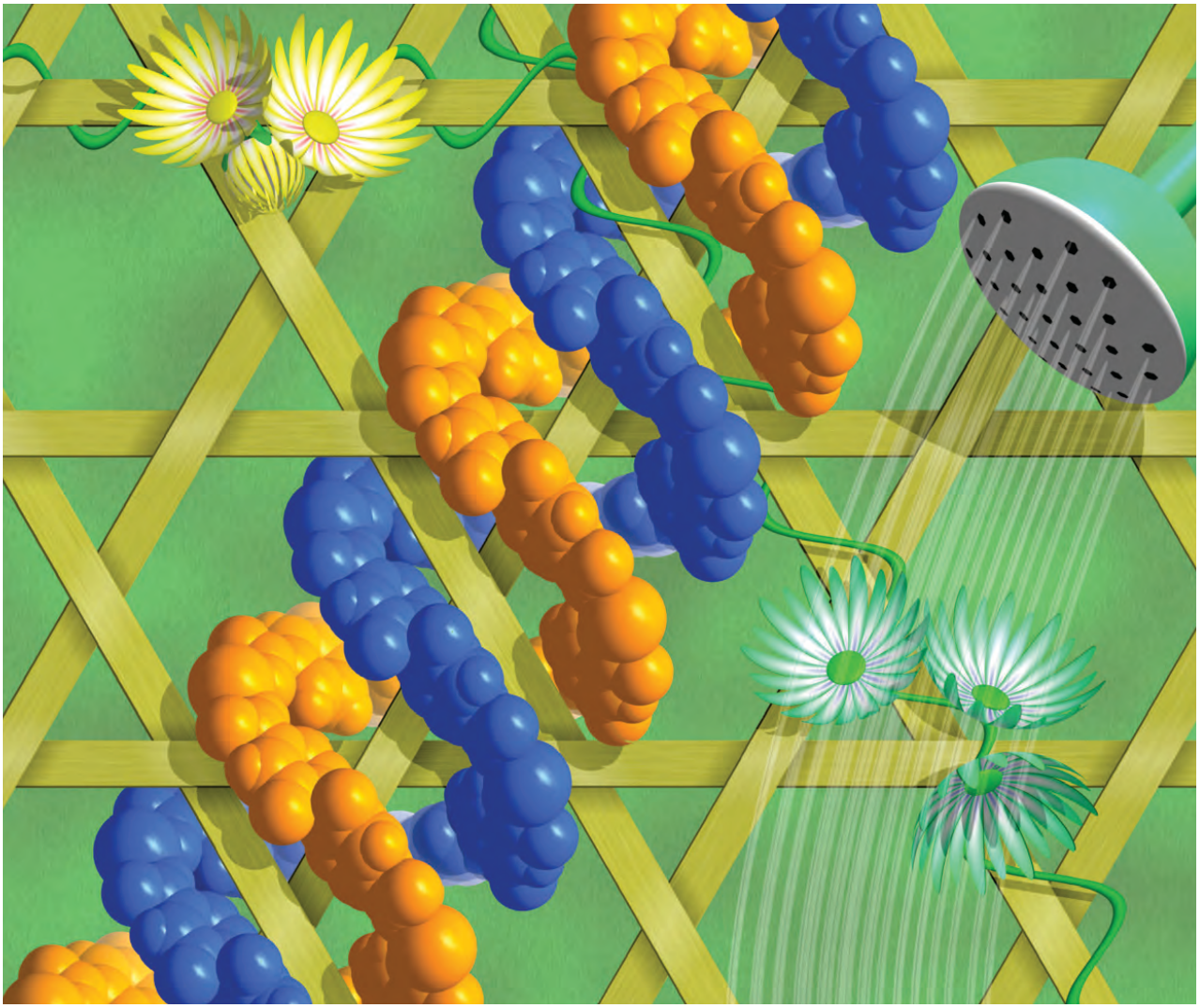

ISSN 1477-9226

RSC Publishing

COVER ARTICLE

Sumby, Doonan *et al.*

Solvent-modified dynamic porosity in chiral 3D kagome frameworks

Dalton Transactions

RSC Publishing

PAPER

View Article Online
View Journal | View Issue

Published on 14 February 2013. Downloaded by UNIVERSITY OF ADELAIDE on 09/09/2015 06:01:02.

Cite this: *Dalton Trans.*, 2013, **42**, 7871

Solvent-modified dynamic porosity in chiral 3D kagome frameworks†

Tony D. Keene,‡[a] Damien Rankine,[a] Jack D. Evans,[a] Peter D. Southon,[b] Cameron J. Kepert,[b] Jade B. Aitken,[b,c,d] Christopher J. Sumby*[a] and Christian J. Doonan*[a]

Received 11th January 2013,
Accepted 13th February 2013

DOI: 10.1039/c3dt00096f

www.rsc.org/dalton

Dynamically porous metal-organic frameworks (MOFs) with a chiral quartz-based structure have been synthesized from the multidentate ligand 2,2′-dihydroxybiphenyl-4,4′-dicarboxylate (H_2diol). Compounds [Ni(II)(H_2diol)$(S)_2$]·xS (where S = DMF or DEF) show marked changes in 77 K N_2 uptake between partially desolvated [Ni(II)(H_2diol)$(S)_2$] (only the pore solvent is removed) and fully desolvated [Ni(II)(H_2diol)] forms. Furthermore, [Ni(II)(H_2diol)$(DMF)_2$] displays additional solvent-dependent porosity through the rotation of DMF molecules attached to the axial coordination sites of the Ni(II) centre. A unique feature of the four coordinate Ni(II) centre in [Ni(II)(H_2diol)] is the dynamic response to its chemical environment. Exposure of [Ni(II)(H_2diol)] to H_2O and MeOH vapour leads to coordination of both axial sites of the Ni centres and to the generation of a solvated framework, whereas exposure to EtOH, DMF, acetone, and MeCN does not lead to any change in metal coordination or structure metrics. MeOH vapour adsorption was able to be tracked by time-dependent magnetometry as the solvated and desolvated structures have different magnetic moments. Solvated and desolvated forms of the MOF show remarkable differences in their thermal expansivities; [Ni(II)(H_2diol)$(DMF)_2$]·DMF displays marked positive thermal expansion (PTE) in the *c*-axis, yet near to zero thermal expansion, between 90 and 450 K, is observed for [Ni(II)(H_2diol)]. These new MOF architectures demonstrate a dynamic structural and colourimetric response to selected adsorbates *via* a unique mechanism that involves a reversible change in the coordination environment of the metal centre. These coordination changes are mediated throughout the MOF by rotational mobility about the biaryl bond of the ligand.

1. Introduction

Metal-organic frameworks have received significant attention due to their potential application to areas such as chemical sensing,[1] heterogeneous catalysis[2] and carbon capture.[3] The modular approach to MOF synthesis allows the pore architectures to be precisely controlled through judicious choice of the organic link. For example, rigid linkers, such as terephthalate, commonly lead to thermally robust materials with exceptionally high surface areas and a monodisperse pore size distribution.[4,5] Conversely, flexible links can give rise to materials that demonstrate crystal-to-crystal 'breathing' and complex adsorption effects such as gating, and sensing, where the MOF responds to the nature and/or pressure of the adsorbate.[6] Link-derived dynamic behaviour necessitates careful control of the flexibility of the ligand;[7] thus links with limited degrees of freedom have most successfully been employed in the synthesis of dynamic MOFs. Framework flexibility derived from both the link[6e,7] and the metal node has been extensively studied.[8–10] For example, Cr-MIL-53 displays reversible solvent-induced porosity switching, becoming non-porous on solvation with water,[9] while CPL-2 shows reversible binding of absorbate molecules onto a bare Cu site that is released by framework contraction.[10] The integration of materials displaying advanced framework flexibility with electronically or magnetically responsive SBUs underlies one approach to sense and respond to small molecule adsorbents.[11]

Here we describe the synthesis of a series of novel MOFs that are constructed from a multidentate organic link 2,2′-dihydroxybiphenyl-4,4′-dicarboxylate composed of carboxylate and phenol donor moieties.[12] This organic building block

[a]*School of Chemistry and Physics, The University of Adelaide, SA 5005, Australia. E-mail: christian.doonan@adelaide.edu.au, christopher.sumby@adelaide.edu.au; Fax: +61 8 8313 4358; Tel: +61 8 8313 5770, +61 8 8313 7406*
[b]*School of Chemistry, The University of Sydney, NSW 2006, Australia*
[c]*Institute of Materials Structure Science, KEK, Tsukuba, Ibaraki 305-0801, Japan*
[d]*Australian Synchrotron, Clayton, Victoria 3168, Australia*

†Electronic supplementary information (ESI) available. CCDC 915130 and 915131. For ESI and crystallographic data in CIF or other electronic format see DOI: 10.1039/c3dt00096f

‡Present address: School of Chemistry, University of Southampton, University Road, Southampton, SO17 1BJ, UK.

This journal is © The Royal Society of Chemistry 2013

Published on 14 February 2013. Downloaded by UNIVERSITY OF ADELAIDE on 09/09/2015 06:01:02.

incorporates rotational mobility about the biaryl bond, along with an essentially inflexible biphenyl backbone. These design features lead to the generation of a series of MOFs that demonstrate dynamic responses to selected adsorbates *via* a unique mechanism that involves a concomitant change in the coordination environment of the metal node and rotation of the organic link. Such properties are desirable for many applications such as chemical sensing and controlled capture and release.

2. Results and discussion

Synthesis and crystal structures

Crystals of $[Ni(H_2diol)(S)_2]\cdot yS$, where S = *N,N′*-dimethylformamide (DMF) or *N,N′*-diethylformamide (DEF), were synthesized by reacting 2,2′-dihydroxybiphenyl-4,4′-dicarboxylic acid (H_4diol) and $Ni(NO_3)_2\cdot 6H_2O$ in DMF or DEF at 85 °C. Slightly greater than 0.5 equivalents of 1,4-diazabicyclo[2.2.2]-octane (DABCO) was added as a base to these reactions. $[Ni(H_2diol)(DMF)_2]\cdot$DMF presents a quartz-like 3D kagome structure (Fig. 1). $[Ni(H_2diol)(DMF)_2]\cdot$DMF crystallises as green prisms (Fig. 1b) in an enantiomorphic space group pair ($P3_121$ and $P3_221$), resulting in double-helical pores in the *c*-axis that are connected to neighbouring channels to form the 3D structure. While individual crystals are chiral the bulk sample is formed as a racemic mixture. The asymmetric unit consists of one Ni(II) ion on a rotation axis, half of a H_2diol unit and one DMF molecule. Bond valence sum analysis confirms that the Ni ion is in the 2+ state. The coordination sphere around the Ni(II) ion is very close to octahedral (ESI, Fig. S4.1 and S4.2†) with a narrow range of O–Ni–O angles of approximately 90°. The hydroxy and carboxylate oxygen atoms of the Ni(II) centre define a local *xy* plane (small deviations of 0.0558 and 0.0276 Å, respectively) with DMF molecules occupying the local *z*-axis. Chirality in these MOFs comes from the twist in the C–C bond between the two phenyl rings in the H_2diol, despite the H_2diol being non-chiral itself. Results from SQUEEZE[13] show one pore positioned at 0,0,0 with the equivalent of 3 × DMF per unit cell, thus one per formula unit (128 e^- for $[Ni(H_2diol)(DMF)_2]\cdot$DMF). The structure of $[Ni(H_2diol)(DEF)_2]\cdot 1/3$DEF is essentially the same, except the DMF is replaced by DEF, which is disordered over two conformations. SQUEEZE shows one pore DEF per unit cell.

A notable feature of the structure of $[Ni(H_2diol)(DMF)_2]\cdot$DMF, (and the $[Ni(H_2diol)(DEF)_2]\cdot 1/3$DEF analogue) is that the carbonyl, not the hydroxyl group of the acid is coordinated to the metal centre. The C–O bond lengths for the coordinated oxygen are 1.243(3) (DMF solvate) and 1.239(8) Å (DEF solvate), while those for the non-coordinated oxygen are 1.282(3) and 1.285(9) Å. These compare with average C–O(–Ni) and C–O bond lengths of 1.23 and 1.29 Å, respectively, for the handful of examples of this bonding motif reported in the Cambridge Structural Database (taken from a search of the Cambridge Structural Database version 5.33, November 2011, plus 3 updates, accessed 13/12/2012). This coordination mode is supported by examination of the IR spectra for the as-synthesised MOFs, which reveals that the C=O stretch is in the range 1645–1655 cm^{-1} compared to the free ligand (1681 cm^{-1}). Additionally, close analysis of the structures indicates that there is a strong hydrogen bond between the phenolic hydroxyl of the H_2diol and the carboxylate oxygen of a neighbouring ligand, in a similar manner to carboxylic acid pairings.[14] The very strong hydrogen bond is probably an important factor in the stability of this framework to both multiple desorption/re-adsorption processes and to high temperatures, as outlined below.

Bulk samples of $[Ni(H_2diol)(DMF)_2]\cdot$DMF and $[Ni(H_2diol)(DEF)_2]\cdot 1/3$DEF were analysed by powder X-ray diffraction (PXRD). The peak positions and relative intensities show excellent agreement with the single crystal structure cell data, thus confirming crystalline phase purity (ESI, Fig. S4.4 and S4.5†).

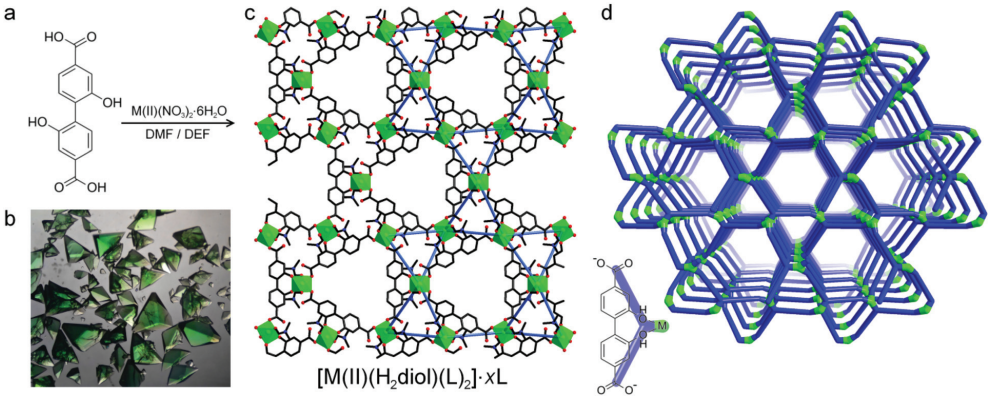

Fig. 1 (a) The synthesis of frameworks $[Ni(H_2diol)(DMF)_2]\cdot$DMF and $[Ni(H_2diol)(DEF)_2]\cdot 1/3$DEF from nickel(II) nitrate salts and 2,2′-dihydroxybiphenyl-4,4′-dicarboxylic acid (H_4diol). (b) Crystals of $[Ni(H_2diol)(DMF)_2]\cdot$DMF. (c) Structural and (d) topological representations of the kagome network in $[Ni(H_2diol)(S)_x]\cdot yS$.

 This journal is © The Royal Society of Chemistry 2013

Published on 14 February 2013. Downloaded by UNIVERSITY OF ADELAIDE on 09/09/2015 06:01:02.

Table 1 Unit cell parameters taken from single crystal data (SCD) at 150 K and Le Bail fitting of the PXRD data at room temperature

Compound	Source	a/Å	c/Å	V/Å^3
[Ni(H$_2$diol)(DMF)$_2$]·DMF	SCD[a]	17.2139(3)	8.5240(5)	2187.42(14)
[Ni(H$_2$diol)(DMF)$_2$]·DMF	SCD[b]	17.149(7)	8.839(5)	2251(3)
[Ni(H$_2$diol)(DMF)$_2$]	Le Bail	17.1362	9.199	2339.4
[Ni(H$_2$diol)]	Le Bail	17.3614	8.5170	2137.6
[Ni(H$_2$diol)(DEF)$_2$]·1/3DEF	SCD[a]	17.3278(4)	9.1188(3)	2371.13(11)
[Ni(H$_2$diol)(DEF)$_2$]	Le Bail	17.3614	9.3559	2442.2

[a] Data collection conducted at 150 K. [b] Unit cell determination conducted at 290 K.

Unit cell parameters of the single crystal data (at 150 and 290 K) and Le Bail refinement of the PXRD data are given in Table 1.

Thermal structural properties

Thermal gravimetric analysis performed on as-synthesized samples of [Ni(H$_2$diol)(DMF)$_2$]·DMF (ESI, Fig. S6.3†) showed three distinct weight loss processes at 420 K, 490 K and 620 K, representing the loss of pore DMF, coordinated DMF and decomposition of the framework, respectively. Removal of the guest DMF and DEF molecules from the pores of [Ni(H$_2$diol)(DMF)$_2$]·DMF and [Ni(H$_2$diol)(DEF)$_2$]·1/3DEF was achieved by initial solvent exchange with CH_2Cl_2 followed by heating at 50 °C (4 h at 3 μbar) to produce [Ni(H$_2$diol)(DMF)$_2$ and [Ni(H$_2$diol)(DEF)$_2$]. Fully desolvated samples were prepared by exchanging DMF with MeOH and heating at 75 °C (4 h at 3 μbar) to produce [Ni(H$_2$diol)].

The permanent porosity of [Ni(H$_2$diol)(DMF)$_2$] and [Ni(H$_2$diol)(DEF)$_2$] was ascertained by performing N_2 adsorption isotherms at 77 K (Fig. 2). The isotherms of both materials are best described as type I and BET analysis (ESI, Fig. S5.5 and S5.6, Table S4†) gives surface areas of 733 and 767 m^2 g^{-1} for [Ni(H$_2$diol)(DMF)$_2$] and [Ni(H$_2$diol)(DEF)$_2$]. Interestingly, the isotherm of [Ni(H$_2$diol)(DMF)$_2$] displays a prominent shoulder in the low pressure region p/p_0 = 0.001 to 0.05, which is reproducible over multiple samples (Fig. 2, inset).

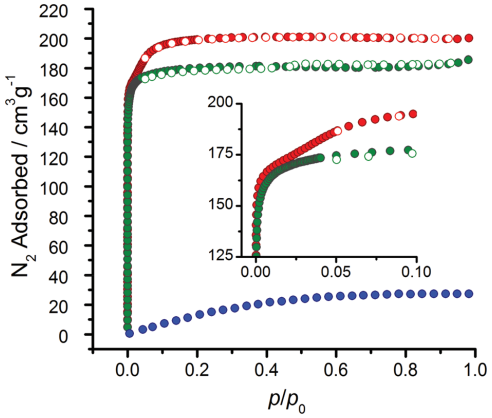

Fig. 2 N_2 adsorption isotherms at 77 K for [Ni(H$_2$diol)(DMF)$_2$] (red), [Ni(H$_2$diol)(DEF)$_2$] (green) and [Ni(H$_2$diol)] (blue). Inset: An enlargement of the prominent linear feature in the low pressure region p/p_0 = 0.001 to 0.05 for [Ni(H$_2$diol)(DMF)$_2$] and the corresponding region for [Ni(H$_2$diol)(DEF)$_2$]. Filled and open circles represent adsorption and desorption points, respectively.

Modelling the structure of [Ni(H$_2$diol)(DMF)$_2$] suggests that the shoulder in the 77 K N_2 adsorption isotherm is due to rotation of the DMF molecules on the Ni centre.[15] By stepping the rotation of the DMF molecules in 10° increments with respect to the O3*ii*–Ni1–O21–C31 torsion angle, we observe a reasonable fluctuation in simulated surface area (Fig. 3). The calculated global energy minimum occurs at 10° (with 0° being the position seen in the crystal structure of [Ni(H$_2$diol)(DMF)$_2$]) and results in a calculated surface area of 1068 m^2 g^{-1}. A local minimum occurs at ~180° with a lower surface area and a moderately small energy barrier between the two conformations. Given the low energy barrier to rotation of the DMF, it is likely that the two DMF energy minima positions are almost equally populated and that the shoulder begins at saturation of the lower surface area form. It is likely that rotation of the DMF molecules is mediated by loading of N_2 gas as the isotherm progresses through the low pressure region. As the DMF molecules rotate, further pore volume is opened, which is then filled, locking the DMF into the energy minimum at 10°. The calculated energy against rotation of [Ni(H$_2$diol)(DEF)$_2$] shows two almost equal minima with large energy barriers that almost certainly precludes rotation of the coordinated DEF. Consequently, [Ni(H$_2$diol)(DEF)$_2$] shows a typical type I isotherm (Fig. 2, inset) without a shoulder as a result of this rotational locking.

MOF materials with coordinatively unsaturated metal sites have shown remarkable gas separation properties[16] and have been effectively utilised as Lewis acid catalysts.[2,17] Accordingly, the coordinated DMF molecules were removed from the metal centres by immersing the MOF in MeOH to afford [Ni(H$_2$diol)(MeOH)$_2$]·2MeOH. Heating [Ni(H$_2$diol)(MeOH)$_2$]·2MeOH at 75 °C under vacuum resulted in abrupt colour change from light green to mustard yellow. This can be attributed to a change in coordination sphere of the Ni(II) centre. As discussed in further detail below, single crystal data on the fully desolvated form could not be obtained and thus a number of techniques were employed to probe the coordination geometry of the Ni(II) centre. We discounted the possibility of an

Published on 14 February 2013. Downloaded by UNIVERSITY OF ADELAIDE on 09/09/2015 06:01:02.

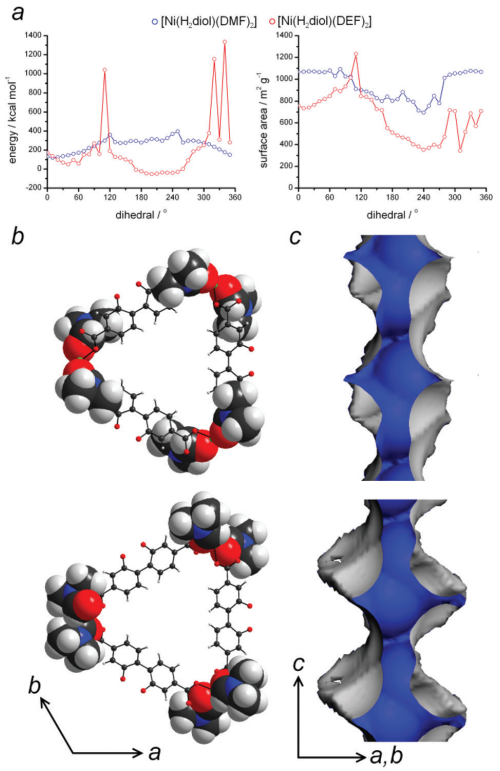

Fig. 3 (a) Calculated global energies for [Ni(H_2diol)(DMF)$_2$] and [Ni(H_2diol)-(DEF)$_2$] and their corresponding surface areas as the coordinated solvents are rotated with respect to the O3*ii*–Ni1–O21–C31 torsion angle. (b) The positions of the DMF molecules in the maximum and minimum surface area arrangements and (c) the N_2 pore surface arising from these conformations.

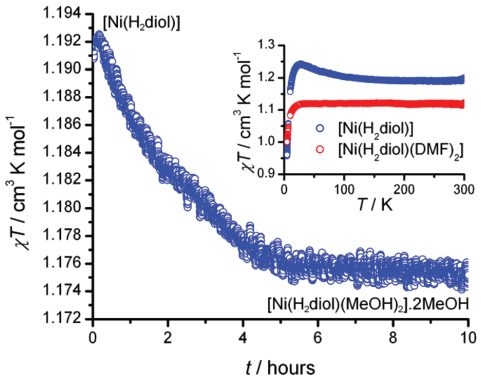

Fig. 4 Time-dependent magnetometry for resolvation of [Ni(H_2diol)] with methanol at 273 K. Inset: Temperature-variable magnetic moments for [Ni(H_2diol)(DMF)$_2$] and [Ni(H_2diol)].

octahedral geometry being maintained for the Ni(II) by contraction or distortion of the framework, allowing a carboxylate oxygen atom from the metals above and/or below to twist and move to fill the axial coordination sites. This would require (i) an approximate 7.4 Å shift of the oxygen atoms; (ii) that the hydrogen bonding that stabilises the coordination around metal is broken; and (iii) an unattainable twist around the biaryl bond given the fact that the diol is chelating. We also dismissed the chelation of the Ni(II) centre by the two coordinated carboxylates on the basis of points (ii) and (iii). Furthermore, we note that the colour is inconsistent with an octahedral species.[18] Thus, we considered a change from octahedral to either 4-coordinate square planar or distorted tetrahedral as likely possibilities upon desolvation. A change to a distorted tetrahedral coordination environment was supported by X-ray absorption near edge spectroscopy (XANES). The Ni(II) XANES spectrum is very sensitive to co-ordination geometry. In particular the absorption edge of square planar Ni(II) is distinctly different to Ni(II) in octahedral and tetrahedral environments.[19] The near edge region of the [Ni(H_2diol)-(DMF)$_2$] and [Ni(H_2diol)] spectra are very similar (ESI, Fig. S6.1†) and do not display the features of a square planar geometry. The small feature at ~8333 eV in both spectra is due to the electronically forbidden 1s–3d transition. Moving from a centrosymmetric O_h to a non-centrosymmetric T_d geometry will give rise to greater mixing of p character into the 3d orbitals, and result in an increased intensity in this pre-edge feature. Peak fitting and integration shows a small increase in the integrated intensity of this peak for the [Ni(H_2diol)]; however, from these data alone it is difficult to precisely assign the geometry as T_d.

Further confirmation of a geometric rearrangement around the Ni centre was afforded from temperature dependent magnetometry experiments. [Ni(H_2diol)] shows a temperature-variable magnetic moment on cooling from 300 K to 2 K with a moment larger than that of [Ni(H_2diol)(DMF)$_2$] (Fig. 4, inset). Given that square planar Ni(II) would be diamagnetic, the combined results of the magnetism and XANES suggest that the Ni(II) ion in [Ni(H_2diol)] is distorted from square planar, but is not ideally tetrahedral. The magnetic properties of [Ni(H_2diol)(DMF)$_2$] are interesting in that the usual coordination sphere of a four-coordinate Ni(II) ion is square planar and thus diamagnetic due to the resolution of the e_g orbital set into its component orbitals with a large energy gap. Tetrahedral Ni(II) is a less common state, usually driven by bulky ligands, but is paramagnetic. Bridgeman[20] recently demonstrated that there are certain ligand spheres that can cause square planar Ni(II) to be paramagnetic while showing similar optical properties to diamagnetic Ni(II). The ligand sphere in this particular case does not support this and the lack of a characteristic XANES pre-edge feature for square planar Ni(II) is also indicative of a non-square planar coordination sphere. In the MOF, the H_2diol ligand is capable of rotation, but to do so to the extent required for a tetrahedral coordination sphere would break up the hydrogen bonding of the alcohols and

This journal is © The Royal Society of Chemistry 2013

Published on 14 February 2013. Downloaded by UNIVERSITY OF ADELAIDE on 09/09/2015 06:01:02.

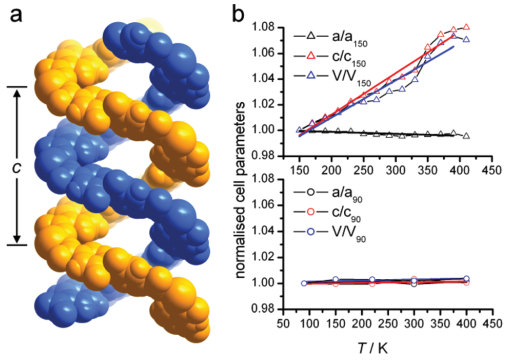

Fig. 5 (a) The helical twist along the *c*-axis pore that gives rise to the high PTE for $[Ni(H_2diol)(DMF)_2]\cdot DMF$. (b) Plots of the cell parameters for $[Ni(H_2diol)(DMF)_2]\cdot DMF$ (normalised for 150 K) and $[Ni(H_2diol)]$ (normalised for 90 K).

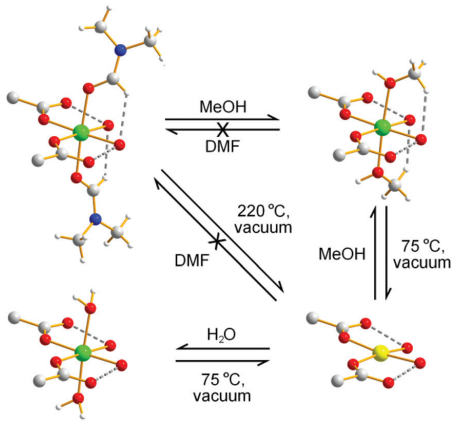

Fig. 6 The dynamic solvent responsive behaviour of $[Ni(H_2diol)(DMF)_2]\cdot DMF$ and its apohost $[Ni(H_2diol)]$. The structure of $[Ni(H_2diol)(DMF)_2]$ is taken from the single crystal structure but the remaining images are cartoon representations.

carboxylate, leading to a less stable framework. It is thus likely that the coordination sphere of Ni in $[Ni(H_2diol)(DMF)_2]$ is intermediate between the two geometries.

The permanent porosity of the fully desolvated material $[Ni(H_2diol)]$ was assessed by collecting 77 K N_2 adsorption isotherm data. Fig. 2 shows that subsequent to full desolvation, $[Ni(H_2diol)]$ loses microporosity yielding a linear N_2 uptake of around 25 $cm^3\ g^{-1}$ at 1 bar. To ascertain the origin of the observed dramatic porosity change upon complete desolvation, variable temperature diffraction experiments were carried out. Unit cells for single crystals of $[Ni(H_2diol)(DMF)_2]\cdot DMF$ were determined at 20 K intervals between 150 and 420 K to investigate the change in cell parameters between the various solvation states. Between 150 and 400 K (Fig. 5b, top), a marked positive thermal expansion (PTE) in the *c*-axis was seen (coefficient of thermal expansion, CTE = $+323(20) \times 10^{-6}\ K^{-1}$) and a small negative thermal expansion was seen in the *a*-axis (CTE = $-16(6) \times 10^{-6}\ K^{-1}$). The high CTE of the *c*-axis drives the PTE of the volume (CTE = $290(24) \times 10^{-6}\ K^{-1}$), comparable to high-expansion materials such as petrol. These unit cell changes are reflected in the MOF by an increase in the helical twist along the *c*-axis (Fig. 5a). Above 420 K, the diffraction was too weak to reliably determine the unit cell, indicating that loss of pore DMF was adversely affecting the stability of the single crystals. As such, attempts to completely desolvate single crystals to obtain the structure were unsuccessful. Despite losing its monocrystallinity, $[Ni(H_2diol)]$ obtained through heating is still crystalline (ESI, Fig. S4.6†). A Le Bail fit of the PXRD data showed a ~6% contraction of the unit cell when compared to $[Ni(H_2diol)(DMF)_2]\cdot DMF$ at 298 K. $[Ni(H_2diol)]$ shows near to zero thermal expansion between 90 and 450 K (Fig. 5b, bottom) with a volume CTE of $8(5) \times 10^{-6}\ K^{-1}$. It is noteworthy that the coincidental contraction of the *c*-axis to approximately half the *a*-axis results in substantial peak overlap and renders full structural refinement unworkable.

Dynamic solvent responsive behaviour of $[Ni(H_2diol)]$

Given that these kagome frameworks are structurally dynamic we investigated their response to a series of adsorbates (Fig. 6). Exposure of $[Ni(H_2diol)]$ to MeOH resulted in a structural rearrangement to the solvated form, $[Ni(H_2diol)(MeOH)_2]\cdot 2MeOH$. This process was tracked by time-dependent magnetometry (Fig. 4) as $[Ni(H_2diol)]$ possesses a larger molar magnetic moment at 273 K than $[Ni(H_2diol)(MeOH)_2]\cdot 2MeOH$ (calculated g = 2.19 and 2.17, respectively). Full resolvation with MeOH was complete in 8 h whereupon the sample changed from yellow to green, consistent with re-establishing an octahedral coordination sphere.

$[Ni(H_2diol)]$ can also be resolvated with water vapour. A 298 K H_2O isotherm (ESI, Fig. S5.2†) was collected and showed an uptake at saturation of 9 mol mol^{-1} at $p/p_0 = 0.914$ with long equilibration times and a large hysteresis. Heating $[Ni(H_2diol)(H_2O)_2]\cdot 7H_2O$ samples to 75 °C under 3 μbar removes all the water, as does heating to 125 °C at 1 bar and this process can be cycled several times with only a negligible change in the uptake capacity (ESI, Fig. S6.4†). Non-coordinating solvents can also adsorb into the pores. For example, rapid uptake of CH_2Cl_2 is observed by addition of 1 mL of CH_2Cl_2 to a 10 mg sample of $[Ni(H_2diol)]$. The sample initially floats (d $[Ni(H_2diol)]$ = 0.77 g cm^{-3}, d CH_2Cl_2 = 1.33 g cm^{-3}), but sinks within seconds, indicating uptake of the solvent into the pores.

The small pore in $[Ni(H_2diol)]$ allows for highly selective size-dependent solvent reabsorption onto the metal centres. H_2O vapour and liquid methanol are slowly taken up onto the metal centre (as seen from the colour change from yellow to green), while EtOH, MeCN, acetone and *n*-butanol do not bind to the metal, although they are absorbed into the pores as seen by the compound sinking in each solvent (d =

Published on 14 February 2013. Downloaded by UNIVERSITY OF ADELAIDE on 09/09/2015 06:01:02.

0.786–0.944 g cm^{-1} compared to [Ni(H_2diol)] d = 0.77 g cm^{-1}). This size selectivity likely stems from the narrow gap between turns of the double-helix pore which only allows access to the metal ions to small molecules. Interestingly, DMF is not re-adsorbed onto the metal: a sample left in DMF for ten weeks showed no change in colour, despite as-synthesised [Ni(H_2diol)(DMF)$_2$]·DMF having two DMF molecules coordinating the Ni atom. A sample of [Ni(H_2diol)] was also MeOH-exchanged and then stood in DMF, but TGA analysis, which has distinctive thermogravimetric behaviour for each solvated form of [Ni(H_2diol)(S)$_2$] (S = H_2O, MeOH, DMF), shows no weight loss consistent with DMF being coordinated to the metal (ESI, Fig. S6.5†).

Discussion

Selective desolvation of [Ni(H_2diol)(DMF)$_2$]·DMF gives rise to dramatically different adsorption behaviour. Partially desolvated [Ni(H_2diol)(DMF)$_2$] possesses a surface area greater than 700 m^2 g^{-1}; however, upon full desolvation to [Ni(H_2diol)] the contraction of the *c*-axis affords a small pore size that reduces access of adsorbates. Careful inspection of the crystal structure and PXRD data for [Ni(H_2diol)] suggests that the pores of [Ni(H_2diol)] consists of aryl C–H bonds which close off access to the polar parts of the framework, thus reducing interactions between the pore walls and adsorbates. This dynamic framework derives from a reversible change in coordination geometry of the metal node upon exposure to selected adsorbates. For example, removal of the axial DMF molecules from [Ni(H_2diol)(DMF)$_2$] results in the Ni adopting an uncommon distorted tetrahedral environment that is supported by the torsional flexibility of the H_2diol ligand. Notably, this coordinatively unsaturated form can be resolvated by water or MeOH to form [Ni(H_2diol)(S)$_2$]. This reversible structural response to selected adsorbates can be monitored optically or magnetically. Accordingly this work provides an important first step towards the development of a multifunctional porous sensor.

A further unique aspect of the dynamic architecture of [Ni(H_2diol)(S)$_2$] (S = DMF, DEF) is the observed porosity differences between the two materials. In [Ni(H_2diol)(DEF)$_2$] the extra steric bulk of the DEF ligands would normally be expected to reduce the available pore size, but it can be seen that the *c*-axis of this compound is increased by 0.6 Å whilst the *a*-axis remains effectively the same as that of [Ni(H_2diol)(DMF)$_2$], offsetting the increase in bulk with respect to the surface area.

The variation of the unit cell with temperature for [Ni(H_2diol)(DMF)$_2$]·DMF is related to the degree of solvation of the framework; in [Ni(H_2diol)(DMF)$_2$]·DMF, vibrational interactions of the solvent molecules drive the expansion on heating, as is usually the case in well-packed systems. Desolvation to [Ni(H_2diol)] removes this interaction and framework vibrational modes become dominant, which often show zero- or negative thermal expansion.[5]

The use of magnetometry to track the resolvation of a metal allows us to decouple the different sorption processes in these MOFs. Conventional pressure- or gravimetric-based measurements are not normally able to differentiate sorption into pores or onto metal sites except by inference from the enthalpy of absorption. By using magnetometry, we can ignore the pore absorption and examine the rate at which the metal site is resolvated. This process could potentially be accomplished by solid-state UV/vis/NIR, but would be heavily affected by the rate of solvation at the surface of particles rather than give a picture of the bulk process. This technique is applicable to metals that show variation in their moment dependent on changes to the coordination sphere, such as Fe(II), Co(II), Ni(II) and Cu(II).

3. Conclusions

In this work we demonstrate that [Ni(H_2diol)(DMF)$_2$]·DMF dynamically responds to its environment by virtue of a multidentate organic ligand that is structurally rigid but facilitates rotation about the biaryl bond. Complete desolvation to [Ni(H_2diol)] effectively leads to a loss of measurable porosity, but partial desolvation to [Ni(H_2diol)(DMF)$_2$] results in a stable permanently porous framework. Furthermore, [Ni(H_2diol)(DMF)$_2$] shares some traits in common with soft MOFs in terms of a pressure-mediated expansion of the pore volume. The combination of dynamic porosity, switchable magnetism, and controllable thermal variation of expansivity places these materials within the select group of multifunctional MOFs that may find application in gas sensing and selective gas adsorption. Additionally, the use of magnetometry to track internal changes to MOF architecture is a tool that will be of use whenever paramagnetic metals are involved.

4. Experimental

General experimental methods

Unless otherwise stated, all reagents were commercially obtained and used without further purification. *N,N′*-Dimethylformamide (DMF) was dried twice consecutively over freshly activated 4 Å molecular sieves and stored under N_2 atmosphere. *N,N′*-Diethylformamide (DEF) was stirred over charcoal overnight, filtered through a plug of celite and stored over activated 4 Å molecular sieves. 2,2′-Dihydroxybiphenyl-4,4′-dicarboxylic acid was synthesised by a literature procedure.[12] Infrared (IR) spectra were recorded on a Perkin–Elmer Fourier Transform Infrared (FT–IR) spectrometer on a zinc–selenide crystal. TGA measurements were performed on a Perkin-Elmer STA 6000 from 30–800 °C under a flow of N_2.

Single crystal X-ray crystallography

Single-crystal X-ray diffraction was performed on a Oxford Diffraction X-Calibur X-ray diffractometer with Mo-Kα radiation (λ = 0.71073 Å) at 150 K. Data collection and reduction (Table 2) was handled through *CrysAlisPro*. The structure was initially solved using SHELXS-97[21] in WinGX[22] using direct methods and refined using SHELXL-97 (Table 2).[21] Highly

 This journal is © The Royal Society of Chemistry 2013

Published on 14 February 2013. Downloaded by UNIVERSITY OF ADELAIDE on 09/09/2015 06:01:02.

Table 2 Crystallographic parameters for $[Ni(H_2diol)(DMF)_2]\cdot DMF$ and $[Ni(H_2diol)(DEF)_2]\cdot 1/3DEF$ after SQUEEZE

Compound	$[Ni(H_2diol)(DMF)_2]\cdot DMF$	$[Ni(H_2diol)(DEF)_2]\cdot 1/3DEF$
Formula	$C_{20}H_{22}NiN_2O_8$	$C_{24}H_{28}NiN_2O_8$
Crystal system	Trigonal	Trigonal
Space group	$P3_121$	$P3_121$
a/Å	17.2139(3)	17.3278(4)
c/Å	8.5240(5)	9.1188(3)
V/Å^3	2187.42(14)	2371.13(11)
ρ/g cm^{-3}	1.082	1.116
Z	3	3
T/K	150	150
μ/mm^{-1}	0.701	0.653
Reflections collected	14 078	16 981
Unique reflections (R_{int})	3165 (0.0412)	3456 (0.0536)
Reflections $I > 2\sigma(I)$	2783	3354
Data/restraints/parameters	3165/0/141	3456/8/154
Goodness of fit (S)	1.102	1.227
R_1/wR_2 [$I > 2\sigma(I)$]	0.0419/0.1150	0.0931/0.2582
R_1/wR_2 (all data)	0.0491/0.1185	0.0948/0.2592

disordered pore solvent electron density was removed after analysis with SQUEEZE in PLATON.[13]

Powder X-ray diffraction

In-house powder X-ray diffraction (PXRD) data was collected on a Rigaku Hiflux Homelab system using Cu-Kα radiation with an R-Axis IV++ image plate detector (λ = 1.54056 Å). Samples were mounted on plastic loops using paratone-N and data collected by scanning 90° in phi for 120 second exposures. The data was converted into *xye* format using the program DataSqueeze. Simulated powder X-ray diffraction patterns were generated from the single crystal data using Mercury 2.3. Le Bail refinement of PXRD patterns was performed in Rietica. Variable-temperature powder X-ray diffraction was collected on the PD beamline at the Australian Synchrotron at an energy of 15 keV. Data was merged using the program DataPro.

Gas adsorption

Gas adsorption measurements were performed on a Micromeritics ASAP 2020 analyser at 77 K for N_2. Surface areas were calculated using the BET method[23,24] and the pressure range validated using the method of Walton and Snurr.[24b]

Magnetic susceptibility measurements

Magnetic susceptibility measurements were made on a Quantum Designs PPMS with vibrating sample measurement system in the range 5–300 K under fields of 2000 G. Time-dependant magnetisation measurements were performed at 273 K.

X-ray adsorption near-edge spectroscopy

XANES data were recorded at 10 K at the Australian National Beamline Facility (ANBF, beamline 20B at the Photon Factory, Tsukuba, Japan). K-edge Ni data were measured in fluorescence with a 36-pixel solid-state planar Ge detector (Eurisys). Harmonic rejection was achieved by detuning the channel-cut Si[111] monochromator by 50%. The energy scale was calibrated using a nickel foil as an internal standard (calibration energy, 8333 eV, corresponding to the first peak of the first derivative of the Ni K edge). Background subtraction and normalization was achieved using BACKSUB software (G. N. George, unpublished).

Synthetic methods

$[Ni(H_2diol)(DMF)_2]\cdot DMF$: 0.1 mmol $Ni(NO_3)_2\cdot 6H_2O$, 0.1 mmol 2,2′-dihydroxybiphenyl-4,4′-dicarboxylic acid and 0.055 mmol DABCO in 1.5 mL DMF at 100 °C for six hours. $[Ni(H_2diol)(DEF)_2]\cdot 1/3DEF$: As for $[Ni(H_2diol)(DMF)_2]\cdot DMF$, but DEF instead of DMF. Full details are provided in the ESI.†

Computational methods

Initial structures were taken from crystal structures with excess solvent molecules removed. DMF and DEF molecules were rotated around the Ni–O formamide coordination axis in 10° increments. For each step of rotation the framework was held rigid and the methyl and ethyl groups allowed to relax in $P1$ symmetry. As the isotherm experiments and simulations occur at 77 K and up to 1 bar, the PTE of the entire framework can be neglected. The relaxation and final structure energy were calculated using the universal forcefield (UFF)[25] within the Forcite module of Materials Studio 5.0 (Accelrys). Nitrogen surface area for each structure were calculated, utilising a probe radius of 1.84 Å, with the "Atoms Volume & Surfaces" package within Materials Studio.

Acknowledgements

We would like to thank Mr John Clements (University of Sydney) for assistance with magnetic measurements and Dr Wendy Queen and Dr Craig Brown (NIST) for additional assistance and advice on treatment of the powder X-ray data. CJD, CJS and CJK gratefully acknowledge the Australian Research Council for funding (FT0991910, FT100100400 and FT100100514). JDE acknowledges CSIRO Materials Science and Engineering for a PhD top-up scholarship. This research is supported by the Science and Industry Endowment Fund. This research was undertaken at the Australian National Beamline Facility at the Photon Factory in Japan, operated by the Australian Synchrotron. We acknowledge the Australian Research Council for financial support and the High Energy Accelerator Research Organisation (KEK) in Tsukuba, Japan, for operations support. Aspects of this research were undertaken on the Powder Diffraction beamline at the Australian Synchrotron, Victoria, Australia.

Notes and references

1 (*a*) M. D. Allendorf, C. A. Bauer, R. K. Bhakta and R. J. T. Houk, *Chem. Soc. Rev.*, 2009, **38**, 1330; (*b*) L. E. Kreno, K. Leong, O. K. Farha, M. Allendorf,

Published on 14 February 2013. Downloaded by UNIVERSITY OF ADELAIDE on 09/09/2015 06:01:02.

R. P. Van Duyne and J. T. Hupp, *Chem. Rev.*, 2012, **112**, 1105; (*c*) Y. Cui, Y. Yue, G. Qian and B. Chen, *Chem. Rev.*, 2012, **112**, 1126.

2 (*a*) J.-R. Li, R. J. Kuppler and H.-C. Zhou, *Chem. Soc. Rev.*, 2009, **38**, 1477; (*b*) J. Lee, O. K. Farha, J. Roberts, K. A. Scheidt, S. T. Nguyen and J. T. Hupp, *Chem. Soc. Rev.*, 2009, **38**, 1450; (*c*) J.-R. Li, J. Sculley and H.-C. Zhou, *Chem. Rev.*, 2012, **112**, 869.

3 (*a*) C. J. Kepert, in *Metal–Organic Framework Materials in Inorganic Materials: Volume One, Porous Materials*, ed. D. W. Bruce, R. I. Walton, D. O'Hare, John Wiley & Sons, Chichester, 2010, pp. 1–68; (*b*) L. J. Murray, M. Dincă and J. R. Long, *Chem. Soc. Rev.*, 2009, **38**, 1294; (*c*) D. M. D'Alessandro, B. Smit and J. R. Long, *Angew. Chem., Int. Ed.*, 2010, **49**, 6058; (*d*) K. Sumida, D. L. Rogow, J. A. Mason, T. M. McDonald, E. D. Bloch, Z. R. Herm, T.-H. Bae and J. R. Long, *Chem. Rev.*, 2012, **112**, 724.

4 (*a*) H. Li, M. Eddaoudi, M. O'Keeffe and O. M. Yaghi, *Nature*, 1999, **402**, 276; (*b*) M. Eddaoudi, J. Kim, N. L. Rosi, D. T. Vodak, J. Wachter, M. O'Keeffe and O. M. Yaghi, *Science*, 2002, **295**, 469.

5 (*a*) S. Adak, L. L. Daemen, M. Hartl, D. Williams, J. Summerhill and H. Nakottea, *J. Solid State Chem.*, 2011, **184**, 2854; (*b*) N. Lock, Y. Wu, M. Christensen, L. J. Cameron, V. K. Peterson, A. J. Bridgeman, C. J. Kepert and B. B. Iversen, *J. Phys. Chem. C*, 2010, **114**, 16181; (*c*) A. L. Goodwin and C. J. Kepert, *Phys. Rev. B: Condens. Matter*, 2005, **71**, 140301.

6 (*a*) S. Kitagawa, R. Kitaura and S.-I. Noro, *Angew. Chem., Int. Ed.*, 2004, **43**, 2334; (*b*) S. Bureekaew, S. Shimomura and S. Kitagawa, *Sci. Tech. Adv. Mater.*, 2008, **9**, 014108; (*c*) G. Ferey and C. Serre, *Chem. Soc. Rev.*, 2009, **38**, 1380; (*d*) E. Coronado and G. M. Espallargas, *Chem. Soc. Rev.*, 2013, **42**, 1525; (*e*) E. J. Cussen, J. B. Claridge, M. J. Rosseinsky and C. J. Kepert, *J. Am. Chem. Soc.*, 2002, **124**, 9574; (*f*) S. Horike, S. Shimomura and S. Kitagawa, *Nat. Chem.*, 2009, **1**, 695; (*g*) N. Yanai, K. Kitayama, Y. Hijikata, H. Sato, R. Matsuda, Y. Kubota, M. Takata, M. Mizuno, T. Uemura and S. Kitagawa, *Nat. Mat.*, 2011, **10**, 787; (*h*) W. M. Bloch and C. J. Sumby, *Chem. Commun.*, 2012, **48**, 2534.

7 For example, see: (*a*) D. Tanaka, K. Nakagawa, M. Higuchi, S. Horike, Y. Kubota, T. C. Kobayashi, M. Takata and S. Kitagawa, *Angew. Chem., Int. Ed.*, 2008, **47**, 3914; (*b*) X.-S. Wang, S. Ma, K. Rauch, J. M. Simmons, D. Yuan, X. Wang, T. Yildirim, W. C. Cole, J. J. López, A. de Meijere and H.-C. Zhou, *Chem. Mater.*, 2008, **20**, 3145; (*c*) J. Tian, L. V. Saraf, B. Schwenzer, S. M. Taylor, E. K. Brechin, J. Liu, S. J. Dalgarno and P. K. Thallapally, *J. Am. Chem. Soc.*, 2012, **134**, 9581; (*d*) C. Hou, Q. Liu, T.-a. Okamura, P. Wang and W.-Y. Sun, *CrystEngComm*, 2012, **14**, 8569; (*e*) R. El Osta, M. Frigoli, J. Marrot, N. Guillou, H. Chevreau, R. I. Walton and F. Millange, *Chem. Commun.*, 2012, **48**, 10639.

8 For examples, see: (*a*) D. N. Dybtsev, H. Chun and K. Kim, *Angew. Chem., Int. Ed.*, 2004, **43**, 5033; (*b*) K. Uemura, Y. Yamasaki, Y. Komagawa, K. Tanaka and H. Kita, *Angew. Chem., Int. Ed.*, 2007, **46**, 6662; (*c*) J. S. Grosch and F. J. Paesani, *J. Am. Chem. Soc.*, 2012, **134**, 4207; (*d*) S. Henke, A. Schneemann, A. Wütscher and R. A. Fischer, *J. Am. Chem. Soc.*, 2012, **134**, 9464.

9 C. Serre, F. Millange, C. Thouvenot, M. Noguès, G. Marsolier, D. Louër and G. Férey, *J. Am. Chem. Soc.*, 2002, **124**, 13519.

10 R. Matsuda, R. Kitaura, S. Kitagawa, Y. Kubota, T. C. Kobayashi, S. Horike and M. Takata, *J. Am. Chem. Soc.*, 2004, **126**, 14063.

11 For example, see: (*a*) G. J. Halder, C. J. Kepert, B. Moubaraki, K. S. Murray and J. D. Cashion, *Science*, 2002, **298**, 1762; (*b*) D. Sarma, K. V. Ramanujachary, S. E. Lofland, T. Magdaleno and S. Natarajan, *Inorg. Chem.*, 2009, **48**, 11660; (*c*) Z. Su, M. Chen, T.-A. Okamura, M.-S. Chen, S.-S. Chen and W.-Y. Sun, *Inorg. Chem.*, 2011, **50**, 985; (*d*) P. D. Southon, L. Liu, E. A. Fellows, D. J. Price, G. J. Halder, K. W. Chapman, B. Moubaraki, K. S. Murray, J.-F. Létard and C. J. Kepert, *J. Am. Chem. Soc.*, 2009, **131**, 10998.

12 D. Rankine, A. Avellaneda, M. R. Hill, C. J. Doonan and C. J. Sumby, *Chem. Commun.*, 2012, **48**, 10328.

13 A. L. Spek, *Acta Crystallogr., Sect. D: Biol. Crystallogr.*, 2009, **65**, 148.

14 See for example: (*a*) U. Ryde, *Biophys. J.*, 1999, **77**, 2777; (*b*) J. D. Crane, D. J. Moreton and E. Rogerson, *Eur. J. Inorg. Chem.*, 2004, 4237; (*c*) Y. Go, X. Wang, E. V. Anokhina and A. J. Jacobson, *Inorg. Chem.*, 2004, **43**, 5360.

15 (*a*) S. Amirjalayer, M. Tafipolsky and R. Schmid, *Angew. Chem., Int. Ed.*, 2007, **46**, 463; (*b*) P. L. Llewellyn, G. Maurin, T. Devic, S. Loera-Serna, N. Rosenbach, C. Serre, S. Bourrelly, P. Horcajada, Y. Filinchuk and G. Férey, *J. Am. Chem. Soc.*, 2008, **130**, 12808; (*c*) F. Salles, A. Ghoufi, G. Maurin, R. G. Bell, C. Mellot-Draznieks and G. Férey, *Angew. Chem., Int. Ed.*, 2008, **47**, 8487.

16 (*a*) N. L. Rosi, J. Kim, M. Eddaoudi, B. L. Chen, M. O'Keeffe and O. M. Yaghi, *J. Am. Chem. Soc.*, 2005, **127**, 1504; (*b*) P. D. C. Dietzel, Y. Morita, R. Blom and H. Fjellvag, *Angew. Chem., Int. Ed.*, 2005, **44**, 6354; (*c*) S. R. Caskey, A. G. Wong-Foy and A. J. Matzger, *J. Am. Chem. Soc.*, 2008, **130**, 10870; (*d*) F. Bonino, S. Chavan, J. G. Vitillo, E. Groppo, G. Agostini, C. Lamberti, P. D. C. Dietzel, C. Prestipino and S. Bordiga, *Chem. Mater.*, 2008, **20**, 4957; (*e*) J. G. Vitillo, L. Regli, S. Chavan, G. Ricchiardi, G. Spoto, P. D. C. Dietzel, S. Bordiga and A. Zecchina, *J. Am. Chem. Soc.*, 2008, **130**, 8386; (*f*) L. Alaerts, C. E. A. Kirschhock, M. Maes, M. A. van der Veen, V. Finsy, A. Depla, J. A. Martens, G. V. Baron, P. A. Jacobs, J. F. M. Denayer and D. E. De Vos, *Angew. Chem., Int. Ed.*, 2007, **46**, 4293.

17 For examples, see: (*a*) O. Ohmori and M. Fujita, *Chem. Commun.*, 2004, 1586; (*b*) K. Schlichte, T. Kratzke and S. Kaskel, *Microporous Mesoporous Mater.*, 2004, **73**, 81; (*c*) S. Horike, M. Dinca, K. Tamaki and J. R. Long, *J. Am. Chem. Soc.*, 2008, **130**, 5854; (*d*) A. Henschel, K. Gedrich, R. Kraehnert and S. Kaskel, *Chem. Commun.*, 2008, 4192.

 This journal is © The Royal Society of Chemistry 2013

Published on 14 February 2013. Downloaded by UNIVERSITY OF ADELAIDE on 09/09/2015 06:01:02.

18 F. A. Cotton and G. Wilkinson, *Advanced Inorganic Chemistry*, Interscience Publishers, New York, USA, 2nd edn, 1966.
19 G. J. Colpas, M. J. Maroney, C. Bagyinka, M. Kumar, W. S. Willis, S. L. Suib, P. K. Mascharak and N. Baidya, *Inorg. Chem.*, 1991, **30**, 920.
20 A. J. Bridgeman, *Dalton Trans.*, 2008, 1989.
21 G. M. Sheldrick, *Acta Crystallogr., Sect. D: Biol. Crystallogr.*, 2008, **64**, 112.
22 L. J. Farrugia, *J. Appl. Crystallogr.*, 1999, **32**, 837.
23 S. Brunauer, P. H. Emmett and E. J. Teller, *J. Am. Chem. Soc.*, 1938, **60**, 309.
24 (*a*) J. Rouquerol, P. Llewellyn, F. Rouquerol, Is the BET equation applicable to microporous adsorbents?, in *Characterization of Porous Solids VII*, ed. P. Lewellyn, F. Rodriguez-Reinoso, J. Rouquerol, N. Seaton, Studies in Surface Science and Catalysis, 2007, vol. 160, pp. 49–56; (*b*) K. S. Walton and R. Q. Snurr, *J. Am. Chem. Soc.*, 2007, **129**, 8552.
25 A. K. Rappe, C. J. Casewit, K. S. Colwell, W. A. Goddard III and W. M. Skiff, *J. Am. Chem. Soc.*, 1992, **114**, 10024.

THE JOURNAL OF PHYSICAL CHEMISTRY C

Article

pubs.acs.org/JPCC

Feasibility of Mixed Matrix Membrane Gas Separations Employing Porous Organic Cages

Jack D. Evans,[†] David M. Huang,[†] Matthew R. Hill,[†,‡] Christopher J. Sumby,[†] Aaron W. Thornton,[†,‡] and Christian J. Doonan*,[†]

[†]Centre for Advanced Nanomaterials, School of Chemistry & Physics, The University of Adelaide, Adelaide, Australia

[‡]CSIRO Materials Science and Engineering, Clayton, Australia

Supporting Information

ABSTRACT: Porous additives offer an attractive pathway to enhance the performance of polymeric gas separation membranes. Previously reported porous additives, such as zeolites and metal−organic frameworks, suffer from poor interfacial binding with the polymer matrix, which leads to nonselective gas transport pathways. Porous organic cages (POCs) are an exciting new family of soluble additives that could ameliorate these transport issues by integrating intimately with the polymer matrix. By using Voronoi network analysis, grand canonical Monte Carlo simulations, and molecular dynamics, we provide a theoretical assessment of the benefit of using POCs as additives for mixed matrix membranes (MMMs). We reveal that some MMMs containing POCs exhibit enhanced selectivity and permeability compared to the neat polymer matrix, particularly for H_2/CO_2 separations.

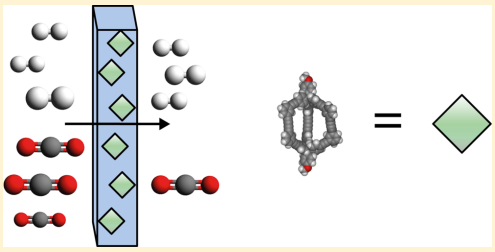

Publication Date (Web): January 9, 2014 | doi: 10.1021/jp4079184

INTRODUCTION

Novel strategies that increase the efficiency of industrial gas separations are of great interest due to their direct application to green energy technologies.[1,2] The specific challenges in this area are to reduce the overall energy cost of separating (i) H_2/N_2 and H_2/CO_2 for the production of hydrogen and the precombustion capture of carbon dioxide from gasified coal following the water−gas shift reaction,[3,4] (ii) CO_2/N_2 for postcombustion "carbon capture" from gas flue streams,[5] and (iii) CO_2/CH_4 for biofuel purification and natural gas sweetening.[6]

Membrane systems are often used to perform gas separations on an industrial scale as they operate via a continuous process. This is more energy efficient than batchwise methods such as physical or chemical adsorption that require periodic energy-intensive regeneration.[3,7,8] Membranes are commonly prepared from organic polymers as they are stable, readily scalable, and cost-efficient. However, pure polymer membranes are hampered by an empirical permeability versus selectivity trade-off limit termed the "upper bound".[9,10] Accordingly, one of the current challenges in membrane separation technology is to design new materials that surpass the upper bound limit and achieve enhanced selectivity, ideally in combination with increased permeability. A promising strategy is to synthesize multicomponent mixed matrix membranes (MMMs) in which a gas-selective porous solid of fixed pore diameter is embedded into a polymer host. Porous additives with narrow pore size distributions, of the order of the kinetic diameter of the target gas, can facilitate efficient size-sieving separations. Additionally, these additives can introduce chemical functionality into the polymer to improve solubility of a target gas and thus enhance membrane selectivity. Porous adsorbents that have been explored as membrane additives include zeolites, metal−organic frameworks, and zeolitic imidizolate frameworks (ZIFs).[11,13,14] Such materials have yielded MMMs that show increased permeability and selectivity compared to neat polymers.[11] However, inhomogeneity of the surface chemistry between the polymer and adsorbent can give rise to nonselective interphase voids that allow unrestricted gas diffusion.[15] This ultimately leads to less than optimal performance for these multicomponent membranes.[16] Thus, in order for MMMs to reach their full potential, synthetic methods that afford "gas-tight" integration between the two phases are required.

Recently, microporous solids composed of solution-processable porous organic cage (POC) molecules have attracted significant attention due to the potential to combine the atomic-scale control over pore size seen in MOFs and ZIFs, with the solution processability of molecular species.[17,18] These novel materials have been reported with surface areas in excess of 1500 $m^2 \cdot g^{-1}$ and have also been shown to carry out size- and shape-specific molecular separations.[19,20] It is noteworthy that for such POC materials the accessible surface area can arise from interconnection of the intrinsically porous cage cavities (intrinsic porosity), from void spaces surrounding the cages that result from inefficient packing (extrinsic porosity) or from a

Received: August 7, 2013
Revised: December 24, 2013
Published: December 30, 2013

ACS Publications © 2013 American Chemical Society

Publication Date (Web): January 9, 2014 | doi: 10.1021/jp4079184

combination of both. As a result, polymorphs of POCs are reported to have very different physical properties.[21,22] Thus, in the present study we have used the reported crystalline structures of POCs as the basis for our feasibility analysis. This approach is validated by the work of Bushell et al. who reported MMMs incorporating a POC that showed both in situ crystal growth and crystal inclusion.[23]

Our study builds upon recent computational work that considered the use of MOFs and ZIFs as additives for MMMs. These studies have enabled the identification of important trends and targeted the development of novel materials.[24,25] POCs are attractive as they are soluble in many common organic solvents, which facilitates intimate mixing with the polymer host at the molecular scale. In silico screening will assist the development of POC-based MMMs as it can provide design principles for new materials.

Figure 1 shows the molecular structure and accessible pore surfaces of five organic cage molecules of varying cavity dimensions, pore window sizes, and molecular architectures. As the packing of cage molecules defines the bulk porosity of the materials we used the reported crystal structures of cages **1**−**5**.[17,19,21] The selectivity and permeability of MMMs containing POCs **1**−**5** were determined from grand canonical Monte Carlo (GCMC) and molecular dynamics (MD) simulations. Furthermore, we considered the effects of structural dynamics of the pore windows using Voronoi network analysis and MD simulations. To verify our modeling data, we calculated MMM permeabilities of **3** and PIM-1, a polymeric host of intrinsic microporosity, and compared these to experimental results.[23]

METHODOLOGY

To simulate the intrinsic permeabilities of **1**−**5**, we extracted their structural data from the Cambridge Structural Database.[26] Supercells (2 × 2 × 2) of structures **1**, **2**, **4**, and **5** were used and the disorder of **2** was randomly chosen across the supercell, analogous to a recent study.[27] Owing to the larger size, a single unit cell of system **3** was used and desolvated crystal structures were used where available. Structures of **1**−**5** were analyzed by Voronoi network analysis using the Zeo++ code[28,29] to calculate the accessible surface area, size, and dimensionality of the pores. A probe radius of 1.82 Å, equivalent to the kinetic diameter of N_2, was used to calculate surface areas.[30]

Equilibrium gas uptakes for H_2, N_2, CH_4, and CO_2 at 10 bar and 298 K were calculated by GCMC simulations employing the RASPA code.[31] Analogous methods have been successfully employed to model porous carbons, zeolites, and metal−organic frameworks.[25,32,33] The universal force field (UFF)[34] was used to describe the nonbonded interactions of the cage atoms. H_2 was described by the Darkrim and Levesque model,[35] N_2 and CH_4 molecules were represented using the TraPPe model,[36] and CO_2 was described using the Elementary Physics 2 model.[37] Mixed-atom interactions were expressed using Lorentz−Berthelot mixing rules.[38] The cage volume of **2** was blocked to prevent the growth of molecules in a 4 Å diameter sphere at the center of mass of the cage molecules. Inspection of the gas density plots from the simulation ensured that the cage volume was blocked and the extrinsic volume was unchanged. Each simulation used 1 million equilibration steps followed by 1 million production steps. The particular force fields chosen have precedence in literature, having been used in previous studies of MOFs.[39]

Diffusion was simulated using equilibrium MD based on the Forcite module within Materials Studio 5.0.[40] UFF was used to describe the dynamics of bonds, angles, and torsions of the

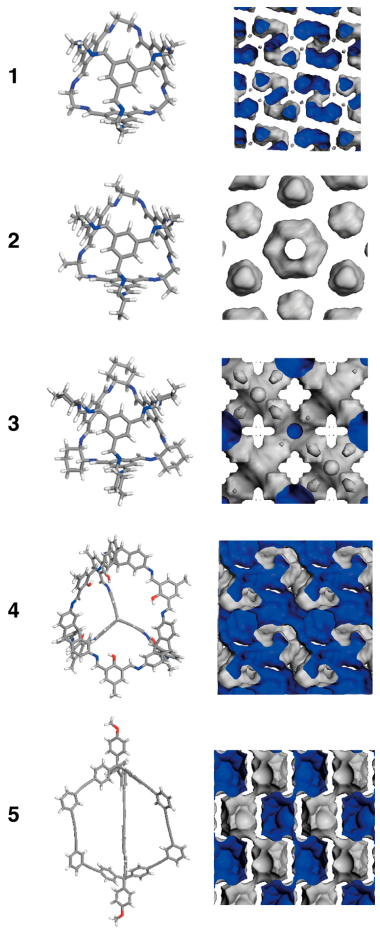

Figure 1. Summary of molecular structures and accessible pore surface (1.2 Å probe radius) of POCs **1**−**5** (gray, carbon; white, hydrogen; red, oxygen; blue, nitrogen).

systems during the MD simulation. Gas molecules at the density predicted by GCMC simulations at 10 bar were randomly placed into the crystal structure with the Amorphous Cell module. NVT dynamics were simulated for 6 ns with a time step of 1 fs with temperature controlled at 300 K using the Nosé-Hoover thermostat.[41] Only the last 5 ns of each simulation trajectory was used to calculate the mean-squared displacement of the gas molecules. The structure was allowed to be flexible to ensure that the dynamic nature of the systems was captured. A total of five unique trajectories were simulated so that an average slope of the mean-squared displacement could be calculated. The Einstein relationship in eq 1 was used to find the self-diffusivity, D_{self}, of the gas molecules from the coordinates, $r(t)$, of the molecules as a function of time, t.

$$D_{self} = \frac{1}{6}\lim_{t\to\infty}\frac{d}{dt}\langle|\mathbf{r}(t) - \mathbf{r}(0)|^2\rangle \quad (1)$$

Publication Date (Web): January 9, 2014 | doi: 10.1021/jp4079184

Intrinsic permeabilities of POC crystals were approximated using eq 2, where c is the equilibrium gas concentration, and f is the operating fugacity.[42] Single-gas properties were computed and selectivity was calculated using this data.

$$P = D_{self}\frac{c}{f} \tag{2}$$

Pore dynamics were calculated using the Zeo++ code for the last nanosecond of a 2 ns NVT dynamics trajectory at 298 K in the absence of gas molecules.

MMM permeabilities were calculated for a cage volumetric fraction of 40% using the Bruggeman's effective-medium model described in eq 3, where P_{MMM} is the permeability of the MMM, P_p the permeability of the polymer, P_{POC} the permeability of the POC, and φ the volume fraction of POC in the membrane.[43]

$$\left(\frac{P_{MMM}}{P_p}\right)^{-1/3}\left[\frac{\frac{P_{MMM}}{P_p}-\frac{P_{POC}}{P_p}}{1-\frac{P_{POC}}{P_p}}\right] = (1-\varphi) \tag{3}$$

RESULTS AND DISCUSSION

Structural Properties. Figure 1 depicts POCs **1**−**5**, showing their different geometries, pore networks, and chemical functionality. Cages **1**-**3** have tetrahedral geometry of equivalent cavity size and can be differentiated by their vertex functionality. Cage **4** is an adamantoid and possesses the largest pore cavity of all the cages investigated. We note that an analogue of this structure has the highest reported surface area for a POC of 2071 $m^2 \cdot g^{-1}$.[19] Finally, cage **5** is best described as an elongated triangular dipyramid and is constructed from carbon−carbon bonds. This molecular connectivity is in contrast to cages **1**−**4**, which are composed of imine moieties.

Static pore sizes, structure metrics, and N_2-accessible surfaces areas were calculated for structures **1**−**5** (Table S-1). The internal pore cavities range from 5.4 to 9.8 Å. The pore limiting (or window) sizes for each of the crystalline POC networks were calculated to lie between 1.8 and 5.1 Å; these values are germane to size-sieving separation of industrially relevant gases N_2, CO_2, CH_4, and H_2.[44] Cages **3** and **5** possess "zeolite-type" pore structures with limiting diameters of 3.7 and 4.4 Å, respectively. Such pore architectures show excellent potential for gas separations, as they contain pore windows in the range of the kinetic diameter of target gases and also have larger cavities providing good solubility.

Structures **1**−**5** were investigated using combined GCMC and Voronoi network analysis simulations to determine representative surface areas. Good agreement between the experimental and calculated data for **1** and **2** was observed. However, discrepancies between experimental and predicted surface areas were found for the structures of cages **3**−**5**. This incongruity can be attributed to the "soft" nature of these structures, which arises from the cage molecules packing in the crystalline phase via relatively weak dispersion forces.[45] In the present study, we find that the simulated surface area of **3** is underestimated. This is anticipated as the simulation uses a "perfect" crystal and increased crystallinity of experimental samples has been shown to result in decreased surface area.[46] In addition, the dynamic pore aperture has been suggested to account for a greater N_2 porosity than expected for a static structure.[47] In contrast to structure **3**, the surface area of **4** is overestimated by a factor of 2 (2410 $m^2 \cdot g^{-1}$ compared with 1291 $m^2 \cdot g^{-1}$). This significant difference can be accounted for by a structural contraction upon solvent removal.[19] Lastly, the difference between the experimental and simulated surface area for cage **5** arises from confinement of N_2 within the pores at the experimental temperature of 77 K.[21]

Equilibrium Gas Uptake. GCMC routines are commonly used to simulate gas uptakes in porous materials. The potential parameters for the cage atoms were obtained from the UFF.

To validate our approach we simulated CO_2 and CH_4 isotherms for structures **2** and **3** and compared the results with experimental data by Tozawa et al. (Figure 2).[17] We note that

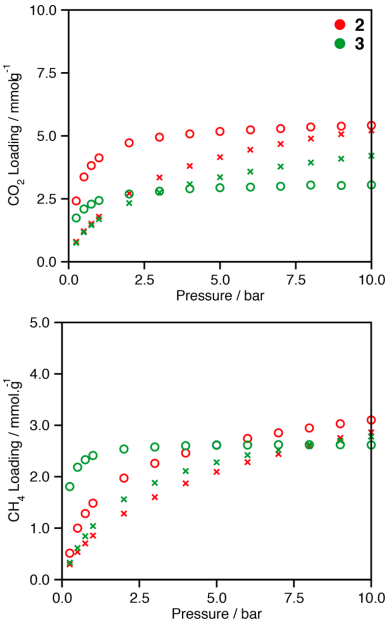

Figure 2. Comparison of experimental (crosses) and theoretical (circles) CO_2 and CH_4 isotherms of POCs **2** and **3**.

CO_2 and CH_4 gas adsorption isotherms have not been reported for **1**, **4**, and **5** and thus could not be included in this comparison. Inaccessible voids of cage **2** were blocked to ensure that the simulated isotherms were not overestimated.[48,49] Inaccessible regions observed in the static crystal structures have been found to contribute to the porosity and it is suggested that dynamic molecular motion allows diffusion into these formally inaccessible cage voids.[17,27] This process is not well understood so the amount of blocked volume was assessed to ensure the best fit to experimental data (Figure S-1). The best agreement to CO_2 and CH_4 experimental data was found for simulations containing 50 and 100% blocked cage volume, respectively.

Figure 2 shows that the larger pores of **2** result in larger uptake at high pressures for CO_2 and CH_4 adsorption. At low pressure, CH_4 has greater adsorption in **3** due to the smaller cavity sizes, which give rise to stronger binding sites from "wall−wall" potential overlaps. This effect is not observed for CO_2 adsorption because of its smaller size and aspherical shape. The observed difference between the calculated and experimental isotherms at low pressure can be attributed to artifacts in the force field, pressure-dependent accessible pockets within the structures, or

Publication Date (Web): January 9, 2014 | doi: 10.1021/jp4079184

defects in the experimental crystal. We note that in general, the gas adsorption of porous molecular crystals are inherently difficult to simulate due to their "soft" 3D structures. As such, we find the agreement to be within an acceptable range.[45] We also simulated the gas loading of H_2, N_2, CH_4, and CO_2 at 10 bar for structures **1**−**5** (Table S-2). The gas uptakes at this pressure are comparable to other porous materials such as ZIFs.[25]

Diffusion and Structural Flexibility. MD simulations at 298 K were employed to estimate the adsorbate diffusion throughout the pore structures of **1**−**5**. We selected these conditions to allow comparison with previously reported data that predicted the kinetic gas separation properties of ZIFs and MOFs.[24,25] As the series of POCs under investigation include different chemical structures a consistent generic force field (UFF) was chosen to describe all systems, in lieu of an imine-specific cage force field.[44] To assess the accuracy UFF for the imine based cages, structures **1**−**4** were optimized and compared to the crystal structures. Small discrepancies are observed between the optimized imine angles (Table S-3) and those present in the crystal structures. However, superimpositions of the optimized and crystal structure geometries of systems **1**−**5** (Figure S-2) are essentially identical, thus, demonstrating the accuracy of UFF for the range of systems compared in this study. From these MD simulations we computed the self-diffusion coefficients of **1**−**5** for H_2, N_2, CO_2, and CH_4 (Table 1).

Table 1. Self-diffusion coefficient of gas molecules in POCs[a].

	$D_{self}/10^{-10}$ m^2·s^{-1}			
cage	H_2 (2.9 Å)	N_2 (3.6 Å)	CO_2 (3.3 Å)	CH_4 (3.8 Å)
1 (1.8 Å)	0.00167	0.332	0.0161	0.00250
2 (3.9 Å)	468	11.5	5.92	3.46
3 (3.7 Å)	532	9.02	3.45	2.16
4 (5.1 Å)	762	81.7	6.43	19.4
5 (4.4 Å)	363	36.8	6.05	23.6

[a]Numbers in parentheses after the cage and gas molecule type are the pore size and gas-molecule kinetic diameter, respectively.

The diffusivities calculated are consistent with the window sizes of the structures. The diminutive pore aperture of **1** results in poor diffusion of all gas molecules. Without the specific pore size required for the kinetic separation of CO_2/N_2, the diffusivities follow the trend for the bulk diffusion of N_2 over CO_2. Structures **2** and **3** show lower diffusivity for CH_4 than CO_2, which is attributed to their limiting pore diameters of 3.9 and 3.7 Å, respectively. In contrast, the larger pore diameters of cages **4** and **5** allow the rapid diffusion of CH_4 (3.8 Å). We note that in the absence of molecular sieving, surface diffusion competes with the strong adsorption of CO_2, producing slower diffusivity of CO_2 compared with CH_4.

Our results indicate that a static pore model does not accurately represent the selectivities for CH_4 separations. As the pore structures of **1**−**5** are formed from weak intermolecular forces, it is likely that the pore window distribution is greater than that of extended frameworks in which the pore network is constructed by strong covalent bonds. Notably, pore size fluctuations have been reported to decrease the CH_4 selectivity in ZIF-8.[50] We note that the standard deviation in the window size is a reduced measure of the complicated structural dynamics and thus cannot capture all the subtleties of the dynamics of the framework structure that could potentially affect gas diffusion, such as correlated breathing motions. However, small standard deviations necessarily imply rigid windows, which likely lead to more efficient kinetic sieving. To gain further insight into the dynamic nature of the cage structures, NVT molecular dynamic simulations were carried out at analogous temperatures to the diffusion simulations described earlier. In these simulations the limiting pore size was calculated at each femtosecond over a 1 ns trajectory, after 1 ns equilibration. The resulting pore size distributions for cages **1**−**5** were calculated (see Figure 3 and Table S-4).

Based on its static structure, **2** was not expected to be a promising candidate for size sieving of CH_4, due to the crystallographic limiting pore size of 3.9 Å. However, the flexible diffusion simulations showed slower diffusivity of CH_4 than CO_2 (Table 1). We observe from the window size distributions that thermal fluctuations of **2** produce a mean window size of 3.56 Å (Table S-4), similar to that of cage **3**, thus, limiting the diffusion of CH_4.

The largest standard deviation of window sizes, 0.3 Å, was calculated for **4** (Figure 3). This may be attributed to the pore network being composed of largely extrinsic volume, which is found to fluctuate by a considerable amount over the time scale of the simulation. In contrast, the structures of **1** and **3** are found to produce narrow distributions of window sizes (standard deviations of 0.05 and 0.07 Å, respectively). The pore structures of these cages are wholly comprised of intrinsic cage volume with cage-to-cage packing linking the pore cavities. These results suggest cage molecules with functionalities that direct strong packing between molecular windows of appropriate dimensions may be more efficient for separations requiring precise size selection.

We note that the window size distribution of **3** found in the present work is different to that found in a previous study.[47] The difference can be attributed to a difference in definition: we have taken the window size to be the narrowest point in the whole cell at a given point in time, whereas the previous study assigned the window size to the diameter of the entrance to the cage cavity. Our definition, which in general gives smaller window sizes, accounts for the effects of fluctuations in the intercage regions and (mis)alignment of cage windows on the accessibility of cage volumes.

MMM Properties. Diffusion data was combined with the simulated gas uptakes to compute the permeabilities for the crystalline cage structures **1**−**5**. MMM permeabilities were extrapolated from intrinsic permeance values using Bruggeman's model, which has been shown to accurately simulate the properties of MMMs composed of polymers and ZIFs for high fractions of additives: up to 40% by volume.[51] Recent work by Bushell et al. reported the permeabilites of a MMM composed of PIM-1 and cage **3**.[23] We compared these experimental results with our simulation data to verify the use of our approach. The simulations were carried out at 1 bar to allow comparison with the experimental work. Figure 4 compares the experimental permeability of CO_2, N_2, and CH_4 with our calculated values.

Both the simulated and the experimental data show an increase in permeability for N_2, CO_2, and CH_4 with increasing loading of **3**. Although the modeled data follow the experimental trends and show good agreement with respect to N_2 permeability, the permeability of CO_2 and CH_4 is underestimated. The observed difference may suggest that additional mechanisms influence the MMM configuration, including interfacial diffusion paths produced by disruption of chain packing at the polymer−POC interface. This effect has been observed to a significant extent for

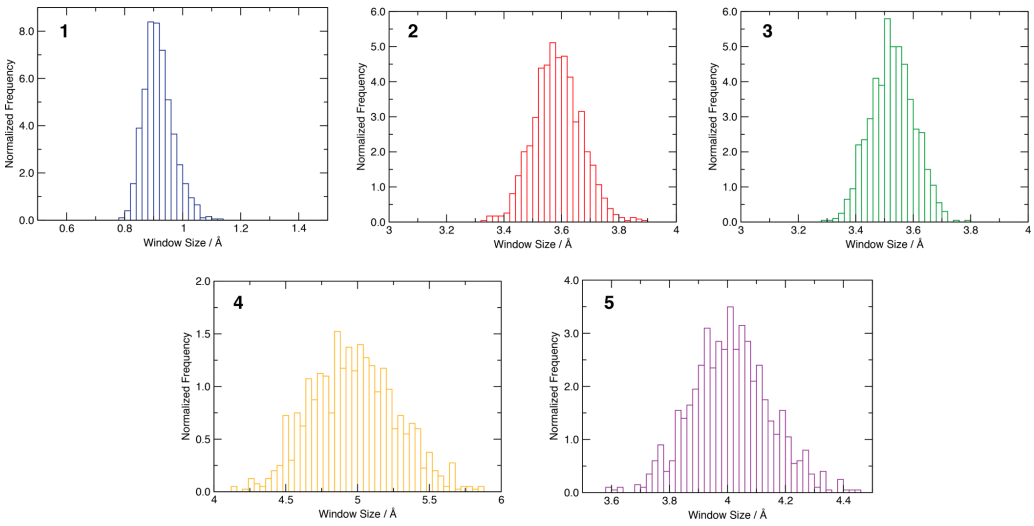

Figure 3. Window size distributions of POCs **1**−**5** over 1 ns at 298 K.

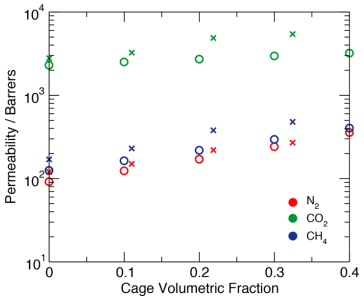

Figure 4. Comparison of the experimental (crosses) and predicted (circles) permeabilities of PIM-1:3 at increasing loadings of **3**.

other additives in MMMs[52] and, although minimized by the organic make up of POCs, it cannot be excluded.

Using Bruggeman's model, the permeabilities and selectivities for 40% volume compositions of MMMs comprised of the polymer hosts Matrimid, Ultem, PIM-1, and PIM-7 were computed.[14,53,54] The permeability and selectivity trade-off plots for the separation of H_2/N_2, H_2/CO_2, CO_2/N_2 and CO_2/CH_4 were predicted for neat POC membranes and MMMs. These are displayed in Figure 5. We find that MMMs containing cage structures **2**−**5** significantly improve the permeability for H_2/N_2 and H_2/CO_2 separations. This enhancement is concomitant with a minor increase in the selectivity for H_2.

Figure 5 shows that the permeability for CO_2/N_2 and CO_2/CH_4 separations increases upon introduction of cages **1**−**5**, bringing the Ultem and Matrimid MMMs toward the polymer upper bound; however, a decrease in selectivity is observed for the PIM membranes. The plots for MMMs composed of cages **2**−**5** and Ultem and Matrimid show considerable overlap of data points. This is due to the difference in permeability of cages being negligible when combined with the low permeability polymer and results in MMMs with very similar permeabilities. We also note that as a result of the discontinuous pore volume of **1**, the MMMs simulated have decreased permeabilities and selectivities compared to cages **2**−**5**.

These results show that the inclusion of crystalline aggregates of POCs in neat polymer matrices result in MMMs that lie on or surpass the polymer upper bound for H_2/N_2 and H_2/CO_2 separations. The separations of CO_2 show an increase in permeability, with the addition of cage molecules advancing Matrimid-based MMMs toward the polymer upper bound. In comparison to previous studies, the performance of POC MMMs is comparable to that of predicted ZIF-containing MMMs, despite their marginally lower affinity for the investigated gases.[25] It is expected however, with the POCs' exclusively organic construction that their potential will not be hindered by poor integration between the two phases.

CONCLUSION

In summary, we have investigated a series of POC-based MMMs for the separation of industrially relevant gas mixtures H_2/N_2, H_2/CO_2, CO_2/N_2 and CO_2/CH_4. This was achieved by employing Voronoi network analysis, GCMC, and MD simulations, with the calculations compared to experimental data for validation. Conservative estimates of gas transport properties within these materials revealed that MMMs composed of POCs can exceed the polymer upper bound for H_2/N_2 separations and more substantially for H_2/CO_2 gas pair. We note the importance of considering flexibility in these materials, as weak packing forces define the pore structures. Accordingly, window size distributions over a 1 ns trajectory were calculated. These properties determined by our investigation, combined with the facile processability and good compatibility with the polymer, indicate that POC-based MMMs have exciting potential for clean energy applications.

Publication Date (Web): January 9, 2014 | doi: 10.1021/jp4079184

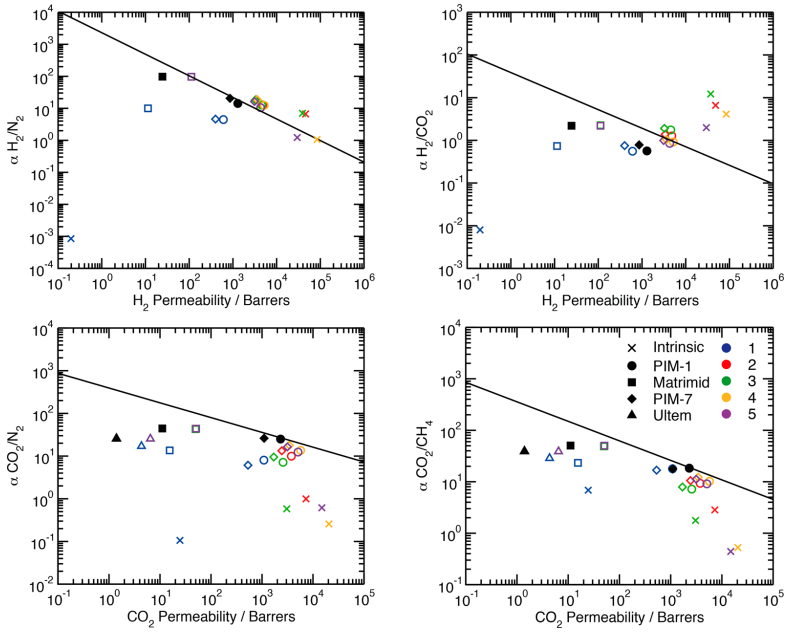

Figure 5. Permeability vs selectivity trade-off plots for neat polymers (solid black symbols), intrinsic POCs **1**−**5** (crosses), POC/polymer MMM predictions (open symbols), and Robeson's 2008 upper bound[10] (line). Open symbols represent 40% volume fraction of POC (see color code) within polymer (see symbol shape).

Publication Date (Web): January 9, 2014 | doi: 10.1021/jp4079184

■ ASSOCIATED CONTENT

Supporting Information

Simulated surface areas, window sizes, cavity sizes, isotherm fitting, gas concentrations, force field validation, and distribution metrics. This material is available free of charge via the Internet at http://pubs.acs.org.

■ AUTHOR INFORMATION

Corresponding Author

*E-mail: christian.doonan@adelaide.edu.au.

Funding

Parts of this research were funded by the Science and Industry Endowment Fund (SIEF).

Notes

The authors declare no competing financial interest.

■ ACKNOWLEDGMENTS

J.D.E. thanks CSIRO Materials Science and Engineering for a Ph.D. top-up scholarship and CSIRO HPSC for computational resources. C.J.D. gratefully acknowledges the ARC for funding parts of this work (FT100100400 and DP120103909)

■ REFERENCES

(1) Haszeldine, R. S. Carbon Capture and Storage: How Green Can Black Be? *Science* **2011**, *325*, 1647−1652.
(2) Jacobson, M. Z. Review of Solutions to Global Warming, Air Pollution, and Energy Security. *Energy Environ. Sci.* **2009**, *2*, 148−173.
(3) Ku, A. Y.; Kulkarni, P.; Shisler, R.; Wei, W. Membrane Performance Requirements for Carbon Dioxide Capture using Hydrogen-selective Membranes in Integrated Gasification Combined Cycle (IGCC) Power Plants. *J. Membr. Sci.* **2011**, *367*, 233−239.
(4) Scholes, C. A.; Smith, K. H.; Kentish, S. E.; Stevens, G. W. CO_2 Capture from Pre-combustion Processes - Strategies for Membrane Gas Separation. *Int. J. Greenhouse Gas Control* **2010**, *4*, 739−755.
(5) Ho, M. T.; Allinson, G. W.; Wiley, D. E. Reducing the Cost of CO_2 Capture from Flue Gases using Membrane Technology. *Ind. Eng. Chem. Res.* **2008**, *47*, 1562−1568.
(6) Park, H. B.; Han, S. H.; Jung, C. H.; Lee, Y. M.; Hill, A. J. Thermally Rearranged (TR) Polymer Membranes for CO_2 Separation. *J. Membr. Sci.* **2010**, *359*, 11−24.
(7) Baker, R. W. *Membrane Technology and Applications*; Wiley: West Sussex, U.K., 2004.
(8) Freeman, B.; Yampolskii, Y.; Pinnau, I. *Materials Science of Membranes for Gas and Vapor Separation*; Wiley: West Sussex, U.K., 2006.
(9) Robeson, L. M. Correlation of Separation Factor versus Permeability for Polymeric Membranes. *J. Membr. Sci.* **1991**, *62*, 165−185.
(10) Robeson, L. M. The Upper Bound Revisited. *J. Membr. Sci.* **2008**, *320*, 390−400.
(11) Li, Y.; Liang, F.; Bux, H.; Yang, W.; Caro, J. Zeolitic Imidazolate Framework ZIF-7 Based Molecular Sieve Membrane for Hydrogen Separation. *J. Membr. Sci.* **2010**, *354*, 48−54.
(12) Süer, M. G.; Baç, N.; Yilmaz, L. Gas Permeation Characteristics of Polymer-Zeolite Mixed Matrix Membranes. *J. Membr. Sci.* **1994**, *91*, 77−86.
(13) Perez, E. V.; Balkus, K. J.; Ferraris, J. P.; Musselman, I. H. Mixed-Matrix Membranes Containing MOF-5 for Gas Separations. *J. Membr. Sci.* **2009**, *328*, 165−173.
(14) Ordoñez, M. J. C.; Balkus, K. J., Jr.; Ferraris, J. P.; Musselman, I. H. Molecular Sieving Realized with ZIF-8/Matrimid Mixed-Matrix Membranes. *J. Membr. Sci.* **2010**, *361*, 28−37.

Publication Date (Web): January 9, 2014 | doi: 10.1021/jp4079184

(15) Mahajan, R.; Koros, W. J. Mixed Matrix Membrane Materials with Glassy Polymers. Part 1. *Polym. Eng. Sci.* **2002**, *42*, 1420−1431.
(16) Merkel, T. C.; Freeman, B. D.; Spontak, R. J.; He, Z.; Pinnau, I.; Meakin, P.; Hill, A. J. Ultrapermeable, Reverse-Selective Nanocomposite Membranes. *Science* **2002**, *296*, 519−522.
(17) Tozawa, T.; Jones, J. T. A.; Swamy, S. I.; Jiang, S.; Adams, D. J.; Shakespeare, S.; Clowes, R.; Bradshaw, D.; Hasell, T.; Chong, S. Y.; Tang, C.; Thompson, S.; Parker, J.; Trewin, A.; Basca, J.; Slawin, A. M. Z.; Steiner, A.; Cooper, A. I. Porous Organic Cages. *Nat. Mater.* **2009**, *8*, 973−978.
(18) Jiang, S.; Jones, J. T. A.; Hasell, T.; Blythe, C. E.; Adams, D. J.; Trewin, A.; Cooper, A. I. Porous Organic Molecular Solids by Dynamic Covalent Scrambling. *Nat. Commun.* **2011**, *2*, 207.
(19) Schneider, M. W.; Oppel, I. M.; Ott, H.; Lechner, L. G.; Hauswald, H. J. S.; Stoll, R.; Mastalerz, M. Periphery-Substituted [4 + 6] Salicylbisimine Cage Compounds with Exceptionally High Surface Areas: Influence of the Molecular Structure on Nitrogen Sorption Properties. *Chem.—Eur. J.* **2012**, *18*, 836−847.
(20) Mitra, T.; Jelfs, K. E.; Schmidtmann, M.; Ahmed, A.; Chong, S. Y.; Adams, D. J.; Cooper, A. I. Molecular Shape Sorting using Molecular Organic Cages. *Nat. Chem.* **2013**, *5*, 276−281.
(21) Avellaneda, A.; Valente, P.; Burgun, A.; Evans, J. D.; Markwell-Heys, A. W.; Rankine, D.; Nielsen, D. J.; Hill, M. R.; Sumby, C. J.; Doonan, C. J. Kinetically Controlled Porosity in a Robust Organic Cage Material. *Angew. Chem.* **2013**, *125*, 3834−3837.
(22) Jones, J. T. A.; Holden, D.; Mitra, T.; Hasell, T.; Adams, D. J.; Jelfs, K. E.; Trewin, A.; Willock, D. J.; Day, G. M.; Bacsa, J.; Steiner, A.; Cooper, A. I. On−Off Porosity Switching in a Molecular Organic Solid. *Angew. Chem.* **2011**, *123*, 775−779.
(23) Bushell, A. F.; Budd, P. M.; Attfield, M. P.; Jones, J. T.; Hasell, T.; Cooper, A. I.; Bernardo, P.; Bazzarelli, F.; Clarizia, G.; Jansen, J. C. Nanoporous Organic Polymer/cage Composite Membranes. *Angew. Chem., Int. Ed.* **2013**, *52*, 1253−1256.
(24) Krishna, R.; van Baten, J. M. In Silico Screening of Metal−Organic Frameworks in Separation Applications. *Phys. Chem. Chem. Phys.* **2011**, *13*, 10593−10616.
(25) Thornton, A. W.; Dubbeldam, D.; Liu, M. S.; Ladewig, B. P.; Hill, A. J.; Hill, M. R. Feasibility of Zeolitic Imidazolate Framework Membranes for Clean Energy Applications. *Energy Environ. Sci.* **2012**, *5*, 7637−7646.
(26) CSD version 5.34, Crystal Structures Database, http://ccdc.caltech.edu/, accessed July 2013.
(27) Hasell, T.; Armstrong, J. A.; Jelfs, K. E.; Tay, F. H.; Thomas, K. M.; Kazarian, S. G.; Cooper, A. I. High-Pressure Carbon Dioxide Uptake for Porous Organic Cages: Comparison of Spectroscopic and Manometric Measurement Techniques. *Chem. Commun.* **2013**, *49*, 9410−9412.
(28) Willems, T. F.; Rycroft, C. H.; Kazi, M.; Meza, J. C.; Haranczyk, M. Algorithms and Tools for High-throughput Geometry-Based Analysis of Crystalline Porous Materials. *Microporous Mesoporous Mater.* **2012**, *149*, 134−141.
(29) Martin, R. L.; Smit, B.; Haranczyk, M. Addressing Challenges of Identifying Geometrically Diverse Sets of Crystalline Porous Materials. *J. Chem. Inf. Model.* **2011**, *52*, 308−318.
(30) Jiang, S.; Jelfs, K. E.; Holden, D.; Hasell, T.; Chong, S. Y.-L.; Haranczyk, M.; Trewin, A.; Cooper, A. I. Molecular Dynamics Simulations of Gas Selectivity in Amorphous Porous Molecular Solids. *J. Am. Chem. Soc.* **2013**, *135*, 17818−17830.
(31) Dubbeldam, D.; Calero, S.; Ellis, D. E.; Snurr, R. Q. *RASPA, 1.0*, Northwestern University, Evanston, 2008.
(32) Cai, Q.; Buts, A.; Biggs, M. J.; Seaton, N. A. Evaluation of Methods for Determining the Pore Size Distribution and Pore-Network Connectivity of Porous Carbons. *Langmuir* **2007**, *23*, 8430−8440.
(33) Akten, E. D.; Siriwardane, R.; Sholl, D. S. Monte Carlo Simulation of Single- and Binary-Component Adsorption of CO_2, N_2, and H_2 in Zeolite Na-4A. *Energy Fuels* **2003**, *17*, 977−983.
(34) Rappé, A. K.; Casewit, C. J.; Colwell, K. S.; Goddard Iii, W. A.; Skiff, W. M. UFF, a Full Periodic Table Force Field for Molecular Mechanics and Molecular Dynamics Simulations. *J. Am. Chem. Soc.* **1992**, *114* (25), 10024−10035.
(35) Darkrim, F.; Levesque, D. Monte Carlo Simulations of Hydrogen Adsorption in Single-Walled Carbon Nanotubes. *J. Chem. Phys.* **1998**, *109*, 4981.
(36) Chen, B.; Siepmann, J. I. Transferable Potentials for Phase Equilibria. 3. Explicit-Hydrogen Description of Normal Alkanes. *J. Phys. Chem. B* **1999**, *103*, 5370−5379.
(37) Harris, J. G.; Yung, K. H. Carbon Dioxide's Liquid-Vapor Coexistence Curve and Critical Properties as Predicted by a Simple Molecular Model. *J. Phys. Chem.* **1995**, *99*, 12021−12024.
(38) Boda, D.; Henderson, D. The Effects of Deviations from Lorentz−Berthelot Rules on the Properties of a Simple Mixture. *Mol. Phys.* **2008**, *106*, 2367−2370.
(39) Keskin, S.; Liu, J.; Rankin, R. B.; Johnson, J. K.; Sholl, D. S. Progress, Opportunities, and Challenges for Applying Atomically Detailed Modeling to Molecular Adsorption and Transport in Metal−Organic Framework Materials. *Ind. Eng. Chem. Res.* **2008**, *48*, 2355−2371.
(40) *Materials Studio*, 5.0, Accelrys Inc., San Diego, CA, 2009.
(41) Nosé, S. A Unified Formulation of the Constant Temperature Molecular Dynamics Methods. *J. Chem. Phys.* **1984**, *81*, 511.
(42) Krishna, R.; van Baten, J. M. In Silico Screening of Zeolite Membranes for CO_2 Capture. *J. Membr. Sci.* **2010**, *360*, 323−333.
(43) Banhegyi, G. Comparison of Electrical Mixture Rules for Composites. *Colloid Polym. Sci.* **1986**, *264*, 1030−1050.
(44) Li, J. R.; Kuppler, R. J.; Zhou, H. C. Selective Gas Adsorption and Separation in Metal−Organic Frameworks. *Chem. Soc. Rev.* **2009**, *38*, 1477−1504.
(45) Li, W.; Grimme, S.; Krieg, H.; Müllmann, J.; Zhang, J. Accurate Computation of Gas Uptake in Microporous Organic Molecular Crystals. *J. Phys. Chem. C* **2012**, *116*, 8865−8871.
(46) Hasell, T.; Chong, S. Y.; Jelfs, K. E.; Adams, D. J.; Cooper, A. I. Porous Organic Cage Nanocrystals by Solution Mixing. *J. Am. Chem. Soc.* **2011**, *134*, 588−598.
(47) Holden, D.; Jelfs, K. E.; Cooper, A. I.; Trewin, A.; Willock, D. J. Bespoke Force Field for Simulating the Molecular Dynamics of Porous Organic Cages. *J. Phys. Chem. C* **2012**, *116*, 16639−16651.
(48) Krishna, R.; van Baten, J. M. Comment on Comparative Molecular Simulation Study of CO_2/N_2 and CH_4/N_2 Separation in Zeolites and Metal-Organic Frameworks. *Langmuir* **2010**, *26*, 2975−2978.
(49) Kim, J.; Martin, R. L.; Rübel, O.; Haranczyk, M.; Smit, B. High-Throughput Characterization of Porous Materials Using Graphics Processing Units. *J. Chem. Theory Comput.* **2012**, *8*, 1684−1693.
(50) Haldoupis, E.; Watanabe, T.; Nair, S.; Sholl, D. S. Quantifying Large Effects of Framework Flexibility on Diffusion in MOFs: CH_4 and CO_2 in ZIF-8. *ChemPhysChem* **2012**, *13*, 3449−3452.
(51) Keskin, S.; Sholl, D. S. Selecting Metal Organic Frameworks as Enabling Materials in Mixed Matrix Membranes for High Efficiency Natural Gas Purification. *Energy Environ. Sci.* **2010**, *3*, 343−351.
(52) Shimekit, B.; Mukhtar, H.; Murugesan, T. Prediction of the Relative Permeability of Gases in Mixed Matrix Membranes. *J. Membr. Sci.* **2011**, *373*, 152−159.
(53) Vu, D. Q.; Koros, W. J.; Miller, S. J. Mixed Matrix Membranes using Carbon Molecular Sieves: I. Preparation and Experimental Results. *J. Membr. Sci.* **2003**, *211* (2), 311−334.
(54) Budd, P. M.; Msayib, K. J.; Tattershall, C. E.; Ghanem, B. S.; Reynolds, K. J.; McKeown, N. B.; Fritsch, D. Gas Separation Membranes from Polymers of Intrinsic Microporosity. *J. Membr. Sci.* **2005**, *251*, 263−269.

THE JOURNAL OF PHYSICAL CHEMISTRY C

Article

pubs.acs.org/JPCC

Molecular Design of Amorphous Porous Organic Cages for Enhanced Gas Storage

Jack D. Evans,[§] David M. Huang,[§] Matthew R. Hill,[†] Christopher J. Sumby,[§] David S. Sholl,[‡] Aaron W. Thornton,*[,†] and Christian J. Doonan*[,§]

[†]CSIRO Manufacturing Flagship, Clayton, Victoria 3169, Australia

[‡]School of Chemical and Biomolecular Engineering, Georgia Institute of Technology, Atlanta, Georgia 30332, United States

[§]Centre for Advanced Nanomaterials, School of Physical Sciences, University of Adelaide, Adelaide, South Australia 5005, Australia

Supporting Information

ABSTRACT: Porous molecular solids are garnering increasing attention with examples of high surface areas and applications in molecular separations. Recently, amorphous networks of molecular cages have shown increased porosity with respect to their crystalline counterparts. However, the structures of amorphous materials cannot be precisely elucidated by X-ray diffraction techniques, thus molecular simulations are vital to understanding their pore structures and the origin of porosity. Here, we use GPU-accelerated molecular dynamics simulations as an efficient methodology to construct representative amorphous network structures. We employ Voronoi network analysis of amorphous networks of seven previously reported cage molecules to provide insight into structure−property relationships. Accordingly, we apply this understanding to delineate synthetic design features that give rise to highly porous analogues of chemically robust cages constructed from carbon−carbon bonds.

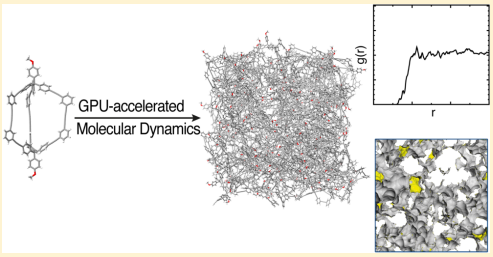

Publication Date (Web): April 1, 2015 | doi: 10.1021/jp512944r

INTRODUCTION

Porous solids are widely researched for their application to heterogeneous catalysis,[1] gas storage,[2] and molecular separations.[3] The majority of such materials are extended networks with interconnected pore channels that facilitate diffusion of adsorbates throughout the material. Recently, solids composed of shape-persistent organic cage molecules have been investigated for their bulk porosity.[4] In contrast to extended materials, such as metal−organic frameworks[5] (MOFs) or zeolites,[6] these discrete cages are soluble and thus may be readily fabricated into composite materials such as mixed-matrix membranes.[7,8]

Porosity in molecular solids can arise from the interconnection of the cage pores (intrinsic porosity), voids surrounding the cages that result from inefficient packing (extrinsic porosity), or a combination of both.[9] Accordingly, intermolecular packing has a dramatic effect on the surface accessibility of the bulk solids. This is clearly demonstrated in recent work by Doonan et al., in which two different polymorphs of the same molecule gave rise to vastly different N_2 uptakes.[10] Structure-dependent porosity has also been reported by Cooper et al. for imine-based cages.[11] Identifying the origin of porosity is most easily achieved via X-ray diffraction experiments; however, in cases where the bulk solid is amorphous, precisely characterizing the pore structure can be challenging. Consequently, the development of nonstructural methods for understanding gas diffusion in such materials is necessary.

Molecular simulations have been used to provide insight into the porosity of disordered systems, such as polymers and rigid molecules.[12,13] Recently, Jiang et al. demonstrated an atomistic understanding of H_2/N_2 separations in amorphous porous solids composed of organic cages of tetrahedral geometry.[14] In the present study, we have improved upon this approach by employing a GPU-accelerated molecular dynamics process to simulate substantially larger amorphous cage networks comprising 100 cages, which was found necessary to adequately sample the configuration space of the porous networks. We simulated amorphous networks of nine cage structures, depicted in Figure 1, to provide insight into how the porosity of these systems can be optimized.

The cage molecules used in this investigation were selected as they encompass a range of geometries, internal volumes, and external functionalities, as shown in Supporting Information (SI) Table SI-1. Specifically, **CC1** and **CC3** have equivalent volumes but possess different exohedral functionality. **CC5** is topologically equivalent to **CC1** and **CC3** but has approximately 3.8 times the internal pore volume. Cage **D1** is of

Received: December 29, 2014
Revised: March 1, 2015
Published: March 4, 2015

ACS Publications © 2015 American Chemical Society

DOI: 10.1021/jp512944r
J. Phys. Chem. C 2015, 119, 7746−7754

Publication Date (Web): April 1, 2015 | doi: 10.1021/jp512944r

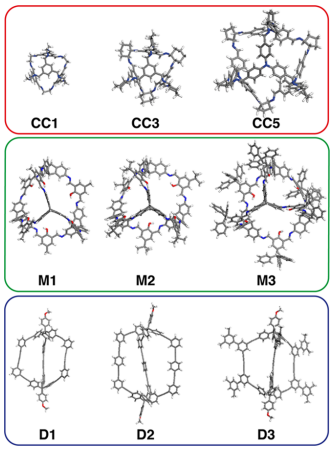

Figure 1. Molecular structures of cages investigated. The structures **CC1**, **CC3**, **CC5**, **M1**−**M3**, and **D1** have been synthesized, but **D2** and **D3** are hypothetical structures.

trigonal dipyramidal geometry and is constructed from "rod-like" alkyne moieties that give rise to very large window sizes and internal voids. Finally, cages **M1**−**M3** are of octahedral geometry with identical internal volumes, but are differentiated by their external functionality: methyl (**M1**), t-butyl (**M2**), and triphenylmethyl (**M3**).[15] Analysis of these systems, which have been synthesized and characterized experimentally, afforded design principles for optimizing the bulk porosity of amorphous solids composed of organic cage molecules. These principles were applied to generate the hypothetical cages **D2** and **D3** in Figure 1. We determined that for amorphous systems, decorating the surface of cage **D1** with sterically demanding groups gives rise to large voids in the packing structure and thus higher surface area.

SIMULATION METHODOLOGY

Molecular dynamics simulations were employed using the LAMMPS GPU-accelerated code.[16,17] A judicious choice of the force field is critical for ensuring that the packing and structural properties are accurately described. Accordingly, we used a cage-specific force field for the structures that was developed exclusively for imine cage systems.[18] Parameters not listed in the cage-specific force field were taken from a polymer-specific force field[19] that was used as the basis for the cage-specific force field. Long-range electrostatic interactions were calculated using the PPPM method.[20] A Nosé−Hoover thermostat and barostat were used to fix the temperature and pressure of the simulations.[21] Notably, the cages **CC1** and **CC3** exist in two different conformers as investigated by Jelfs and co-workers.[22] We have simplified the systems, herein, by simulating only tetrahedral conformers, specifically **CC1-R** and **CC3-R** enantiomers.

The simulation procedure used in this study is outlined in Figure 2. In the loading stage, the simulation cells were packed with 100 molecular cage structures at a density of 0.1 g·cm^{-3}, as performed by the amorphous cell module in Materials Studio 6.0. A low-density structure was used to ensure that interlocking of cage molecules or ring spearing was minimized. The assembly step comprised an NVT molecular dynamics simulation at 300 K for 500 ps with a step size of 1 fs. As depicted in Figure 3, this assembly step equilibrates the low-density structure, allowing for self-assembly and aggregation of molecules. Following the assembly step was the compression step, which was composed of an NPT molecular dynamics simulation with 1000 atm of external pressure applied at 300 K for 1000 ps with a step size of 1 fs. During this step, the simulation cell shrinks to give a reasonable target density for

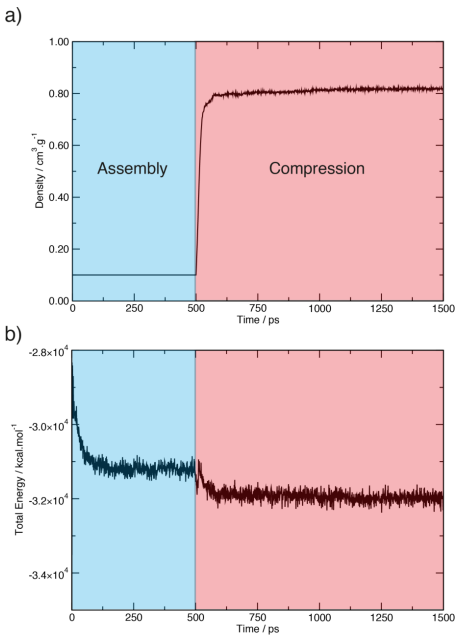

Figure 3. Representative sample of the density and total energy during assembly and compression steps of the generation procedure.

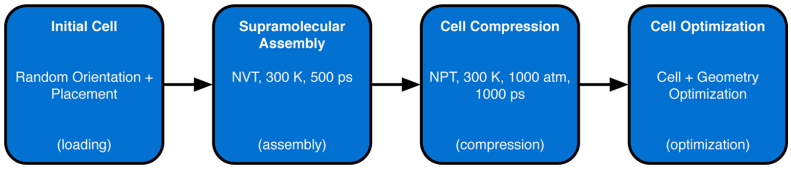

Figure 2. Outline of simulation procedure used for production of amorphous cells.

DOI: 10.1021/jp512944r
J. Phys. Chem. C 2015, 119, 7746−7754

the amorphous structure when compared with an experimentally measured density of a known amorphous cage structure.[23] Finally, the amorphous system and simulation cell were optimized by minimizing the system energy to give a final amorphous structure for subsequent analysis, as shown in Figure 4. The generation procedure was repeated for 10 independent, randomly generated initial configurations so as to sample the amorphous structural landscape and to allow the sensitivity of the amorphous porous structure to initial conditions to be quantified. All analyses discussed below are averaged over these 10 independent representations of the amorphous structure.

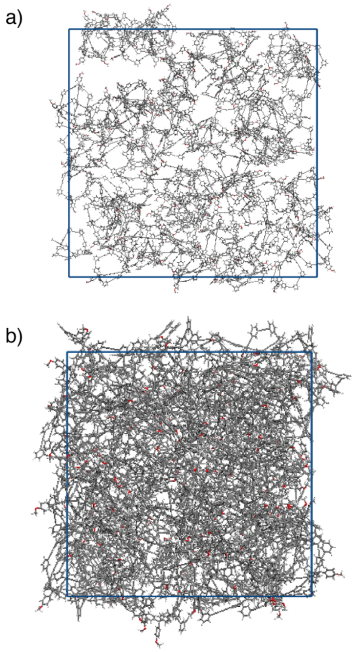

Figure 4. Example of structure **D1** at the loading step (density of 0.10 g·cm^{-3}) and after the minimization step (density of 0.78 g·cm^{-3}).

This procedure was adapted from the work of Jiang et al., with the addition of cell compression performed under an external pressure of 1000 atm. The generation methodology of Jiang and co-workers[14] required over 16×10^6 steps, whereas in this work we were able to decrease this to 2×10^6 molecular dynamic steps. To ensure the compression pressure did not collapse the cage molecules, we tested it on crystalline cells of **CC1**, **CC3**, **CC5**, **D1**, and **M1** and found the external pressure did not appreciably compress the molecules or cells, as shown in SI Table SI-2.

Geometric surface areas and pore volumes for the amorphous systems were calculated using the Zeo++ code. This code uses a Voronoi network to obtain a representation of the pore space for a periodic system.[24,25] For a specified probe size Zeo++ can determine the accessible and inaccessible pore volume. Importantly, soft materials such as porous organic cages have been reported to have dynamic connectivity between accessible and inaccessible regions. This has been investigated in crystalline materials,[26] but has not been elucidated for amorphous systems owing to the disordered alignment of pores. As a consequence, we have defined the total surface area and pore volume as the sum of the accessible and inaccessible regions as defined by Zeo++ so that regions accessible by dynamic pore-opening events are not overlooked. Finally, extrinsic volumes were calculated for He probe sizes and by blocking the internal cage volume with a sphere of size equivalent to the internal van der Waals diameter of the cage, as shown in SI Table SI-3.

RESULTS AND DISCUSSION

Effect of System Size on Porosity and Density of CC3. One of the primary challenges encountered when simulating amorphous materials is to efficiently capture the disorder of a real system with finite periodic simulation cells. To accurately describe such systems, large periodic cells combined with many independent iterations are required. The methodology employed in this study allows us to efficiently simulate cells with more than 100 molecules. We note that a previous report used cells that contained a maximum of 60 molecules.[14] As a test, we chose to study the resulting density and porosity of **CC3** as a function of the number of cage molecules per periodic cell. **CC3** was chosen for this preliminary investigation as it had been previously studied in detail by Cooper et al. Figure 5 shows that the average density and total surface area of the amorphous networks are essentially the same for all system sizes studied, but a significant change in the variance is observed as the number of molecules per simulation cell is increased, as expected from the Central Limit Theorem.[27] This is consistent with simulation data reported for amorphous polymeric structures and is attributed to the inability of small simulation sizes to effectively sample the 3-D molecular arrangement and pore structures.[28] Upon increasing the sample size to 100 or more molecules per simulation cell, the simulations converge to a density and surface area in reasonable agreement with the experimentally reported surface area.[14] For systems of 50 molecules or less, the simulated surface area overlaps the experimental value, but the standard deviation is over 18%. This analysis highlights the importance of employing large molecular sample sizes to capture, with minimal variance, the density and porosity of amorphous materials.

To further highlight the importance of sample size in molecular amorphous materials, we measured the radial distribution functions (RDFs) of the molecular centers-of-mass for the systems with 25, 50, and 100 molecules per simulation cell, as shown in Figure 6. The RDF measures the density distribution of cage molecules around a cage molecule centered at the origin. It is clear from this plot that structural correlations between molecules extend beyond half the simulation box length for samples of less than 50 molecules. This means that a molecule could be spatially correlated with more than one periodic image of another particle, potentially introducing unphysical structural correlations that would make the simulated structure unrepresentative of that of an extended amorphous system. In contrast, the RDF of the sample containing 100 molecules converges to one at half the box length and thus finite-size effects should not be significant in this system.

Amorphous Networks of CC1, CC3, CC5, D1, and M1−M3. We applied the methodology outlined in Figure 2 to seven reported cage systems: **CC1**, **CC3**, **CC5**, **D1**, and **M1−M3**

Publication Date (Web): April 1, 2015 | doi: 10.1021/jp512944r

DOI: 10.1021/jp512944r
J. Phys. Chem. C 2015, 119, 7746−7754

Publication Date (Web): April 1, 2015 | doi: 10.1021/jp512944r

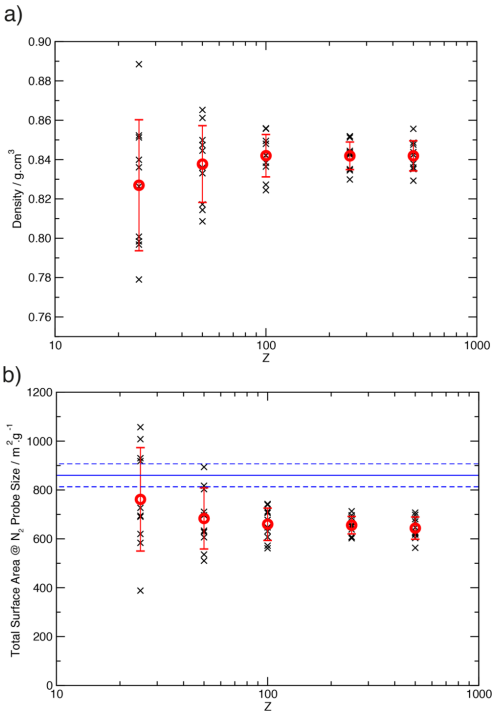

Figure 5. (a) Density and (b) total surface area of amorphous **CC3** structures as a function of number of molecules per simulation cell (Z). Data from unique simulations are depicted as crosses (black) and the average over these simulations is shown as circles (red). A blue solid line denotes the experimental surface area, with the error depicted as a blue dotted line.

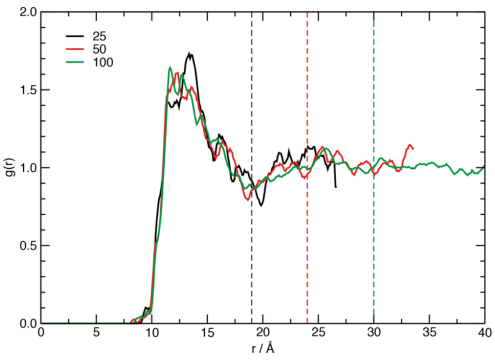

Figure 6. Radial distribution functions (RDFs) for the cage center-of-mass for samples of **CC3** with 25, 50, and 100 molecules per simulation cell. Half-cell lengths are depicted by vertical dotted lines.

(Figure 1), resulting in structural models of amorphous networks with average densities listed in Table 1. We note that the density of the amorphous networks lies between 0.566 and 0.873 g·cm^{-3} and varies significantly for the selected cage molecules. The densest amorphous structure is observed for **CC1** as a consequence of the smaller cage volume and bare external functionality. By comparison, a much less dense structure is found for **M3** as a result of the large cage volume and bulky external triphenylmethyl moieties.

Table 1. Resulting Amorphous Cell Densities

cage	density/g·cm^{-3}
CC1	0.873 ± 0.013
CC3	0.842 ± 0.011
CC5	0.658 ± 0.018
D1	0.791 ± 0.010
M1	0.838 ± 0.018
M2	0.671 ± 0.023
M3	0.556 ± 0.017

To aid in the comparison of supramolecular arrangements, we calculated the radial distribution function for the centers-of-mass of each of the cages in the simulation cell. The average RDF from the 10 independent simulations for each of the seven cage systems is displayed in Figure 7. The RDFs calculated for networks of **CC1**, **CC3**, and **CC5** (Figure 7a) demonstrate the effect of external functionality and cage size on the supramolecular arrangement of the molecular units. Attachment of sterically demanding cyclohexyl moieties in **CC3** yields a broad distribution, an effect of the cyclohexyl groups directing the cage units to pack into a less dense network than the functionally bare units of **CC1**. The distribution is broadened further and displaced to greater distance as a consequence of the larger cage size of **CC5** generating an increased average cage−cage distance of ∼15 Å, thus producing low-density amorphous structures. The first peak in the RDF of **D1** (Figure 7b), unlike that in the RDFs of **CC1**, **CC3**, and **CC5**, does not correspond to the size of the molecule, with significant density observed at distances less than 10 Å. This behavior can be attributed to the elongated pyramidal geometry of the cage unit, which allows the units to pack in a dense interdigitated fashion, as shown in Figure 8. Finally, the calculated RDFs for the amorphous structures of **M1**−**M3** provide further evidence that bulky functional groups yield inefficient packing and larger cage−cage distances. For example, increasing the external functional groups from methyl (**M1**) to t-butyl (**M2**) and triphenylmethyl (**M3**) results in a broadening of the primary RDF peak and a displacement to a larger average distance.

Pore Structure Analysis of CC1, CC3, CC5, D1, and M1−M3: Role of Extrinsic Porosity. The bulk porosity of the amorphous networks was probed by Voronoi network analysis. Pore volumes and surface areas were simulated using probe sizes equivalent to the kinetic diameters of He (2.60 Å) and N_2 (3.64 Å), respectively, to give the resulting average values in Table 2. The average pore volume is plotted against the intrinsic cage volume and radius of gyration in Figure 9. The radius of gyration was used as a measure of the size of the cage molecule. Our simulations show no correlation between the cage volume and total pore volume. For example, a large difference in pore volume is observed for the series **M1**−**M3** as a result of external functionality influencing the pore structure, but the cage volume itself does not vary across this series of molecules. In addition, in spite of the large cage volume of **D1**, the resulting pore volume is modest by virtue of the close packing of molecular units. In contrast to the lack of correlation for cage volume, there is a general trend for porosity with the radius of gyration, which varies with both the internal cage

DOI: 10.1021/jp512944r
J. Phys. Chem. C 2015, 119, 7746−7754

Publication Date (Web): April 1, 2015 | doi: 10.1021/jp512944r

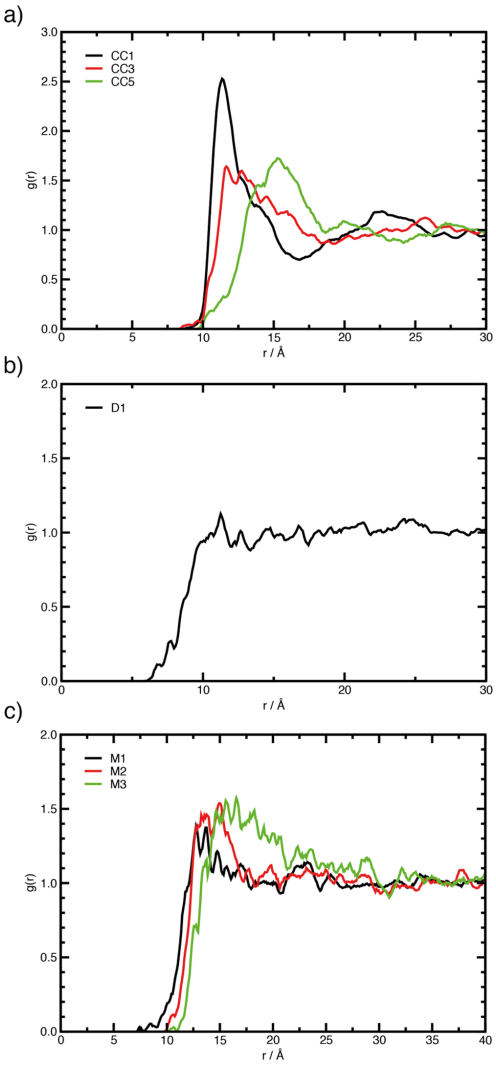

Figure 7. RDFs for the cage center-of-mass for structures (a) **CC1**, **CC3**, and **CC5**; (b) **D1**; and (c) **M1**−**M3**.

volume and external functionality (Figure 9b). For instance, the largest radii of gyration are a result of bulky external functionality (**M3**) or large cage structure (**CC5**), which in turn produce amorphous pore networks of large volumes and surface areas. From these results we can qualitatively conclude that molecules with large size produce amorphous structures with high surface areas and pore volumes and that this can be achieved by either constructing large cages or by decorating the surface of the cage with sterically bulky groups.

To further understand the porosity in these systems, pore size distributions were calculated and averaged over the 10 independent simulations; the distributions are depicted in

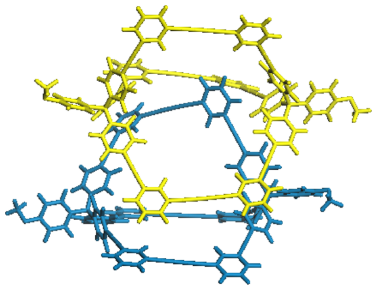

Figure 8. Representation of the interdigitated motif observed in amorphous structures of **D1**.

Table 2. Average Total Surface Areas for N_2 Probe Size and Total Pore Volume for He Probe Size for the Amorphous Cage Structures

cage	total surface area/$m^2 \cdot g^{-1}$	total pore volume/$cm^3 \cdot g^{-1}$
CC1	528 ± 77	0.076 ± 0.021
CC3	660 ± 66	0.097 ± 0.013
CC5	1815 ± 73	0.377 ± 0.034
D1	1211 ± 70	0.187 ± 0.012
M1	1168 ± 95	0.186 ± 0.021
M2	1759 ± 100	0.410 ± 0.044
M3	1892 ± 73	0.722 ± 0.056

Figure 10. Pore size distributions were simulated using the Zeo++ code; details of this method have been reported previously.[29] Cage **CC1**, as the result of close packing of cage units, has a pore size distribution with a sharp peak at ∼5 Å. Sholl and co-workers have shown that materials with sharp and rigid pore size distributions are amendable to kinetic gas separations.[30] Importantly, this has been observed experimentally with amorphous samples of **CC1** prepared by freeze-drying, which possess excellent H_2/N_2 selectivity.[14] The pore structure of **CC3** differs from that of **CC1**, with exohedral cyclohexane groups supporting larger pore diameters with sizes of 5−10 Å. Notably, **CC1** and **CC3** possess identical cages and this results in their pore networks having equivalent limiting pore sizes. Finally, the pore structure of **CC5** has a broad distribution, owing to the combination of the large cage volume and bulky external functionality. The pore size distributions of **M1**−**M3** clearly demonstrate the increase in porosity supported by increasingly bulky moieties. First, the distribution for **M1** reflects the internal cage cavities, as the peak observed is equivalent to the internal diameter of the molecular cage. In comparison, **M2** and **M3** have larger molecular size increased by the attachment of bulky functionality. This produces broader pore size distributions as the disruption of close packing by the external functionality creates large extrinsic voids. Experimentally, Mastalerz and co-workers found that amorphous materials of **M1**−**M3** had similar BET surface area.[15] However, these materials were analyzed as synthesized, not produced amorphously on purpose and thus may not be truly amorphous networks.

Amorphous molecular cage structures differ from their polymer analogues, as the source of disordered porous networks made from molecular cages differ fundamentally from their polymer analogues in that porosity can originate from two distinct sources: the internal cavity of the molecule

DOI: 10.1021/jp512944r
J. Phys. Chem. C 2015, 119, 7746−7754

Publication Date (Web): April 1, 2015 | doi: 10.1021/jp512944r

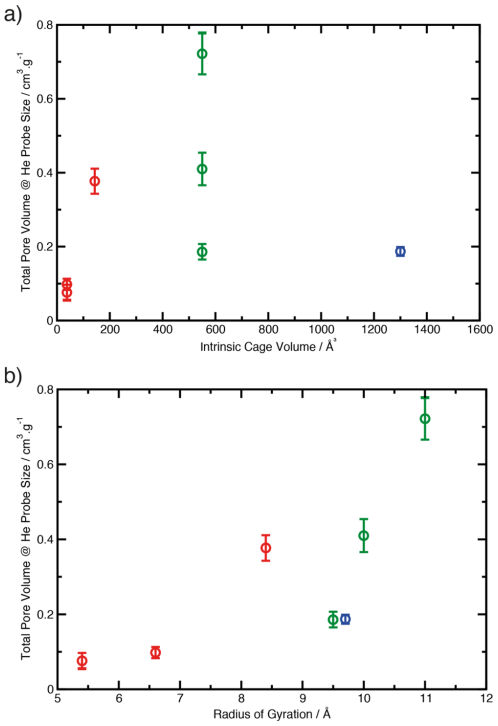

Figure 9. Average total pore volume for He probe radius against the (a) intrinsic cage volume and (b) radius of gyration. **CC1**, **CC3**, and **CC5** (red), **D1** (blue), and **M1**−**M3** (green).

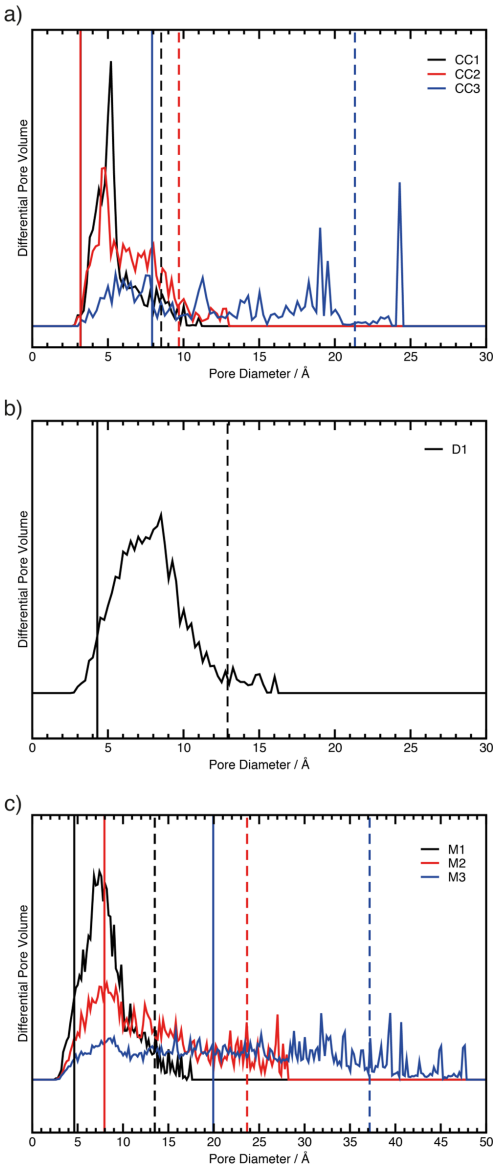

Figure 10. Pore size distributions for the amorphous networks resulting from structures (a) **CC1**, **CC3**, and **CC5**, (b) **D1**, and (c) **M1**−**M3**, along with average limiting pore diameter (vertical solid line) and average largest pore diameter (vertical dotted line).

(intrinsic porosity) and the space external to the molecules formed by the supramolecular arrangement (extrinsic porosity). It is important to consider the source of the porosity when discussing the pore structure in these materials; as such the intrinsic and extrinsic pore volumes were measured in our generated systems, with the results displayed in Figure 11. Importantly, the amount of extrinsic porosity observed for **CC1** and **CC3** amorphous systems is equivalent to estimates previously reported; the larger cyclohexyl groups in **CC3** produce a greater extrinsic volume by disrupting close packing. Increasing the cage size in **CC5** results in an amorphous network with a slightly smaller ratio of extrinsic:intrinsic volume compared with **CC3**, as the intrinsic volume of the cage is larger but the external packing is similar to that of **CC3**. In contrast, **D1** has significantly less extrinsic porosity than **CC1**, **CC3**, and **CC5**, as shown in Figure 11b, as a result of the molecular units packing in close proximity, which interconnects cage volumes. Finally, the trend in pore volume and pore size distributions for **M1**−**M3** is clearly explained by the extrinsic pore percentage. Cages with bulky external moieties, such as **M3**, support large extrinsic voids, as depicted in Figure 11c. This packing results in broad and undefined pore sizes, as observed in the pore size distributions. In summary, the source of porosity in these materials is vital to understand the trends in porosity observed in this study: we find an increase in porosity in these amorphous systems is primarily a result of increasing the extrinsic porosity.

The potential advantages of amorphous networks are clearly evident when their surface areas and densities are compared with those of their crystalline counterparts. For example, SI

DOI: 10.1021/jp512944r
J. Phys. Chem. C 2015, 119, 7746−7754

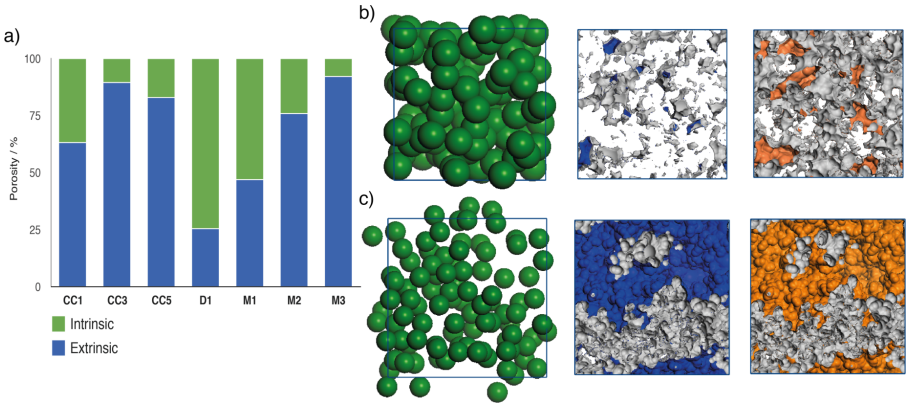

Figure 11. (a) Averaged contribution to the pore structure from intrinsic and extrinsic porosity and an example for (b) **D1** and (c) **M3**, with green spheres denoting the intrinsic pore structure, blue regions showing the extrinsic pore structure, and orange regions illustrating the total.

Publication Date (Web): April 1, 2015 | doi: 10.1021/jp512944r

Table SI-4 shows how amorphous packing is able to unlock porosity that may not be possible to realize in crystalline polymorphs.

In Silico Design of D1 Analogues. The analysis above has outlined several general principles for designing the porosity of amorphous cage molecules. We sought to use these observations to optimize **D1** analogues for increased surface area in the amorphous state. The present study has found two general strategies, applied to the molecular units, to increase the porosity of amorphous cage systems: increasing the encapsulated cage volume (**CC3** and **CC5**) and introducing sterically bulky groups to the external surface of the cage (**M1**−**M3**). Accordingly, we have applied these principles to **D1** in the effort to produce an extremely porous structure. The hypothetical structure **D2** was realized by increasing the volume of **D1** by incorporation of phenyl rings to the dialkyne struts. Furthermore, a cage with bulky external functionality, **D3**, was constructed by adding mesityl groups to the vertices of **D1**. The two **D1** analogues, both shown in Figure 1, were selected to be synthetically feasible.

The density, surface area, and pore volume of amorphous cage networks for the **D1**−**D3** series is displayed in Table 3. It

Table 3. Average Densities, Total Surface Areas, and Pore Volumes for Amorphous Structures D1−D3

cage	density/g·cm^{-3}	total surface area/ m^2·g^{-1}	total pore volume/ cm^3·g^{-1}
D1	0.791 ± 0.010	1211 ± 70	0.187 ± 0.012
D2	0.859 ± 0.011	804 ± 66	0.118 ± 0.011
D3	0.593 ± 0.024	1933 ± 70	0.554 ± 0.069

is clear that the larger volume cage **D2** structure produces an amorphous network with higher density and lower surface area and pore volume than the original **D1**. In contrast, functionalization by bulky mesityl groups in **D3** results in a less dense amorphous structure with increased surface area and pore volume.

Examination of RDFs in Figure 12a reveals the underlying reason for these observations. The increased cage size of **D2** not only produces large internal volume but also generates larger molecular windows and greater flexibility. A consequence

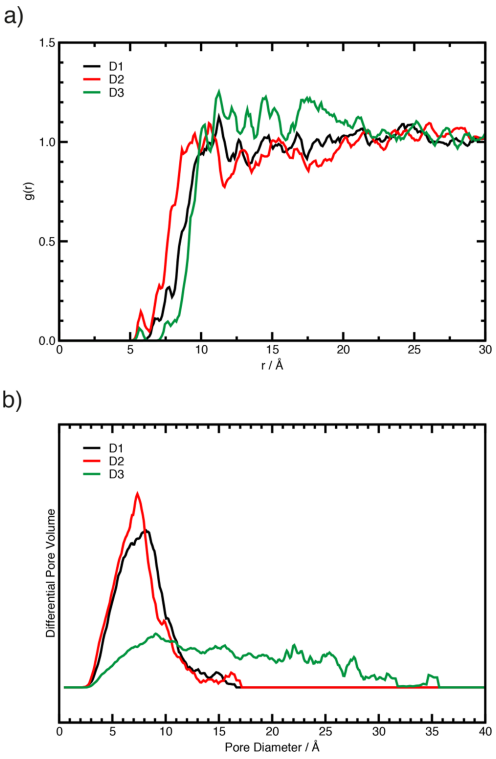

Figure 12. Average (a) RDFs and (b) pore size distributions for **D1**−**D3**.

of this is a greater degree of interdigitation, as evidenced by the peak in the RDF at shorter distances and higher density compared with **D1**. In contrast, the RDF for amorphous structures of **D3** is displaced to larger distance and broadened.

DOI: 10.1021/jp512944r
J. Phys. Chem. C 2015, 119, 7746−7754

Absence of close packing cages at <8 Å and the broad distribution suggests that the mesityl functionality disrupts the close-packing motif observed for **D1** and **D2**. Additionally, calculation of the ratio of extrinisic:intrinsic porosity of the amorphous networks supports this conclusion, as shown in SI Table SI-5. Porosity for **D1** and **D2** structures is primarily a consequence of the intrinsic volume of the molecular cages, whereas **D3** has 76% of its pore volume associated with regions extrinsic to molecular units. Furthermore, the pore size distribution (Figure 11b) for **D3** demonstrates larger pore sizes are present in the amorphous system and the lack of defined pore sizes observed for **D1** and **D2**.

We have successfully tested the amorphous networks of hypothetical analogues of **D1** for porosity and morphology. In contrast to what was found for the **CC1** analogues, **CC3** and **CC5**, we find that increasing the internal volume in **D2** results in lower porosity due to the shape of molecular units allowing closer packing. However, by increasing the steric bulk external to the cage, as observed for **M1**−**M3**, we find the structure **D3** has increased pore volume and surface area, making this cage molecule an ideal candidate for synthesis.

CONCLUSION

Herein we describe an efficient computational methodology for generating representative amorphous cells composed of porous organic cages. Importantly, we have improved significantly on previously reported methods through the use of external pressure during the compression stage and the use of GPU-accelerated molecular dynamics. Moreover, we have examined the porosity and morphology of the structures using Voronoi network analysis and center-of-mass radial distribution functions. We find good agreement between the simulated surface area of our **CC3** model and previously reported adsorption experiments. It is clear that the models described in this study give fundamental insight into these amorphous materials, which is unobtainable by experimental methods alone.

Our investigation has elucidated several important features of the nature of porous organic cage amorphous networks. First, on the subject of generation of representative amorphous models, we have demonstrated a modest effect of system size on the resulting density and porosity of the generated amorphous structure. Specifically, the **CC3** system demonstrates a large variance in the density and porosity of systems comprising less than 100 molecules per simulation cell. This result directed our methodology to use simulation cells of 100 molecules to ensure an accurate and precise representation of random packing of cage units. Second, we have gleaned general principles that govern the morphology and porosity in the amorphous state by applying our methodology to seven reported cage structures encompassing several distinct molecular geometries. Two key relationships are observed: a large encapsulated internal volume of the cage molecule can produce high-porosity amorphous structures (**CC5**), and bulky external functionality can yield highly porous structures by supporting greater pore volume extrinsic to the molecular units (**M3**). However, cage geometry is crucial to defining the resulting morphology. In particular, we find that the cage **D1** is able to interdigitate and consequently produces amorphous networks with unexceptional pore volume despite the large internal volume and cage size. Lastly, we have applied this understanding to optimizing the surface area of hypothetical analogues of **D1**. A novel analogue, **D3**, with bulky mesityl groups attached external to the cage was found to produce an amorphous structure with increased porosity as a consequence of extrinsic pore volume.

This investigation has unequivocally demonstrated that molecular simulations can give atomistic insight into amorphous porous organic cages. This has allowed us to carry out de novo design of amorphous solids for applications in gas storage, which has previously only been applied for crystalline porous solids.

ASSOCIATED CONTENT

Supporting Information

Structural features, high-pressure crystalline simulations, blocking sphere diameters, crystalline porosity, and extrinsic:intrinsic pore volumes for **D1**−**D3**. This material is available free of charge via the Internet at http://pubs.acs.org.

AUTHOR INFORMATION

Corresponding Authors

*aaron.thornton@csiro.au.
*christian.doonan@adelaide.edu.au.

Author Contributions

The manuscript was written through contributions of all authors. All authors have given approval to the final version of the manuscript.

Notes

The authors declare no competing financial interest.

ACKNOWLEDGMENTS

A.W.T. and J.D.E .acknowledge the Computational and Simulation Sciences Transformational Capability Platform at the CSIRO for funding and resources. D.S.S. acknowledges support from the U.S. Department of Energy Office of Basic Energy Sciences under award DE-FG02-12ER16362 as part of the Nanoporous Materials Genome Center. C.J.D. thanks the Australian Research Council for Funding (DP120103909 and FT100100400).

REFERENCES

(1) Lee, J.; Farha, O. K.; Roberts, J.; Scheidt, K. A.; Nguyen, S. T.; Hupp, J. T. Metal−organic Framework Materials as Catalysts. *Chem. Soc. Rev.* **2009**, *38*, 1450−1459.
(2) Morris, R. E.; Wheatley, P. S. Gas Storage in Nanoporous Materials. *Angew. Chem., Int. Ed.* **2008**, *47*, 4966−4981.
(3) Li, J.-R.; Sculley, J.; Zhou, H.-C. Metal−Organic Frameworks for Separations. *Chem. Rev.* **2012**, *112*, 869−932.
(4) Cooper, A. I. Nanoporous Organics Enter the Cage Age. *Angew. Chem., Int. Ed.* **2011**, *50*, 996−998.
(5) Furukawa, H.; Cordova, K. E.; O'Keeffe, M.; Yaghi, O. M. The Chemistry and Applications of Metal-Organic Frameworks. *Science* **2013**, *341*, 1230444.
(6) Davis, M. E. Ordered Porous Materials for Emerging Applications. *Nature* **2002**, *417*, 813−821.
(7) Evans, J. D.; Huang, D. M.; Hill, M. R.; Sumby, C. J.; Thornton, A. W.; Doonan, C. J. Feasibility of Mixed Matrix Membrane Gas Separations Employing Porous Organic Cages. *J. Phys. Chem. C* **2014**, *118*, 1523−1529.
(8) Bushell, A. F.; Budd, P. M.; Attfield, M. P.; Jones, J. T. A.; Hasell, T.; Cooper, A. I.; Bernardo, P.; Bazzarelli, F.; Clarizia, G.; Jansen, J. C. Nanoporous Organic Polymer/Cage Composite Membranes. *Angew. Chem., Int. Ed.* **2013**, *52*, 1253−1256.
(9) Tozawa, T.; Jones, J. T. A.; Swamy, S. I.; Jiang, S.; Adams, D. J.; Shakespeare, S.; Clowes, R.; Bradshaw, D.; Hasell, T.; Chong, S. Y.; et al. Porous Organic Cages. *Nat. Mater.* **2009**, *8*, 973−978.

Publication Date (Web): April 1, 2015 | doi: 10.1021/jp512944r

(10) Avellaneda, A.; Valente, P.; Burgun, A.; Evans, J. D.; Markwell-Heys, A. W.; Rankine, D.; Nielsen, D. J.; Hill, M. R.; Sumby, C. J.; Doonan, C. J. Kinetically Controlled Porosity in a Robust Organic Cage Material. *Angew. Chem.* **2013**, *125*, 3834−3837.
(11) Jones, J. T. A.; Holden, D.; Mitra, T.; Hasell, T.; Adams, D. J.; Jelfs, K. E.; Trewin, A.; Willock, D. J.; Day, G. M.; Bacsa, J.; et al. On−Off Porosity Switching in a Molecular Organic Solid. *Angew. Chem.* **2011**, *123*, 775−779.
(12) Abbott, L. J.; Colina, C. M. Formation of Microporosity in Hyper-Cross-Linked Polymers. *Macromolecules* **2014**, *47*, 5409−5415.
(13) Abbott, L. J.; McDermott, A. G.; Del Regno, A.; Taylor, R. G. D.; Bezzu, C. G.; Msayib, K. J.; McKeown, N. B.; Siperstein, F. R.; Runt, J.; Colina, C. M. Characterizing the Structure of Organic Molecules of Intrinsic Microporosity by Molecular Simulations and X-Ray Scattering. *J. Phys. Chem. B* **2013**, *117*, 355−364.
(14) Jiang, S.; Jelfs, K. E.; Holden, D.; Hasell, T.; Chong, S. Y.; Haranczyk, M.; Trewin, A.; Cooper, A. I. Molecular Dynamics Simulations of Gas Selectivity in Amorphous Porous Molecular Solids. *J. Am. Chem. Soc.* **2013**, *135*, 17818−17830.
(15) Schneider, M. W.; Oppel, I. M.; Ott, H.; Lechner, L. G.; Hauswald, H.-J. S.; Stoll, R.; Mastalerz, M. Periphery-Substituted [4 + 6] Salicylbisimine Cage Compounds with Exceptionally High Surface Areas: Influence of the Molecular Structure on Nitrogen Sorption Properties. *Chem. − Eur. J.* **2012**, *18*, 836−847.
(16) Brown, W. M.; Wang, P.; Plimpton, S. J.; Tharrington, A. N. Implementing Molecular Dynamics on Hybrid High Performance Computers − Short Range Forces. *Comput. Phys. Commun.* **2011**, *182*, 898−911.
(17) Plimpton, S. Fast Parallel Algorithms for Short-Range Molecular Dynamics. *J. Comput. Phys.* **1995**, *117*, 1−19.
(18) Holden, D.; Jelfs, K. E.; Cooper, A. I.; Trewin, A.; Willock, D. J. Bespoke Force Field for Simulating the Molecular Dynamics of Porous Organic Cages. *J. Phys. Chem. C* **2012**, *116*, 16639−16651.
(19) Sun, H. Ab Initio Calculations and Force Field Development for Computer Simulation of Polysilanes. *Macromolecules* **1995**, *28*, 701−712.
(20) Pollock, E. L.; Glosli, J. Comments on P3M, FMM, and the Ewald Method for Large Periodic Coulombic Systems. *Comput. Phys. Commun.* **1996**, *95*, 93−110.
(21) Evans, D. J.; Holian, B. L. The Nose−Hoover Thermostat. *J. Chem. Phys.* **1985**, *83*, 4069−4074.
(22) Jelfs, K. E.; Schiffmann, F.; Jones, J. T. A.; Slater, B.; Cora, F.; Cooper, A. I. Conformer Interconversion in a Switchable Porous Organic Cage. *Phys. Chem. Chem. Phys.* **2011**, *13*, 20081−20085.
(23) Jiang, S.; Jones, J. T. A.; Hasell, T.; Blythe, C. E.; Adams, D. J.; Trewin, A.; Cooper, A. I. Porous Organic Molecular Solids by Dynamic Covalent Scrambling. *Nat. Commun.* **2011**, *2*, 207.
(24) Martin, R. L.; Smit, B.; Haranczyk, M. Addressing Challenges of Identifying Geometrically Diverse Sets of Crystalline Porous Materials. *J. Chem. Inf. Model.* **2012**, *52*, 308−318.
(25) Willems, T. F.; Rycroft, C. H.; Kazi, M.; Meza, J. C.; Haranczyk, M. Algorithms and Tools for High-Throughput Geometry-Based Analysis of Crystalline Porous Materials. *Microporous Mesoporous Mater.* **2012**, *149*, 134−141.
(26) Holden, D.; Jelfs, K. E.; Trewin, A.; Willock, D. J.; Haranczyk, M.; Cooper, A. I. Gas Diffusion in a Porous Organic Cage: Analysis of Dynamic Pore Connectivity Using Molecular Dynamics Simulations. *J. Phys. Chem. C* **2014**, *118*, 12734−12743.
(27) Reichl, L. E. *A Modern Course in Statistical Physics*, 3rd revised and updated ed.; Wiley-VCH: Weihheim, 2009.
(28) Hart, K. E.; Abbott, L. J.; Colina, C. M. Analysis of Force Fields and BET Theory for Polymers of Intrinsic Microporosity. *Mol. Simul.* **2013**, *39*, 397−404.
(29) Pinheiro, M.; Martin, R. L.; Rycroft, C. H.; Jones, A.; Iglesia, E.; Haranczyk, M. Characterization and Comparison of Pore Landscapes in Crystalline Porous Materials. *J. Mol. Graph. Model.* **2013**, *44*, 208−219.
(30) Haldoupis, E.; Watanabe, T.; Nair, S.; Sholl, D. S. Quantifying Large Effects of Framework Flexibility on Diffusion in MOFs: CH_4 and CO_2 in ZIF-8. *ChemPhysChem* **2012**, *13*, 3449−3452.

Publication Date (Web): April 1, 2015 | doi: 10.1021/jp512944r

DOI: 10.1021/jp512944r
J. Phys. Chem. C 2015, 119, 7746−7754